THE UNIVERSITY OF CHICAGO

PROBING UNIVERSAL FINGERPRINTS OF QUANTUM STATES: FROM QUANTUM ENTANGLEMENT TO CONFORMAL FIELD THEORY

A DISSERTATION SUBMITTED TO
THE FACULTY OF THE DIVISION OF THE PHYSICAL SCIENCES
IN CANDIDACY FOR THE DEGREE OF
DOCTOR OF PHILOSOPHY

DEPARTMENT OF PHYSICS

BY
YUHAN LIU

CHICAGO, ILLINOIS
JUNE 2023

To my parents

TABLE OF CONTENTS

LIST OF FIGURES

LIST OF TABLES

ACKNOWLEDGMENTS

First and foremost, I would like to thank my advisor, Shinsei Ryu. Shinsei's curiosity and knowledge of a wide range of realms in theoretical physics are an inspiration for me. During our discussions, he always amazes me with his insight to relate seemingly uncorrelated pieces of knowledge, which turns out to be crucial to many of our discoveries. Besides being an outstanding theoretical physicist with profound insights, he is also very down to earth. I still remember vividly that in my third year, he showed me how to do numerical simulation for quantum spin chains using Python, line by line, to confirm our field theory prediction. I will keep learning from him for the years to come.

I was very fortunate to have the chance to visit KITP and work with Andreas Ludwig. Andreas pushed me to think thoroughly about whatever I brought up and never missed a detail, and supported my academic pursuit, for which I am deeply grateful.

It is hard to count how much I have learned from all my wonderful collaborators: Paolo Glorioso, Kohei Kawabata, Jonah Kudler-Flam, Yuya Kusuki, Hassan Shapourian, Ramanjit Sohal, and Yijian Zou. The discussions with them show me the true enthusiasm of young scientists and make me believe young scientists can choose to work on what they truly value, not merely follow the trends. I will not forget all those excitements of breakthrough, like the shining stars in the night sky.

I am grateful to my committee members, Clay Cordova, Michael Levin, and Jon Simons for all their support and instructive suggestions.

The PhD journey is impossible without the support and accompanies of friends. I thank my amazing 18' cohort, and friends at Kadanoff Center, Jadwin Hall, and Kavli Institute. Moving to new places can be frightening, and it is a blessing to have the friendship with all of you.

I thank my parents, who endure the separation of thousands of miles over the past five years. I will never come this far without their support and encouragement. Both my parents

set me examples of lifelong readers and learners; I miss the old days when we spent the whole Sunday afternoons in the city library. I wish my parents could also be here at this moment and share my joy.

Finally, I am grateful to Changtai for his encouragement, patience, accompany, love, small animal poems, and hand-drawn comics. I am looking forward to the next chapter ahead of us.

ABSTRACT

Understanding the universal behaviors in quantum phases of matter lies among the long-term dreams of condensed matter physicists. However, relating universal behaviors to physical observables is challenging. Surprisingly, knowledge from other realms of physics brings unique insights into this subject. In this thesis, we will develop two useful tools: quantum entanglement and conformal field theory, which are widely used in the study of quantum information science and string theory, respectively. We will show how they reveal the previously unknown universal information of three different systems: topological liquid, random quantum states, and critical spin chains. These three systems are typical examples of the area law entanglement scaling phase, volume law entanglement scaling phase, and logarithmic law entanglement scaling phase, respectively.

We start by examing the topological liquids. The universal features of topological liquids make them useful for topological quantum computation and quantum error correction. In such systems, a piece of universal information, the quantum dimension, is encoded in the constant term of von Neumann entanglement entropy. However, von Neumann entanglement entropy only captures the bipartite entanglement structure, while more universal features can be encoded in the multipartite entanglement structures. Specifically, we investigate the reflected entropy – a tripartite entanglement quantity. We unveil the reflected entropy yields a novel universal form of two-dimensional chiral topological liquid, capturing its central charge. To derive this result, we exploit the bulk-boundary correspondence, approximating the ground state of chiral topological liquid by vertex state in boundary conformal field theory. The entanglement quantities of the vertex state are then computed by explicit numerical calculation and the conformal interface method.

We next move on to random quantum states. The entanglement entropy of a typical state in a random ensemble exhibits the volume law scaling. Understanding the typical entanglement of random states thus provides insights into thermalization and quantum chaos.

Specifically, we study von Neumann entanglement entropy of random free fermion states in the presence of ten fundamental symmetry classes. We find the fingerprint of different symmetries lies in the constant term of typical entanglement entropy and the entanglement variance. Our results establish the symmetry classification of typical quantum entanglement and the role of symmetry in quantum chaos.

The discussion of boundary conformal field theory brings us to the second important tool, conformal field theory, a powerful framework for studying the critical (gapless) phases. Given a critical quantum lattice model, it is crucial yet difficult to extract the underlying conformal data. In this subject, we develop the method of wavefunction overlap, which can extract all conformal data from a critical quantum lattice model. Our key insight is that the universal finite-size correction of the wavefunction overlap is dictated by the orbifold conformal field theory, obtained by gauging the symmetry in the replicated theory. Importantly, our method bridges the gap of operator product expansion coefficient extraction, where a numerical method was lacking. The power of our method is readily demonstrated by unveiling new data of the newly proposed Haagerup model built from the Haagerup fusion category.

Finally, we discuss how the tools developed in this thesis can be generalized to study more exotic quantum systems, which might lead to future projects.

CHAPTER 1

INTRODUCTION

One fascinating task of physicists is exploring and understanding the world around us. While high-energy physicists question the particles at high energy scales, condensed matter physicists are devoted to going to low energy. Indeed, many seemingly different systems show the *universal* behaviors at low energy and long distance: the behaviors governed by the symmetry or topology of the state, insensitive to the microscopic details.

The quest for universal properties in classical phases of matter dated back to Landau, who realized the importance of *symmetry* and developed the theory of spontaneous symmetry breaking and phase transition theory. Many physical observables, such as the two-point correlation functions, are universally governed by critical exponents.

Thanks to the development of experimental techniques, condensed matter physicists are able to go to even lower temperature where the quantum effect starts to dominate. This brings the quest for universal properties in the quantum phases of matter. Ever since the discovery of integer and fractional quantum hall effect, physicists began to realize the importance of *topology*, which is closely tied to the universal non-local properties such as boundary current, ground state degeneracy, and fractional excitations.

This brings up the questions: how to detect these universal fingerprints given the low energy states; and based on that, how to distinguish different quantum phases of matter. In this thesis, we target these questions, but from the points of view of quantum entanglement and conformal field theory (CFT).

Quantum entanglement stems in the center of quantum mechanics. Regarded as a "spooky action" in the early days, the existence of quantum entanglement is well established in our era with the experimental verification of Bell inequalities and quantum teleportation. Quantum entanglement is a significant resource in various quantum technologies: quantum cryptography, quantum teleportation, and quantum computation, to name but a few.

Perhaps surprisingly, quantum entanglement also provides a valuable tool to probe the universal behaviors of quantum matters. Specifically, we separate the degrees of freedom of a state into two or more parts and compute the entanglement among these subregions. We ask how the entanglement changes as we change the size of the subregions, dubbed "entanglement scaling". Depending on the systems under interest, the entanglement scaling shows the following three drastically different behaviors: area law, volume law, and logarithmic law. For the gapped ground state, the von Neumann entanglement entropy follows the *area law* scaling behavior. One universal feature of the two-dimensional topological liquids, the quantum dimension, is encoded in the subleading term of area law entanglement scaling dubbed as the topological entanglement entropy. Furthermore, our work pointed out that tripartite entanglement quantity can capture another universal feature, the central charge of chiral topological liquid. To show this, we exploit the bulk-boundary correspondence and define the vertex state using boundary conformal field theory (see Chapter 3).

Moving beyond the gapped ground state entanglement property, the entanglement of typical quantum states obeys *volume law* scaling. An extreme example is the infinite temperature state where the density matrix is proportional to the identity matrix; the infinite temperature state produces maximal entanglement. Recently, maximal entanglement attracted much interest as a signature of quantum chaos. The (nearly) maximal entanglement can arise in various physical contexts, including the typical entanglement of random pure state ensemble, and the ground state ensemble of the SYK model. Furthermore, our work pointed out that the symmetry of the system is encoded in the subleading term of typical free fermion entanglement scaling and the variance of entanglement (see Chapter 4).

Finally, for the ground states of one-dimensional gapless (critical) systems, the entanglement follows the *logarithmic law*. Moreover, the coefficient of the logarithmic scaling encodes the central charge of the theory. The universal behavior of entanglement measures in the critical spin model was beautifully established using the replica method and twist field. The

logarithmic entanglement scaling is determined by the dimension of the twist operator in the cyclic orbifold conformal field theory, obtained by gauging out the cyclic symmetry in the original theory.

The above discussion about entanglement in the gapless systems demonstrates the importance of conformal field theory and the twist field; Indeed, conformal field theory plays a pivotal role in the investigation of gapless (critical) systems. The conformal symmetries dictate the universal properties without knowing the microscopic details. For the interest of condensed matter systems, an important question is: given a lattice model, how to extract the conformal data? As mentioned before, part of the conformal data can be obtained using quantum entanglement. However, the extraction of one piece of conformal data, the operator product expansion coefficient, remains a challenging task. Our work provides a unifying method to extract all the conformal data using wavefunction overlap. Specifically, the family of twist fields plays an important role in our method. The significance of our method is twofold. Numerically, it provides a practical numerical method to understand new critical systems, as we demonstrated using the newly proposed Haagerup model built from the Haagerup fusion category. Theoretically, it reveals the role of orbifold conformal field theory (obtained from gauging the symmetry in the replicated conformal field theories) in studying phases of matter (See Chapter 5).

At this point, the reader might begin to ponder the power of interdisciplinary research. Remarkably, the knowledge from quantum information theory and string theory manifests again and again in the research of phases of matter – sometimes unexpectedly and brings a lot of surprises. In this thesis, I will make precise my previous statements and I wish to convey such surprise and joy.

1.1 Thesis overview

This thesis is organized as follows. In chapter 2, we introduce the two toolkits to probe the universal fingerprints: quantum entanglement and conformal field theory. The core concepts will be introduced without heavy derivation. Sec. 2.1 is devoted to quantum entanglement. The precise definition of entanglement will be discussed before diving into the details of three entanglement scalings. Sec. 2.2 is devoted to conformal field theory. CFT is too big a subject to introduce, and we shall focus on the operator formalism, which is relevant to spin chain conformal data extraction; and the boundary conformal field theory, which is relevant to bulk-boundary correspondence. Fun examples will be used to solidify the abstract concepts. In Sec. 2.3, we will apply CFT to two problems in quantum entanglement: the first is computing entanglement of the one-dimensional critical chain; the second is computing topological entanglement entropy by boundary conformal field theory. This chapter is not simply an inorganic assembling of known results; it sets the foundation for discoveries in the later chapters.

In Chapter 3, we focus on the topological liquid, where bipartite entanglement exhibits area law scaling. We study the tripartite entanglement and uncover a new universal entanglement feature. In Chapter 4, we focus on the random Gaussian systems which exhibit volume law entanglement scaling and discover the fingerprints of symmetry in typical quantum entanglement. Finally, in Chapter 5, we focus on the critical spin chain which exhibits logarithmic law entanglement scaling. We develop a new method to extract all universal conformal data by wavefunction overlap.

More technical details are left in the appendix. Appendix A includes details of vertex state calculation for tripartite entanglement, and Appendix B includes details of the wavefunction overlap method. Finally, a thesis would be less interesting if it is just a resummation of the author's publication; in Appendix C, we discuss the numerical methods and techniques for condensed matter system simulation that we find useful.

CHAPTER 2

DIAGNOSIS TOOLBOX: QUANTUM ENTANGLEMENT AND CONFORMAL FIELD THEORY

In this section, I will give a short introduction to our toolbox to diagnose the universal behaviors of quantum matters: quantum entanglement and conformal field theory. After introducing the entanglement measures, I will elaborate on the well-established three different entanglement scalings in detail. Then I introduce the covariance matrix method for Gaussian states entanglement calculation. This will prepare us for the later three sections, where the system under concern belongs to each of these three entanglement scalings.

For conformal field theory, I will first briefly introduce the essential concepts of conformal symmetry, Hilbert space formalism, and the minimal model. Next, I will introduce my favorite lattice model, the Ising spin chain to illustrate all the above concepts. Finally, I give a short introduction to the boundary conformal field theory, preparing for later discussions of bulk-boundary correspondence in topological liquid.

Equipped with the basic knowledge of quantum entanglement and conformal field theory, we present two interesting applications of conformal field theory in quantum entanglement in Sec. 2.3. The first application is the calculation of quantum entanglement of the one-dimensional critical chain, and the second is applying boundary conformal field theory to compute topological entanglement entropy in topological liquid. Beautiful on their own, these two examples set the foundation for our discoveries in the next three sections.

To follow the spirit of my advisor Shinsei, I will try to use explicit lattice models as examples with numerical results to support the theoretical statement whenever I find it necessary. To not lose readers, this chapter will rely less on math derivation and more on the physical pictures.

2.1 Quantum entanglement

Quantum entanglement is one of the pillars of quantum mechanics. What exactly is quantum entanglement? In this section, I will define entanglement from inseparability, which fundamentally distinguishes the classical and quantum correlation. Next, I will review the entropy quantification of quantum entanglement, the *von Neumann entanglement entropy*. The role and limitation of von Neumann entanglement entropy will be discussed. I will then shift the gear to condensed matter systems and introduce entanglement scaling.

In practice, calculating the von Neumann entanglement entropy for a many-body state is generally difficult. Simplification can be achieved for a special type of quantum state, the Gaussian state. I will introduce the formalism of Gaussian state entanglement computation – the correlation method.

2.1.1 Entanglement: inseparability

Quantum entanglement stems from the superposition of quantum states, which is fundamentally different from classical correlation. To motivate it, let's first define the quantum state that only possesses the classical correlation – the separable state. We take a general density matrix ρ_{AB} of the total system supported on region $A \cup B$, which is positive semi-definite, and its trace is equal to 1. We restrict to the case where the total Hilbert space $\mathcal{H}$ is the direct product of Hilbert spaces on subregions $\mathcal{H} = \mathcal{H}_A \otimes \mathcal{H}_B$. Using ρ_{AB}, the reduced density matrix ρ_A is obtained by tracing out subregion B: $\rho_A = \mathrm{Tr}_B \rho_{AB}$, and similarly $\rho_B = \mathrm{Tr}_A \rho_{AB}$.

Definition 1 (separable state)**.** *The state ρ is separable, iff it can be written as a convex summation of product states,*

$$\rho_{AB} = \sum_i p_i \rho_i^A \otimes \rho_i^B. \tag{2.1}$$

Convex summation requires that $p_i \geq 0$ and $\sum_i p_i = 1$; each product state takes the form of

$\rho_i^A \otimes \rho_i^B$.

In the special case where ρ_{AB} is a pure state $\rho_{AB} = |\psi\rangle\langle\psi|$, the separable condition is simplified to

$$|\psi\rangle = |\psi_A\rangle \otimes |\psi_B\rangle. \tag{2.2}$$

Separable state only possesses classical correlation, because it can be produced by local operations and classical communication (LOCC).

Definition 2 (entangled state)**.** *A state ρ is quantum entangled iff it is inseparable.*

Simple as it is defined, determining whether a state ρ is separable or not turns out to be an NP-hard problem. There exist various sufficient conditions for entanglement (which are, necessary conditions for separability). But until today, no general solution is known except for simple cases such as the two-qubit system.

The sufficient conditions for entangled states can be associated with entanglement witness or entanglement measure. Although in this thesis we shall focus on the entanglement measure, it is worth mentioning that entanglement witness is commonly used for experimental detection of quantum entanglement. Let's now focus on the entanglement measure $E(\rho)$ associated with a quantum state ρ. Entanglement measure is a function that quantifies entanglement. Moreover, the basic requirements of entanglement measures include:

1. $E(\rho)$ shall vanish for a separable state.

2. $E(\rho)$ shall be invariant under a local change of basis.

3. $E(\rho)$ shall not increase under LOCC. This is because LOCC can only create classical correlations.

In the history of the quest for entanglement measures, various functions were studied: entanglement of distillation, and entanglement cost, to name but a few. It was shown that

with a few reasonable assumptions, the unique entanglement measure of pure states is just the von Neumann entanglement entropy [4]. We shall introduce it in the next subsection.

2.1.2 von Neumann entanglement entropy

The von Neumann entanglement entropy of a state ρ is defined as

$$S = -\mathrm{Tr}\,(\rho \ln \rho). \tag{2.3}$$

It can be regarded as the quantum counterpart of the classical Shannon entropy $s(X)$ associated with a random variable X. When ρ is a pure state, one can show $S(\rho) = 0$ and the requirements of entanglement measure are satisfied.

Alternatively, von Neumann entanglement entropy can be viewed as the limit of Renyi entropy $S^{(n)}$ at $n \to 1$, where the Renyi entropy is defined by

$$S^{(n)} = \frac{1}{1-n} \ln \mathrm{Tr}\,(\rho^n). \tag{2.4}$$

The Renyi entropy satisfies the α-entropy inequalities [5, 6, 7], which states that for any separable state, ρ_{AB}, the α-th Renyi entropy ($\alpha \geq 1$) of the subsystem cannot be greater than that of the whole system,

$$S^{(\alpha)}(\rho_{AB}) \geq S^{(\alpha)}(\rho_A), \quad S^{(\alpha)}(\rho_{AB}) \geq S^{(\alpha)}(\rho_B). \tag{2.5}$$

α-entropy inequalities provide a necessary condition for separability. It is worth noting its similarity to the inequalities of Shannon entropy: the Shannon entropy associated with a single random variable X cannot be greater than that of two variables,

$$s(X,Y) \geq s(X), \quad s(X,Y) \geq s(Y). \tag{2.6}$$

Indeed, in the classical realm, subsystems cannot be more disordered than the whole system. The violation of α-entropy inequalities signals the quantum entanglement as a sufficient condition.

Renyi entropy is useful because only the power of ρ is involved, which makes it more readily to be measured in the experiments compared to von Neumann entanglement entropy. Specifically, the second Renyi entropy is closely related to purity and concurrence. Furthermore, Renyi entropy plays a central role in the theoretical technique such as the replica approach, which we will introduce in the later section.

One can view the reduced density matrix ρ_A as a thermal state and define the entanglement Hamiltonian (modular Hamiltonian) K_A via

$$K_A = -\ln \rho_A. \tag{2.7}$$

Now, EE is simply the expectation value of entanglement Hamiltonian, $S_A = \langle K_A \rangle$. The spectrum of entanglement Hamiltonian K_A is called entanglement spectrum $\{\xi\}$. The entanglement spectrum provides richer information than entanglement entropy. Remarkably, the low-lying part of the entanglement spectrum of a ground state wavefunction resembles the physical edge spectrum [8]. In other words, the ground state wavefunction "knows" about the physical edge spectrum which includes the excited states on the edge. We will explore more about this insight in Sec. 2.3.2.

As a simple example of entanglement entropy calculation, let's consider the Bell pair state that consists of two qubits, $|\psi\rangle = \frac{1}{\sqrt{2}}(|01\rangle + |10\rangle)$. The entanglement entropy associated with one of the qubits is $\ln 2$. In some sense, $\ln 2$ is the "natural unit" of entanglement entropy.

2.1.3 Entanglement scaling

Introduced first in quantum information theory, von Neumann entanglement entropy was later widely studied in the context of condensed matter physics to understand the phases of quantum matter. One specific question is the entanglement scaling: given a quantum pure state $|\psi\rangle$ supported on $\mathcal{H} = \mathcal{H}_A \otimes \mathcal{H}_B$, how the entanglement entropy $S_A \equiv S(\rho_A)$ grows as the size of subregion A increases? Naively, one may expect the entanglement entropy to be an extensive quantity and shall grow linearly with the growth of the volume of subregion A. While this intuition applies to the thermal states, there exist other entanglement entropy scaling for the states under physics interest. Below, we introduce three types of entanglement scaling: area law, volume law, and logarithmic law.

Area law

The ground state of the local gapped Hamiltonian typically follows area law entanglement scaling. Area law entanglement scaling states that the entanglement entropy grows like the boundary ∂A of the subregion A (see [9] for a nice review). In other words, the quantum entanglement between two regions is established via their boundary; the entanglement comes from local correlations. The area-law scaling for a general gapped spin chain can be proven using the Lieb-Robinson theorem [10].

An important case is one-dimensional systems, where the boundary ∂A of an interval A consists of two endpoints. Therefore, the "length" of the boundary does not grow when increasing the length of A, and subsequently, the entanglement is (mostly) a constant. The fact that entanglement keeps constant in one-dimensional systems is the key for numerical simulation[1], allowing the efficient marix product state representation [11].

Example As a first numerical example, let's take a look a the Su–Schrieffer–Heeger (SSH)

1. In higher dimensional case, area law generally allows, but does not guarantee the PEPS representation. A counterexample is the bulk of the integer quantum Hall system.

model, which is a one-dimensional free fermion chain with the nearest-neighbor hopping,

$$H_{\text{SSH}} = \sum_{i=1}^{N} v f_{i,A}^{\dagger} f_{i,B} + w f_{i+1,A}^{\dagger} f_{i,B} + h.c. \tag{2.8}$$

There are two atoms within a unitcell, labeled by A and B. The hopping amplitude within a unitcell is v, and between two unitcells is w. The SSH model is gapless when $v = w$ and gapped otherwise. We adopt the periodic boundary condition with parameters $v = 1, w = 2$ and the total system consists of $N = 80$ unitcells. The entanglement scaling of the ground state and several excited states are shown in the left panel of Fig. 2.1, including the first excited state. The subregion A consists of N_A unitcells, and the entanglement cut is chosen between the unitcells. We observe that only the ground state exhibits the area law scaling. On the right panel of Fig. 2.1 we plot the half-chain ground state entanglement entropy with respect to w, and $v = 1$ is fixed. We see that in the gapped phase $w \neq v$, the entanglement entropy does not increase when increasing the total system size N. Furthermore, $S_A = 0$ deep in the trivial phase ($w < v$) and $S_A = 2 \ln 2$ deep in the topological phase ($w > v$). This is because the entanglement boundary cuts through two Bell pairs in the topological phase, each contributing to $\ln 2$.

□

Moving forward to the ground state of two-dimensional gapped Hamiltonian, the entanglement entropy scales as

$$S_A = \alpha L - \gamma, \tag{2.9}$$

where L is the length of ∂A (the boundary of region A). The leading term is the area law term; and more interestingly, the subleading term γ captures the topological data. For the state possess topological order and A being a disk-like geometry, γ is the *topological*

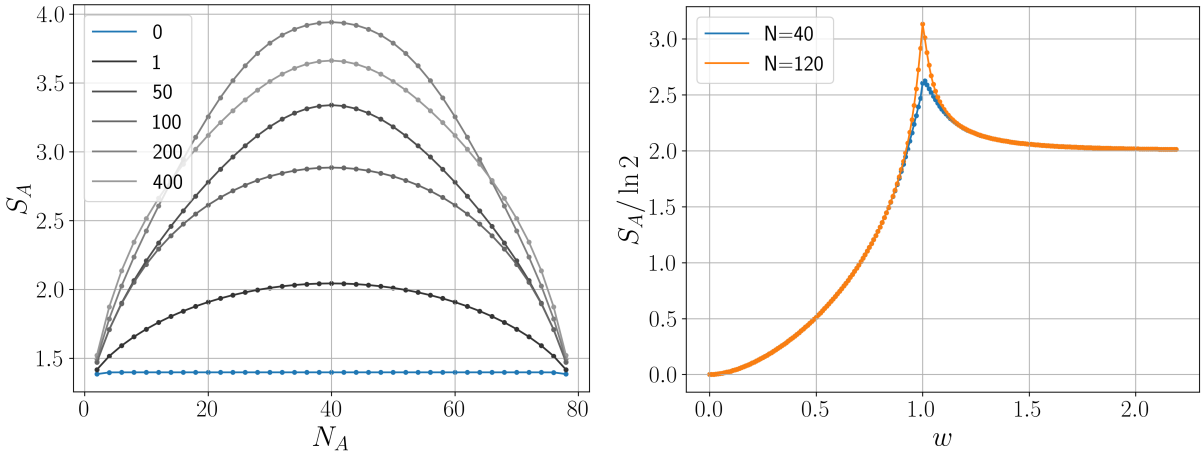

Figure 2.1: (Left panel) Entanglement scaling of the ground state (0) and several excited states (1,50,100,200,400) of the gapped SSH model at $v = 1, w = 2$ with system size $N = 80$. (Right panel) Half chain entanglement entropy with respect to parameter w (the value $v = 1$ is fixed).

entanglement entropy [12, 13], encoding the total quantum dimension

$$\gamma = \ln \mathcal{D} = \ln \sqrt{\sum_i d_i^2}, \tag{2.10}$$

where d_i is the quantum dimension of anyon i, and $\mathcal{D}$ is the total quantum dimension. The topological entanglement entropy can be derived in various ways; after introducing the conformal field theory, I will show proof based on boundary CFT in Sec. 2.3.2. Furthermore, more information about the topological order can be revealed by tripartite entanglement, which will be the focus of Chapter 3.

Volume law

While the ground state typically exhibits area law entanglement scaling, the entanglement of the thermal states scales with the volume of the subregion. The quantum entanglement comes from the nonlocal correlations. An extremal point of the thermal state is the infinite temperature state $\rho \propto \mathbb{1}$, where the entanglement entropy saturates and reaches the maximal

value $S_A = \ln d_A$, where d_A is the dimension of $\mathcal{H}_A$.

Besides the featureless infinite temperature state, the maximal entanglement appears in another context: the average entanglement entropy of random pure states, known as the Page curve [14, 15, 16]. Concretely, the random pure state in $\mathcal{H}_A \otimes \mathcal{H}_B$ takes the form of

$$|\psi\rangle = \sum_{i=1}^{d_A} \sum_{\alpha=1}^{d_B} X_{i\alpha} |i\rangle_A \otimes |\alpha\rangle_B. \tag{2.11}$$

Here, d_A, d_B are dimensions of $\mathcal{H}_A$ and $\mathcal{H}_B$, and $\{|i\rangle_A\}$ and $\{|\alpha\rangle_B\}$ form orthonormal bases on $\mathcal{H}_A$ and $\mathcal{H}_B$. The coefficients $X_{i\alpha}$ are independent and identically distributed complex Gaussian random variables satisfying $\langle X_{i\alpha} X^*_{j\beta}\rangle = \frac{1}{d_A d_B}\delta_{ij}\delta_{\alpha\beta}$. Using random matrix techniques, one can show that in the thermodynamics limit (large total system limit), the average entanglement entropy is given by

$$\langle S_A \rangle = \ln d_A - \frac{d_A}{2d_B} \tag{2.12}$$

when $d_A \leq d_B$. If the degree of freedom on each site is the qubit, the Hilbert space dimension is related to the number of qubits via $d_A = 2^{N_A}$, and the above Page curve relation is reduced to

$$\langle S_A \rangle = N_A \ln 2 - 2^{N_A - N_B - 1}. \tag{2.13}$$

The first term is the volume law scaling term with maximal entanglement. The deviation from the maximal entanglement $N_A \ln 2$ is $2^{N_A - N_B - 1}$, which is exponentially small for $N_A \ll N_B$ and is at most order one (1/2) when $N_A = N_B$.

Another type of system that exhibits the (nearly) maximal entanglement is the Sachdev-Ye-Kitaev (SYK) model, which is a zero-dimensional system [2] of N Majorana or complex fermions with all-to-all coupling with random coefficients. The SYK models for $q > 2$ are

2. Zero-dimension is important; Otherwise, the locality would bring a subleading $\sqrt{V}$ scaling term where V is the volume of the system. See the discussion in Ref. [17].

maximally chaotic, thus it is expected that the average ground state EE shall also reach maximal entanglement. The numerical calculations [18, 19] show that the entanglement is nearly maximal: volume law entanglement is observed with coefficient 0.675 (0.665) for Majorana (complex) fermion, which is slightly smaller than $\ln 2 = 0.6931$.

An interesting question arises: if we restrict ourselves to a corner of the whole Hilbert space by considering the random free fermion state, how does the average entanglement behave? It turns out that they still follow the volume law entanglement scaling but with coefficients depending on the subsystem fraction. More interestingly, when imposing symmetries, the universal features of symmetries are encoded in the constant term. This will be the subject of Chapter 4.

Logarithmic law

Besides area law and volume law, another entanglement scaling is also ubiquitous in physical systems: the logarithmic law, where entanglement scales as logarithmic of the subregion size N_A. It applies to the ground state of one-dimensional local gapless Hamiltonian exhibiting criticality. Moreover, the coefficient is proportional to the central charge c of the model,

$$S_A = \frac{c}{3} \log N_A + c_1, \tag{2.14}$$

and c_1 is a non-universal constant. We will derive this result in Sec. 2.3 after introducing conformal field theory. Conversely, the logarithmic entanglement scaling is an efficient way to extract the central charge of the critical lattice model.

The canonical examples of critical one-dimensional lattice models include the free fermion model, SSH model at critical point $v = w$, transverse field Ising model at the critical point, and XXZ model at radius $R = \sqrt{2}$.

The logarithmic law can be generalized to higher dimensional gapless systems, with the

extra subtlety coming from the shape of the Fermi surface. There are two scenarios. The first is the higher dimensional free fermion systems with the Fermi surface being a sphere surface. One can show $S_A \sim L_A^{d-1} \ln L_A$ for cubelike domain [20]. Crudely speaking, each antipodal points on the sphere surface contribute $\ln L_A$ of entanglement. The second scenario is the system described by higher dimensional CFT. Depending on the dimension, higher dimensional CFT predicts $S_A \sim L_A^{d-1}$ or $S_A \sim L_A^d$ entanglement scaling [21].

2.1.4 Covariance matrix method

We have seen that there exist free fermion models that exhibit area law, volume law, and logarithmic law scaling. Free fermion states belong to Gaussian states defined as below [22],

Definition 3 (Gaussian state)**.** *Gaussian states are those states for which Wick's theorem holds. A fermionic Gaussian state is a thermal state of quadratic Hamiltonian,*

$$\rho = C \exp\left(\frac{1}{4}\overrightarrow{\psi}^T \Omega \overrightarrow{\psi}\right), \tag{2.15}$$

where $\overrightarrow{\psi}$ *is a vector of Majorana fermions and* Ω *is an imaginary antisymmetric matrix.*

In our convention, the Majorana fermion operators are related to the complex fermion operators via $f_i = \frac{1}{2}(\psi_{2i-1} - i\psi_{2i}), f_i^\dagger = \frac{1}{2}(\psi_{2i-1} + i\psi_{2i})$. The entanglement calculation of Gaussian states is much simpler than the general many-body state, thanks to the covariance matrix method [23, 24, 25].

Let's first define the covariance matrix. Given a density matrix of a fermionic Gaussian state ρ, the covariance matrix Γ is defined by the two-point function of the Majorana fermions,

$$\Gamma_{jk} := \frac{1}{2}\mathrm{Tr}\left(\rho[\psi_j, \psi_k]\right). \tag{2.16}$$

Here the indices j, k run over all relevant degrees of freedom, site, spin, orbital, etc. Γ is also an imaginary antisymmetric matrix with eigenvalues come in pairs $\{\pm\gamma_k\}$. The covariance

matrix is related to Ω via $\Gamma = -\tanh(\Omega/2)$, which can be shown by using orthogonal transformation to bring Ω into canonical form in the rotated basis ψ'. In the rotated basis, the density matrix takes a simple form $\rho = \prod_k \frac{1}{2}(1+\gamma_k \psi'_{2i-1}\psi'_{2i})$, from which we can derive the formula of entanglement entropy,

$$S = -\sum_k{}' \left[\left(\frac{1}{2}+\frac{\gamma_k}{2}\right) \ln\left(\frac{1}{2}+\frac{\gamma_k}{2}\right) + \left(\frac{1}{2}-\frac{\gamma_k}{2}\right) \ln\left(\frac{1}{2}-\frac{\gamma_k}{2}\right) \right]. \tag{2.17}$$

Here, the prime on $\sum$ means we only sum over one of the eigenvalues in the $\pm\gamma_k$ pairs. To summarize, when computing S_A corresponds to a subregion A, all required is to find the covariance matrix Γ_A using ρ_A. The entanglement entropy is ready to be computed once knowing the eigenvalues $\{\gamma_k\}$ of Γ_A. In practice, one can first compute the correlation matrix Γ_{AB} of the whole system on $A \cup B$ and take Γ_A as a submatrix of Γ_{AB} by keeping only the degrees of freedom ψ in the region A; this has the effect of tracing out region B.

Given a physical free fermion Hamiltonian, it is typically more convenient to compute the correlation matrices C, F,

$$\begin{aligned} C_{ij} &:= \mathrm{Tr}\,(\rho f_i^\dagger f_j) \\ F_{ij} &:= \mathrm{Tr}\,(\rho f_i^\dagger f_j^\dagger). \end{aligned} \tag{2.18}$$

The covariance matrix can be expressed in terms of C, F as

$$\Gamma = (C - C^T)\otimes \mathbb{1} + (\mathbb{1} - C - C^T)\otimes \sigma_y + (F + F^\dagger)\otimes \sigma_z - i(F - F^\dagger)\otimes \sigma_x, \tag{2.19}$$

where the Pauli matrices act on the space of odd and even indices of the Majorana fermions. Let's consider a special case of the single particle Hamiltonian $\hat{H} = \sum_{i,j=1}^N f_i^\dagger H_{ij} f_j$, and find its ground state correlation matrix. The $N \times N$ matrix H can be diagonalized by a unitary matrix U via $U^\dagger H U = D$ where D is a diagonal matrix of eigenvalues, arranged from smallest to largest. We denote the rotated basis as $\tilde{\boldsymbol{f}} = U^\dagger \boldsymbol{f}$. If the first N_f eigenvalues are negative, the many-body ground state is a product state filled with the first N_f eigenstates,

$|GS\rangle = \tilde{f}_1^\dagger \cdots \tilde{f}_{N_f}^\dagger |0\rangle$. We denote V as a $N \times N_f$ submatrix of U consisting of its first N_f columns, and the correlation matrix $C_{ij} = \langle GS | f_i^\dagger f_j | GS \rangle$ can now be expressed using V by

$$C = V^* V^T. \tag{2.20}$$

The correlation matrix $F = 0$ because the above Hamiltonian preserves the particle number. Finally, C_A is obtained by truncating C, keeping only the degree of freedom in A.

In particle-number-conserving systems, the eigenvalues γ_k are related to the single-particle entanglement spectrum ϵ_k, which are eigenvalues of H_E defined from the reduced density matrix

$$\rho \propto \exp\left[-\sum_{ij} f_i^\dagger (H_E)_{ij} f_j \right]$$

by $\epsilon_k = \ln\left[(1-\gamma_k)/(1+\gamma_k)\right]$. For η_k being eigenvalues of C, ϵ_k can be expressed equivalently as $\epsilon_k = \ln\left[(1-\eta_k)/\eta_k\right]$. Entanglement entropy can also be expressed using $\{\eta_k\}$ by

$$S = -\sum_k \left[\eta_k \ln \eta_k + (1-\eta_k) \ln(1-\eta_k) \right]. \tag{2.21}$$

To have a better grasp of the correlation matrix method, let's play with the following example of free fermion.

Example Consider the 1d free fermion hopping Hamiltonian with periodic boundary condition,

$$H = -t \sum_{i=1}^{N} (c_i^\dagger c_{i+1} + h.c.). \tag{2.22}$$

This is a gapless model. From the tight-binding method, the eigenvalues of H are $E_k = -2t \cos k$, which are labeled by momentum k in the range of $[-\pi, \pi]$; the corresponding eigenstates are simply the plane waves. When $t > 0$, the ground state is formed by filling the momentum modes in the range $[-\pi/2, \pi/2]$, and the correlation matrix takes the form

of (using Eq. (2.20))

$$C_{ij} = \begin{cases} \frac{\sin(i-j)\pi/2}{\pi(i-j)} & i \neq j \\ \frac{1}{2} & i = j. \end{cases} \tag{2.23}$$

We see the correlation matrix elements exhibit power law decay, $C_{ij} \sim 1/|i-j|$. Let's take the region A as the first N_A sites of the chain, therefore C_A is simply the upper-left $N_A \times N_A$ submatrix of C. By numerically calculating the eigenvalues η of C_A, we can obtain the entanglement S_A using Eq. (2.21). The numerical result gives $S_A = \frac{1}{3}\ln N_A + c_1$, from which we extract the central charge $c = 1$.

In fact, the above scaling can be derived analytically by the cumulant method [26]. The cumulant method states that the leading term of EE is governed by the second moment of charges, which can be expressed using the trace of C_A and C_A^2,

$$S_A = \frac{\pi^2}{3}\mathrm{Tr}\,(C_A - C_A^2). \tag{2.24}$$

From the above correlation matrix, $\mathrm{Tr}\,C_A$ is simply given by $\mathrm{Tr}\,C_A = N_A/2$. The trace of C_A^2 can be evaluated by

$$\begin{aligned} \mathrm{Tr}\,C_A^2 &= \sum_{ij=1}^{N_A} C_{A,ij}C_{A,ji} \\ &= \frac{N_A}{4} + \frac{2}{\pi^2}\left[L_A \sum_{n=1}^{N_A/2} \frac{1}{(2n-1)^2} - \sum_{n=1}^{N_A/2} \frac{1}{2n-1}\right] \\ &\approx \frac{N_A}{2} - \frac{1}{\pi^2}\ln N_A + O(1). \end{aligned}$$

The polygamma functions are used to obtain the large N_A result in the last line, where we keep the contributions up to the constant term. Knowing $\mathrm{Tr}\,C_A$ and $\mathrm{Tr}\,C_A^2$, the entanglement entropy is

$$S_A = \frac{\pi^2}{3}\left[\frac{N_A}{2} - (\frac{N_A}{2} - \frac{1}{\pi^2}\ln N_A + O(1))\right] = \frac{1}{3}\ln N_A + O(1), \tag{2.25}$$

as what we observe from the numerical simulation.

□

2.2 Conformal field theory

Having introduced quantum entanglement, we now shift the gear to two-dimensional conformal field theory. Conformal field theory is an important subject from the string theory as the language to describe the worldsheet. In statistical mechanics, it enjoys much success as the field theory of second-order phase transition. The conformal invariance beautifully yields the universal behaviors of physical quantities, for example, the two-point correlation function. Perhaps it is too ambitious to introduce such a profound subject in a short section. In this section, I will take a condensed matter physics point of view and focus on the emergence of CFT in lattice models where the lattice Ising model will be used as a concrete example. In Sec. 2.3, we will see how CFT helps derive elegant results of quantum entanglement of critical systems and topological entanglement entropy.

"It is worth learning CFT at least once in your life"; for readers who would like to learn CFT more systematically, I recommend [27, 28] and [29].

2.2.1 Conformal invariance

A conformal field theory is a quantum field theory that is invariant under conformal transformations.

Definition 4 (Conformal transformation)**.** *Conformal transformation is an invertible coordinate transformation $f : p \to f(p)$ (in terms of coordinates, $f : x \to x'$) that leaves the metric tensor g invariant up to a scale,*

$$f^*(g(f(p))) = \Lambda(x)g(p). \tag{2.26}$$

In terms of components, the above equation is

$$\frac{\partial x'^{\alpha}}{\partial x^{\mu}} \frac{\partial x'^{\beta}}{\partial x^{\nu}} g_{\alpha\beta}(f(p)) = \Lambda(x) g_{\mu\nu}(p). \tag{2.27}$$

For general dimension $d \geq 3$, the group of conformal transformation is generated by translation, rotation, dilation, and special conformal transformation. Under the current discussion of Euclidean spacetime, the conformal group is isomorphic to $SO(d+1,1)$; the algebra of infinitesimal conformal transformation is finite.

The conformal group in $d = 2$, the case of our interest, is drastically different from $d > 3$. Let's introduce the complex variables $z = x^0 + ix^1, \bar{z} = x^0 - ix^1$. One can show that: any holomorphic function $f(z) = z + \epsilon(z)$ gives rise to an infinitesimal two-dimensional conformation transformation $z \to f(z)$. The algebra of infinitesimal conformal transformations is Witt algebra with generators $\{l_n\}$, which is *infinite* dimensional. Thanks to the structure of infinite dimensional algebra, 2d CFT is sometimes exactly solvable.

The Witt generators take the form of $l_n = -z^{n+1}\partial_z$ and $\bar{l}_n = -\bar{z}^{n+1}\partial_{\bar{z}}$. In particular, when using the polar coordinate (r, ϕ), one can form the combinations

$$l_0 + \bar{l}_0 = -r\partial_r \quad \text{and} \quad i(l_0 - \bar{l}_0) = -\partial_\phi. \tag{2.28}$$

We see that $l_0 + \bar{l}_0$ is the generator for dilations and $i(l_0 - \bar{l}_0)$ of rotations. This intuition will be useful in the later discussion of operator formalism.

We now introduce the primary fields, which are representations of conformal algebra. Primary fields will play an important role in our later discussion on Hilbert space formalism and the minimal model.

Definition 5 (Primary field)**.** *A spinless field is called a primary field of conformal dimen-*

sions $(h, \bar{h})$ *if it transforms under conformal transformation* $z \to f(z)$ *according to*

$$\phi(z, \bar{z}) \to \phi'(z, \bar{z}) = \left(\frac{\partial f}{\partial z}\right)^h \left(\frac{\partial \bar{f}}{\partial \bar{z}}\right)^{\bar{h}} \phi(f(z), \bar{f}(\bar{z})). \tag{2.29}$$

If the above relation holds only for global conformal transformation $f \in SL(2, \mathbb{C})/\mathbb{Z}_2$*, then* ϕ *is called a quasi-primary field.*

One can show that the two-point function of two quasi-primary fields is fixed by the global conformal symmetry $f \in SL(2, \mathbb{C})/\mathbb{Z}_2$,

$$\langle \phi_1(z_1, \bar{z}_1)\phi_2(z_2, \bar{z}_2)\rangle = \frac{C_{12}\delta_{h_1,h_2}\delta_{\bar{h}_1,\bar{h}_2}}{(z_1 - z_2)^{2h_1}(\bar{z}_1 - \bar{z}_2)^{2\bar{h}_1}}. \tag{2.30}$$

We can always normalize C_{12} to 1 by rescaling the field ϕ. The three-point function of three quasi-primary fields is also fixed by $f \in SL(2, \mathbb{C})/\mathbb{Z}_2$,

$$\begin{aligned}\langle \phi_1(z_1, \bar{z}_1)\phi_2(z_2, \bar{z}_2)\phi_3(z_3, \bar{z}_3)\rangle = \\ C_{123}\frac{1}{z_{12}^{h_1+h_2-h_3} z_{23}^{h_2+h_3-h_1} z_{13}^{h_3+h_1-h_2}} \frac{1}{\bar{z}_{12}^{\bar{h}_1+\bar{h}_2-\bar{h}_3} \bar{z}_{23}^{\bar{h}_2+\bar{h}_3-\bar{h}_1} \bar{z}_{13}^{\bar{h}_3+\bar{h}_1-\bar{h}_2}},\end{aligned} \tag{2.31}$$

up to the structure constant C_{123}. We will see in the following that $h_i, \bar{h}_i$ and C_{ijk} are among the conformal data of a given CFT.

In the Lagrangian formalism, the action S is invariant under conformal transformation. By the Noether theorem, one can define the stress-energy tensor $T(z)$ from the infinitesimal transformation of metric. One can show that $T(z)$ is a quasi-primary field and its operator product expansion (OPE) takes the form of

$$T(z)T(w) = \frac{c/2}{(z-w)^4} + \frac{2T(w)}{(z-w)^2} + \frac{\partial_w T(w)}{z-w} + \cdots, \tag{2.32}$$

where c is the *central charge* and $|z| > |w|$. Central charge c is another conformal data of a

given CFT.

Central charge c captures the *conformal anomaly*. It is related to the breaking of conformal symmetry by introducing a macroscopic scale into the system [27]. The macroscopic scale can be introduced by the boundary condition, or the curvature in the system. For example, the vacuum energy density on the cylinder is $\langle T_{cyl} \rangle = -\frac{c\pi^2}{6L^2}$, where the central charge is proportional to the Casimir energy; the scale is introduced by the periodic boundary condition with circumference L. The entanglement entropy scaling of a subregion of an infinite chain is $S_A \sim \frac{c}{3} \log N_A$; the scale is introduced by the entanglement cut.

2.2.2 Hilbert space formalism

Having introduced the Lagrangian formalism, we now wish to quantize the CFT. To do so, we first need to choose the space and time directions. Let's take a 2d plane and choose the space direction along concentric circles centered at the origin, and the time direction as the radial direction which is orthogonal to the space direction. This choice of spacetime leads to *radial quantization* of 2d CFT. The radial quantization can be obtained from the usual Minkowski quantization from a conformal transformation $z = e^w = e^{x^0 + ix^1}$. Specifically, the past infinity $x^0 = -\infty$ is mapped to the origin $z = 0$.

Operator-state correspondence

Given a quasi-primary field ϕ with conformal dimension $(h, \bar{h})$, one can perform the mode expansion (Laurent expansion) around the origin,

$$\phi(z, \bar{z}) = \sum_{n,m \in \mathbb{Z}} z^{-n-h} \bar{z}^{-m-\bar{h}} \phi_{n,m}. \tag{2.33}$$

We define an asymptotic in-state $|\phi\rangle$ to be

$$|\phi\rangle = \lim_{z,\bar{z}\to 0} \phi(z,\bar{z})|0\rangle. \tag{2.34}$$

To have a non-singular state, we need to require $\phi_{n,m}|0\rangle = 0$ for $n > -h, m > -\bar{h}$. Under this requirement, the state $|\phi\rangle$ is

$$|\phi\rangle = \lim_{z,\bar{z}\to 0} \phi(z,\bar{z})|0\rangle = \phi_{-h,-\bar{h}}|0\rangle. \tag{2.35}$$

In other words, each primary field ϕ corresponds to a state $|\phi\rangle$. In particular, the identity field $\mathbb{1}$ corresponds to the vacuum state (ground state) $|0\rangle$.

Hamiltonian

To define the Hamiltonian, we perform the mode expansion of stress tensor $T(z)$,

$$T(z) = \sum_{n\in\mathbb{Z}} z^{-n-2} L_n, \quad \text{where} \quad L_n = \frac{1}{2\pi i}\oint dz z^{n+1} T(z). \tag{2.36}$$

The Laurent modes L_m can be identified with the generators of infinitesimal conformal transformations. One way to understand this is by noting that L_m satisfies the Virasoro algebra (can be proven using OPE of T),

$$[L_m, L_n] = (m-n)L_{m+n} + \frac{c}{12}(m^3 - m)\delta_{m,-n}, \tag{2.37}$$

and the Virasoro algebra is the central extension of the Witt algebra of l_m.

Hamiltonian is the generator of time translation, which is the dilation operator in radial quantization. Similarly, the momentum operator is the generator of space translation and

corresponds to rotation. This allows us to identify (see Eq. (2.28))

$$H = L_0 + \bar{L}_0, \quad P = i(L_0 - \bar{L}_0). \tag{2.38}$$

Using the OPE between $T(z)$ and $\phi(w)$, one can show the state $|\phi\rangle$ is eigenstate of H and P,

$$\begin{aligned} H|\phi\rangle &= (h + \bar{h})|\phi\rangle = \Delta|\phi\rangle, \\ P|\phi\rangle &= i(h - \bar{h})|\phi\rangle = is|\phi\rangle. \end{aligned} \tag{2.39}$$

Here we define the scaling dimension $\Delta = h + \bar{h}$ and spin $s = h - \bar{h}$.

The Laurent expansion of $T(z)$ also requires

$$L_n|0\rangle = 0 \quad \text{for} \quad n \geq -1. \tag{2.40}$$

This leads to the ground state $|0\rangle$ indeed having zero energy; Moreover, the ground state is annihilated by global conformal transformation generators L_{-1}, L_0, L_1.

Highest weight representation

We saw above that each primary field ϕ corresponds to a state. On the other hand, each primary field gives rise to an infinite set of descendant fields by taking derivative ∂^k and normal ordered product with T. The primary field ϕ and its descendant form a conformal family $[\phi]$. These descendant fields also correspond to states in the Hilbert space, with higher energy.

For simplicity let's only consider the chiral states, where $|\phi\rangle = \phi_{-h}|0\rangle$ has energy h: $H|\phi\rangle = h|\phi\rangle$. The first descendant field $\partial\phi$ corresponds to the first excited state $L_{-1}\phi_{-h}|0\rangle$ with energy $h+1$. The next two descendant fields are $\partial^2\phi$ and $N(\phi T)$, which corresponds to states $L_{-1}L_{-1}\phi_{-h}|0\rangle$ and $L_{-2}\phi_{-h}|0\rangle$ with energy $h+2$. More generally, the field $N(\phi\partial^n T)$ corresponds to the state $L_{-n-2}\phi_{-h}|0\rangle$. Taking a special example of $\phi = \mathbb{1}$ and $n = 2$, we

arrive at the statement that stress tensor $T(z)$ is the descendant field of identity field $\mathbb{1}$.

In the highest weight representation, we start from a primary field $\phi(z, \bar{z})$ and build the Hilbert space as

$$|\phi\rangle, L_{-1}|\phi\rangle, L_{-1}L_{-1}|\phi\rangle, L_{-2}|\phi\rangle, \cdots \tag{2.41}$$

The set of all these states is called the Verma module $V_{h,c}$. There might exist null states and negative norm states in the Verma module. Requiring the absence of negative norm states leads to the unitary minimal model.

In Sec. 2.2.4, we will take the lattice Ising model as an example to illustrate the state-operator mapping and highest weight representation.

2.2.3 Minimal model

The appearance of null states in the Verma module imposes constraints on the operator algebra of conformal families. In general, there exists an infinite number of conformal families. However, under periodicity conditions, only a finite number of conformal families arise, and the corresponding model is called the minimal model.

For simplicity, we only discuss the unitary minimal model, which can be labeled by an integer $m \geq 3$. The central charge and primary fields of $(m, m+1)$ minimal model is

$$\begin{aligned} c &= 1 - 6\frac{1}{m(m+1)} \\ h_{r,s} &= \frac{((m+1)r - ms)^2 - 1}{4m(m+1)}, \quad 1 \leq r \leq m-1, 1 \leq s \leq m. \end{aligned} \tag{2.42}$$

The Hilbert space is the direct sum of irreducible modules $M_{r,s}$,

$$\mathcal{H} = \oplus_{1 \leq r \leq m-1, 1 \leq s \leq m} M(h_{r,s}, c) \otimes \bar{M}(h_{r,s}, c), \tag{2.43}$$

where the irreducible module $M_{r,s}$ is obtained from the Verma module $V_{h_{r,s},c}$ by quotienting

out submodules associated with null vectors. The *character* of the irreducible representation $M_{r,s}$ is defined by

$$\chi_{r,s}(q) = \mathrm{Tr}\, q^{L_0 - \frac{c}{24}}. \tag{2.44}$$

The character encodes the information on the number of states in a given level, from which we can read the location of null states. The characters of irreps in the minimal models can be derived analytically.

The simplest minimal model is the Ising CFT where $m = 3$. One can read the central charge $c = \frac{1}{2}$ and there are three primary fields $\mathbb{1}, \sigma, \epsilon$ with conformal dimension $h = 0, \frac{1}{16}, \frac{1}{2}$, respectively. In Sec. 2.2.4, we will study the lattice model where Ising CFT emerges.

Minimal model on the torus

Finally, when putting the CFT on a torus (a lattice with period α_1, α_2), one can define the torus partition function parametrized by $\tau = \alpha_2/\alpha_1$

$$Z(\tau, \bar{\tau}) = \mathrm{Tr}_{\mathcal{H}}(q^{L_0 - \frac{c}{24}} \bar{q}^{\bar{L}_0 - \frac{c}{24}}), \tag{2.45}$$

where $q = e^{2\pi i \tau}$. For the minimal models, the torus partition function is related to the characters by

$$Z = \sum_{r,s} \chi_{r,s}(q) \bar{\chi}_{r,s}(\bar{q}). \tag{2.46}$$

There exist different choices of (α_1, α_2) that give the same lattice and leave the torus invariant. These transformations form the modular group, which acts on the modular parameter τ as

$$\tau \to \frac{a\tau + b}{c\tau + d}, \quad \text{where} \quad \begin{pmatrix} a & b \\ c & d \end{pmatrix} \in SL(2, \mathbb{Z})/\mathbb{Z}_2. \tag{2.47}$$

The modular group is generated by the S and T modular transformations, defined as,

$$\begin{aligned} T &: \tau \to \tau + 1 \\ S &: \tau \to -\frac{1}{\tau}. \end{aligned} \tag{2.48}$$

Now, for the minimal model, the characters transform into each other under the modular transformation,

$$\begin{aligned} \chi_i(-\frac{1}{\tau}) &= \mathcal{S}_{ij}\chi_j(\tau) \\ \chi_i(\tau+1) &= \mathcal{T}_{ii}\chi_i(\tau). \end{aligned} \tag{2.49}$$

The matrix $\mathcal{S}$ and $\mathcal{T}$ are called modular matrices, which are symmetric and unitary. In particular, $\mathcal{T}$ is a diagonal matrix with diagonal elements associated with the conformal dimension, $\mathcal{T}_{ii} = e^{2\pi i(h_i - \frac{c}{24})}$. The modular $\mathcal{S}$ matrix determines the fusion rule by the Verlinde formula, which will be useful in Sec. 5.

2.2.4 An example: lattice Ising model

Having introduced the basic ingredients of CFT, we now ask the following question: given a lattice model at the second-order phase transition point, how do we identify the emergent conformal field theory? More concretely, how do we identify the conformal data: central charge c, conformal dimension of primary fields h_i, and OPE coefficients C_{ijk}? Some solutions were proposed in [30, 31, 32, 33].

Let's consider the ferromagnetic critical lattice Ising model as a canonical example. The lattice Hamiltonian under periodic boundary condition is

$$H = -\sum_{i=1}^{N} \sigma_i^x \sigma_{i+1}^x - \sigma_i^z. \tag{2.50}$$

The Hamiltonian exhibits the translational symmetry T_x, which allows us to find simultaneous eigenstate of H and T_x, $H|\psi\rangle = \Delta|\psi\rangle, T_x|\psi\rangle = e^{i\frac{2\pi s}{N}}$. In Fig. 2.2, we plot the

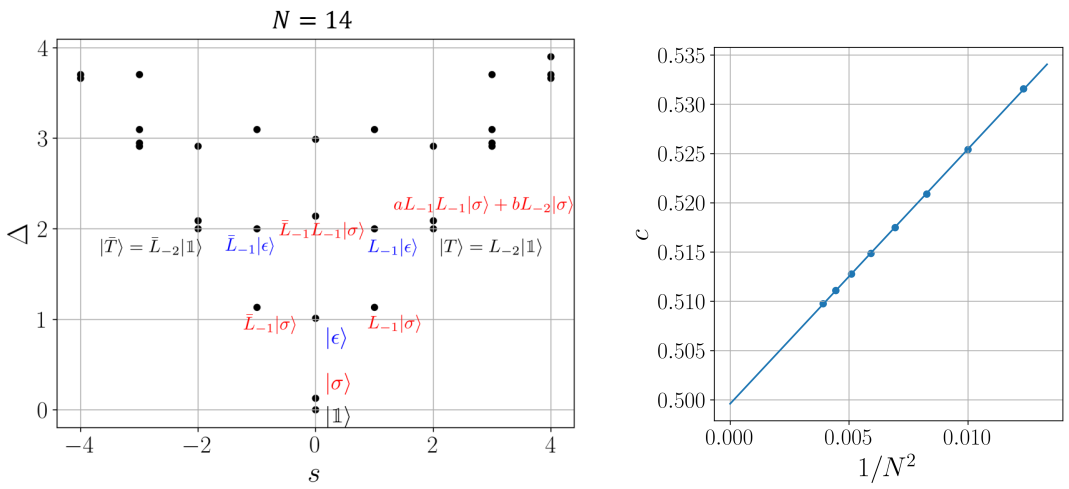

Figure 2.2: (Left) Energy-momentum spectrum of critical Ising lattice model on a $N = 14$ chain. There are three primary fields, corresponding to the three lowest energy states $|\mathbb{1}\rangle$,$|\sigma\rangle$, and $|\epsilon\rangle$. Therefore, there exist three conformal families $[\mathbb{1}], [\sigma], [\epsilon]$. (Right) Finite-size scaling of extracted central charge from the Koo-Saleur method.

energy-momentum (Δ versus s) spectrum of $N = 14$ Ising spin chain. The energy Δ is rescaled by fixing $\Delta_T - \Delta_{\mathbb{1}} = 2$, and move the ground state $|\mathbb{1}\rangle$ to zero energy.

From the spectrum, we can read the three lowest energy states as $|\mathbb{1}\rangle$,$|\sigma\rangle$, and $|\epsilon\rangle$. Indeed, the energy Δ of the first excited state $|\sigma\rangle$ is $\frac{1}{8}$ and of the second excited state $|\epsilon\rangle$ is 1, in agreement with the Ising CFT data,

$$h_\sigma = \bar{h}_\sigma = \frac{1}{16}, \quad h_\epsilon = \bar{h}_\epsilon = \frac{1}{2}. \tag{2.51}$$

Furthermore, the clear conformal towers emerge for low energy states:

$$\begin{aligned} &|\mathbb{1}\rangle, L_{-2}|\mathbb{1}\rangle, \cdots \\ &|\sigma\rangle, L_{-1}|\sigma\rangle, L_{-1}\bar{L}_{-1}|\sigma\rangle, (aL_{-1}L_{-1} + bL_{-2})|\sigma\rangle, \cdots \\ &|\epsilon\rangle, L_{-1}|\epsilon\rangle, \cdots . \end{aligned} \tag{2.52}$$

The level one descendant of $|\mathbb{1}\rangle$ does not exist, agrees with the fact that $L_{-1}|0\rangle = 0$. At the level two descendants of state $|\sigma\rangle$, there exists only one state rather than two states $L_{-2}|\sigma\rangle$

and $L_{-1}L_{-1}|\sigma\rangle$, which indicates the existence of a null state at level two. Applying the Virasoro algebra yields the null state solution as $|\chi\rangle = [L_{-2} - \frac{4}{3}L_{-1}^2]|\sigma\rangle$.

The next conformal data is the central charge. As discussed previously, the central charge can be read off from the ground state entanglement scaling. The central charge can also be obtained by entanglement-independent methods, including the ground state energy scaling and the Koo-Saleur generator method. Here we briefly introduce the Koo-Saleur method [34, 30].

Starting from the Virasoro algebra with $m = 2, n = -2$, $[L_2, L_{-2}] = 4L_0 + \frac{c}{2}$, the norm of the state $L_{-2}|0\rangle$ is $\langle 0|L_2L{-}2|0\rangle = \frac{c}{2}$. In the lattice simulation, $|T\rangle$ is the normalized, thus $|T\rangle = \sqrt{\frac{2}{c}}L_{-2}|0\rangle$. This leads to,

$$\langle T|L_{-2}|0\rangle = \sqrt{\frac{c}{2}}. \tag{2.53}$$

Once knowing the lattice representation of L_{-2}, we can use the above formula to compute c. The lattice version of the Virasoro generator is the Koo-Saleur generator, given by

$$L_{-n}^{\text{lat.}} = \sum_{j=1}^{N} e^{ijn\frac{2\pi}{N}} h_j, \tag{2.54}$$

where h_j is the lattice Hamiltonian density, $h_j = -\sigma_j^x\sigma_{j+1}^x - \sigma_j^z$ in the lattice Ising model. On the finite lattice size $N = 14$, one extracts $c = 0.5128$. The deviation from $c = 1/2$ is due to the finite size effect. The finite size scaling of c is shown in the right panel of Fig. 2.2 using system size from $N = 9$ to $N = 16$, and the intercept yields $c = 0.4996$.

There is one more piece of conformal data, the OPE coefficient C_{ijk}. Efficient numerical methods are lacking until recently. This will be the focus of Chapter 5.

2.2.5 Boundary conformal field theory

The last piece of this introduction is devoted to boundary conformal field theory (BCFT). BCFT studies the CFT on a manifold with boundaries. In the presence of a boundary, the boundary conditions need to be specified when computing the partition function. It was realized [35] that using open-closed duality, the effect of boundary condition can be captured by the *boundary state* in the closed sector.

It is perhaps surprising that boundary state is very useful in understanding quantum phases. It marks its appearance in various contexts: entanglement of topological order phase, quantum systems with defect, and boundary entropy, to name but a few. In the following, I will introduce the boundary state, and its application will be discussed in Sec. 2.3.2. Furthermore, I will generalize the boundary state to *vertex state* in Chapter 3 and use it to study the tripartite entanglement.

Consider the CFT on the upper half plane, where the boundary is the real axis. Every boundary condition has to preserve conformal symmetry; in other words, no energy-momentum flow shall go across the boundary. This leads to the "gluing condition" on the boundary state

$$(L_n - \bar{L}_{-n})|B\rangle = 0. \tag{2.55}$$

In the presence of $U(1)$ symmetry, the condition can be formulated using the current operator,

$$(j_n \pm \bar{j}_{-n})|B_{N/D}\rangle = 0, \tag{2.56}$$

where N and D stand for Neumann and Dirichlet boundary conditions. One can show Eq. (2.56) leads to Eq. (2.55).

Given a CFT, there might exist multiple solutions of the gluing condition, and their arbitrary superposition is also a valid solution. However, not all states can arise on the physical boundary. The physical boundary state should further satisfy Cardy's condition

coming from the open-closed duality.

Consider an annulus with width L and circumference T, with the boundary condition α and β on the two boundaries. The partition function on this annulus is $Z_{\alpha\beta} = \mathrm{Tr}\,\mathcal{H}_{\alpha\beta}(q^{L_0-c/24})$. Note that only chiral algebra appears because, for the CFT on a manifold with boundaries, the chiral and anti-chiral operators are not independent. Now, by open-closed duality, this partition function allows a different interpretation as the propagation of closed strings, emitted and absorbed by the boundary states. This allows us to write

$$\begin{aligned} Z_{\alpha\beta} &= tr_{\mathcal{H}_{\alpha\beta}}(q^{L_0-\frac{c}{24}}) \\ &= \langle\alpha|e^{-L\tilde{H}}|\beta\rangle = \langle\alpha|e^{-L\frac{2\pi}{T}(L_0+\bar{L}_0-\frac{c}{12})}|\beta\rangle \\ &= \langle\alpha|(\tilde{q}^{1/2})^{(L_0+\bar{L}_0-\frac{c}{12})}|\beta\rangle, \end{aligned} \tag{2.57}$$

where $q = e^{i2\pi\tau}, \tau = iT/2L$ and $\tilde{q} = e^{-\frac{i2\pi}{\tau}}$. The open and closed interpretations are related by the modular $\mathcal{S}$ transformation. This is Cardy's condition, which imposes constraints on the superposition coefficients of the boundary states.

For later convenience, we write down the boundary state solution for free Majorana fermions and the rational CFT in the following.

Free Majorana fermion

Free Majorana fermion field allows the mode expansion $\psi(\sigma) = \sum_{r\in\mathbb{Z}+1/2} e^{-i\sigma r}\psi_r$ in the Neveu Schwarz sector (namely, under anti-periodic boundary condition). For free Majorana fermion, the boundary condition takes the form of

$$(\bar{\psi}_r - \epsilon\psi_{-r})|B\rangle = 0, \tag{2.58}$$

where $\epsilon = 1$ for Neumann boundary condition and $\epsilon = -1$ for Dirichelet boundary condition. The solution can be found as

$$|B\rangle \sim \exp\left(-\epsilon \sum_{r=0}^{\infty} \psi_{-r-1/2}\bar{\psi}_{-r-1/2}\right)|0\rangle. \tag{2.59}$$

We see the solution is a fermionic Gaussian state.

Minimal model

The boundary states of the minimal model (and its generalization, rational CFT) will play an important role in the later discussion of bulk-boundary correspondence and topological entanglement entropy.

In the minimal model, each primary field ϕ_i corresponds to a solution of gluing condition, and the solutions are called the Ishibashi states. The explicit form of Ishibashi state is the summation over all states $|h_i, N; k\rangle$ in the irreducible module $M(h_\phi, c)$, tensor producted with its corresponding state $|\overline{h_i, N; k}\rangle$ in the anti-chiral module $\bar{M}(\bar{h}_\phi, \bar{c})$,

$$|B_i\rangle = \sum_{N=0}^{\infty} \sum_{k=1}^{d_{h_i}(N)} |h_i, N; k\rangle \otimes \overline{|h_i, N; k\rangle}, \tag{2.60}$$

where i is the label for primary field,N is the level, and $d_{h_i}(N)$ is the dimension of subspace for level N. Note that $|h_i, N; k\rangle$ form an orthonormal basis in space $M(h_\phi, c)$. We observe that the Ishibashi state is the maximally entangled state in $M(h_\phi, c)$ [36]. The general form of a boundary state is the linear superposition of Ishibashi states,

$$|B_\alpha\rangle = \sum_i c_{\alpha,i}|B_i\rangle, \tag{2.61}$$

with $c_{\alpha,i}$ being superposition coefficients.

The Cardy condition imposes constraints on the coefficients $c_{\alpha,i}$. Using the Verlinde

formula, one can show the Cardy state satisfies such constraints and takes the form of

$$|B_\alpha\rangle = \sum_i \frac{\mathcal{S}_{\alpha i}}{\sqrt{\mathcal{S}_{0i}}}|B_i\rangle, \tag{2.62}$$

where $\mathcal{S}$ is the modular $\mathcal{S}$ matrix.

Example Let's take the Ising CFT as an example. Using the known $\mathcal{S}$ matrix, the three physical boundary states in Ising CFT are,

$$\begin{aligned}
|+\rangle &:= |\tilde{0}\rangle = \frac{1}{\sqrt{2}}|\mathbb{1}\rangle + \frac{1}{\sqrt{2}}|\epsilon\rangle + \frac{1}{2^{1/4}}|\sigma\rangle \\
|-\rangle &:= |\frac{\tilde{1}}{2}\rangle = \frac{1}{\sqrt{2}}|\mathbb{1}\rangle + \frac{1}{\sqrt{2}}|\epsilon\rangle - \frac{1}{2^{1/4}}|\sigma\rangle \\
|f\rangle &:= |\frac{\tilde{1}}{16}\rangle = |\mathbb{1}\rangle - |\epsilon\rangle.
\end{aligned} \tag{2.63}$$

The three Cardy states are identified with the up-spin, down-spin, and free boundary condition $+, -, f$ [35]. One application of the boundary state is to derive the dimension of the boundary condition changing operator. The changing of boundary condition from α to β is equivalent to the insertion of boundary condition changing (b.c.c.) operator $\phi_{\alpha\beta}$. As an example, let's consider ϕ_{+-}. Its conformal dimension can be obtained by noting

$$\begin{aligned}
Z_{+-} = \langle\tilde{0}|(\tilde{q}^{1/2})^{L_0+\bar{L}_0-\frac{c}{24}}|\frac{\tilde{1}}{2}\rangle &= \frac{1}{2}\chi_0(\tilde{q}) + \frac{1}{2}\chi_\epsilon(\tilde{q}) - \frac{1}{\sqrt{2}}\chi_\sigma(\tilde{q}) \\
&= \frac{1}{2}S_{0j}\chi_j(q) + \frac{1}{2}S_{\epsilon j}\chi_j(q) - \frac{1}{\sqrt{2}}S_{\sigma j}\chi_j(q) = \chi_\epsilon,
\end{aligned} \tag{2.64}$$

which gives the conformal dimension of ϕ_{+-} as $h = \frac{1}{2}$.

□

2.3 Quantum entanglement meets conformal field theory

As advertised (several times), now is a good time to apply CFT to compute the entanglement quantities. We will show two examples: entanglement entropy in 1d critical chain, and topological entanglement entropy of 2d topological liquid.

2.3.1 Entanglement in 1d critical chain

In this section, we compute the simplest case: ground state entanglement of an interval $A = [u, v]$ on a 1d infinite chain at criticality, where the length of the subregion is $L_A = v-u$. The von Neumann entanglement entropy can be viewed as $n \to 1$ limit of Renyi entropy $S^{(n)}$; we will evaluate the Renyi entropy using the replica approach. The key ingredient is the twist field in CFT [37, 1, 38], whose two-point function governs the logarithmic entanglement scaling. We introduce the replica method and twist field in this example.

The starting point is to formulate the path integral representation of $\mathrm{Tr}\,(\rho_A^n)$. Let's take the density matrix of a thermal state at temperature β, $\rho = \frac{1}{Z}e^{-\beta H}$, and take the $\beta \to \infty$ limit at the end. In the Euclidean path integral formalism, the matrix element of ρ is

$$\rho(\{\phi(x'')''\} \,|\, \{\phi(x')'\}) = Z^{-1} \int [\mathcal{D}\phi(x,\tau)] \prod_x \delta(\phi(x,0) - \phi(x')') \prod_x \delta(\phi(x,\beta) - \phi(x'')'') e^{-S_E}, \tag{2.65}$$

where $S_E = \int_0^\beta L_E d\tau = \int_0^\beta H d\tau$. It can be viewed as a path integral on a strip, with boundary configuration $\phi'(x')$ at one boundary $\tau = 0$ and configuration $\phi''(x'')$ at another boundary $\tau = \beta$. Now, the trace $Z = \mathrm{Tr}\,(e^{-\beta H})$ is simply found by sewing these two boundaries, by setting $\{\phi'(x')\} = \{\phi''(x'')\}$. Namely, $Z = \mathrm{Tr}\,(e^{-\beta H})$ is a cylinder path integral. Similarly, the reduced density matrix $\rho_A = \mathrm{Tr}_{\bar{A}}(e^{-\beta H})$ is obtained by sewing the region $\bar{A}$, the complement of A. The path integral of $\mathrm{Tr}\,(\rho_A)$ is on a cylinder with a slit, as shown in Fig. 2.3(a).

Now, $\mathrm{Tr}\,(\rho_A^n)$ can be computed by taking n copies of ρ_A and sewing the slits such that

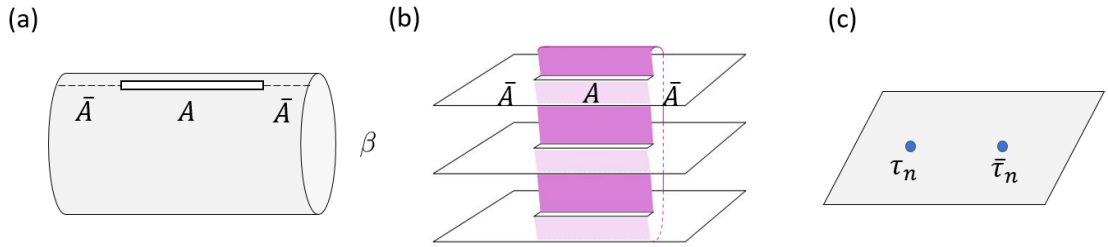

Figure 2.3: (a) Path integral representation of ρ_A at finite β. (b) Path integral representation of $\mathrm{Tr}\,(\rho_A^n)$ at $\beta \to \infty$. The illustration (b) is taken from [1].

$\phi_k'(x) = \phi_{k+1}''(x)$ for all $x \in A$ (ϕ_{n+1} is identified with ϕ_1). This forms a n-sheeted Riemann surface $\mathcal{R}$ as shown in Fig. 2.3(b), and $Z_n(A)$ is the path integral on $\mathcal{R}$. After normalization,

$$\mathrm{Tr}\,(\rho_A^n) = \frac{Z_n(A)}{Z^n}, \tag{2.66}$$

and von Neumann EE can be obtained by taking the limit

$$S_A = -\lim_{n\to 1} \frac{\partial}{\partial n} \mathrm{Tr}\,\rho_A^n. \tag{2.67}$$

This is the so-called "replica method".

Next, we need to compute the path integral $Z_n(A)$ on the Riemann surface $\mathcal{R}$. We adopt the ansatz that the effect of n-sheeted Riemann surface $\mathcal{R}$ is equivalent to inserting two twist operators $\tau, \bar{\tau}$ on the complex plane $\mathbb{C}$. In fact, the twist fields $\tau_n, \bar{\tau}_n$ are the primary fields in the cyclic orbifold CFT, obtained by gauging the $\mathbb{Z}_n$ cyclic symmetry of n copies of original CFT. Under this ansatz, $\mathrm{Tr}\,\rho_A^n$ of an interval $A = [u, v]$ is the two-point function of the twist fields, whose behavior is dictated by CFT

$$\mathrm{Tr}\,\rho_A^n = \frac{Z_n(A)}{Z^n} = c_1 \langle \tau_n \bar{\tau}_n \rangle^n = c_1 \left(\frac{|v-u|}{a} \right)^{-4nh_{\tau n}}. \tag{2.68}$$

Here h_{τ_n} is the conformal dimension of the twist operator [3], and a is the lattice constant acting as a cutoff.

We then proceed to evaluate h_{τ_n}. The trick is to use a conformal transformation to bring the n-sheeted Riemann surface with coordinate w to the complex plane with coordinate z: $z = ((w-u)/(w-v)^{1/n}$. Using the above ansatz, the stress tensor shall satisfy

$$\langle T(\omega)\rangle_{\mathcal{R}} = \frac{\langle T(\omega)\tau_n(u)\bar{\tau}_n(v)\rangle_{\mathbb{C}}}{\langle \tau_n(u)\bar{\tau}_n(v)\rangle_{\mathbb{C}}}. \tag{2.69}$$

The left-hand side can be evaluated by the conformal transformation of the stress tensor which involves Schwarzian derivative $\{z,\omega\}$. The result gives

$$\langle T(\omega)\rangle_{\mathcal{R}} = \frac{c}{12}\{z,\omega\} = \frac{c(1-(1/n)^2)}{24}\frac{(v-u)^2}{(\omega-u)^2(\omega-v)^2}. \tag{2.70}$$

The right-hand side can be computed using Ward identity, which yields

$$\langle T(\omega)\tau_n(u)\bar{\tau}_n(v)\rangle_{\mathbb{C}} = \frac{h_{\tau_n}(v-u)^2}{(\omega-u)^2(\omega-v)^2|u-v|^{4h_{\tau_n}}}, \tag{2.71}$$

and the denominator $\langle \tau_n(u)\bar{\tau}_n(v)\rangle_{\mathbb{C}}$ is simply a two-point function $1/|u-v|^{4h_{\tau_n}}$. Identifying the left and right-hand side, the conformal dimension of the twist field can be read out as

$$h_{\tau_n} = \frac{c}{24}(1-\frac{1}{n^2}). \tag{2.72}$$

This finishes the calculation of $\mathrm{Tr}\,\rho_A^n$ using Eq. (2.68).

Finally, the entanglement entropy can be computed by the replica method. Denote

3. In the literature, there exists another convention in defining the twist operator; their conformal dimensions differ by a factor of n.

$L_A = |v - u|$ as the length of the interval, the results read

$$\begin{aligned} S_A &= -\lim_{n\to 1} \frac{\partial}{\partial n} \mathrm{Tr}\, \rho_A^n = \frac{c}{3} \ln \frac{L_A}{a} \\ S_A^{(n)} &= \frac{1}{1-n} \ln \mathrm{Tr}\, \rho_A^n = \frac{c}{6}(1 + \frac{1}{n}) \ln \left(\frac{L_A}{a} \right). \end{aligned} \tag{2.73}$$

The logarithmic entanglement scaling is correctly predicted by conformal field theory.

By further conformal transformation, the above method can give results for entanglement entropy on the periodic chain, or finite temperature. By fusion of twist operators, one can compute the logarithmic negativity.

As briefly mentioned above, the twist operator τ_n is a primary field in the cyclic orbifold CFT. In cyclic orbifold CFT, there exists a family of twist operators, and the one introduced here is the "leading" twist operator, the one with the lowest conformal dimensional. We will see in Chapter 5 that the whole family of the twist operators plays an important role in the context of universal finite-size correction.

2.3.2 BCFT and topological entanglement entropy

Moving beyond the critical spin chain described by CFT, for the general quantum field theories, calculating entanglement entropy is a difficult task. Among them, topological quantum field theory is a special case where entanglement is computable. There exist various techniques, and we shall use the bulk-boundary correspondence, which we call the "edge-theory approach". Specifically, we will use the boundary CFT to evaluate the topological entanglement entropy of the 2d bulk.

Edge-theory approach

Here, we consider a two-dimensional bulk theory of topological liquid. In the edge-theory approach [39, 40, 41, 42, 43, 44, 45], we compute the entanglement between subregions of a

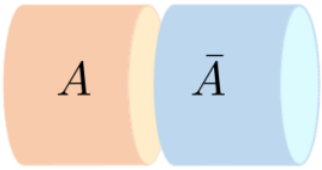

Figure 2.4: Entanglement cut of bipartite entanglement on the cylinder geometry.

topological phase by first physically cutting the system along the entanglement cut, which gives rise to the edge states. We then "glue" the system back together by introducing a tunneling interaction to gap out the edge states. Since the correlation length vanishes in the bulk, we can approximate the entanglement between the bulk subregions as arising solely from entanglement between the gapped edge modes. The first step in this computation is then to determine the ground state of this gapped interface along the entanglement cut. For the case of a simple bipartition, this ground state is known to take the form of a conformal boundary state, or more precisely, an Ishibashi state [39, 42].

Let's illustrate the above argument using a simple example, the chiral p-wave superconductor on an infinite spatial cylinder. The entanglement cut partitions the cylinder into two half cylinders A and $\bar{A}$ (see Fig. 2.4), and the entangling boundary is a circle. We physically cut the cylinder along the entanglement cut, As described above, we physically cut the system along the entanglement cut, resulting in gapless edge modes on the boundaries of regions A and $\bar{A}$, respectively. In the case of the chiral p-wave superconductor, they are described by chiral real (Majorana) fermion theories with opposite chiralities, denoted by γ_L and γ_R. Their dynamics at low energies can be described by

$$H_0 = \int_0^{2\pi} d\sigma \big[\gamma_L i\partial_\sigma \gamma_L + \gamma_R(-i\partial_\sigma)\gamma_R\big]. \tag{2.74}$$

Here, we take the circumference of the cylinder to be $L = 2\pi$ for simplicity. For later

purposes, it is convenient to introduce

$$\psi^1(\sigma) \equiv \gamma_L(\sigma), \quad \psi^2(\sigma) \equiv \gamma_R(2\pi - \sigma). \tag{2.75}$$

The edge state Hamiltonian is then written as

$$H_0 = \int_0^{2\pi} d\sigma \sum_{I=1,2} \psi^I i\partial_\sigma \psi^I. \tag{2.76}$$

In the Neveu-Schwarz sector, the chiral Majorana fermion field $\psi(\sigma)$ can be Fourier expanded as $\psi(\sigma) = \sum_{s\in\mathbb{Z}+1/2} e^{-i\sigma s}\psi_s$, and the vacuum of the NS sector is defind by $\psi_s|0\rangle = 0$ for $s > 0$.

In order to "glue" the system back together, we introduce a tunneling term that gaps out the chiral edge degrees of freedom. Explicitly, we describe the gapped edge with the Hamiltonian $H_0 + H_{int}$, where

$$H_{int} = im \int_0^{2\pi} d\sigma\, \gamma_L \gamma_R = im \int_0^{2\pi} d\sigma\, \psi^1(\sigma)\psi^2(2\pi - \sigma). \tag{2.77}$$

As described above, we identify the entanglement between A and $\overline{A}$ as arising purely from the entanglement between the chiral and anti-chiral Majorana fermions in this gapped state (i.e. the "left-right" entanglement [46]).

The gapped ground state is in fact related to a conformal boundary state, or more precisely, an Ishibashi state, $|B\rangle$, of the gapless theory described by H_0. In terms of ψ^1, ψ^2, the boundary condition is

$$[\psi^1(\sigma) - i\psi^2(2\pi - \sigma)]|B\rangle = 0. \tag{2.78}$$

One can show that

$$|B\rangle = \exp(i \sum_{r\geq 1/2} \psi^1_{-r}\psi^2_{-r})|0\rangle \tag{2.79}$$

is the ground state of H in the limit $|m| \to \infty$. From the Ishibashi boundary state, we can approximate the ground state of the (2+1)d topological phase near the entanglement boundary for large but finite m with the regularized state,

$$|G\rangle = \mathcal{N} e^{-\beta H_0}|B\rangle. \tag{2.80}$$

Here, the regulator β is inversely proportional to the bulk energy gap. Indeed, the conformal boundary condition (and the explicit form of the Ishibashi states) pairs up the left and right movers, just as a tunneling interaction would gap out the left and right movers at the interface. The reduced density matrix can then be constructed from $|G\rangle$ by tracing over $\bar{A}$, $\rho_A = \mathrm{Tr}_{\bar{A}} |G\rangle\langle G|$. We emphasize that, while we took the non-interacting fermion theory as an example, essentially the same construction of the reduced density matrix using the Ishibashi boundary state can be done for a much broader class of theories.

Topological entanglement entropy

We now apply the edge-theory approach to topological liquid whose bulk is described by the Chern-Simons theory. After physically cutting the cylinder, the edge modes on the boundaries of A and $\bar{A}$ are described by a corresponding rational CFT (TQFT/CFT correspondence). As we introduced in Sec. 2.2.5, each primary field ϕ_i yields a solution of Ishibashi state $|B_i\rangle$. We can approximate the ground state of the (2+1)d topological phase near the entanglement boundary by a regularized boundary state,

$$|G\rangle = \sum_i c_i \, |\mathbf{B}_i\rangle \, , \quad |\mathbf{B}_i\rangle = \frac{e^{-\beta H_0}}{\sqrt{n_i}}|B_i\rangle. \tag{2.81}$$

Here H_0 is the CFT Hamiltonian $H_0 = \frac{2\pi}{L}(L_0 + \bar{L}_0 - \frac{c}{12})$, where $L_0, \bar{L}_0$ are zero modes of the stress tensor $T, \bar{T}$, c is the central charge, and L is the length of the entanglement cut. The normalization factor n_i is defined such that these regularized states are orthonormal $\langle \mathbf{B}_i | \mathbf{B}_j \rangle = \delta_{ij}$. In the context of the bipartition of the cylinder, the Ishibashi state $|\mathbf{B}_i\rangle$ describes the gapped interface along the entanglement cut when a single anyon line i pierces the entanglement cut.

With the description of the interface in hand, we can approximate the entanglement entropy between the bulk regions A and $\bar{A}$ as the "left-right" entanglement entropy of the boundary state – that is, the entanglement entropy between the chiral and anti-chiral sectors of the interface Hilbert space. Explicitly, for an interface state of the form $|G\rangle = \sum_i c_i |\mathbf{B}_i\rangle$, corresponding to the density matrix

$$\rho = \sum_{i,j} \frac{c_i c_j^*}{\sqrt{n_i n_j}} e^{-\beta H_0} |B_i\rangle \langle B_j| e^{-\beta H_0}, \tag{2.82}$$

describing a superposition of states with single anyon lines threading the entanglement cut, we can explicitly compute the reduced density matrix for the left-movers (or chiral sector, with states $|\overline{h_i, N; k}\rangle$),

$$\rho_L = \mathrm{Tr}_R\big[\, |\psi\rangle \langle\psi| \,\big], \tag{2.83}$$

where the trace is performed over the right-movers (anti-chiral sector). The entanglement entropy is then straightforwardly computed using the replica trick,

$$S_A = -\mathrm{Tr}\left[\rho_L \log \rho_L\right] = \lim_{n\to 1} \frac{1}{1-n} \ln \mathrm{Tr}\, \rho_L^n. \tag{2.84}$$

Carrying this through with the modular $\mathcal{S}$ transformation [42], one finds

$$S_A = \frac{c\pi L}{24\beta} - S_{\text{topo}}, \tag{2.85}$$

where the first is the non-universal area law contribution while the second term is the topological entanglement entropy,

$$S_{\text{topo}} = \ln \mathcal{D} + \sum_i |c_i|^2 \ln |c_i|^2 - \sum_i |c_i|^2 \ln d_i, \tag{2.86}$$

where d_i is the quantum dimension of anyon i and $\mathcal{D} = \sqrt{\sum_i d_i^2}$ is the total quantum dimension. For an Ishibashi state $c_i = \delta_{i,a}$, corresponding to a state with a definite anyon line threading the entanglement cut, the topological contribution is $S_{\text{topo}} = \ln \mathcal{D} - \ln d_a$; this further reduces to $S_{\text{topo}} = \ln \mathcal{D}$ in the absence of anyon line insertion ($a = \mathbb{1}$). For Abelian topological order, all quantum dimensions $d_i = 1$ and the topological entanglement entropy reduces to $S_{\text{topo}} = \ln \mathcal{D} + \sum_i |c_i|^2 \ln |c_i|^2$, where the second term is the Shannon entropy associated with the probability distribution $\{|c_i|^2\}$. We thus see that the boundary state description of the interface captures the expected bipartite entanglement structure of the bulk topological phase. It correctly yields the topological entanglement entropy in the absence of anyon insertion.

The edge-theory approach is applicable to more interesting cases, for example, the 2d torus with anyon insertion. Due to the possible ground state degeneracy of 2d topological order, the bulk ground state under interest can be a superposition of degenerate ground states $|\Psi\rangle = \sum_i c_i |\Phi_i\rangle$; this bulk state precisely corresponds to the boundary state $|G\rangle = \sum_i c_i |\mathbf{B}_i\rangle$ with the same superposition coefficient. When dividing the torus into two finite cylinders $A, \bar{A}$, so that each region is non-contractible, the resulting topological entanglement entropy

is [42]

$$S_{\text{topo}} = 2\ln \mathcal{D} + \sum_i |c_i|^2 \log |c_i|^2 - 2\sum_i |c_i|^2 \log d_i. \tag{2.87}$$

The edge-theory results agree with TQFT calculation and lattice calculation [47, 48].

In this section, we have learned how to compute bipartite entanglement entropy of topological liquid from the edge-theory approach using the boundary CFT. This prepares us for the topic of the next chapter: tripartite entanglement in topological liquid.

CHAPTER 3

TOPOLOGICAL LIQUID

Topologically ordered phases of matter are characterized not by local order parameters but by their pattern of long-range entanglement. Concretely, from the scaling of the entanglement entropy of a bipartition, one can extract a universal property of topological ground states, the so-called topological entanglement entropy [12, 13], as discussed in the last chapter. While the topological entanglement entropy provides a signature for topological ground states, it is far from a full characterization of topological data; there are topological states that share the same topological entanglement entropy yet are distinct from each other.

Recent publications [45, 49, 50, 51, 52] initiated the study of multipartite entanglement of topological ground states in two spatial dimensions. In particular, Refs. [45, 49, 52] investigated the recently introduced reflected entropy [53] as well as the entanglement negativity for tripartitions of topological ground states, in which the three spatial subregions meet at junctions. For a system of three spin 1/2 degrees of freedom, the reflected entropy (or more precisely, the Markov gap which is the difference between the reflected entropy and mutual information – see below) detects the tripartite entanglement of the W-state, while it is insensitive to GHZ-type tripartite entanglement [54]. The reflected entropy can thus capture quantum correlations beyond simple Bell or EPR-type bipartite correlations. Indeed, a structure theorem was proven in Ref. [55], classifying the set of states with zero Markov gap [1]. There, the reflected entropy was further studied for gapped as well as critical ground states in one spatial dimension.

In this chapter, we dicuss the reflected entropy $S_R(A, B)$ for two regions A and B for the ground state of two-dimensional topological liquid [45, 52]. Here, the total system is put on a spatial sphere and tripartitioned into three regions A, B, and C that meet at two points (junctions). The region $C = \overline{AB}$ is partially traced out to obtain the reduced density ρ_{AB}

1. See Ref. [56] for further discussion that gave the Markov gap its name.

matrix for $A \cup B$. By using the bulk-boundary correspondence and techniques from string field theory, we found for the chiral p-wave superconductor and the integer quantum Hall state [45] that the Markov gap, which is the difference between the reflected entropy and the mutual information, is independent of the subregion sizes and given by the universal formula

$$h(A, B) := S_R(A, B) - I(A, B) = \frac{c}{3} \ln 2, \tag{3.1}$$

where c is the central charge of the topological liquid, and $c = 1$ and $c = 1/2$ for the integer quantum Hall state and chiral p-wave superconductor, respectively. On the other hand, Ref. [49] studied the Markov gap for string-net models (the Levin-Wen models), for which the central charge is zero, and found that $h(A, B) = 0$. (See also Ref. [57].) Equation (3.1) relates tripartite quantum entanglement to the central charge and hence captures the universal data of topological liquid beyond the topological entanglement entropy. These calculations were done for ideal, representative topological ground states realized deep inside a topological phase. Refs. [45, 49] also numerically studied the reflected entropy in a lattice model of Chern insulators. While the Markov gap was still found to be insensitive to the subregion and systems sizes, the formula (3.1) does not hold verbatim, but its RHS provides a lower bound of the Markov gap, $h(A, B) \geq (c/3) \ln 2$. Putting these results together, the Markov gap in the tripartition setup above is conjectured to capture the central charge of stable (ungappable) degrees of freedom at the boundary of topological liquid; that is to say, a non-zero Markov gap may be an obstruction to completely gap out the boundary (edge) theory.

We next [52] generalize the above result and present an analytical approach to multipartite entanglement that can be applied to generic (chiral) topological ground states in two spatial dimensions. Following Ref. [45], we use the bulk-boundary correspondence and reduce the calculations of the entanglement quantities to calculations in conformal field theory (CFT). Specifically, we will show that the calculations can be reformulated in terms of defect

(interface) CFT, and furthermore simplified by taking the advantage the limit of small β/L, where $1/\beta$ is the bulk gap and L is the length of the entangling boundary. By using a series of conformal transformations, a given entanglement quantity can be evaluated as a path integral on a cylinder with topological interfaces.

This chapter will be organized as follows. The tripartite entanglement of interest, the reflected entropy and the Markov gap, will be introduced in Sec. 3.1. To evalute the tripartite entanglement, we generalize the edge-theory approach and define the vertex state in Sec. 3.2, based on Ref. [45]. The explicit vertex state solution for the chiral p-wave superconductor will be constructed, with the numerical results for the Markove gap. This result is generalized to general topological ground states in Sec. 3.3 by conformal interface technique, based on Ref. [52].

3.1 Reflected entropy and Markov gap

Reflected entropy $S_R(A,B)$ provides a correlation measure for tripartite Hilbert spaces. Given a reduced density matrix ρ_{AB} supported on $A\cup B$, we can obtain its canonical purification $|\sqrt{\rho}\rangle\!\rangle$ in the doubled Hilbert space $(A\cup B)\cup(\tilde{A}\cup\tilde{B})$, where $\tilde{A}$ and $\tilde{B}$ are identical copies of A and B, respectively (with complex conjugation). The reflected entropy $S_R(A,B)$ is defined as the entanglement entropy of the purified state $|\sqrt{\rho}\rangle\!\rangle$ when tracing out the degrees of freedom in $B,\tilde{B}$:

$$S_R(A,B)=S(\rho_{A\cup\tilde{A}}),\quad \rho_{A\cup\tilde{A}}=\mathrm{Tr}_{B\cup\tilde{B}}\left(|\sqrt{\rho}\rangle\!\rangle\langle\!\langle\sqrt{\rho}|\right). \tag{3.2}$$

The reflected entropy has been studied in various many-body quantum systems. For example, in (1+1)d CFT, the reflected entropy has been studied for the ground state [53], and for time-dependent states after quantum quench [58, 59, 60]. The reflected entropy was also computed for multi-sided thermofield double states in (non-chiral) (1+1)d CFT (which has

some similarly to vertex states that we will introduce later) [61]. The reflected entropy is a more sensitive probe of multipartite entanglement than the von Neumann entropy [54, 55]. The difference between the reflected entropy and mutual information

$$h(A,B) = S_R(A,B) - I(A,B), \tag{3.3}$$

is bounded from below, $h(A,B) \geq 0$ [53], and called the Markov gap in Ref. [62] as it is related to the fidelity of a particular Markov recovery process on the canonical purification. The difference $h(A,B)$ is proposed as a non-negative universal tripartite entanglement invariant [33]. It was also shown that for the ground states of 1d lattice quantum systems at conformal critical points when the subregion A and B are adjacent to each other, $h(A,B)$ takes a universal value, $h(A,B) = (c/3)\ln 2$, where c is the (non-chiral) central charge [33].

For the ground states of (2+1)d topological liquids, it was recently conjectured in Ref. [49] that $h(A,B)$, when computed for the tripartite setting in Fig. 3.1, captures the total central charge of the topological liquid. Specifically, from the topological ground state $|\Psi\rangle$, we consider a state $U|\Psi\rangle$ where a local unitary U acts near the junction. This unitary U can be optimized such that it removes non-universal, short-range correlation near the junction. Then, the claim in [49] is that the optimized version of $h(A,B)$,

$$h^{IR}(A,B) = \min_U h(A,B)(U|\Psi\rangle), \tag{3.4}$$

takes the universal value,

$$h^{IR}(A,B) = \frac{c}{3}\ln 2 + \mathcal{O}(e^{-\ell/\xi}), \tag{3.5}$$

where ξ is the correlation length, ℓ is the length scale for the three regions, and c is the central charge of the topological liquid that measures ungappable edge degrees of freedom,

i.e., $c_L + c_R$ where $c_{L/R}$ is the left/right central charge. This conjecture was tested in Ref. [49] for sting-net models, for which $c = 0$, and for a non-interacting Chern insulator model with proper optimization over U.

3.1.1 Gaussian state approach

For Gaussian states, the reflected entropy can also be computed conveniently using the covariance matrix method [63]. Using the orthogonal transformation O to bring ρ and Γ to canonical forms:

$$\begin{aligned} \rho &= \prod_k \frac{1}{2}(1 + \gamma_k c'_{2k-1} c'_{2k}) \quad \text{where} \quad c' = Oc, \\ \Gamma &= O^T \left[\oplus_k \begin{pmatrix} 0 & i\gamma_k \\ -i\gamma_k & 0 \end{pmatrix} \right] O. \end{aligned} \tag{3.6}$$

The purified state is given by

$$|\sqrt{\rho}\rangle\rangle = \prod_k \left[\sqrt{\frac{1+\gamma_k}{2}} |0\rangle_k |\tilde{0}\rangle_k + \sqrt{\frac{1-\gamma_k}{2}} |1\rangle_k |\tilde{1}\rangle_k \right], \tag{3.7}$$

where $|\tilde{0}\rangle_k, |\tilde{1}\rangle_k$ are states in the second copy of the Hilbert space for the k-th mode. The associated covariance matrix for $|\sqrt{\rho}\rangle\rangle$ is

$$\Gamma_{\sqrt{\rho}} = O \left[\oplus_k \begin{pmatrix} \gamma_k \sigma^y & -i\sqrt{1-\gamma_k^2}\mathbb{1} \\ i\sqrt{1-\gamma_k^2}\mathbb{1} & -\gamma_k \sigma^y \end{pmatrix} \right] O^T. \tag{3.8}$$

The reflected entropy $S_R(A, B)$ is then computed as the von Neumann entanglement entropy using the $A, \tilde{A}$ blocks in $\Gamma_{\sqrt{\rho}}$.

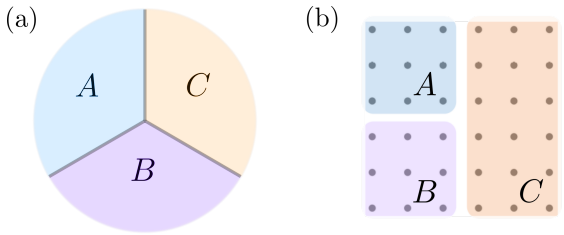

Figure 3.1: Tripartition of topological liquid on a two-dimensional plane (a) and two-dimensional square lattice (b).

3.2 Edge theory approach: vertex state

In this section, we use the edge theory approach to evalute the tripartite entanglement quantities by generalize the boundary state to its tripartite analog, the vertex state. After motivating the definition of vertex state in Sec. 3.2.1, we introduce the Neumann coefficient method in Sec. 3.2.2 as a vertex state solution ansatz for free fermion. The Neumann coefficient method is versatile and can be applied to both Neveu Schwarz (NS) and Ramond (R) sector. The explicit solution of vertex state and the numerical result for entanglement are presented for bipartition and tripartition in Sec. 3.2.3 and Sec. 3.2.4, respectively.

3.2.1 Vertex state

Having defined the tripartite entanglement quantity, the reflected entropy, we proceed to evaluate it for the topological liquid and show $h(A, B) = \frac{c}{3} \ln 2$. In the edge-theory approach, the bipartite entanglement quantities are evaluated using boundary state defined on the entanglement cut. We now extend this method to tripartition and define the *vertex state*. For simplicity, we first consider the free fermion case, the chiral p-wave superconductor.

We first note that the configuration in Fig. 3.1(a) is topologically equivalent to the one obtained by first considering three cylinders, corresponding to the regions A, B, C, and then gluing these cylinders together [Fig. 3.2(a)]. As in the case of a bipartition, we cut open the system along the cut, resulting in an edge theory comprising three free Majorana fermions,

as described by the Hamiltonian,

$$H_0 = \int_0^{2\pi} d\sigma \sum_{I=1}^{3} \psi^I i\partial_\sigma \psi^I. \tag{3.9}$$

We again heal the cut by introducing tunneling terms of the form,

$$H_{int} = im \int_0^{\pi} d\sigma \sum_I \psi^{I+1}(\sigma)\psi^I(2\pi - \sigma), \tag{3.10}$$

such that the total Hamiltonian is $H_0 + H_{int}$. (Here and henceforth, we use the convention $\psi^4 \equiv \psi^1$). Analogously to the Ishibashi boundary state satisfying the condition (2.78), the ground state in the limit $|m| \to \infty$ is given by a conformal boundary state, $|V\rangle$, which satisfies

$$\left[\psi^{I+1}(\sigma) - i\psi^I(2\pi - \sigma)\right]|V\rangle = 0, \quad 0 \leq \sigma \leq \pi. \tag{3.11}$$

Solving the constraint, the state $|V\rangle$ is given in the form of a fermionic coherent state (which is Gaussian state). These types of states, which we will refer to as vertex states, have been considered in the context of string field theory [64, 65, 66, 67] where they describe the interaction among strings. As before, we regularize this state and consider $|G\rangle = \mathcal{N}e^{-\beta H_0}|V\rangle$, which provides an approximation to the ground state of H for large but finite $|m|$. Once $|G\rangle$ is obtained, we can compute the reduced density matrices ρ_{AB}, ρ_{BC}, and ρ_{CA} as well as the entanglement measures.

Although Eq. (3.11) uniquely defines the Majorana fermion vertex state, an equivalent and more general definition of vertex states, which also motivates the so-called Neumann coefficient approach to constructing them, proceeds as follows. In the interest of generality, we consider the most general case of an N-junction, such that N edge theories meet at a single point (the tripartition setup of our interest corresponds to $N = 3$). Hence, we start

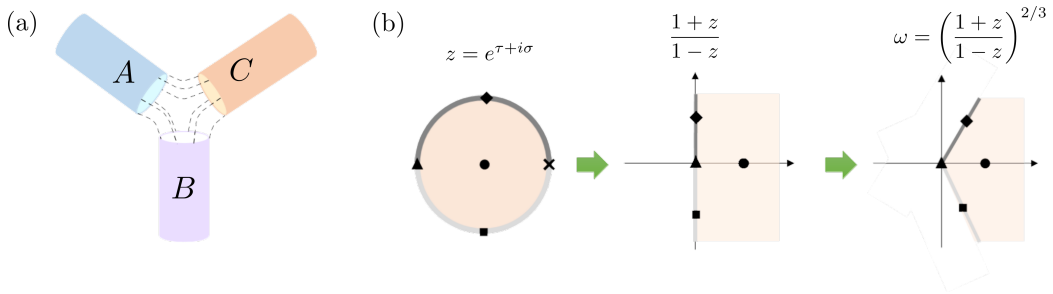

Figure 3.2: (a) Gluing three cylinders from edge theory point of view. (b) The conformal map used to define vertex states for tripartition. One disk ($0 \le \sigma \le 2\pi, \tau < 0$) is mapped to the one-third of the whole plane. The past infinity point $\tau = -\infty$, denoted by the black filled circle, is mapped to $\omega_{1,0} = e^{i\pi/3}, \omega_{2,0} = e^{-i\pi/3}, \omega_{3,0} = e^{-i\pi}$ for $I = 1, 2, 3$ by Eq. (3.16).

with N copies of chiral CFTs (edge theories) defined on a spatial circle parameterized by $0 \le \sigma \le 2\pi$. Their Hilbert spaces are denoted by $\mathcal{H}_{1,2,\ldots,N}$, respectively. Together with the (imaginary) time direction τ, we have a cylindrical spacetime. As usual, we can map each theory to the conformal plane through the coordinate transformation $z = e^{\tau+i\sigma}$, such that the half of the cylinder $-\infty \le \tau \le 0$ is mapped to the unit disk, $|z| \le 1$. We next consider conformal maps ω_I from the I-th unit disk to the complex plane $\mathbb{C}$ that are analytic inside the unit disk. In particular, they map each disk to a separate wedge of the complex plane $\mathbb{C}$, with the requirement that the edges of each wedge are flush with one another so that the desired boundary conditions are implemented. This sequence of maps for one disk is illustrated for the case $N = 3$ in Fig. 3.2(b). We will elaborate more on this after we present the explicit form of the conformal maps momentarily. Then, we define a vertex state $|V\rangle \in \mathcal{H}_1 \otimes \mathcal{H}_2 \otimes \cdots \otimes \mathcal{H}_N$ by requiring it reproduce correlation functions on the complex plane as follows [67]:

$$\begin{aligned} &\langle V| \left(O_\alpha |0\rangle_1 \otimes O_\beta |0\rangle_2 \otimes \cdots \otimes O_\gamma |0\rangle_N \right) \\ &= \left\langle \, \omega_1[O_\alpha] \, \omega_2[O_\beta] \, \cdots \, \omega_N[O_\gamma] \, \right\rangle_{\mathbb{C}} \end{aligned} \tag{3.12}$$

where $|0\rangle_I$ is the vacuum in $\mathcal{H}_I$, $O_{\alpha,\beta,\cdots,\gamma}$ represents an arbitrary (primary) operator acting

on $\mathcal{H}_{1,2,\cdots,N}$, $\omega_I[O]$ represents the transformation of a primary operator O by ω_I, $\omega_I[O(z)] = [\omega_I'(z)]^h O(\omega_I(z))$, where h is the conformal dimension of O. In order to fix the form of the conformal transformations ω_I which define the vertex state, we must impose additional constraints on $|V\rangle$. First, it is clear that, since the N Hilbert space copies are equivalent, the vertex states must invariant under their cyclic permutation. That is to say, focusing on $N = 3$,

$$\langle V_{123}| = \langle V_{231}| = \langle V_{312}|, \tag{3.13}$$

where the subscripts label the Hilbert space indices. Physically, this is just the statement that the trijunction is invariant under 120° rotations. A second, less obvious requirement is given by, again focusing on $N = 3$,

$$\langle V_{125}|\langle V_{5\dagger 34}| = \langle V_{235}|\langle V_{5\dagger 41}|, \tag{3.14}$$

The two sides of this expression correspond to gluing together two $N = 3$ vertex states to obtain $N = 4$ vertex states. This constraint expresses the fact that this $N = 4$ vertex state must also be invariant under cyclic permutations of the Hilbert spaces (i.e. under 90° rotations of the "tetrajunction").[2] Enforcing these constraints restricts the choice of conformal transformations ω_I, which in turn define the vertex state $|V\rangle$. We next describe choices of the ω_I satisfying these constraints, which then lead to vertex states satisfying Eq. (3.11).

For $N = 2$, we can choose the following conformal maps [68]:

$$\omega_I(z) = \omega_{I,0}\frac{1+z}{1-z}; \quad \omega_{I,0} = -ie^{i\pi I},\ I = 1, 2. \tag{3.15}$$

In this way, the first disk is mapped to the upper half plane and the second to the lower

2. In the original string field theory context in which these vertex states first appeared, these cyclicity constraints follow from demanding gauge invariance of the string interaction vertex.

half plane. Note also that the infinite past $\tau = -\infty$ is mapped to $\pm i$, respectively. Here, we note that a quantum state at $\tau = 0$ or $|z| = 1$ can be obtained by a path integral from $\tau = -\infty$ or $|z| = 0$ with possibly an insertion of an operator. By the conformal maps $\omega_{1,2}$, the $\tau = 0$ slices of the disks are both mapped to the real axis. Hence, the field configurations for ψ^1 and ψ^2 are subject to the constraint in (2.78); we will show this more explicitly in the following subsection.

Likewise, for $N = 3$, we can choose $\omega_{1,2,3}$ as

$$\omega_I(z) = \omega_{I,0} \left(\frac{1+z}{1-z} \right)^{\frac{2}{3}} ; \omega_{I,0} = e^{\frac{4\pi i I}{3} - i\pi}, \; I = 1, 2, 3. \tag{3.16}$$

Note that $\omega_I(2\pi - \sigma) = \omega_{I+1}(\sigma)$ for $0 \leq \sigma \leq \pi$. These conformal maps bring three disks ($0 \leq \sigma \leq 2\pi, \tau < 0$) to the whole plane, such that each unit disk is mapped to a separate 120° wedge of the conformal plane, as shown in Fig. 3.2(b) and Fig. 3.4(a). Here, the points at infinity are identified. We note that this construction is similar to, but slightly different from, the conformal maps used in open string field theory by Witten [69]; the CFTs we consider obey (potentially twisted) periodic boundary conditions. Though this alternative definition of the vertex states seems obtuse at first glance, we will see in the following that it provides an elegant way of deriving the explicit form of said states.

3.2.2 The Neumann coefficient method

Let us now move on to the methods of constructing vertex states. On the one hand, the overlap condition (3.11) can be solved directly, and the vertex state can be constructed as a coherent state. We discussed the direct construction in Appendix A of Ref. [45] and showed the two methods give consistent results numerically.

On the other hand, the definition of vertex states (3.12) suggests the following strategy to construct vertex states, which we call the the Neumann coefficient method. For now, we

focus on the NS sector for simplicity. We postulate the following Gaussian ansatz for $|V\rangle$:

$$|V\rangle = \exp\Big(\sum_{r,s\geq 1/2} \frac{1}{2}\psi^I_{-r} K^{IJ}_{rs} \psi^J_{-s}\Big)|0\rangle. \tag{3.17}$$

(Here and henceforth, we adopt the convention in which repeated flavor indices $I, J, \cdots$ are summed over implicitly, unless otherwise stated.) The coefficients K^{IJ}_{rs} are chosen to reproduce the correlation function on the right-hand side of (3.12). Since $|V\rangle$ is Gaussian, it is sufficient to consider the two point functions of the fermion fields. We then consider, at $\tau = 0$, the Neumann function

$$\begin{aligned} K^{IJ}(\sigma,\sigma') &\equiv \langle\, \omega_I[\psi^I(\sigma)]\, \omega_J[\psi^J(\sigma')]\,\rangle_{\mathbb{C}} \\ &= \left(\frac{d\omega_I}{id\sigma}\right)^{1/2} \left(\frac{d\omega_J}{id\sigma'}\right)^{1/2} \frac{1}{\omega_I - \omega_J}. \end{aligned} \tag{3.18}$$

(Here, I, J are not summed on the right hand side.) The Neumann function is constructed using the conformal map ω_I. The Neumann coefficients K^{IJ}_{rs} are related to the mode expansion of $K^{IJ}(\sigma,\sigma')$ as

$$K^{IJ}(\sigma,\sigma') = \sum_{r,s\geq 1/2} e^{ir\sigma} e^{is\sigma'} K^{IJ}_{rs} + \delta_{IJ} \sum_{r\geq 1/2} e^{-ir(\sigma-\sigma')}. \tag{3.19}$$

Note that there are two contributions to K^{IJ}: the regular piece that contains K^{IJ}_{rs} and the singular piece $\delta_{IJ}\sum_{r\geq 1/2} e^{-ir(\sigma-\sigma')}$. The presence of the singular piece is non-trivial, and needs to be verified case by case.

We now show the ansatz solution indeed satisfies the boundary condition (3.11). We first note that, with a proper choice of a branch in the conformal factor $(d\omega_I/id\sigma)^{1/2}$, the

Neumann function satisfies

$$iK^{IJ}(2\pi-\sigma,\sigma') = K^{I+1,J}(\sigma,\sigma'), \quad 0\le\sigma\le\pi, \tag{3.20}$$

which reflects the cyclic constraint of Eq. (3.13). Using the mode expansion $\psi^I(\sigma) = \sum_r \psi^I_r e^{ir\sigma}$, $\psi^I(\sigma)|V\rangle$ can be expressed as

$$\begin{aligned}
&\psi^I(\sigma)|V\rangle \qquad (3.21)\\
&= \sum_{r\ge 1/2} \psi^I_{-r} e^{-ir\sigma}|V\rangle + \sum_{r,s\ge 1/2} e^{ir\sigma} K^{IJ}_{rs}\psi^J_{-s}|V\rangle \\
&= \int \frac{d\sigma'}{2\pi} K^{IJ}(\sigma,\sigma')\psi^J_{\rm cr.}(\sigma')|V\rangle, \qquad (3.22)
\end{aligned}$$

where $\psi^I_{\rm cr.}(\sigma) = \sum_{r\ge 1/2}\psi^I_{-r}e^{-ir\sigma}$. Using the cyclic property of the Neumann function given in Eq. (3.20), we find,

$$\begin{aligned}
\psi^I(2\pi-\sigma)|V\rangle &= \int \frac{d\sigma'}{2\pi} K^{IJ}(2\pi-\sigma,\sigma')\psi^J_{\rm cr.}(\sigma')|V\rangle \\
&= (-i)\int \frac{d\sigma'}{2\pi} K^{I+1,J}(\sigma,\sigma')\psi^J_{\rm cr.}(\sigma')|V\rangle \\
&= -i\psi^{I+1}(\sigma)|V\rangle. \qquad (3.23)
\end{aligned}$$

This completes the proof. Note that it was crucial to carefully take into account the singular part of the Neumann function. The proof presented here applies for the NS sector, and we leave the more complicated case of the R sector (Sec. 3.2.4) to Appendix A.1.1, A.1.2.

The direct and Neumann coefficient methods complement one other. When both methods can be applied, they give rise to the same (consistent) vertex states. In other sectors, because of the presence of zero modes, and because of the branch cuts, sometimes one method has an advantage over the other method. In general, vertex states obtained from these two methods are consistent, but may differ by an extra operator insertion at the junction [70, 71].

Complex fermion

We close this subsection by commenting on the case of complex fermions, which parallels the treatment for real fermions. Indeed, the desired vertex state is obtained by combining two copies of real fermions. We consider complex fermion fields $f^I(\sigma), f^{I,\dagger}(\sigma)$. In the NS sector, they can be expanded as

$$\begin{aligned} f(\sigma) = \sum_{s\in\mathbb{Z}+1/2} e^{-i\sigma s} f_s, \quad f^\dagger(\sigma) = \sum_{s\in\mathbb{Z}+1/2} e^{i\sigma s} f_s^\dagger, \\ \text{with} \quad \{f_s, f_{s'}^\dagger\} = \delta_{s,s'}. \end{aligned} \tag{3.24}$$

We have a similar mode expansion in the R-sector. We consider a vertex state obeying the overlap condition,

$$\begin{aligned} \big[f^{I+1}(\sigma) - i f^I(2\pi-\sigma)\big]|V\rangle = 0, \\ \big[f^{I+1,\dagger}(\sigma) - i f^{I,\dagger}(2\pi-\sigma)\big]|V\rangle = 0. \end{aligned} \tag{3.25}$$

The complex fermion field $f, f^\dagger$ can be decomposed into two real fermion fields, ψ and φ as $f = (\psi - i\varphi)/\sqrt{2}$, $f^\dagger = (\psi + i\varphi)/\sqrt{2}$. Correspondingly, the Fourier modes of $f^\dagger$ and f, $f(\sigma) = \sum_r e^{ir\sigma} f_r$ ($\{f_r^\dagger, f_s\} = \delta_{r,s}$), are related to the Fourier modes of ψ and φ as $f_r = (\psi_r - i\varphi_r)/\sqrt{2},$, $f_r^\dagger = (\psi_{-r} + i\varphi_{-r})/\sqrt{2}$. The ansatz solution is then

$$\begin{aligned} |V\rangle &= \exp\Big(\frac{1}{2}\sum_{r,s\geq 1/2} \psi^I_{-r} K^{IJ}_{rs} \psi^J_{-s} + \varphi^I_{-r} K^{IJ}_{rs} \varphi^J_{-s}\Big)|0\rangle \\ &= \exp\Big(\sum_{r,s\geq 1/2} f_r^{I\dagger} K^{IJ}_{rs} f^J_{-s}\Big)|0\rangle. \end{aligned} \tag{3.26}$$

The treatment of the R sector follows similarly, although we need to take into account the presence of zero modes properly, as we shall see in the following subsections.

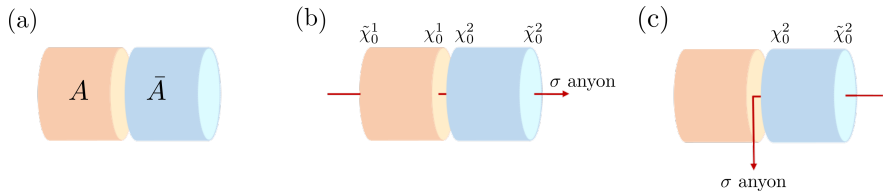

Figure 3.3: Flux insertion configurations considered in computation of the bipartite entanglement on the cylinder geometry. (a) No fluxes are inserted. All edge fermions obey NS boundary conditions. (b) A single π-flux, corresponding to the insertion of a σ anyon flux, through the cylinder. All edge fermions obey R boundary conditions. (c) A single π-flux is inserted through the right half of the cylinder, but exits through the entanglement cut. The edge fermions on the left (right) cylinder obey NS (R) boundary conditions. In (b) and (c), the zero modes on the inner (outer) edge are χ_0^1, χ_0^2 ($\bar{\chi}_0^1, \bar{\chi}_0^2$).

3.2.3 Bipartite boundary states and entanglement

As a warm-up, in this subsection we consider the bipartitions of a chiral p-wave superconductor and a Chern insulator, using the Neumann coefficient method described above. We investigate the effect of inserting non-trivial π-fluxes through the cylinder on the entanglement. As shown in Fig. 3.3, we consider the insertion of (a) no flux (b) π-flux through the cylinder, and (c) a π-flux through one end of the cylinder, which exits through the entanglement cut. For the chiral superconductor, a π-flux is an extrinsic defect which traps a Majorana zero-mode, forming an Ising anyon. Thus, (b) can be viewed as creating a pair of Ising anyons in the bulk and dragging them to opposite ends of the cylinder, while (c) results from dragging only one Ising anyon to an edge and leaving the other in the bulk. In the bulk language, the creation and manipulation of the Ising anyons leaves behind a Wilson line on the cylinder or, equivalently, an anyon flux through the cylinder. At the level of the edge theories, the braiding of the Majorana fermions around the Ising anyon flux results in a phase of -1. Hence, the three configurations in Fig. 3.3 are described by the boundary condition sectors of the edge theories: (a) NS-NS, in which all fermions obey anti-periodic boundary conditions (b) R-R, in which all fermions obey periodic boundary conditions, and (c) NS-R, in which the fermions on the left (right) cylinder obey anti-periodic (periodic) boundary conditions. We compute the entanglement in each sector in turn. As is well-established,

we obtain an area law for case (a) and an area law term plus a subleading $\ln\sqrt{2}$ correction from the Ising anyons for case (b), which requires a careful treatment of the zero modes [72, 43, 44]. The case (c) has not been considered before and we find a novel subleading correction to the entanglement.

The NS-NS sector

The setup of the calculation for the NS-NS sector is already outlined above; all that remains is to explicitly evaluate the Neumann functions. Noting $\frac{d\omega_I}{id\sigma} = \frac{2z\omega_{I,0}}{(1-z)^2}$ and choosing the branch cuts carefully ($\sqrt{\omega_{1,0}} = \sqrt{i}$, $\sqrt{\omega_{2,0}} = i\sqrt{i}$, which leads to $\sqrt{\omega_{1,0}\omega_{2,0}} = -1$), we obtain:

$$\begin{aligned} K^{11} = K^{22} &= \frac{\sqrt{zz'}}{z-z'} = \sum_{r\geq 1/2} e^{-ir(\sigma-\sigma')}, \\ K^{12} = -K^{21} &= \frac{i\sqrt{zz'}}{1-zz'} = i\sum_{r\geq 1/2} e^{ir(\sigma+\sigma')}. \end{aligned} \tag{3.27}$$

Note that $K^{11} = K^{22}$ yields the expected singularity. We also note that under $\sigma \to 2\pi - \sigma$ ($z \to 1/z$, $\sqrt{z} \to -1/\sqrt{z}$), the Neumann function satisfies $K^{1J}(2\pi-\sigma,\sigma') + iK^{2J}(\sigma,\sigma') = 0$ and $K^{2J}(2\pi-\sigma,\sigma') - iK^{1J}(\sigma,\sigma') = 0$ for $0 \leq \sigma \leq 2\pi$. From the expansion of K^{12}, we conclude $K^{12}_{rs} = -K^{21}_{rs} = \delta_{rs}$. Plugging this into Eq. (3.17), we obtain the Ishibashi state (2.79) as expected.

The R-R sector

Let us now consider the vertex state in the R-R sector. We denote the fermion fields with the R boundary condition as $\chi^I(\sigma)$. As before, the vertex state satisfies

$$\begin{aligned} &[\chi^1(\sigma) + i\chi^2(2\pi-\sigma)]|V\rangle \\ &= [\chi^2(\sigma) - i\chi^1(2\pi-\sigma)]|V\rangle = 0 \end{aligned} \tag{3.28}$$

for $0 \leq \sigma \leq 2\pi$. In the bulk, this situation corresponds to a flux or, Ising anyon Wilson line, threading the hole of the cylinder [Fig. 3.3 (b)]. From the edge theory point of view, we need to include suitable twist operators to introduce branch cuts, which enforce periodic boundary conditions for the fermions. This will modify the Neumann function, which we now denote as R^{IJ}. It is related to the Neumann function in the NS sector via:

$$R^{IJ}(\sigma, \sigma') = K^{IJ}(\sigma, \sigma') g^{IJ}(\sigma, \sigma'), \tag{3.29}$$

where g^{IJ} is the new factor arising from the branch cuts. (Here, the summation convention does not apply in the right hand side.) We work with the following choice of the branch cuts,

$$g^{IJ} = \frac{1}{2}\left[\sqrt{\frac{(\omega_I - \omega_{1,0})(\omega'_J - \omega_{2,0})}{(\omega'_J - \omega_{1,0})(\omega_I - \omega_{2,0})}} + (\omega_I \leftrightarrow \omega'_J)\right], \tag{3.30}$$

where we recall $\omega_{1,0} = i, \omega_{2,0} = -i$. Other choices are also possible and give an identical vertex state, as we demonstrate in Appendix A.1.1. Using the conformal map in Eq. (3.15), the explicit form of g^{IJ} is

$$\begin{aligned} g^{11} = g^{22} &= \frac{1}{2}\left(\sqrt{\frac{z}{z'}} + \sqrt{\frac{z'}{z}}\right), \\ g^{12} = g^{21} &= \frac{1}{2}\left(\sqrt{zz'} + \frac{1}{\sqrt{zz'}}\right). \end{aligned} \tag{3.31}$$

These functions satisfy $g^{1J}(\sigma, \sigma') = -g^{2J}(2\pi - \sigma, \sigma')$ (using $z \to 1/z, \sqrt{z} \to -1/\sqrt{z}$). The Neumann function is:

$$\begin{aligned} R^{11} = R^{22} &= \frac{1}{2}\frac{z + z'}{z - z'} = \frac{1}{2} + \sum_{n \geq 1} e^{-in(\sigma - \sigma')}, \\ R^{12} = -R^{21} &= \frac{i}{2}\frac{1 + zz'}{1 - zz'} = \frac{i}{2} + i\sum_{n \geq 1} e^{in(\sigma + \sigma')}. \end{aligned} \tag{3.32}$$

They satisfy $R^{1J}(2\pi-\sigma,\sigma')-iR^{2J}(\sigma,\sigma')=R^{2J}(2\pi-\sigma,\sigma')+iR^{1J}(\sigma,\sigma')=0$. Again, the correct singular terms show up in R^{11} and R^{22}. The solution for $|V\rangle$ for real fermions in the R-R sector is then

$$|V\rangle=\exp\Big(-i\sum_{n\geq 1}\chi^1_{-n}\chi^2_{-n}\Big)|\Omega\rangle, \tag{3.33}$$

with an additional requirement $[\chi^1_0+i\chi^2_0]|\Omega\rangle=0$. One can verify that they satisfy the boundary condition (3.28). The requirement that $|V\rangle$ has definite parity for the zero mode can also be understood from the $i/2$ term in R^{12}.

The zero modes χ^1_0,χ^2_0 of the real fermion need to be handled with extra care. χ^1_0,χ^2_0 live on the inner edges of the cylinders. To have a well-defined Hilbert space, we also need to include the zero modes on the outer edges of the cylinders, which we denote as $\bar{\chi}^1_0,\bar{\chi}^2_0$, as shown in Fig. 3.3(b). Indeed, we recall that before making a physical cut along the entanglement cut, the cylinder with an Ising anyon flux passing through it is topologically equivalent to a sphere with a pair of Ising anyon defects. The anyons yield a double degeneracy, as each has quantum dimension $\sqrt{2}$. This corresponds to choosing whether the complex fermion formed from the corresponding zero modes, $\bar{\chi}^1_0+i\bar{\chi}^2_0$, is occupied or unoccupied. We must make a choice of which state in this degenerate subspace we wish to compute the entanglement for. For concreteness, we choose the state in which this fermion is unoccupied, which amounts to imposing the boundary condition $[\bar{\chi}^1_0+i\bar{\chi}^2_0]|\Omega\rangle=0$ for the outer edge zero modes. If we define the complex fermion

$$g_i=\frac{1}{\sqrt{2}}(\chi^1_0+i\chi^2_0),\quad g_o=\frac{1}{\sqrt{2}}(\bar{\chi}^1_0+i\bar{\chi}^2_0), \tag{3.34}$$

the zero-mode vacuum state is $|\Omega\rangle=|0_i,0_o\rangle$. This completes the construction of the boundary state.

Note that g_i and g_o mix the Hilbert spaces of the left and right cylinders. When we

compute the entanglement we must trace out one of these cylinders, and so it is necessary to perform a change of basis to complex fermion modes localized on either the left or right cylinder: $g_A = (\chi_0^1 + i\bar{\chi}_0^1)/\sqrt{2},\ g_B = (\chi_0^2 + i\bar{\chi}_0^2)/\sqrt{2}$. In this basis, the vacuum is a maximally entangled state:

$$|\Omega\rangle = |0_i, 0_o\rangle = (|0_A 0_B\rangle - i|1_A 1_B\rangle)/\sqrt{2}. \tag{3.35}$$

Below, we will see this gives a contribution of $\ln 2$ to the entanglement entropy.

The NS-R sector

Finally, we consider the NS-R sector which, as described above, describes a novel configuration in which we insert an anyon flux through one end of the cylinder which then exits through the entanglement cut. From Fig. 3.3(c), we see that the fermions on the right cylinder braid around the anyon flux and so obey R boundary conditions, whereas the fermions on the left cylinder do not and hence are in the NS sector. In order to describe the gapped edge state at the entanglement cut, we must impose a modified boundary condition:

$$[\psi(\sigma) + i\mathrm{sgn}(\pi - \sigma)\chi(2\pi - \sigma)]\,|V\rangle = 0, \tag{3.36}$$

for $0 \leq \sigma < 2\pi$. Here, ψ (χ) obeys NS (R) boundary conditions. Formally, the sign function is needed to ensure the above expression is well-defined under shifts of $\sigma \to \sigma + 2\pi$. Physically, it represents the fact that an anyon flux is piercing the entanglement cut. Indeed, the Ising twist field is precisely the operator at the level of the edge CFT which introduces such a "kink" for the Majorana fields.

To the best of our knowledge, the vertex state in this case was first constructed in [68]. In the NS-R sector, we only need to introduce the branch cut for the second string. The

branch cut factor g^{IJ} is chosen as [68]:

$$g^{IJ}(\sigma,\sigma') = \frac{1}{2}\left[\sqrt{\frac{\omega_I - \omega_{2,0}}{\omega'_J - \omega_{2,0}}} + \sqrt{\frac{\omega'_J - \omega_{2,0}}{\omega_I - \omega_{2,0}}}\right]. \tag{3.37}$$

Explicitly,

$$\begin{aligned}
g^{11} &= \frac{1}{2}\left(\sqrt{\frac{1-z'}{1-z}} + \sqrt{\frac{1-z}{1-z'}}\right), \\
g^{12} &= \frac{i}{2}\left(\sqrt{\frac{1-z'}{1-z}}\frac{1}{\sqrt{z'}} - \sqrt{z'}\sqrt{\frac{1-z}{1-z'}}\right), \\
g^{22} &= \frac{1}{2}\left(\sqrt{\frac{1-z'}{1-z}}\sqrt{\frac{z}{z'}} + \sqrt{\frac{1-z}{1-z'}}\sqrt{\frac{z'}{z}}\right).
\end{aligned} \tag{3.38}$$

R^{IJ} satisfies $R^{IJ}(\sigma,\sigma') = -iR^{I+1,J}(2\pi-\sigma,\sigma')$ for $0 \le \sigma \le \pi$. The mode expansion of R^{IJ} needed to extract the R^{IJ}_{rs} in the definition of the vertex state, takes a more complicated form than that of the preceding two cases:

$$\begin{aligned}
R^{11}_{rs} &= \frac{r-s}{2(r+s)}u_{2r-1}u_{2s-1}, \\
R^{12}_{rn} &= -R^{21}_{nr} = \frac{n+r}{2(n-r)}u_{2r-1}u_{2n}, \\
R^{22}_{nm} &= \frac{n-m}{2(n+m)}u_{2n}u_{2m},
\end{aligned} \tag{3.39}$$

where u_n is the expansion coefficients of $u(x)$:

$$u(x) = \sqrt{\frac{1+x}{1-x}} = \sum_{n=0}^{\infty} u_n x^n. \tag{3.40}$$

Making use of this mode expansion and separating the oscillator and zero-mode contributions, we can write out the vertex state of Eq. (3.17) as

$$|V\rangle = \exp\Big(\sum_{r,s\geq 1/2} \frac{1}{2}\psi_{-r} R^{11}_{rs} \psi_{-s} + \sum_{m,n\geq 1} \frac{1}{2}\chi_{-n} R^{22}_{nm} \chi_{-m} + \sum_{r\geq 1/2, n\geq 1} \psi_{-r} R^{12}_{rn} \chi_{-n} + \sum_{r\geq 1/2} 2\psi_{-r} R^{12}_{r0} \chi_0 + \sum_{n\geq 1} 2\chi_{-n} R^{22}_{n0} \chi_0 \Big) |\Omega\rangle. \tag{3.41}$$

Now, as in the R-R sector, to fix the form of the vacuum $|\Omega\rangle$, we must treat the zero-mode sector carefully. Indeed, due to the π flux through one half of the cylinder, we have another zero mode, $\bar{\chi}_0$, on the outer edge of the left cylinder [Fig. 3.3(c)]. We can combine them to define the complex fermion operator g_0:

$$g_0 = \frac{1}{\sqrt{2}}(\chi_0 - i\bar{\chi}_0), \quad g_0^\dagger = \frac{1}{\sqrt{2}}(\chi_0 + i\bar{\chi}_0). \tag{3.42}$$

Now, prior to making the entanglement cut, this flux configuration is again topologically equivalent to a sphere supporting a pair of Ising anyons, corresponding to the χ_0 and $\bar{\chi}_0$ zero modes, yielding a double degeneracy associated with the occupation of g_0. (Note that, in contrast to the R-R case, cutting the system along the entanglement cut does not introduce additional zero modes). We must again make a choice of which state in which to compute the entanglement. We can fix the state by choosing a value for the occupation number of g_0 of the reference state $|\Omega\rangle$; for simplicity, we take g_0 to be unoccupied, so that $|\Omega\rangle = |0\rangle$. Finally, to simplify the expression for the vertex state, we observe that $X \equiv \sqrt{2}(\sum_{r\geq 1/2} \psi_{-r} R^{12}_{r0} + \sum_{n\geq 1} \chi_{-n} R^{22}_{n0}) g_0^\dagger$ and $Y \equiv \sqrt{2}(\sum_{r\geq 1/2} \psi_{-r} R^{12}_{r0} + \sum_{n\geq 1} \chi_{-n} R^{22}_{n0}) g_0$, commute, $[X, Y] = 0$, and hence $e^{X+Y} = e^X e^Y$. The vertex state thus takes the form

$$|V\rangle = \exp\Big(\sum_{r,s\geq 1/2} \frac{1}{2}\psi_{-r} R^{11}_{rs} \psi_{-s} + \sum_{m,n\geq 1} \frac{1}{2}\chi_{-n} R^{22}_{nm} \chi_{-m} + \sum_{r\geq 1/2, n\geq 1} \psi_{-r} R^{12}_{rn} \chi_{-n} + \sqrt{2}\Big(\sum_{r\geq 1/2} \psi_{-r} R^{12}_{r0} + \sum_{n\geq 1} \chi_{-n} R^{22}_{n0} \Big) g_0^\dagger \Big) |0\rangle. \tag{3.43}$$

Entanglement entropy

Having constructed the relevant boundary states for the NS-NS, R-R, NS-R sectors, we now proceed to compute the entanglement entropy S_A after tracing out one half of the cylinder. Let us start with the NS-NS sector. We recall that the ground state of the entanglement interface is given by a regularized version of the boundary state, as stated in Eq. (2.80); this amounts to replacing $\psi^I_{-r} \to \psi^I_{-r} e^{-\epsilon r}$ in Eq. (2.79). The entanglement entropy can directly be evaluated as

$$S = \left(1 - \epsilon \frac{d}{d\epsilon}\right) \ln \left[\prod_{r \geq 1/2} (1 + q^r) \right] \tag{3.44}$$

where $q = e^{2\pi i \tau} = e^{-4\epsilon}$ and $\tau = \frac{2i\epsilon}{\pi}$. We can write the argument of the logarithm in terms of the Dedekind η function and a Jacobi θ function:

$$\prod_{r \geq 1/2} (1 + q^r) = q^{1/48} \sqrt{\frac{\theta_3(\tau)}{\eta(\tau)}}. \tag{3.45}$$

Under the modular $\mathcal{S}$ transformation and taking the limit $\epsilon \to 0$ limit (which corresponds to taking the bulk gap to be very large), we have:

$$\frac{\theta_3(\tau)}{\eta(\tau)} = \frac{\theta_3(-\frac{1}{\tau})}{\eta(-\frac{1}{\tau})} \to \frac{1}{(e^{-\frac{2\pi i}{\tau}})^{1/24}} = e^{\frac{\pi^2}{24\epsilon}}. \tag{3.46}$$

We thus find,

$$S^{\text{Real.}}_{NS-NS} \to \frac{\pi(1/2)}{24} \frac{L}{\epsilon} \quad \text{as} \quad \frac{L}{\epsilon} \to \infty, \tag{3.47}$$

as expected. Here, we reinstated the IR length scale L (which has been set to 2π for simplicity) to make the area law form of the entropy more explicit and so that the dimensions are correct. We also make the chiral central charge $c = 1/2$ dependence explicit.

The entanglement entropy in the R-R sector can be computed similarly. However, the presence of the zero modes make the calculations slightly more subtle. Let us first compute

the contribution from the oscillator modes $n \geq 1$. With the regulator ϵ, it can be computed as

$$S_{\text{oscil.}} = \left(1 - \epsilon \frac{d}{d\epsilon}\right) \ln [\prod_{n\geq 1} (1 + q^n)]. \tag{3.48}$$

The product can be identified with θ_2 function:

$$\prod_{n\geq 1} (1 + q^n) = \frac{1}{\sqrt{2}} \sqrt{\frac{\theta_2(\tau)}{\eta(\tau)}} q^{-1/24}. \tag{3.49}$$

Under the modular $\mathcal{S}$ transformation and again taking the limit $\epsilon \to 0$, we have:

$$\frac{\theta_2(\tau)}{\eta(\tau)} = \frac{\theta_4(-\frac{1}{\tau})}{\eta(-\frac{1}{\tau})} \to \frac{1}{(e^{-\frac{2\pi i}{\tau}})^{1/24}} = e^{\frac{\pi^2}{24\epsilon}}. \tag{3.50}$$

This gives

$$S_{\text{oscil.}} = \frac{\pi(1/2)}{24} \frac{L}{\epsilon} - \frac{1}{2} \ln 2. \tag{3.51}$$

For the zero mode part, after the basis transformation, the vacuum takes the form of a maximally entangled state, $|\Omega\rangle = |0_i, 0_o\rangle = (|0_A 0_B\rangle - i|1_A 1_B\rangle)/\sqrt{2}$, which gives a contribution of $\ln 2$. Summing up these two terms, the total entanglement entropy is:

$$S_{R-R}^{\text{Real.}} = \frac{\pi(1/2)}{24} \frac{L}{\epsilon} + \ln \sqrt{2}. \tag{3.52}$$

Compared with $S_{NS-NS}^{\text{Real.}}$, the extra contribution $\ln \sqrt{2}$ is exactly the topological entanglement entropy from the σ anyon, as expected [72].

We now proceed to the NS-R case. Since the entanglement entropy in this case is not amenable to analytical calculations, we will perform a numerical computation using the correlation matrix method introduced in Sec. 2.1.4 with a cutoff of mode N_c. For a given value of ϵ, we take N_c to be sufficiently large such that S_A does not appreciably change with further increases in N_c. We collect the results in Table 3.1. We observe that the area law

ϵ	0.005	0.008	0.01	0.02
$S^{\text{Real.}}_{R-R}$	82.5933	51.7508	41.4699	20.9082
$S^{\text{Real.}}_{R-NS}$	82.3433	51.5008	41.2199	20.6582
ΔS	0.2500	0.2500	0.2500	0.2500

Table 3.1: $S^{\text{Real.}}_{R-R}$ and $S^{\text{Real.}}_{R-NS}$ for various choices of ϵ. For each fixed ϵ, we increase cutoff N until S saturates. We observe that the difference $\Delta S = S^{\text{Real.}}_{R-R} - S^{\text{Real.}}_{R-NS}$ is a constant.

contributions ($O(L/\epsilon)$) to $S^{\text{Real.}}_{R-R}$ and $S^{\text{Real.}}_{NS-R}$ cancel out exactly, and the difference

$$\Delta S = S^{\text{Real.}}_{R-R} - S^{\text{Real.}}_{R-NS} = 0.2500 \tag{3.53}$$

appears to be remarkably well quantized. Now, we recall that, in the R-R sector, the presence of the anyon flux passing through the cylinder (i.e. the presence of Ising anyons on the ends of the cylinder) led to a contribution of $\Delta S_0 = S^{\text{Real.}}_{R-R} - S^{\text{Real.}}_{NS-NS} = \ln\sqrt{2} = 0.3466$ to the entanglement entropy over the NS-NS case, in which there was no flux. We see that $0 < \Delta S < \Delta S_0$. This seems reasonable, as one expects the two halves of the cylinder in the present NS-R case where one Ising anyon straddles entanglement cut to somehow be less entangled than the R-R case, where the Ising anyons are located deep in the bulks of the two subregions. Evidently, $\Delta S_0 - \Delta S = 0.0966$ corresponds to a contribution to the entanglement from the anyon flux which pierces the entanglement cut. We should, however, perhaps be careful in identifying this as a universal contribution, as this cut-and-glue approach likely corresponds to a particular choice of regularization of how the anyon flux pierces the cut. The value of this new topological contribution may depend on this regularization. Additionally, we note that the examination of the entanglement spectrum in the NS-R sector shows that levels are all equally spaced with no degeneracy. The equal spacing structure encodes the CFT signature.

Finally, we consider the entanglement entropy for the case of complex fermion, i.e., the edge theory of a Chern insulator with unit Hall conductivity, and make a comparison with

the above results. In the NS-NS sector, the entanglement entropy for the complex fermion is simply twice as large as the real fermion case,

$$S_{NS-NS}^{\text{Cplx.}} = 2S_{NS-NS}^{\text{Real.}} = \frac{\pi}{24} \cdot \frac{L}{\epsilon}. \tag{3.54}$$

In the R-R sector, we need to include the effect of the fermion zero modes properly, while the treatment for the oscillator part is essentially the same. For the zero mode part, since χ_0 is already a well-defined degree of freedom, paired with $\chi_0^\dagger$, we can only consider the inner edges. The vacuum $|\Omega\rangle$ needs to satisfy $(\chi_0^1 - i\chi_0^2)|\Omega\rangle = 0, (\chi_0^{1,\dagger} - i\chi_0^{2,\dagger})|\Omega\rangle = 0$, which can be chosen as $|\Omega\rangle = (\chi_0^{2,\dagger} + i\chi_0^{1,\dagger})|0\rangle$. This is a maximally-entangled pair state and gives $S_0 = \ln 2$ contribution to S. To sum up,

$$S_{R-R}^{\text{Cplx.}} = 2S_{\text{oscil.}} + S_0 = \frac{\pi}{24} \cdot \frac{L}{\epsilon}. \tag{3.55}$$

There is no topological contribution for the complex fermion. Furthermore, the numerical calculation of the NS-R case shows $S_{NS-NS}^{\text{Cplx.}} = S_{NS-R}^{\text{Cplx.}} = S_{R-R}^{\text{Cplx.}}$. This is desired since we expect $S_{NS-R}^{\text{Cplx.}}$ to lie between $S_{NS-NS}^{\text{Cplx.}}$ and $S_{R-R}^{\text{Cplx.}}$. Once again, the NS-R entanglement spectrum shows equal spacing behavior with no degeneracy.

3.2.4 Tripartite vertex states and entanglement

Having illustrated how the Neumann coefficient method reproduces the expected boundary states and entanglement entropy for a bipartition on the cylinder with and without flux threading it, as well as having derived a new result for the entanglement in the case where a flux pierces the cut, we turn to the main focus of this work, namely the entanglement for a tripartition [Fig. 3.1(b)]. We will again focus primarily on the case of a chiral p-wave superconductor and consider the effect of inserting π-fluxes through the cylinders. In particular, we investigate the entanglement when no fluxes are inserted and when two fluxes

are inserted through two cylinders such that one flux exits through the remaining cylinder and the other flux through the entanglement cut [Fig. 3.4(a)]. At the level of the edge theories, these correspond to the NS-NS-NS and R-R-R sectors, respectively. We construct the vertex states for each case next before discussing the tripartite entanglement measures introduced in Sec. 3.1.

As a complement to the Neumann coefficient approach, we also introduced a direct calculation method for computing the vertex state in Ref. [45]. We showed these two methods give identical results for the vertex state solution numerically.

The NS-NS-NS sector

We first consider the simplest case in which no fluxes are inserted through the cylinders. The required vertex state $|V\rangle$ is given by the Gaussian ansatz of Eq. (3.17), the construction of which is outlined in Sec. 3.2.2. All that remains is to determine the explicit form of the Neumann coefficients from the correlation function, Eq. (3.18). The conformal factor in Eq. (3.18) is given explicitly as $(\frac{d\omega_I}{id\sigma})^{1/2} = \frac{1}{\omega_I^{1/4}}(\frac{(\omega_I^3+1)}{3})^{1/2}$. We choose the branch such that $\omega_I^{1/4}(2\pi-\sigma) = i\omega_{I+1}^{1/4}(\sigma)$. This can be achieved by the following choice:

$$\omega_I^{1/4}(\sigma) = \tilde{\omega}_I \left(\frac{1+e^{i\sigma}}{1-e^{i\sigma}}\right)^{1/6}$$
$$\text{with} \quad \tilde{\omega}_1 = e^{i\pi/12}, \quad \tilde{\omega}_2 = e^{-i7\pi/12}, \quad \tilde{\omega}_3 = e^{i3\pi/4}. \tag{3.56}$$

The explicit form of the Neumann coefficients K_{rs}^{IJ} is technically involved and not particularly physically illuminating, and so we relegate it to Appendix A.1.3.

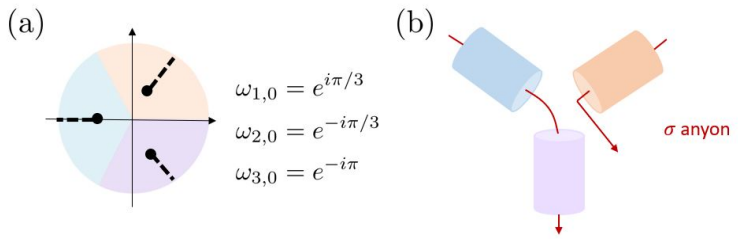

Figure 3.4: (a) The σ anyon flux insertion in the R-R-R sector. One σ-anyon is forced to be exited at the junction. (b) The choice of the branch cuts for the R-R-R sector tripartition vertex state. The branch cuts connect $\omega_{I,0}$ to ∞.

The R-R-R sector

Next we consider the case in which all fermions are in the R sector. Similar to the NS-R sector discussed for the case of a bipartition, in the R-R-R sector, the conservation of topological charge enforces the presence of an Ising anyon at the junction where all three entanglement boundaries meet. From the edge theory point of view, we must again compute the Neumann functions for periodic fermions, which takes the form in Eq. (3.29) with the factor g^{IJ} accounting for the branch cuts. We choose to work with the branch cut configuration in Fig. 3.4(b).

To determine the branch cut factor $g^{IJ}(\sigma, \sigma')$, the following general properties should be satisfied [29]: (i) ω and ω' are symmetric in g^{IJ} (thus anti-symmetric in R^{IJ}); (ii) The branch points include $\omega_{1,0}$, $\omega_{2,0}$, and $\omega_{3,0}$; (iii) g reduces to 1 when $\omega' \to \omega$, so R^{IJ} reduces to K^{IJ} in this limit. Furthermore, for our specific problem, R^{IJ} should also satisfy: (iv) The singular term in R^{IJ} must be $\delta^{IJ} \sum_{n\geq 1} e^{-in(\sigma-\sigma')}$ to ensure the boundary condition is properly satisfied, as we show in Appendix A.1.2. This extra requirement is non-trivial, and may rule out some of the candidates that satisfy (i-iii).

We propose to use the following branch cut factor:

$$g^{IJ}(\sigma,\sigma') = \frac{1}{2}\left[\left(\frac{(\omega_I-\omega_{1,0})(\omega_I-\omega_{2,0})(\omega_I-\omega_{3,0})}{(\omega'_J-\omega_{1,0})(\omega'_J-\omega_{2,0})(\omega'_J-\omega_{3,0})}\right)^{1/2} + \left(\frac{(\omega'_J-\omega_{1,0})(\omega'_J-\omega_{2,0})(\omega'_J-\omega_{3,0})}{(\omega_I-\omega_{1,0})(\omega_I-\omega_{2,0})(\omega_I-\omega_{3,0})}\right)^{1/2}\right], \tag{3.57}$$

where $\omega_{1,0} = e^{i\pi/3}, \omega_{2,0} = e^{-i\pi/3}, \omega_{3,0} = e^{-i\pi}$, and $\omega_I(\sigma), \omega'_J(\sigma')$ are defined in Eq. (3.16). It is easy to check that this candidate fulfills the requirements (i-iii). The branch points also include ∞. The branch cuts can be chosen from $\omega_{1,0}$ to ∞, $\omega_{2,0}$ to ∞, and $\omega_{3,0}$ to ∞, as shown in Fig. 3.4(b). We will compute the singular terms explicitly later, which verifies requirement (iv).

It turns out that g^{IJ} is the same for any I, J, and the mode expansion of g^{IJ} in powers of $z = e^{i\sigma}$ is given by

$$\begin{aligned} g^{IJ} &= \frac{1}{2}\left[\left(\frac{1}{\sqrt{z'}} - \sqrt{z'}\right)\sum_{r\geq 1/2} z^r + \left(\frac{1}{\sqrt{z}} - \sqrt{z}\right)\sum_{r\geq 1/2} z'^r\right] \\ &= \frac{1}{2}\sum_{m=0}^{\infty}\left[e^{i\sigma(\frac{1}{2}+m)-i\frac{\sigma'}{2}} - e^{i\sigma(\frac{1}{2}+m)+i\frac{\sigma'}{2}} + e^{i\sigma'(\frac{1}{2}+m)-i\frac{\sigma}{2}} - e^{i\sigma'(\frac{1}{2}+m)+i\frac{\sigma}{2}}\right]. \end{aligned} \tag{3.58}$$

It is worth noting that this expression is valid for the vertex state of an N-junction with arbitrary N and the insertion of N twist operators. As an example, we give the construction of the vertex state for $N = 2$ using this branch cut factor in Appendix A.1.1, which reproduces the result for the R-R sector bipartition calculation of the preceding section.

We are now ready to examine requirement (iv). Combining the singular term of the Neumann coefficient in the NS-NS-NS sector $K^{IJ}_{\text{sing.}} = \delta^{IJ}\sum_{r\geq 1/2} e^{-ir(\sigma-\sigma')}$ with the branch

cut factor g^{IJ}, we obtain:

$$K^{IJ}_{\text{sing.}} g^{IJ} = \delta^{IJ} \sum_{r\geq 1/2}^{\infty} e^{-i(r+1/2)(\sigma-\sigma')} + \frac{\delta^{IJ}}{2}\Big[\sum_{m=0}^{\infty} e^{im\sigma} - \sum_{m\geq 1} e^{im\sigma'}\Big]. \tag{3.59}$$

The first term gives the correct singular term in the R-R-R sector,

$$R^{IJ}_{\text{sing.}} = \delta^{IJ} \sum_{m\geq 1}^{\infty} e^{-im(\sigma-\sigma')},$$

and the second term contributes to the zero mode parts $R_{0,m}, R_{m,0}, R_{0,0}$. This shows that our choice of g^{IJ} is indeed a valid one. We thus verified the Neumann function has the following expansion:

$$R^{IJ}(\sigma,\sigma') = \sum_{m\geq 0, n\geq 0} e^{im\sigma} R^{IJ}_{mn} e^{in\sigma'} + \delta^{IJ} \sum_{n\geq 1} e^{-in\sigma} e^{in\sigma'}. \tag{3.60}$$

The non-singular terms can be worked out easily in a similar way. We summarize the expansion coefficients below:

$$\begin{aligned}
R^{IJ}_{r'+1/2,s'+1/2} &= \frac{1}{2}\Big[\sum_{r=1/2}^{r'} (K^{IJ}_{r,s'+1} - K^{IJ}_{r,s'}) + \sum_{s=1/2}^{s'} (K^{IJ}_{r'+1,s} - K^{IJ}_{r',s})\Big], \\
R^{IJ}_{0,s'+1/2} &= \frac{1}{2}\sum_{s=1/2}^{s'} K^{IJ}_{1/2,s} - \frac{1}{2}\delta^{IJ}, \\
R^{IJ}_{s'+1/2,0} &= \frac{1}{2}\sum_{s=1/2}^{s'} K^{IJ}_{s,1/2} + \frac{1}{2}\delta^{IJ}, \\
R^{IJ}_{00} &= \frac{1}{2}\delta^{IJ}.
\end{aligned} \tag{3.61}$$

Finally, using the Neumann coefficients, the vertex state can be constructed as

$$|V\rangle = \exp\left(\sum_{m,n\geq 1} \frac{1}{2}\chi^I_{-m} R^{IJ}_{mn} \chi^J_{-n} + \sum_{m\geq 1} 2\chi^I_{-m} R^{IJ}_{m0} \chi^J_0\right)|\Omega\rangle. \tag{3.62}$$

We show this state satisfies the boundary condition explicitly in Appendix A.1.2.

As discussed in Sec. 3.2.3, to have a well-defined Hilbert space, we need to combine the χ^I_0 zero modes with $\bar{\chi}^I_0$ at the outer edges. Indeed, physically speaking, prior to physically cutting the system along the entanglement cut, the R-R-R sector configuration is topologically equivalent to a sphere with one Ising anyon placed on the entanglement cut and three Ising anyons in the three regions A, B, and C. These correspond to the three outer edge Majorana fermion zero modes and one of the zero modes that appears at the inner edge when we physically cut along the entanglement cut. This results in a four-fold degeneracy and we must choose one of these states for which to compute the entanglement. To do so, we define the complex fermion as in Eq. (3.42), $\chi^I_0 = (g^I_0 + g^{I,\dagger}_0)/\sqrt{2}$. Denoting $X = \sqrt{2}\sum_{m\geq 1} \chi^I_{-m} R^{IJ}_{m0} g^{\dagger,J}_0, Y = \sqrt{2}\sum_{m\geq 1} \chi^I_{-m} R^{IJ}_{m0} g^J_0$, one can show $[X, Y] = 0$ and hence $e^{X+Y} = e^X e^Y$. In order to fix a state within the four-fold degenerate subspace, we must fix the occupations of the zero modes. For simplicity, we choose the reference state $|\Omega\rangle$ to be one of definite fermion parity take $|\Omega\rangle = |000\rangle$, which is annihilated by all g^I_0. Under this choice, the solution is simplified to:

$$|V\rangle = \exp\left(\sum_{m,n\geq 1} \frac{1}{2}\chi^I_{-m} R^{IJ}_{mn} \chi^J_{-n} + \sum_{m\geq 1} \sqrt{2}\chi_{-m} R^{IJ}_{m0} g^{\dagger,J}_0\right)|0\rangle. \tag{3.63}$$

Finally, by combining two copies of real fermions, we can construct the complex fermion vertex state as

$$|V\rangle = \exp\left(\sum_{m,n\geq 1} g^I_{-m} R^{IJ}_{mn} g^{\dagger,J}_n + \sum_{m\geq 1} 2R^{IJ}_{m0}(g^I_{-m} g^{\dagger,J}_0 + g^{\dagger,I}_m g^J_0)\right)|\Omega\rangle. \tag{3.64}$$

	a_{-1}	a_0	a_1	b_{-1}	b_0	b_1
Majorana (NS-NS-NS)	0.0654	0.0299	-0.0232	0.0491	0.0310	-0.4021
Majorana (R-R-R)	0.0654	0.6227	-5.3746	0.0491	0.3341	-0.2984
Dirac (NS-NS-NS)	0.1309	0.0597	-0.0119	0.0982	0.0600	0.3657
Dirac (R-R-R)	0.1309	-0.1139	22.9493	0.0982	0.0025	15.1538

Table 3.2: The scaling of the entanglement entropy and negativity with respect to L/ϵ from the numerical analysis.

Again, we postpone the verification of boundary condition in Appendix A.1.2. We choose $|\Omega\rangle$ to be the vacuum that is annihilated by g_0^I. Identifying $X = 2\sum_{m\geq 1} R_{m0}^{IJ} g_{-m}^I g_0^{\dagger,J}$, $Y = 2\sum_{m\geq 1} R_{m0}^{IJ} g_m^{\dagger,I} g_0^J$, and $[X,Y] = 4\sum_{m,n\geq 1} R_{m0}^{IJ} R_{n0}^{I'J} g_n^{\dagger,I'} g_{-m}^I$, the solution is simplified to

$$|V\rangle = \exp\left(\sum_{m,n\geq 1} g_{-m}^I \tilde{R}_{mn}^{IJ} g_n^{\dagger,J} + \sum_{m\geq 1} 2 g_{-m}^I R_{m0}^{IJ} g_0^{\dagger,J}\right)|0\rangle, \tag{3.65}$$

with $\tilde{R}_{mn}^{IJ} = R_{mn}^{IJ} - 2R_{m0}^{IK} R_{n0}^{JK}$.

Entanglement entropy, negativity and reflected entropy

With the tripartite vertex states in hand, we now proceed to the calculations of the correlation measures, namely, the entanglement entropy S_A and spectrum when tracing out B and C, and negativity $\mathcal{E}_{A:B}$ and the spectra when tracing out C, and the reflected entropy $R_{A:B}$ when tracing out C. Once again, the regularization $|V\rangle \to |G\rangle = \mathcal{N} e^{-\epsilon H_0}|V\rangle$ amounts to multiplying the Neumann coefficients by an exponential factor, e.g., $R_{mn}^{IJ} \to R_{mn}^{IJ} e^{-\epsilon(m+n)}$. As the resulting state $|G\rangle$ is Gaussian, we can use the correlator method to compute various entanglement measures, as described in Sec. 3.1.1. The technical details are left to Appendix A.3. To evaluate the correlators (covariance matrices) numerically, we need to introduce a cutoff N_c to truncate the Neumann coefficients. The correlation measures (for a given L/ϵ) are then computed for different N_c and the results are extrapolated to $N_c \to \infty$. We typically take $N_c \geq 200 - 800$.

We first present our results for the entanglement entropy and negativity. For both cases, we find that they scale with L/ϵ as

$$\begin{aligned} S_A &= a_{-1}\frac{L}{\epsilon} + a_0 + a_1\frac{\epsilon}{L} + \cdots , \\ \mathcal{E}_{A:B} &= b_{-1}\frac{L}{\epsilon} + b_0 + b_1\frac{\epsilon}{L} + \cdots , \end{aligned} \tag{3.66}$$

for both the NS-NS-NS and R-R-R sectors. The numerically extracted coefficients are summarized in Table 3.2. The coefficients a_{-1} and b_{-1} are the same for the NS-NS-NS and R-R-R sectors. The numerical result for a_{-1} is consistent with $a_{-1} = \pi c/24$ (see Sec. 3.2.3). On the other hand, the numerically computed b_{-1} is consistent with $b_{-1} = 3\pi c/96$. These may be understood as commonly appearing coefficients in the entanglement entropy and negativity in topological liquids. For example, for the mutual information and negativity on the torus, when A, B, C are non-contractible and A and B are adjacent, the area law terms of these quantities are proportional to $(1/n + 1)(\pi c/12)$ $(n \to 1)$, and $(4/n_e - n_e)(c\pi/48)$ $(n_e \to 1)$ [42]. We also note that the area law terms should cancel in $\mathcal{E}_3 = 2\mathcal{E}_{A:B} - \mathcal{E}_{A\cup C:B}$, and we know $\mathcal{E}_{A\cup C:B} = S^{(1/2)}_{A\cup C:B} \sim (3\pi c/48)(L/\epsilon)$. The constant term a_0 in the NS-NS-NS sector is small compared with $\ln 2 \sim 0.693$, and may be consistent with $a_0 = 0$, the result we expect from the calculation for a bipartition. On the other hand, in the R-R-R sector, a_0 is an order of magnitude larger. We may attribute it to the extra σ anyon positioned at the junction. We recall that we obtained a similar result in the NS-R sector for a bipartition.

In Fig. 3.5 we plot the entanglement and negativity spectra. Here, we focus on the NS-NS-NS sector (as the R-R-R sector shows the same features). Both the entanglement and negativity spectra exhibit an equal-spacing structure. For the entanglement spectrum, this is expected as it is given by the spectrum of the CFT realized on a physical edge [8]. Similarly, the equal-spacing structure of the negativity spectrum may suggest that it is described by some CFT. For the Majorana fermions, the entanglement spectrum is non-degenerate while the negativity spectrum is two-fold degenerate. For the complex fermions, the degeneracy of

the entanglement spectrum is two-fold, while that for the negativity spectrum is four-fold. We will see in the next section that the degeneracy matches with the lattice calculation result deep in the topological region.

Plotted in Fig. 3.5(b) is the single-body spectrum $\{\zeta\}$ of $\rho_{A\cup B}^{T_A}$ (the spectrum of the correlation matrix Γ_+). The eigenvalues appear to come in various branches; those that are circularly distributed and those that are clustered near the real axis. The non-trivial distribution of the spectrum over the complex plane can be regarded as a smoking gun of topological non-triviality of the bulk. As a comparison, we note that for a simple product state the spectrum $\{\zeta\}$ consists of just two eigenvalues, $\zeta = 1$ and $\zeta = -1$. We also note that such non-trivial distribution of the eigenvalues $\{\zeta\}$ was found previously in (1+1)d fermionic CFTs [73], and (1+1)d SPT phases (the Kitaev chain) [74]. In these examples, the many-body spectrum of $\rho_{A\cup B}^{T_A}$ has a 8-fold rotation symmetry. On the other hand, we do not find such a symmetric pattern for the case of our (2+1)d topological liquids. In the next section, we will see that a similar distribution of $\{\zeta\}$ is also found in the lattice Chern insulator calculation.

Finally, we turn to the reflected entropy and the conjecture (3.5). We study this difference for the four aforementioned cases and show the results in Fig. 3.6. For the Majorna and Dirac fermion edge theories in the NS-NS-NS sector, and the Majoran fermion edge theory in the R-R-R sector, $h_{A:B}$ does not change with ϵ, with the values being 0.1172, 0.2344, 0.2850 respectively. The results for the NS-NS-NS sector are consistent with the prediction $(c/3)\ln 2 = 0.1155, 0.2310$ for $c = 1/2$ and $c = 1$, respectively. (Alternatively, if we extract the central charge from our numerics, we obtain $c = 0.5073, 1.0145, 1.2335$, respectively.) For the R-R-R sector, the numerics suggests that $h_{A:B}$ is slightly bigger than $(c/3)\ln 2$, which once again may be attributed to the Ising anyon at the junction. Finally, for the Dirac fermion in the R-R-R sector, $h_{A:B}$ changes with ϵ and the polynomial fit up to second order gives the intercept 0.5698. Notice that 0.2344 is twice as large as 0.1172, and 0.5698 is

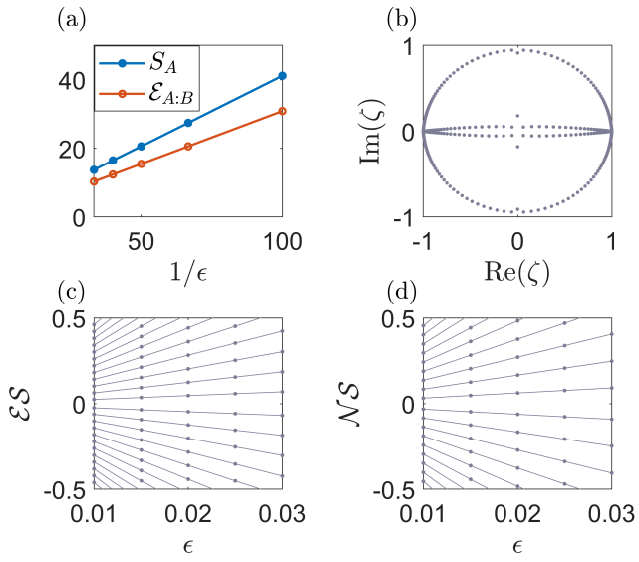

Figure 3.5: (a) The evolution of S_A and negativity $\mathcal{E}_{A:B}$ with different regulator ϵ at $N_c \to \infty$ limit, in the NS-NS-NS sector for the Majorana fermion. (b) Distribution of the eigenvalues of Γ_+, at $N_c = 500$ and $\epsilon = 0.02$ for the complex fermion. (c,d) Entanglement spectrum and negativity spectrum for $N_c = 200$ at different ϵ, which shows equal spacing behavior.

(almost) twice as large as 0.2850. We note that to get the universal result in the edge theory calculations, we do not have to consider a local unitary that remove short-range correlations at the junction(s).

3.3 Conformal interface technique

The numerical results using tripartite vertex state in the last section suggests $h(A, B) = \frac{c}{3} \ln 2$. In this section, we turn to an analytical approach to multipartite entanglement that can be applied to generic (chiral) topological ground states in two spatial dimensions. We show the calculation of multipartite entanglement of vertex state can be reformulated in terms of defect (interface) CFT. In this approach, a given entanglement quantity can be evaluated as a path integral on a cylinder with topological interfaces after using a series of conformal transformations.

In addition to reflected entropy and the Markov gap, this approach also allows us to

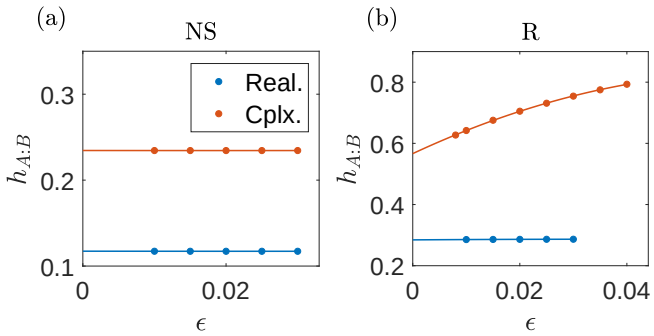

Figure 3.6: The difference between reflected entropy and mutual information $h_{A:B} = R_{A:B} - I_{A:B}$. (a) The NS-NS-NS sector for Majorana fermion and complex fermion. The intercept (0.2344) is twice of that of the Majorana fermion (0.1172). (b) The R-R-R sector for Majorana fermion and complex fermion. Using a power two polynomial fit, the intercept (0.5698) is almost the twice of that of the Majorana fermion (0.2850). In (a) and the real fermion case of (b), $h_{A:B}$ does not change with ϵ.

calculate the so-called corner contribution to the bipartite entanglement entropy studied in Refs. [75, 76, 77]. In these works, the subregions for bipartitions containing sharp corners or cusps were considered. It was found that the entanglement entropy receives a geometric angle-dependent contribution. (See also several works on closely-related quantities and setups, such as the charge fluctuations for a subregion with a sharp corner [78, 79], and others [80, 77, 81]. Quantum Hall states on surfaces with cusp singularities were also studied in the literature [82, 83, 84]. As we will see, the corner contribution from our approach, Eq. (3.88), does not seem to match precisely with the previous works above. We will speculate on the possible source of the discrepancies. Nevertheless, we will show that our prediction (3.88) agrees with numerically-computed entanglement quantities for four vertex states in the free fermion theory. Here, we extend the construction of three-vertex states (vertex states that can be used to tripartition a topological liquid) in the free fermion theory in Ref. [45] to four vertex states. This allows us to tetrapartition the topological liquid, and test our analytical predictions for the corner contribution and the reflected entropy (Markov gap).

The rest of the chapter is organized as follows. In Sec. 3.3.1, we revisit the calculation of bipartite entanglement entropy for topological ground states in two dimensions using

the bulk-boundary correspondence. As is well known, the calculation can be formulated in terms of boundary states in boundary conformal field theory (BCFT). For later use, we reformulate the calculation in terms of defects (interfaces) in CFT and also show that the calculation can be simplified in the $\beta/L \to 0$ limit. In Sec. 3.3.2, we generalize and extend the approach of Sec. 3.3.1 to multipartitions by considering p-vertex states ($p > 2$). This allows us to calculate the corner contribution to bipartite entanglement entropy and the reflected entropy in Sec. 3.3.3. In Sec. 3.3.4, we present the construction of four-vertex states and the numerical calculations of entanglement quantities, verifying the predictions of previous sections.

3.3.1 Conformal interface technique: bipartition

As we reviewed in Sec. 2.3.2, the explicit form of the Ishibashi states are known for generic rational CFTs, allowing for a simple and direct computation of the bipartite entanglement entropy, reproducing the known result for the topological entanglement entropy. Similarly, for a multipartitioning, as discussed in Sec. 3.2.1, the configuration of gapped interfaces can be approximated by a so-called *vertex* state. The explicit form of such states for generic rational CFTs is *not* known, necessitating an alternative approach to computing the entanglement. With this in mind, we introduce a complementary path integral approach to computing the bipartite entanglement entropy, making use of conformal interfaces. Furthermore, we present an approximation of the preceding path integral, which reduces the computation of the entanglement of a CFT partition function on a torus to one of CFT partition functions on two cylinders. We emphasize that these two subsections, while simply reproducing known results for the bipartite entanglement entropy, lay the technical foundations for the subsequent computations of the corner contributions to the bipartite entanglement entropy in Sec. 3.3.2 and the reflected entropy in Sec. 3.3.3.

Conformal interface approach

As described at the beginning of this section, a direct computation of the entanglement entropy from the ground state will not be possible when we later consider multipartitions of the bulk topological phase. While the ground state will satisfy similar conformal boundary conditions as the Ishibashi states, its explicit form for general CFTs is not known. With this in mind, we now develop an alternative approach to computing the bipartite entanglement entropy using path integral and conformal interface methods [85, 86], which *will* generalize to the multipartite case. Our strategy will be to re-express the Rényi moments of (reduced) density matrices formed from regularized boundary states as CFT partition functions on closed manifolds with insertions of conformal interfaces through a series of conformal mappings.

First, we start by expressing the density matrix ρ in Eq. (2.82) as a path integral as depicted pictorially in Fig. 3.7(a). The top and bottom rows correspond, respectively, to the ket $|\mathbf{B}_i\rangle$ and bra $\langle\mathbf{B}_i|$. Focusing first on the ket, the two spacetime sheets correspond to the chiral and anti-chiral sectors of the the theory. The horizontal direction is the spatial direction, of length L, with the tildes indicating periodic boundary conditions. The bottom of the path integral denotes the unregularized boundary state $|B_i\rangle$. The dashed lines connecting the segments a and b indicate how the chiral and anti-chiral sectors are glued together as per the conformal boundary condition. The vertical direction denotes imaginary time evolution by β, yielding the regularized state $|\mathbf{B}_i\rangle$. More generally, we can start from a linear superposition $\sum_i c_i \sqrt{n_i}^{-1} |B_i\rangle$, and the Euclidean path integral prepares the regularized state $\sum_i c_i \sqrt{n_i}^{-1} e^{-\beta H_0} |B_i\rangle$.

Combining these elements yields the glued path integral representation of the ket in the right-most column. Similar considerations hold for the bra, $\langle\mathbf{B}_i|$, represented in the second row of the same subfigure. Combining the bra and ket gives the path integral representation of the density matrix $\rho = |\mathbf{B}_i\rangle \langle\mathbf{B}_i|$. When computing the trace $\mathrm{Tr}\,(\rho)$, the top red lines of

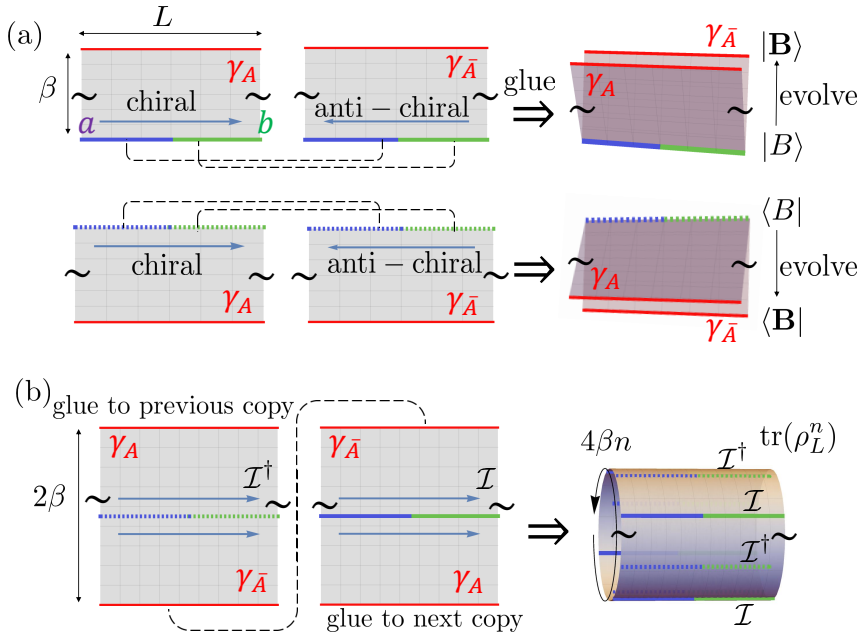

Figure 3.7: (a) Spacetime path integral representation of the regularized boundary state $|\mathbf{B}\rangle$ starting from the unregularized boundary state $|B\rangle$ as the initial condition, as well as $\langle B|$ and $\langle \mathbf{B}|$ as path integral. The vertical direction denotes the imaginary time evolution. "gluing" amounts to identifying chiral and anti-chiral copies, and we consider the case of two anyon lines insertion a and b. The black tilde symbol means taking periodic boundary condition. (b) Unfolding the boundary state. In this picture $Z_n = \mathrm{Tr}\,(\rho_L^n)$ can be expressed as path integral of a chiral theory on the torus with interfaces inserted.

bra and ket are glued together (γ_A to γ_A, $\gamma_{\bar{A}}$ to $\gamma_{\bar{A}}$), and the spacetime manifold becomes a torus.

Now, the computation of entanglement entropy requires computing the Rényi moments of the reduced density matrix, $\mathrm{Tr}\,(\rho_L)^n$. These quantities can be represented as path integrals with conformal interface insertions, as we now demonstrate. We first take the path integral of ρ, and unfold the boundary state $|\mathbf{B}_i\rangle$ and $\langle \mathbf{B}_i|$, as shown in the left of Fig. 3.7(b). After the unfolding, the doubled sheet of width β becomes a single sheet with width 2β. We define the interface operator $\mathcal{I}_i$ as the unfolded boundary state $|B_i\rangle$:

$$\mathcal{I}_i = \sum_{N=0}^{\infty} \sum_{k=1}^{d_{h_i}(N)} |h_i, N; k\rangle\langle h_i, N; k|, \tag{3.67}$$

where the ket of anti-chiral mode is "flipped" to the bra of chiral mode. In other words, $\mathcal{I}_i$ is an Ishibashi-type projector on the chiral sector i, $\mathcal{I}_i : \mathcal{V}_i \to \mathcal{V}_i$. Note this is a well-defined projector since $|h_i, N; k\rangle$ is an orthonormal basis in $\mathcal{V}_i$. In general we can consider the linear superposition $\mathcal{I} = \sum_i c_i \sqrt{n_i}^{-1} \mathcal{I}_i$. Moreover, in the present context, these interfaces are topological, meaning they can be freely deformed in spacetime. Thus, after unfolding, each boundary state $|B\rangle$ ($\langle B|$) maps to an insertion of the interface operator $\mathcal{I}$ ($\mathcal{I}^\dagger$).

To obtain ρ_L, we take the path integral of $\mathcal{I}, \mathcal{I}^\dagger$, and glue the red lines $\gamma_{\bar{A}}$ for $\mathcal{I}$ and $\mathcal{I}^\dagger$, as shown in the left of Fig. 3.7(b) by the black dashed line. Then to obtain $\mathrm{Tr}\,(\rho_L^n)$, we take n copies of path integral of ρ_L, and glue the red line γ_A for $\mathcal{I}$ of copy i to the the red line γ_A for $\mathcal{I}^\dagger$ of copy $i+1$, where i runs from 1 to n. After this gluing, we obtain a torus with circumferences L and $4\beta n$, and the path integral on this torus is $\mathrm{Tr}\ (\rho_L^n)$:

$$Z_n \equiv \mathrm{Tr}\ (\rho_L^n) = \mathrm{Tr}\left((\mathcal{I}\mathcal{I}^\dagger)^n e^{-4n\beta H_L}\right). \tag{3.68}$$

The Hamiltonian H_L in this expression is the *chiral* Hamiltonian $H_L = \frac{2\pi}{L}(L_0 - \frac{c}{24})$ [3]. This is shown in the right of Fig. 3.7(b). In Fig. 3.8(a), we show an equivalent path integral representation of $\mathrm{Tr}\,(\rho_L)$ where the order of gluing is changed (first glue $\gamma_A, \gamma_{\bar{A}}$, then glue a and b). In this way, the spacetime path integral can be constructed by gluing annulus amplitudes where each annulus has width 2β and circumference L. The closed boundary condition is made explicit in this picture.

The path integral on the torus can be evaluated readily using standard CFT techniques. In CFT, the character of primary field sector i is defined as $\chi_i(q) = \mathrm{Tr}\,_{\mathcal{V}_i}(q^{L_0 - \frac{c}{24}})$. As a first example, let's consider the special case of Z_1 with $c_i = \delta_{i,a}$. Z_1 can be directly related

3. We treat our BCFT as an interface CFT (ICFT) by the unfolding. Then, the ICFT corresponds to a chiral part of the BCFT.

to the character:

$$Z_1 = \text{Tr } (\mathcal{I}\mathcal{I}^\dagger e^{-4\beta H_L}) = \frac{1}{n_a}\chi_a(q), \quad q = e^{2\pi i(4\beta i/L)}. \tag{3.69}$$

Since $Z_1 = 1$ by definition, one can read out the normalization factor $n_a = \chi_a(q)$.

We now compute Z_n in the large gap limit of interest $\beta \to 0$. To work in this limit, we need to use the modular $\mathcal{S}$ transformation that brings $q = e^{2\pi i(4\beta i/L)}$ to $\tilde{q} = e^{2\pi i(-L/4\beta i)}$, and $\beta \to 0$ corresponds to the limit of $\tilde{q} \to 0$. The characters are related by $\chi_i(q) = \mathcal{S}_{ii'}\chi_{i'}(\tilde{q})$ under the modular $\mathcal{S}$ transformation. Taking $\tilde{q}$ as a small quantity, the new character can be expanded as $\chi_{i'}(\tilde{q}) = \tilde{q}^{h_{i'} - \frac{c}{24}} + \cdots$ and only the lowest order term shall be kept. By keeping only the lowest order term, Z_n is:

$$\begin{aligned} Z_n &= \text{Tr } \left((\mathcal{I}\mathcal{I}^\dagger)^n e^{-4n\beta H_L}\right) = \sum_i \frac{|c_i|^{2n}}{\chi_i^n(q)}\chi_i(q^n) \\ &= \sum_i |c_i|^{2n} \frac{\sum_{i'} \mathcal{S}_{ii'}\chi_{i'}(\tilde{q}^{\frac{1}{n}})}{(\sum_{i'} \mathcal{S}_{ii'}\chi_{i'}(\tilde{q}))^n} \to e^{\frac{\pi Lc}{48\beta}(\frac{1}{n} - n)} \sum_i |c_i|^{2n} \mathcal{S}_{i0}^{1-n}, \end{aligned} \tag{3.70}$$

and we make another approximation to keep only the lowest order term in χ_0: $\tilde{q}^{-c/24}$ [4]. Using this result, the entanglement entropy between the bulk regions A and $\bar{A}$ is:

$$\begin{aligned} S_A &= \lim_{n\to 1} \frac{1}{1-n} \ln Z_n \\ &= \frac{\pi Lc}{24\beta} - \sum_i |c_i|^2 \ln |c_i|^2 + \sum_i |c_i|^2 \ln \mathcal{S}_{i0}. \end{aligned} \tag{3.71}$$

Recalling $\mathcal{S}_{i0} = d_i/\mathcal{D}$, this reproduces the known result of Eq. (2.85) and Eq. (2.86). We stress that although, at this point, conformal interface is simply a reformulation of boundary

4. While the first line appears to indicate that we have a single path-integral representation for Z_n, due to the normalization of the Ishibashi states, we need separate path integrals for the numerators and denominators. If we were to interpret Z_n as a single path integral, the normalization factors would contribute to the spectrum as states with negative dimension. This subtlety, however, does not matter in the $\beta/L \to 0$ limit where we only keep the vacuum block as in the last line.

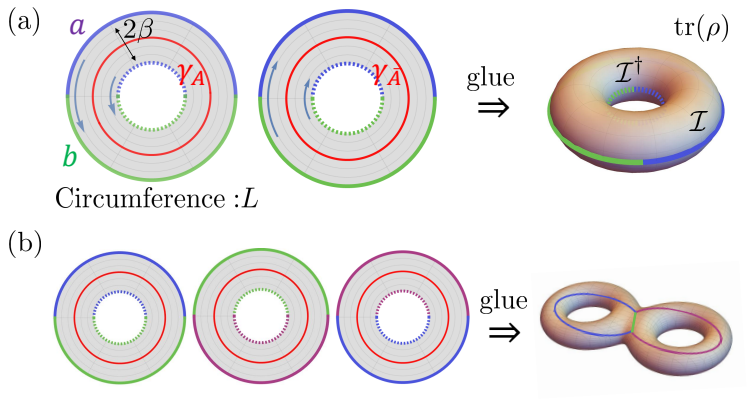

Figure 3.8: The spacetime path integral can be constructed by gluing annulus amplitudes (the annulus has width 2β and circumference L). Here, as an example, $Z_1 = \mathrm{Tr}\,(\rho)$ is constructed for (a) $p = 2$ and (b) $p = 3$. After the gluing, the spacetime manifold becomes torus and 2-genus, respectively.

CFT approach, the path integral viewpoint will be useful in the later discussion of tripartite entanglement. Finally, we also note that for the pure state density matrix ρ, the reflected entropy is simply related to the entanglement entropy S_A by $S_R = 2S_A$. One can verify this relation using conformal interface approach.

Path integral decomposition

Before concluding our discussion of bipartite entanglement, we introduce one final ingredient. The preceding path integral computation was tractable, as it amounted to computing CFT partition functions on the torus. When we turn to multipartite configurations, the exact path integral representation of the entanglement quantities of interest will be defined on higher genus surfaces, for which the partition functions are not readily obtained – see Fig. 3.8(b) for an example of the tripartite configuration. Here, we make use of a pair-of-pants decomposition, valid in the $\beta \to 0$ (i.e., large bulk gap) limit, which reduces the torus path integral to a product of two cylinder path integrals. This decomposition will likewise simplify the multipartite path integrals to render the computations tractable.

We first note that the replicated path integral (partition function) $Z_n = \mathrm{Tr}\,\rho_L^n$ can be

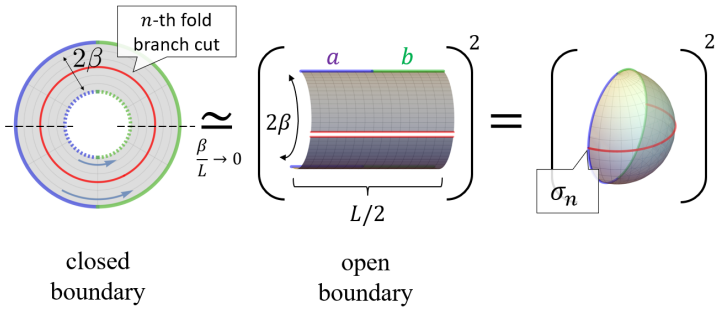

Figure 3.9: Pants-like decomposition of Z_{closed}. In the limit $\beta/L \to 0$, the replica partition function Z_{closed} can be approximated by $(Z_{\text{open}})^2$ (Center Figure). Each of the two strips has width 2β and length $L/2$. The partition function Z_{open} can be thought of as a disk partition function with two twist operators (Right Figure).

obtained by gluing the annulus in Fig. 3.8(a). In the limit $\beta/L \to 0$, the annulus is thin and hence only the lowest dimension states (lowest energy states) propagate, taking the spatial direction as a fictitious time direction.

Consider cutting the annulus into two strips with length $L/2$ and width 2β (Fig. 3.9). Here, cutting the strip is equivalent to inserting a complete set of states at the cut. When crossing the cut, the gluing condition is changed so the leading non-zero contribution in the complete set comes from:

$$\sum_p \mathcal{W}_p \frac{|p\rangle\langle p|}{\langle p|p\rangle} \simeq \mathcal{W}_{p_0} \frac{|p_0\rangle\langle p_0|}{\langle p_0|p_0\rangle}, \tag{3.72}$$

where p_0 are the lowest energy states, which correspond to the twist operator σ_n with conformal dimension $h_{p_0} = h_{\sigma_n} \equiv \frac{c}{24}\left(n - \frac{1}{n}\right)$. The (regularized) normalization factor is [87]:

$$\mathcal{N}_n = \langle p_0|p_0\rangle = \sum_i |c_i|^{2n} \mathcal{S}_{i0}^{1-n}. \tag{3.73}$$

In general, we interpret the constant $\mathcal{W}_p$ as the number of states p. However, in this case, this is not necessary to be an integer because the normalization of the Ishibashi state depends

on the moduli parameter. We can show that

$$\mathcal{W}_{p_0} = \mathcal{N}_n. \tag{3.74}$$

This just comes from the closed channel expansion of (3.70),

$$Z_n \simeq \mathcal{W}_{p_0} \mathrm{e}^{-h_{p_0} \frac{\pi L}{2\beta}}. \tag{3.75}$$

Before giving the expression in terms of these constants, we would first like to explain the motivation for expressing the partition function in the closed string channel expansion (i.e. the quantization with the time direction along the interface). Unfortunately, it is difficult to fix these theory-dependent constants [e.g. the normalization factor (3.73) and the coefficients $\mathcal{W}_p$ (3.74)] in general, as we will see later in Sec. 3.3.3. Nevertheless, the closed string channel expansion is useful because we can easily evaluate the kinematic parts in this expression. In fact, we only need the kinematic parts to study the quantities of interest (i.e., the area law term, the corner contribution, and the Markov gap). In other words, for our purpose, the closed string channel expansion is more useful even though it involves the theory-dependent constants.

By this approximation, valid in the limit $\beta/L \to 0$, each annulus amplitude can be approximated as a product of two strip amplitudes. Correspondingly, the total partition function Z_n can be approximated as a product of two partition functions, each obtained by gluing the strips,

$$Z_n \equiv Z_{\text{closed}} \simeq \mathcal{N}_n^{-2} \cdot \mathcal{N}_n \cdot (Z_{\text{open}})^2. \tag{3.76}$$

Here, the factor of $\mathcal{N}_n^{-2}$ comes from the normalization factor while $\mathcal{N}_n$ comes from the coefficient $\mathcal{W}_{p_0}$. Note that while we have the double insertions of the complete sets, we do

not need to square Eq. (3.74) since $\langle p_0|q_0\rangle = \delta_{p_0,q_0}$. Each factor of $\mathcal{N}_n$ contributes to the entanglement entropy by $\lim_{n\to 1}\frac{1}{1-n}\ln \mathcal{N}_n = -S_{\rm topo}$. Taking care of these contributions, we recover the entanglement entropy (2.85):

$$\begin{aligned} S_{\rm closed} &= 2S_{\rm open} + 2S_{\rm topo} - S_{\rm topo} \\ &= 2\left(\frac{\pi c L}{48\beta} - S_{\rm topo}\right) + S_{\rm topo} = \frac{\pi c L}{24\beta} - S_{\rm topo}. \end{aligned} \tag{3.77}$$

Finally, we stress that using the open boundary condition introduces the cutoffs at the two boundaries (at $-L/4$ and $L/4$) of the strip. After the conformal transformation $z \to e^{z\frac{2\pi}{4\beta}}$, the cutoff is (see the right figure of Fig. 3.9):

$$\epsilon = e^{-\frac{L}{4}\frac{2\pi}{4\beta}} = e^{-\frac{\pi L}{8\beta}}. \tag{3.78}$$

The area law term in $S_{\mathbf{r}open}$ can be equivalently expressed in terms of the cutoff as:

$$S_{\rm open,area} = \frac{\pi c L}{48\beta} = \frac{c}{6}\ln \epsilon^{-1}. \tag{3.79}$$

This expression will be convenient in the following to take care of the contribution to the entanglement entropy by conformal transformation. Namely, the change of the entanglement entropy is encoded in the change of cutoff $\epsilon \to \epsilon'$. More generally, if the cutoffs on the left and right end of an interval are ϵ_1 and ϵ_2, respectively, the area law part can be expressed as:

$$S_{\rm open,area} = \frac{c}{12}\ln\frac{1}{\epsilon_1\epsilon_2}. \tag{3.80}$$

We also note that the topological term $S_{\rm topo}$ is independent of the cutoff ϵ.

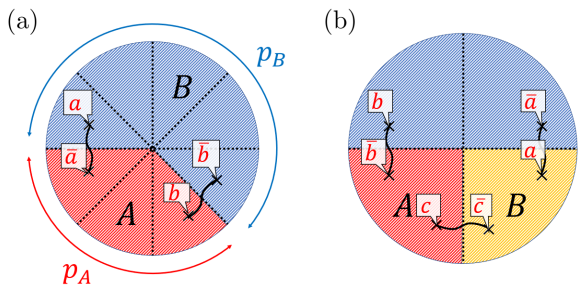

Figure 3.10: (a) Bipartition setup: A spatial sphere divided into two regions A, B, and with four anyons $(a, \bar{a}, b, \bar{b})$ insertion. We take the size of the subsystem as p_A $(p_A + p_B = p)$, which leads to a corner with an angle $\theta = 2\pi p_A/p$. (b) Tripartition setup: A spatial sphere divided into three regions A, B and $\overline{A \cup B}$, and with six anyons $(a, \bar{a}, b, \bar{b}, c, \bar{c})$ insertion.

3.3.2 Vertex States: Corner contributions to Entanglement Entropy

We are now ready to generalize the previous discussions to more complicated setups. First, we can consider the bipartition setup where we partition the two-dimensional space into two regions A and B with a sharp corner (cusp) [Fig. 3.10(a)]. This type of bipartition was considered in Refs. [75, 76, 77] and a contribution to the entanglement entropy, the so-called geometric or corner contribution, has been identified. Second, we can consider the multipartition setup where we partition the two-dimensional space into multiple regions $A, B, C, \ldots$ where all subregions meet at a junction (or junctions) [Fig. 3.10(b)]. This setup was discussed in Refs. [45, 49], and the reflected entropy (the Markov gap) and entanglement negativity were computed. We note that the first setup can be obtained from the multipartition setup by simply grouping the multiple regions $A, B, C, \ldots$ into two groups and regarding the regions in the same group belonging to the same Hilbert space.

In this section, we focus on the corner contribution to bipartite entanglement entropy. To provide a unified treatment, we will consider the setup in Fig. 3.10(b) throughout the paper, in which we p-partition the spatial sphere, and consider two regions A and B (and the rest). The corner angle of the region A is denoted by $\theta = 2\pi p_A/p$ $(1 < p_A \leq p)$. We limit out discussion to the case where A and B are adjacent, unless specified otherwise. We also

insert pairs of anyons (a and $\bar{a}$, etc.) across the interfaces (entangling boundaries) that give rise to extra topological contributions to bipartite entanglement entropy, while they have nothing to do with the geometrical contribution.

Vertex state in RCFT

As discussed in Sec. 3.2.1, using the bulk-boundary correspondence, the multipartition setup can be related to vertex states in CFT. Specifically, the topological ground states near the multipartite entangling boundary can be approximated by a p-vertex state. Analogously to boundary states, a vertex state $|V\rangle$ defined in the tensor product of p-copies of the CFT (defined on a spatial circle of length L) satisfies

$$[T^i(\sigma) - T^{i+1}(L-\sigma)]|V\rangle = 0, \quad 0 \leq \sigma \leq L/2, \tag{3.81}$$

where $T^i(\sigma)$ is the stress-energy tensor of the i-th copy ($i = 1, \ldots, p$), and σ coordinatizes the spatial circle. If there is a (conserved) current in CFT, vertex states satisfy, additionally, a condition as Eq. (3.11) in terms of the current. For general CFTs (RCFTs), on the other hand, finding vertex states is a yet challenging task. However, as we will show below, by using the path integral representation and conformal interface approach, we can still obtain the universal behaviors of its entanglement measures.

We have to mention that the p-vertex state is defined *after* the conformal map (see Fig. 3.11),

$$z \to z^{\frac{p}{2}}. \tag{3.82}$$

The reason is as follows. On the one hand, the multipartite entanglement measures are computed on the two-dimensional spatial sphere with a p-partition setup. On the other hand, by definition, the density matrix of p-vertex state is defined on the spacetime manifold with four excess angles, each takes the value $2\pi(\frac{p}{2} - 1)$ as shown in Fig. 3.11 (a) (and after

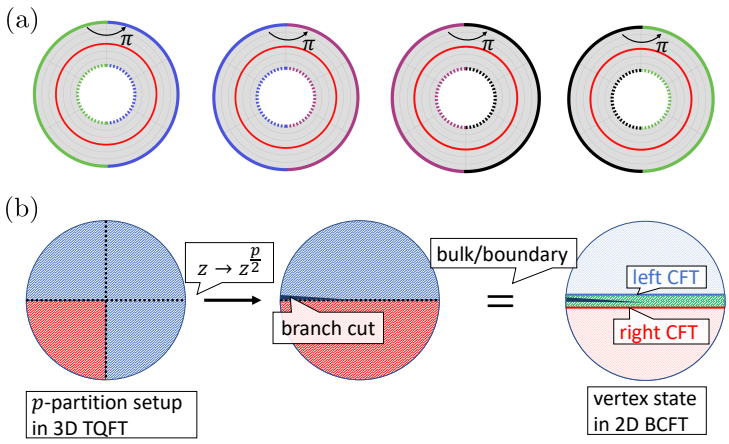

Figure 3.11: (a) Illustration of the excess angle of the p-vertex state density matrix path integral. As shown in the figure, on the outer edge of the top of the annulus, the total angle is $p\pi$, thus the excess angle is $p\pi - 2\pi = 2\pi(\frac{p}{2} - 1)$. Similarly, the excess angles on the inner edge of the top, and the outer and inner edge of the bottom of the annulus are also $2\pi(\frac{p}{2} - 1)$. (b) The p-partition setup of the two-dimensional spatial sphere, where the multipartite entanglement measures are computed. To obtain the corresponding p-vertex state on the entanglement boundary, we first map the spatial sphere (Left) into the Riemann surface with exceed angle $2\pi\left(\frac{p}{2} - 1\right)$ (Center) by conformal transformation $z \to z^{p/2}$. Applying the bulk-boundary correspondence to this surface, we obtain the vertex state (Right), whose density matrix is defined on spacetime manifold with four exceed angles, each taking the value $2\pi(\frac{p}{2} - 1)$.

taking the trace of ρ, the spacetime path integral becomes a $p-1$ genus). Thus, the conformal transformation in Eq. (3.82) is required to bridge them, as shown in Fig. 3.11 (b). If this is not included, the final results for all entanglement measures would carry an extra factor of $\frac{c}{3} \ln \frac{p}{2}$.

Entanglement entropy with corner contribution

We are now ready to calculate the entanglement entropies S_A, S_B, and S_{AB} associated to the regions A, B, and AB. in Fig. 3.10(b). The multipartition can be done by using the p-vertex state. The corresponding replica path integral for computing n-th Rényi entropy is defined on a Riemann surface. For example, when $p_A = 1$, the path integral is on a Riemann surface with genus $n(p-2)+1$. The path integral on the higher genus surface is not readily

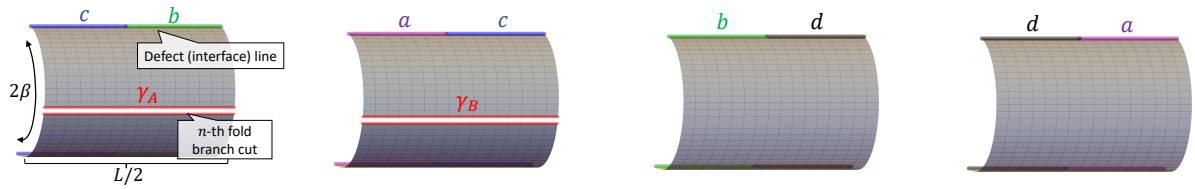

Figure 3.12: Sketch of our setup for 4-vertex state partition function with open boundary condition. The width of each strip is 2β and the length is $L/2$. When evaluating n-th Rényi entropy, the intervals γ_A and γ_B denote the n-th fold branch cut. On the top and bottom, we have the excess angle $2\pi(\frac{4}{2}-1)=2\pi$.

obtained. However, in the limit of $\beta/L \to 0$, it can be evaluated by using the path integral decomposition described in Sec. 3.3.1. Here, we factorize the partition function (with closed boundary condition) into two with open boundary condition by inserting a complete set of states. In the limit $\beta/L \to 0$, the open partition function can be approximated by taking the leading twisted operator or vacuum. Thus, the replica partition function Z_{closed} can be approximated by $Z_{\text{closed}} \approx \mathcal{N}^{-1}\left(Z_{\text{open}}\right)^2$. The constant $\mathcal{N}$ is a combination of the normalization factor and the coefficient $\mathcal{W}_p$, which contributes to the entanglement entropy as the topological entropy, as discussed in Eq. (3.77). This strip partition function can be illustrated as in Fig. 3.12 for the case of $p=4$, where the width and length of each strip are 2β and $L/2$, respectively. We take two intervals γ_A and γ_B as shown in the figure, namely, the two bulk regions A, B are adjacent. The intervals γ_A and γ_B denote the n-th fold branch cut when evaluating n-th Rényi entropy.

The entanglement entropy S_A and S_{AB} can be computed by the open partition function Z_{open}. To evaluate the partition function Z_{open}, we consider the following conformal maps (the following figures are illustrated for $p=4, p_A=p_B=1$):

1. Mapping from cylinder to hemisphere: $z \to \mathrm{e}^{-\frac{\pi}{2\beta}z}$.
2. Rotating : $z \to \frac{1+z}{1-z}$.

   (insertion points of twist operators $(0,\infty)$ mapped to $(1,-1)$)
3. Unwrapping: $z \to z^{\frac{2}{p}}$ and gluing p copies.

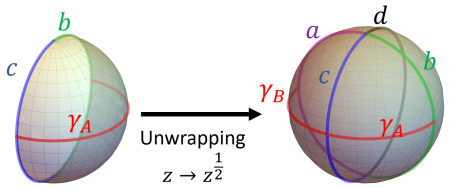

4. Rotating : $z \to -\mathrm{e}^{\frac{2\pi i}{p}} \frac{z-\mathrm{e}^{-\frac{2\pi i}{p}}}{z-\mathrm{e}^{\frac{2\pi i}{p}}}$.

   (insertion points of twist operators $(\mathrm{e}^{-\frac{2\pi i}{p}}, 1, \mathrm{e}^{\frac{2\pi i}{p}})$ mapped to $(0, 1, \infty)$)

5. Mapping from sphere to cylinder $z \to \ln z$.

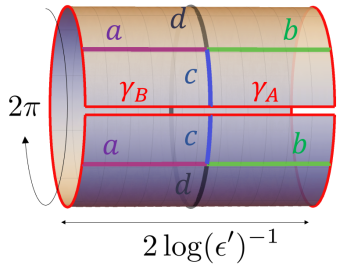

In Step (4), the interval γ_B is mapped to $(0, 1)$ and the interval γ_A is mapped to $(1, \infty)$. The cutoff $\epsilon = e^{-\frac{\pi L}{8\beta}}$ at the end of the intervals $(z = 0, 1, \infty)$ transforms as

$$\begin{aligned} \epsilon \to \epsilon' &= \frac{2}{p \sin \frac{2\pi}{p}} \epsilon, \quad \text{at } z = 0, \\ \epsilon \to \epsilon' &= \frac{4}{p \tan \frac{\pi}{p}} \epsilon, \quad \text{at } z = 1, \\ \frac{1}{\epsilon} \to \frac{1}{\epsilon'} &= \frac{p \sin \frac{2\pi}{p}}{2} \frac{1}{\epsilon}, \quad \text{at } z = \infty. \end{aligned} \tag{3.83}$$

The interval $\gamma_A \cup \gamma_B$ is mapped to $(0, \infty)$. By using Eq. (3.79) with the modified cutoffs in Eq. (3.83) ($S_{\text{open,area}} = \frac{c}{6} \ln(\epsilon')^{-1}$), and the normalization factor from Eq. (3.73) and the coefficient $\mathcal{W}_{p_0}$ from Eq. (3.74), the entanglement entropy S_{AB} including the corner

contribution is given by

$$\begin{aligned} S_{AB} &= 2S_{\text{open}} + S_{\text{topo}} \\ &= 2\left(\frac{\pi cL}{48\beta} + \frac{c}{6}\ln\sin\frac{2\pi}{p}\right) - S_{\text{topo}} \\ &= \frac{\pi cL}{24\beta} + \frac{c}{3}\ln\sin\frac{2\pi}{p} + \ln\frac{d_a d_b}{\mathcal{D}}. \end{aligned} \tag{3.84}$$

The topological term comes from the anyons insertion $a, \bar{a}$ and $b, \bar{b}$, where unique fusion channel is assumed We set d as the trivial interface from now on. In this expression the factor $\frac{c}{3}\ln\frac{p}{2}$ is removed by Eq. (3.82). Similarly, to find the entanglement entropy for interval γ_A, we can perform an additional shift $z \to z - 1$ such that the interval γ_A is mapped to $(0, \infty)$ and apply Eq. (3.80):

$$\begin{aligned} S_A &= \frac{\pi cL}{24\beta} + \frac{c}{6}\ln\left[\frac{1}{2}\sin\frac{2\pi}{p}\tan\frac{\pi}{p}\right] + \ln\frac{d_b d_c}{\mathcal{D}} \\ &= \frac{\pi cL}{24\beta} + \frac{c}{3}\ln\sin\frac{\pi}{p} + \ln\frac{d_b d_c}{\mathcal{D}}. \end{aligned} \tag{3.85}$$

And similarly, for S_B,

$$S_B = \frac{\pi cL}{24\beta} + \frac{c}{3}\ln\sin\frac{\pi}{p} + \ln\frac{d_a d_c}{\mathcal{D}}. \tag{3.86}$$

Combining these results, we can also obtain the mutual information:

$$\begin{aligned} I(A,B) &= S_A + S_B - S_{AB} \\ &= \frac{\pi cL}{24\beta} + \frac{c}{3}\ln\frac{\tan\frac{\pi}{p}}{2} + \ln\frac{d_c^2}{\mathcal{D}}. \end{aligned} \tag{3.87}$$

The above results, presented for $p_A = 1$, can be readily generalized to $1 < p_A \leq p$. I.e., subregion A has a cusp with angle $\theta = 2\pi p_A/p$. The entanglement entropy S_A in this case is given by

$$S_A = \frac{\pi cL}{24\beta} + \frac{c}{3}\ln\sin\frac{\theta}{2} - S_{\text{topo}}. \tag{3.88}$$

This is the central result of this section. The second term $\frac{c}{3}\ln\sin\frac{\theta}{2}$ can be identified as the corner contribution to the entanglement entropy. Recalling that we have two corners with equal angles in our setup, we may introduce $a(\theta) := -(1/2)\times\frac{c}{3}\ln\sin\frac{\theta}{2}$ that represents contribution from each corner (with the minus sign to be consistent with the convention in [75, 76, 77]. We note that $-2a(\theta)$ takes the same form as the entanglement entropy of the ground state of (1+1)d CFT on a finite periodic chain (of length p) associated with an interval (of length p_A). It is known that the same contribution arises when the subregion of our interest includes a physical edge [80], although there is no physical edge in our setup.

In Sec. 3.3.4, we will compute the corner contribution for the case of the free Majorana fermion CFT ($c = 1/2$) and $p = 4$. There, we will construct the $p = 4$ vertex states explicitly, and calculate the bipartite entanglement entropy numerically. We will confirm, within numerical errors, the above result (3.88).

We also note that the corner contribution $a(\theta)$ was previously discussed in the literature for the integer quantum Hall ground states [75, 76, 77]. In [76], it was numerically observed that the corner contribution (from one corner) behaves as $a(\theta) \sim \kappa/\theta$ for small θ while $a(\theta) \sim \sigma(\theta-\pi)^2$ for $\theta \sim \pi$, where numerical constants κ and σ were determined numerically. While the latter behavior of the corner contribution near $\theta \sim \pi$ is consistent with ours, the small θ behavior disagrees with $(-c/6)\ln\sin\theta/2 \sim (-c/6)\ln\theta$. We also note that in [76], the constant σ is estimated for the $\nu = 1$ integer quantum Hall state as $\sigma \sim 0.02836$, that should be contrasted with $(-c/6)\ln\sin\theta/2 \sim (c/48)(\theta-\pi)^2$ with $c/48 \sim 0.02083$ for $c = 1$. The source of the discrepancy is not entirely clear. We nevertheless recall that the (single-particle) bipartite entanglement spectrum for the integer quantum Hall state in the lowest Landau level is linear only for small momentum along the entangling boundary [88], while in our ansatz state (2.82) a perfectly relativistic spectrum is assumed. It is also possible that for small enough θ, the representation of the topological ground state near the cusp by using the vertex state, $e^{-\beta H_0}|V\rangle$, is not entirely accurate. Our numerics in Sec.

3.3.4, where we verify the formula (3.88) for relatively large θ by using the explicit form of $e^{-\beta H_0}|V\rangle$, is in favor of these speculations. Finally, we should also note that not all bulk geometrical properties of topological liquid may be captured by using the edge states and the bulk-boundary correspondence [89].

3.3.3 Vertex states: Reflected entropy and Markov gap

In this section, we consider the multipartition setup as in Fig. 3.10(b) and compute the reflected entropy as well as the Markov gap for the p-vertex state for the case where A and B are adjacent and $p_A = p_B = 1$. We will use the replica trick to compute the reflected entropy and show that the Markov gap is $\frac{c}{3}\ln 2$ analytically.

To compute the reflected entropy, two replica indices m, n shall be introduced and the open partition function to be evaluated is:

$$Z_{n,m} = \mathrm{Tr}_{AA^*}\left(\mathrm{Tr}_{BB^*}|\rho_{AB}^{m/2}\rangle\!\rangle\langle\!\langle\rho_{AB}^{m/2}|\right)^n. \tag{3.89}$$

Here n is the index for Rényi replicas, and m is the index for handling the square root of the reduced density matrix, where we take $m \to 1$ at the end of the calculation. The n-th Rényi reflected entropy is computed using:

$$S_R^n = \lim_{m\to 1}\frac{1}{1-n}\ln\frac{Z_{n,m}}{(Z_{1,m})^n}, \tag{3.90}$$

and the reflected entropy is $S_R = \lim_{n\to 1} S_R^n$.

Similar to the previous discussion, the path integral for evaluating S_R^n is performed on a higher genus surface and is hard to compute. Using the path-integral decomposition as in Sec. 3.3.1, we again focus on the open partition function. For reflected entropy, the normalization factor and the density of the lowest energy states become highly complicated. Therefore, we first focus on the special case where the topological term can be neglected and

give a few comments later.

To evaluate the partition function $Z_{n,m}$, we consider the following conformal maps. The steps (1)-(4) are the same as in Sec. 3.3.2, and the conformal maps from step (5) are:

5. Unwrapping: $z \to z^{\frac{1}{m}}$.

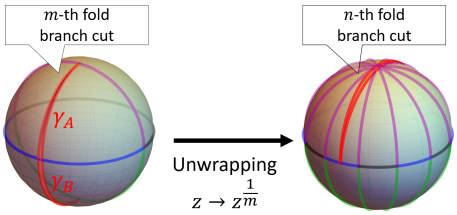

6. Rotating : $z \to \frac{1+z}{1-z}$.

   (insertion points of twist operators $(-1, 1)$ mapped to $(0, \infty)$)

7. Unwrapping: $z \to z^{\frac{1}{n}}$.

8. Map from sphere to cylinder: $z \to \ln z$.

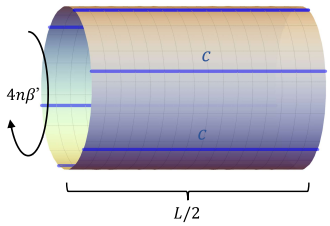

After the above conformal transformations, $Z_{n,m}$ is brought to a partition function on a cylinder with interfaces, and with a new cutoff:

$$\epsilon \to \epsilon' = \frac{1}{2m} \frac{4}{p \tan \frac{\pi}{p}} \epsilon. \tag{3.91}$$

This conformal factor $(2m)^{-2h_n}$ is the OPE coefficient $C_{\sigma g_A \sigma g_B^{-1} \sigma g_A^{-1} g_B}$ of twist operators [53]. Since we assume the interfaces to be topological, we can freely move junction fields

so that the net of the interfaces is simplified as shown in step (8), where $\beta' = -\frac{\pi L}{8\ln(\epsilon')} = \beta(1 + \frac{8\beta}{\pi L}\ln\frac{1}{2}\frac{4}{p\tan\frac{\pi}{p}} + O(\beta^2))$.

Using the new cutoff ϵ', the reflected entropy can be evaluated by Eq. (3.79):

$$S_R = \frac{c}{3}\ln\epsilon'^{-1} = \lim_{m\to 1}\frac{c}{3}\left[\ln\epsilon^{-1} + \ln 2m + \ln\frac{p\tan\frac{\pi}{p}}{4}\right], \tag{3.92}$$

where we use the assumption that the topological contribution is zero. Taking into account the effect of the conformal map (3.82), we obtain the reflected entropy for the p-partition setup,

$$S_R(A,B) = \frac{c}{24}\frac{\pi L}{\beta} + \frac{c}{3}\ln\frac{\tan\frac{\pi}{p}}{2} + \frac{c}{3}\ln 2. \tag{3.93}$$

The first term corresponds to the area law term. The second term comes from the conformal transformation (3.83). This term can be understood as a corner contribution. The third term comes from the $(2m)^{-1}$ factor in (3.91). This is the universal contribution related to the OPE coefficient $C_{\sigma g_A \sigma g_B^{-1}\sigma g_A^{-1} g_B}$.

With the above results on mutual information and reflected entropy, let us now evaluate the Markov gap. Combining the results from the previous two subsections and assuming the topological contribution can be neglected, we find the Markov gap is:

$$h = S_R(A,B) - I(A,B) = \frac{c}{3}\ln 2. \tag{3.94}$$

In summary, the corner contribution from mutual information and reflected entropy cancel out exactly, and the Markov gap does not receive the corner contribution. This is verified numerically in the Majorana fermion CFT in Sec. 3.3.4.

Now, to reiterate, we restricted our computation to the case in which the reflected entropy does not receive additional topological contributions from anyon insertions. In previous sections, we considered configurations in which a single pair of anyons pierces each interface, with the anyon label being determined by the corresponding interface operator, as depicted

in Fig. 3.10(b). While we have been unable to compute the Markov gap in this more general case, we suspect that it should still vanish. Indeed, as noted in the Introduction, Ref. [55] proved that the Markov gap vanishes for so-called "sum-of-triangle" states. For a tripartition of a Hilbert space $\mathcal{H} = \mathcal{H}_A \otimes \mathcal{H}_B \otimes \mathcal{H}_C$ and further bipartitions of each subspace, $\mathcal{H}_\alpha = \bigoplus_j \mathcal{H}_{\alpha_L^j} \otimes \mathcal{H}_{\alpha_R^j}$ a sum of triangle states takes the form

$$|\psi\rangle = \sum_j \sqrt{p_j} \, |\psi_j\rangle_{A_R^j B_L^j} \, |\psi_j\rangle_{B_R^j C_L^j} \, |\psi_j\rangle_{C_R^j A_L^j}$$

where $\sum_j p_j = 1$ and $|\psi_j\rangle_{\alpha_R^j \beta_L^j}$ has support in $\mathcal{H}_{\alpha_R^j} \otimes \mathcal{H}_{\beta_L^j}$. Qualitatively, the anyon configuration Fig. 3.10(b) takes this triangle state form, with each anyon pair entangling two of the three subregions. Based on this heuristic, we suspect that this particular configuration of anyons will not lead to a non-zero Markov gap. It is possible that other, non-trivial anyon configurations could lead to a non-vanishing Markov gap.

3.3.4 Four-vertex states in the Majorana fermion CFT and correlation measures

In this section, we consider the free real fermion CFT with $c = 1/2$, and construct four-vertex states explicitly. From the explicit form of the vertex states, various correlations measures (entanglement entropy, reflected entropy, entanglement negativity, etc.) can be calculated numerically. We will see that the numerics is consistent with the analytical results in the preceding sections. In addition, we can calculate the correlation measures in the setups that are not amendable in the analytical treatment. For example, we will discuss the correlation measures when subregions A and B are not adjacent.

In the following, we will present two approaches to construct vertex states; the direct method and the Neumann function method (see Sec. 3.2.2). We will also note that there are at least two vertex states, which satisfy what we call "usual" and "kink" boundary conditions.

We will show that the Neumann function method, when applied naively, gives rise to the vertex state with the kink boundary condition, and the kink boundary condition reproduces the correlation measures as predicted in the previous sections.

Usual and kink boundary conditions

Let us consider four copies of the Majorana fermion CFT and construct the vertex state. We denote the Majorana fermion fields by $\psi^i(\sigma)$ where $i = 1, \ldots, 4$ denotes the copy index, and $0 \leq \sigma \leq 2\pi$ coordinatizes the spatial circle. For simplicity in this section we set the circumference of the circle to be $L = 2\pi$. They satisfy the canonical anticommutation relation $\{\psi^i(\sigma), \psi^j(\sigma')\} = 2\pi\delta^{ij} \sum_{n\in\mathbb{Z}} \delta(\sigma - \sigma' - 2\pi n)$. We will work with the Neveu-Schwartz (antiperiodic) boundary condition in σ. Under the antiperiodic boundary condition, the fermion field can be expended in the Fourier modes labeled by half-integers as $\psi^i(\sigma) = \sum_{r\in\mathbb{Z}+1/2} \psi^i_r e^{-ir\sigma}$. Using the Fourier modes, the canonical anticommutation relation reads $\{\psi^i_r, \psi^j_s\} = \delta^{ij}\delta_{r+s,0}$.

As discussed in Sec. 3.2.1, we define a vertex state $|V\rangle$ in terms of the boundary condition it satisfies. First, we introduce the usual boundary condition by

$$[\psi^i(\sigma) + i\psi^{i+1}(2\pi - \sigma)]|V_u\rangle = 0, \quad i = 1, \cdots, 4 \tag{3.95}$$

where $0 < \sigma < \pi$, and the periodic boundary condition $\psi^5 \equiv \psi^1$ is understood. On the other hand, we introduce the kink boundary condition by

$$\begin{aligned} &[\psi^i(\sigma) + i\psi^{i+1}(2\pi - \sigma)]|V_k\rangle = 0, \quad i = 1, 2, 3 \\ &[\psi^i(\sigma) - i\psi^{i+1}(2\pi - \sigma)]|V_k\rangle = 0, \quad i = 4, \end{aligned} \tag{3.96}$$

where again $0 < \sigma < \pi$. Here, we observe that the boundary state – which can be regarded as the two-vertex state – satisfies a similar kink boundary condition: $[\psi^1(\sigma)+i\psi^2(2\pi-\sigma)]|B\rangle =$

$[\psi^2(\sigma) - i\psi^1(2\pi - \sigma)]|B\rangle = 0$ $(0 \leq \sigma \leq \pi)$. The kink boundary condition is "natural" from this perspective. We will also see that the Neumann function method applied p-vertex states with p even naturally gives rise to the kind boundary condition. We will see below that the kink boundary condition yields the predicted entanglement behaviors in Secs. 3.3.2 and 3.3.3.

Direct method

We first present the Dirac method, which is able to solve for the vertex state for both usual and kink boundary conditions. Since there is no interaction, the solution to Eq. (3.95) or (3.96) can be explicitly constructed as a coherent state (Gaussian state). For simplicity, we will focus below the usual boundary condition and delegate the details for the case of the kink boundary condition to Appendix A.2.2. It can be numerically verified that for the kink boundary, direct calculation method gives the same result as the Neumann coefficient method.

The boundary condition (3.95) can be diagonalized by a unitary transformation. Explicitly, we introduce the "rotated" fields as $\boldsymbol{\eta} = U\boldsymbol{\psi}$ where the unitary matrix U is given by

$$U = \frac{1}{2}\begin{pmatrix} 1 & 1 & 1 & 1 \\ -i & -1 & i & 1 \\ -1 & 1 & -1 & 1 \\ i & -1 & -i & 1 \end{pmatrix}. \tag{3.97}$$

The transformed fields obey the anticommutation relation

$$\{\eta^1(\sigma), \eta^1(\sigma')\} = \{\eta^3(\sigma), \eta^3(\sigma')\} = \{\eta^2(\sigma), \eta^4(\sigma')\} = 2\pi \sum_{n\in\mathbb{Z}} \delta(\sigma - \sigma' - 2\pi n).$$

We note that the matrix U diagonalizes the "shift" matrix as

$$\begin{pmatrix} 0 & 1 & 0 & 0 \\ 0 & 0 & 1 & 0 \\ 0 & 0 & 0 & 1 \\ 1 & 0 & 0 & 0 \end{pmatrix} = U^\dagger \begin{pmatrix} 1 & 0 & 0 & 0 \\ 0 & i & 0 & 0 \\ 0 & 0 & -1 & 0 \\ 0 & 0 & 0 & -i \end{pmatrix} U. \tag{3.98}$$

The original boundary condition is translated into the boundary condition of the transformed fields η:

$$\begin{aligned} &[\eta^1(\sigma) + i\mathrm{sgn}\,(\sigma)\eta^1(2\pi-\sigma)]|V_u\rangle = 0, \\ &[\eta^3(\sigma) - i\mathrm{sgn}\,(\sigma)\eta^3(2\pi-\sigma)]|V_u\rangle = 0, \\ &[\eta^2(\sigma) - \eta^2(2\pi-\sigma)]|V_u\rangle = 0, \\ &[\eta^4(\sigma) + \eta^4(2\pi-\sigma)]|V_u\rangle = 0. \end{aligned} \tag{3.99}$$

We note that the boundary conditions for η^1 and η^3 are decoupled and take the form $[\eta(\sigma) - i\mathrm{sgn}\,(\sigma)e^{i\mathrm{sgn}\,(\sigma)\theta}\eta(2\pi-\sigma)]|V\rangle = 0$ $(0 \le \sigma \le 2\pi)$ where $\theta = 0$ or π. The solution to this boundary condition is derived in [45] and given by

$$|V\rangle \propto \exp\Big(\sum_{r,s\ge 1/2} \frac{1}{2} K_{rs}(\theta)\eta_{-r}\eta_{-s}\Big)|0\rangle, \tag{3.100}$$

where $|0\rangle$ is the ground state of the η-fermion field. Given θ, the explicit form of $K(\theta)$ is summarized in Appendix A.2.1. As for the boundary conditions for η^2 and η^4, they can be written in terms of the Fourier modes as

$$\left[\begin{pmatrix} \eta_r^4 \\ \eta_r^2 \end{pmatrix} + \begin{pmatrix} 0 & 1 \\ -1 & 0 \end{pmatrix} \begin{pmatrix} \eta_{-r}^2 \\ \eta_{-r}^4 \end{pmatrix}\right] |V_u\rangle = 0. \tag{3.101}$$

The modes with different r decouple, which allows a simple boundary state solution.

To summarize, the vertex state in the η basis can be constructed as

$$|V_u\rangle \propto \exp\Big(\sum_{r,s\geq 1/2} \frac{1}{2}\eta^a_{-r} K^{ab}_{\eta,rs} \eta^b_{-s}\Big)|0\rangle \tag{3.102}$$

where the matrix K_η is given by

$$K_\eta = \begin{pmatrix} K(\pi) & 0 & 0 & 0 \\ 0 & 0 & 0 & \mathbb{1} \\ 0 & 0 & K(0) & 0 \\ 0 & -\mathbb{1} & 0 & 0 \end{pmatrix}, \tag{3.103}$$

in the basis $(\eta^1_{-r}, \eta^2_{-r}, \eta^3_{-r}, \eta^4_{-r})^T$. Finally, $|V_u\rangle$ can be written in the original ψ basis by "rotating back",

$$|V_u\rangle \propto \exp\Big(\sum_{r,s\geq 1/2} \frac{1}{2}\psi^i_{-r} K^{ij}_{rs} \psi^j_{-s}\Big)|0\rangle, \tag{3.104}$$

where the matrix K is obtained from K_η as $K = U^T K_\eta U$.

Neumann function method

In the Neumann function method, we start from the Gaussian ansatz solution of the form (3.104) and find the matrix K such that the vertex state reproduces the two-point correlation function (Neumann function) on the plane. Specifically, we consider the two-point correlation function of the fermion field $\sim 1/(w - w')$ on the complex plane and consider

$$K^{ij}(\sigma, \sigma') = \left(\frac{\partial w_i}{i\partial\sigma}\right)^{\frac{1}{2}} \frac{1}{w_i(\sigma) - w_j(\sigma')} \left(\frac{\partial w_j}{i\partial\sigma'}\right)^{\frac{1}{2}}. \tag{3.105}$$

Here, w_i is the conformal transformation from p copies of half cylinders to the full complex plane:

$$w_i(z) = w_{i,0}\Big(\frac{1+z}{1-z}\Big)^{\frac{2}{p}}, \quad z = e^{i\sigma} \tag{3.106}$$

with the constant term satisfies $w_{i+1,0} = (e^{i\pi})^{\frac{2}{p}} w_{i,0}$. From the Fourier transform of the Neumann function we read off K_{rs}^{ij} as

$$K^{ij}(\sigma,\sigma') = \sum_{r,s\geq 1/2} e^{ir\sigma} e^{is\sigma'} K_{rs}^{ij} + \delta^{ij} \sum_{r\geq 1/2} e^{-ir(\sigma-\sigma')}. \tag{3.107}$$

From the given Neumann function (3.105) one can check explicitly the presence of the second term ("singular term") – see Appendix A.1.4 for details.

In order to see the boundary condition satisfied by the so-constructed vertex state, we need to check the behavior of the Neumann function under the reflection $\sigma \to 2\pi - \sigma$. This amounts to $z \to 1/z$ and leads to:

$$\begin{aligned} w_i\Big(\frac{1}{z}\Big) &= w_{i,0}\Big(\frac{1+\frac{1}{z}}{1-\frac{1}{z}}\Big)^{\frac{2}{p}} = w_{i,0}\Big(\frac{1+z}{1-z}\Big)^{\frac{2}{p}} \frac{1}{(-1)^{\frac{2}{p}}} \\ &= w_i \frac{1}{(-1)^{\frac{2}{p}}} = w_{i-1}(z). \end{aligned} \tag{3.108}$$

On the other hand, the derivative is transformed as

$$\Big(\frac{\partial w_i}{i\partial\sigma}\Big)^{\frac{1}{2}} \to \Big(\frac{-4z}{p(1-z^2)} \frac{w_i}{(-1)^{\frac{2}{p}}}\Big)^{\frac{1}{2}}. \tag{3.109}$$

where we noted

$$\frac{\partial w_i}{i\partial\sigma} = w_{i,0}\frac{2}{p}\Big(\frac{1+z}{1-z}\Big) = \frac{4z w_i}{p(1-z^2)}. \tag{3.110}$$

To satisfy the usual boundary condition $K^{ij}(2\pi-\sigma,\sigma') = -iK^{i-1,j}(\sigma,\sigma')$ $(i = 1,\cdots,4)$,

we need to choose to branch cut of $\omega_{i,0}^{1/2}$ such that:

$$\left(\frac{w_{i,0}}{(-1)^{\frac{2}{p}-1}}\right)^{\frac{1}{2}} = -iw_{p-1,0}^{\frac{1}{2}}. \tag{3.111}$$

For $p = 4$, this leads to $e^{3i\pi/4}w_{i,0}^{1/2} = w_{i-1,0}^{1/2}$, which cannot be satisfied no matter how the branch cut is chosen. On the other hand, the kink boundary condition is

$$\begin{aligned} K^{ij}(2\pi - \sigma, \sigma') &= -iK^{i-1,j}(\sigma, \sigma'), \quad i = 2, 3, 4, \\ K^{ij}(2\pi - \sigma, \sigma') &= iK^{i-1,j}(\sigma, \sigma'), \quad i = 1, \end{aligned} \tag{3.112}$$

which can be satisfied by choosing $w_{1,0} = i, w_{2,0} = -1, w_{3,0} = -i, w_{4,0} = 1$ and $w_{1,0}^{1/2} = e^{i\pi/4}, w_{2,0}^{1/2} = e^{i3\pi/2}, w_{3,0}^{1/2} = e^{i3\pi/4}, w_{4,0}^{1/2} = 1$.

To summarize, from the Neumann function (3.105), we can construct the vertex state $|V_k\rangle$ obeying the kink boundary condition explicitly as a fermionic Gaussian state with the coefficient K_{rs}^{ij} in (3.107). More details and the explicit form of the matrix K_{rs}^{ij} are given in Appendix A.1.4.

Correlation measures

With the explicit forms of the vertex states $|V_u\rangle$ and $|V_k\rangle$, we are ready to calculate the correlation measures, i.e., entanglement entropy, mutual information, reflected entropy, and entanglement negativity. As the constructed vertex states are Gaussian, we can calculate these quantities numerically and efficiently [23, 63, 90, 91]. Specifically, we partition the 4 copies of the CFTs (edge states) into three parties, A, B, and the compliment of $A \cup B$. The particular partitions we consider are listed in Table 3.3. The first two partitions correspond to the case where subregions A and B are adjacent which can be directly compared with the analytical results in the previous sections, as we will discuss in details below. We set the

Partition		1	2	3
		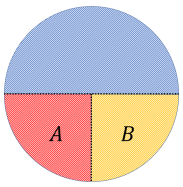	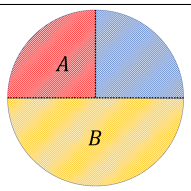	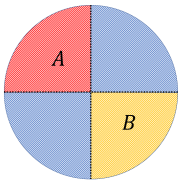
S_{AB}	(p)	41.2389	41.1811	82.2467
	(k)	41.2389	41.1811	82.2467
	(u)	41.2389	41.1811	82.2467
$I(A,B)$	(p)	41.1234	41.2389	0.1155
	(k)	41.1233	41.2389	0.1155
	(u)	41.1233	41.2389	0.1155
$S_R(A,B)$	(p)	41.2389	41.3544	0.2471
	(k)	41.2389	41.3544	0.2471
	(u)	41.2276	41.3481	0.2471
h	(p)	$0.1155(=\frac{c}{3}\ln 2)$	$0.1155(=\frac{c}{3}\ln 2)$	0.1316
	(k)	0.1155	0.1155	0.1316
	(u)	0.1043	0.1093	0.1316
$\mathcal{E}(A,B)$	(p)	30.8425	30.9292	-
	(k)	30.8185	30.9054	0.0708
	(u)	30.8191	30.9054	0.0708

Table 3.3: Three different partitions and the corresponding entanglement measures for $|V_u\rangle$ and $|V_k\rangle$ at $\beta = 0.01$. For each entanglement measure, the first row (p), second row (k) and third row (u) record predicted value, numerical result using kink boundary condition, and numerical result using usual boundary condition, respectively. Reference value: for $\beta = 0.01$, $\frac{\pi^2}{24\beta} = 41.1234$ and $\frac{\pi^2}{32\beta} = 30.8425$.

regulator (cutoff) $\beta = 0.01$ in this subsection. We also recall that the circumference is set to $L = 2\pi$.

First, for the entanglement entropy of bipartition S_{AB}, the two boundary conditions give the same result. For Partitions 1 and 2, we can also check that the numerics agrees with the prediction Eq. (3.88). Here, we note that we need to restore the extra contribution $\frac{c}{3}\ln\frac{p}{2}$ discussed in Eq. (3.82) and that the topological piece is zero, $S_{\text{topo}} = 0$, in the free fermion model,

$$S_{AB} = \frac{\pi c L}{24\beta} + \frac{c}{3}\ln\sin\frac{\pi p_{AB}}{4} + \frac{c}{3}\ln 2, \tag{3.113}$$

where $p_{AB} = 2, 3$ for Partition 1 and 2, respectively.

For Partition 3 where the region $A \cup B$ consists of two disconnected parts (A and B), the calculation in Sec. 3.3.2 does not apply since the subregion was assumed to be simply connected there. Nevertheless, recall that we observed below Eq. (3.88) the corner contribution is identical to the bipartite entanglement entropy of the ground state of (1+1)-dimensional CFT. Motivated by this, it is then tempting to compare the numerical result for Partition 3 with the entanglement entropy of the ground state of (1+1)-dimensional CFT with disjoint intervals. For the free fermion CFT, it is given by [38]

$$S_{1d} = \frac{c}{3} \ln \left[\frac{\sin|x_{21}| \sin|x_{32}| \sin|x_{43}| \sin|x_{41}|}{\sin|x_{31}| \sin|x_{42}|} \right] - \frac{2c}{3} \ln 2, \tag{3.114}$$

where the end points of the two disjoint intervals $[x_1, x_2]$ and $[x_3, x_4]$ using the cord coordinate are given by $x_1 = 0, x_2 = \pi/2, x_3 = \pi, x_4 = 3\pi/2$, and $x_{ij} := x_i - x_j$. Thus, we compare our numerics with

$$S_{AB} = 2 \left(\frac{\pi c L}{24\beta} + \frac{c}{3} \ln 2 \right) - \frac{2c}{3} \ln 2 = \frac{\pi c L}{12\beta}. \tag{3.115}$$

Here, the factor of 2 in the first term comes from doubling the number of twist operators in this case. The mutual information $I(A, B)$ can be obtained from S_{AB}. As demonstrated in Table 3.3, the numerics agrees well with Eq. (3.115).

Unlike the entanglement entropy S_{AB} and mutual information $I(A, B)$, we found that the reflected entropy and Markov gap depend on the boundary conditions. For Partitions 1 and 2, we checked that the numerical results with the kind boundary condition agree with the CFT prediction (3.93), and reproduce the Markov gap $h = \frac{c}{3} \ln 2$. For Partition 3, the usual and kink boundary conditions seem to give the same result. Once again, the CFT prediction (3.93) is not directly applicable here since region A and B are not adjacent. Nevertheless, the numerical calculation on the 1d free fermion model shows $h_{1d} = 0.1316$

(when extrapolating to $L \to \infty$), which again agrees with the above prediction.

We can also discuss logarithmic negativity $\mathcal{E}(A, B)$ for the same configurations 1,2 and 3. For the case of integer quantum Hall states, logarithmic negativity in these configurations was studied in Ref. [81]. While we do not have the corresponding CFT calculations along the line of Sec. 3.3.2 and Sec. 3.3.3, we once again borrow the corresponding one-dimensional result [92], leading to the following prediction:

$$\mathcal{E}(A, B) = \frac{\pi c L}{32\beta} + \frac{c}{4} \ln 2 + \frac{c}{4} \ln \left[\frac{\sin(\frac{p_A \pi}{p}) \sin\left(\frac{p_B \pi}{p}\right)}{\sin(\frac{(p_A + p_B)\pi}{p})} \right], \tag{3.116}$$

when region A and B are adjacent. For Partition 2, the predicted value is $\frac{\pi^2}{32\beta} = 30.8425$, which does not match perfectly with 30.8185 from numerics. Nevertheless, the difference between the negativities for Partition 1 and 2 is $\Delta\mathcal{E}(A, B) = 0.0869$, and close to the predicted value $\frac{c}{4} \ln 2 = 0.0866$.

There is a potential ambiguity in the $O(1)$ term in the one-dimensional result for logarithmic negativity due to the OPE coefficient between twist operators. Unlike the reflected entropy, where the OPE coefficient is universal, depending only on the central charge, the OPE for negativity depends on the full operator content of the theory because the replica manifold is a Riemann surface with genus growing with replica number. We have set the OPE coefficient to one by hand and have found good agreement with numerics.

3.4 Summary

We have investigated correlation measures, i.e., entanglement entropy, entanglement negativity, and reflected entropy, in the ground states of topological liquid in (2+1) dimensions, in the multipartition setting (Fig. 3.1). This was done by constructing vertex states explicitly in various configurations with or without fluxes.

In the bipartition case, we study the entanglement entropy in the NS-NS, R-R, and NS-R

sectors, and unveil a new topological contribution in the NS-R case. This contribution is due to the non-trivial configuration where a σ-anyon exits from the entanglement cut.

In the tripartition case, we find the correlation measures capture various universal characteristics of topological liquids. For example, we found that the spectrum of the partially transposed density matrix is non-trivially distributed over the complex plane. This is somewhat similar to the spectrum previously computed for (1+1)d fermionic conformal field theory and symmetry-protected topological phases. There, a non-trivial dependence of the spectrum on the spin structures was observed [73, 74]. We also found universal topological contribution to negativity and $h_{A:B}$. In the NS-NS-NS case, we verified the conjecture (3.5) for the reflected entropy, while there exists an additional contribution to $h(A, B)$ in the R-R-R sector due to the σ-anyon.

The conjecture (3.5) was further proven by developing an analytical approach. Using the conformal interface approach, we calculate the corner contribution to bipartite entanglement entropy and multipartite entanglement quantities (reflected entropy and Markov gap in particular) for generic (2+1)-dimensional topologically-ordered ground states. Some of our central results are presented in Eqs. (3.88), (3.93) and (3.94). This then supports the conjecture on the Markov gap made in the previous works by looking at examples, $h = (c/3) \ln 2$. We hope this analytical approach helps us better understand the conjecture that relates the Markov gap and gappable boundaries. It is of fundamental importance to understand this better.

CHAPTER 4

RANDOM GAUSSIAN STATE

Quantum entanglement provides insight into thermalization of isolated quantum systems or lack thereof [93, 94, 95]. In fact, entanglement entropy of typical states in quantum chaotic systems is maximal and proportional to the volume of the subsystem (i.e., volume law), resulting in thermalization and thereby validating thermodynamics and statistical physics [96, 97, 98, 99, 100, 101, 102]. Such typical quantum entanglement entropy also holds significant importance in black hole physics [14, 103]. Recently, researchers have also studied quantum entanglement of typical Gaussian states in free fermions and found a signature of thermalization [104, 105, 106, 107, 108, 17, 109, 110]. Correspondingly, the single-particle quantum chaos of free fermions has attracted growing interest [111, 112, 113, 114, 115].

An important signature of quantum chaos manifests in spectral statistics [116, 117]. It is widely believed that the spectrum of a nonintegrable quantum system exhibits random-matrix statistics [118] whereas that of an integrable system obeys Poisson statistics [119]. The universality classes of random matrices are determined solely by the fundamental tenfold symmetry classes of time reversal, charge conjugation, and chiral transformation, known as the Altland-Zirnbauer (AZ) symmetry classes [120]. As a prime example of quantum chaotic many-body systems, the Sachdev-Ye-Kitaev (SYK) model [121, 122, 123, 124] is classified by these tenfold symmetry classes and exhibits tenfold quantum chaotic behavior [125, 126, 127, 128, 129, 130, 131, 132]. Furthermore, the AZ symmetry determines the universality classes of Anderson transitions [133, 134] and topological insulators and superconductors [135, 136, 137, 138, 139]. Despite the significance of the AZ symmetry in quantum chaos and the physics of free fermions, its impact on typical quantum entanglement has remained unclear.

In this chapter, we establish the classification of typical quantum entanglement in free fermions on the basis of the tenfold fundamental symmetry classes. We show that the volume-law term of average entanglement entropy is invariant in all the classes. Conversely,

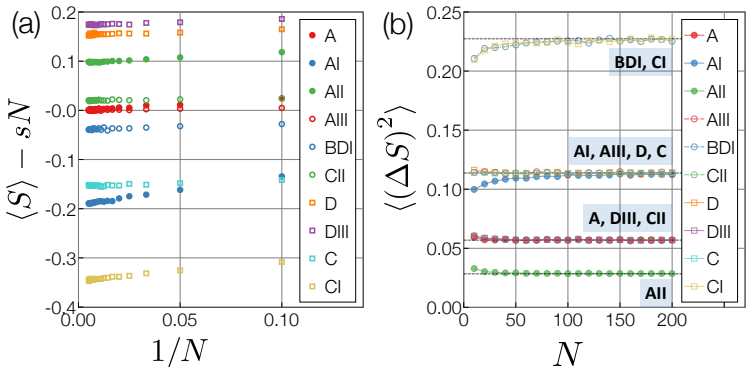

Figure 4.1: Typical entanglement entropy in the tenfold Altland-Zirnbauer symmetry classes. All the results are calculated for particle-number-conserving free fermions at half filling and for half the degrees of freedom. Each datum is averaged over 10^5 disorder realizations. (a) Average entanglement entropy $\langle S \rangle$ with respect to the volume-law term sN as functions of the inverse of the total system size N without internal degrees of freedom [$s = \log 2 - 1/2$ in the standard classes and $s = 2(\log 2 - 1/2)$ in the chiral and Bogoliubov-de Gennes (BdG) classes]. (b) Variance of entanglement entropy, $\langle (\Delta S)^2 \rangle$, as functions of N. The black dashed lines are the analytical results $\langle (\Delta S)^2 \rangle = 2(3/4 - \log 2)/\beta$ in the standard classes and $\langle (\Delta S)^2 \rangle = 4(3/4 - \log 2)/\beta$ in the chiral and BdG classes with the Dyson index $\beta = 1, 2, 4$.

we find that the constant terms of the average and variance of entanglement entropy depend on symmetry and yield tenfold universal values unique to each symmetry class (Table 4.1 and Fig. 4.1). In addition to numerical calculations, we analytically derive these tenfold universal values of typical entanglement, using random matrix theory (Weingarten calculus [140, 141, 142, 143, 144]). Our findings clarify the role of symmetry in typical quantum entanglement and quantum chaos.

4.1 Altland-Zirnbauer symmetry

We consider a generic free fermionic system

$$\hat{H} = \sum_{ij} f_i^\dagger H_{ij} f_j, \tag{4.1}$$

where f_i's ($i = 1, 2, \cdots, N$) are complex fermion operators, and H is an $N \times N$ single-particle Hamiltonian. In general, H is classified according to the fundamental internal symmetries of time reversal, charge conjugation, and chiral transformation:

$$T^{-1}H^*T = H, \quad T^*T = \pm 1, \tag{4.2}$$

$$C^{-1}H^*C = -H, \quad C^*C = \pm 1, \tag{4.3}$$

$$S^{-1}HS = -H, \quad S^2 = +1, \tag{4.4}$$

where, T, C, and S are unitary operators. Fermions include the spin (particle-hole) degree of freedom in the presence of time-reversal symmetry with sign $T^*T = -1$ (chiral or particle-hole symmetry). Time-reversal symmetry T gives the threefold Wigner-Dyson symmetry classes [145, 146], and its combination with particle-hole symmetry C and chiral symmetry S gives the tenfold AZ symmetry classes [120]. Spectral properties of Hermitian random matrices are universally determined by their symmetry [147, 148, 116], characterized by the random-matrix indices (α, β) (Table 4.1).

Depending on the symmetry classes, single-particle eigenstates are Haar-randomly chosen from different classifying spaces [149]. For clarity, we focus on half-filled many-body eigenstates and calculate entanglement entropy of a subsystem with half the size. Notably, our random free fermionic Hamiltonians are equivalent to the two-body SYK model with complex fermions [121, 122, 123, 124], whose entanglement entropy was studied in the absence of symmetry (i.e., class A) [105, 17]. Below, we demonstrate that additional symmetry changes the constant terms of the average and variance of entanglement entropy and yields tenfold universal values unique to each symmetry class. The AZ symmetry classification does not include unitary symmetry that commutes with Hamiltonians, the effect of which can be studied in subspaces of fixed conserved charge [109, 150]. By contrast, the AZ symmetries cannot be captured in such a manner.

Table 4.1: Tenfold classification of typical entanglement entropy based on the Altland-Zirnbauer (AZ) symmetry classes. The AZ symmetry classes consist of time-reversal symmetry (TRS), particle-hole symmetry (PHS), and chiral symmetry (CS). For TRS and PHS, the entries "± 1" mean the presence of symmetry and its sign, and the entries "0" mean the absence of symmetry. For CS, the entries "1" and "0" mean the presence and absence of symmetry, respectively. Each class is characterized by the classifying space and the random-matrix indices (α, β). The constant terms of the average $\langle S_0 \rangle$ and variance $\langle (\Delta S)^2 \rangle$ of entanglement entropy are shown with $\sigma_0^2 := 3/4 - \log 2$. All the results of entanglement entropy are calculated for particle-number-conserving free fermions with the half bipartition and half filling. For Bogoliubov-de Gennes Hamiltonians that do not conserve the particle number, the average is one-half and the variance is one-quarter in each symmetry class.

AZ class	TRS	PHS	CS		Classifying space	β	α	$\langle S_0 \rangle$	$\langle (\Delta S)^2 \rangle$
A	0	0	0	$\mathcal{C}_0$	$\mathrm{U}(2N)/\mathrm{U}(N) \times \mathrm{U}(N)$	2	N/A	0	σ_0^2
AIII	0	0	1	$\mathcal{C}_1$	$\mathrm{U}(N)$	2	1	0	$2\sigma_0^2$
AI	+1	0	0	$\mathcal{R}_0$	$\mathrm{O}(2N)/\mathrm{O}(N) \times \mathrm{O}(N)$	1	N/A	$-(\log 2 - 1/2)$	$2\sigma_0^2$
BDI	+1	+1	1	$\mathcal{R}_1$	$\mathrm{O}(N)$	1	0	$-((3/2)\log 2 - 1)$	$4\sigma_0^2$
D	0	+1	0	$\mathcal{R}_2$	$\mathrm{O}(2N)/\mathrm{U}(N)$	2	0	$(1 - \log 2)/2$	$2\sigma_0^2$
DIII	−1	+1	1	$\mathcal{R}_3$	$\mathrm{U}(2N)/\mathrm{Sp}(N)$	4	1	$(\log 2)/4$	σ_0^2
AII	−1	0	0	$\mathcal{R}_4$	$\mathrm{Sp}(2N)/\mathrm{Sp}(N) \times \mathrm{Sp}(N)$	4	N/A	$(\log 2 - 1/2)/2$	$\sigma_0^2/2$
CII	−1	−1	1	$\mathcal{R}_5$	$\mathrm{Sp}(N)$	4	3	$((3/2)\log 2 - 1)/2$	σ_0^2
C	0	−1	0	$\mathcal{R}_6$	$\mathrm{Sp}(N)/\mathrm{U}(N)$	2	2	$-(1 - \log 2)/2$	$2\sigma_0^2$
CI	+1	−1	1	$\mathcal{R}_7$	$\mathrm{U}(N)/\mathrm{O}(N)$	1	1	$-(\log 2)/2$	$4\sigma_0^2$

Table 4.2: Tenfold classification of typical quantum entanglement based on the Altland-Zirnbauer (AZ) symmetry classes. The AZ symmetry classes consist of time-reversal symmetry (TRS), particle-hole symmetry (PHS), and chiral symmetry (CS). For TRS and PHS, the entries "± 1" mean the presence of symmetry and its sign, and the entries "0" mean the absence of symmetry. For CS, the entries "1" and "0" mean the presence and absence of symmetry, respectively. The ten AZ classes are divided into two complex classes that only involve unitary symmetry (i.e., CS) and the eight real classes that involve antiunitary symmetry (i.e., TRS and PHS). Each class is characterized by the classifying space and the random-matrix indices (α, β). The numerical fitting results of the average entanglement entropy by $\langle S \rangle = S_1 N + S_0 + S_{-1}/N$, as well as those of the variance of entanglement entropy by $\langle (\Delta S)^2 \rangle = \sigma_0^2 + \sigma_-^2/N$, are shown [$S_1 = \log 2 - 1/2$ for the standard classes (classes A, AI, and AII) and $S_1 = 2(\log 2 - 1/2)$ for the chiral classes (classes AIII, BDI, and CII) and Bogoliubov-de Gennes classes (classes D, DIII, C, and CI)]. All the results of entanglement entropy are calculated for particle-number-conserving free fermions with the half bipartition and the half filling.

AZ class	TRS	PHS	CS		Classifying space	β	α	S_0	S_{-1}	σ_0^2	σ_{-1}^2
A	0	0	0	$\mathcal{C}_0$	$\mathrm{U}(2N)/\mathrm{U}(N) \times \mathrm{U}(N)$	2	N/A	2×10^{-5}	0.245	0.057	0.023
AIII	0	0	1	$\mathcal{C}_1$	$\mathrm{U}(N)$	2	1	-1×10^{-4}	0.056	0.114	0.0082
AI	+1	0	0	$\mathcal{R}_0$	$\mathrm{O}(2N)/\mathrm{O}(N) \times \mathrm{O}(N)$	1	N/A	−0.192	0.587	0.113	−0.142
BDI	+1	+1	1	$\mathcal{R}_1$	$\mathrm{O}(N)$	1	0	−0.0392	0.118	0.227	−0.168
D	0	+1	0	$\mathcal{R}_2$	$\mathrm{O}(2N)/\mathrm{U}(N)$	2	0	0.154	0.107	0.113	0.028
DIII	−1	+1	1	$\mathcal{R}_3$	$\mathrm{U}(2N)/\mathrm{Sp}(N)$	4	1	0.173	0.123	0.057	0.037
AII	−1	0	0	$\mathcal{R}_4$	$\mathrm{Sp}(2N)/\mathrm{Sp}(N) \times \mathrm{Sp}(N)$	4	N/A	0.0964	0.219	0.028	0.044
CII	−1	−1	1	$\mathcal{R}_5$	$\mathrm{Sp}(N)$	4	3	0.0198	0.045	0.057	0.039
C	0	−1	0	$\mathcal{R}_6$	$\mathrm{Sp}(N)/\mathrm{U}(N)$	2	2	−0.154	0.118	0.114	0.0027
CI	+1	−1	1	$\mathcal{R}_7$	$\mathrm{U}(N)/\mathrm{O}(N)$	1	1	−0.346	0.389	0.227	−0.177

4.2 Symmetry classification of typical entanglement entropy

In this section, we summarize the results of the tenfold symmetry classification of typical entanglement entropy. We explicit write down the ensemble of eigenvectors for each symmetry class, which is the starting point of numerical evaluation (Sec. 4.2) as well as analytical calculation (Sec. 4.3). The numerical results in this section demonstrate the volume law term in typical entanglement entropy is universal for all symmetry classes; in contrast, the constant term encodes the symmetry classes, which can be positive or negative. Furthermore, the variance in entanglement entropy depends universally on time-reversal symmetry index β. The analytical derivation will be outlined in the next section.

4.2.1 Standard (Wigner-Dyson) class (classes A, AI, and AII)

In the standard (Wigner-Dyson) class (classes A, AI, and AII), Hamiltonians are only concerned with time-reversal symmetry. In the many-body Hilbert (Fock) space, time-reversal symmetry is described by the antiunitary operation defined by

$$\hat{\mathcal{T}}\hat{c}_m\hat{\mathcal{T}}^{-1} = \sum_n T_{mn}\hat{c}_n, \quad \forall\, z \in \mathbb{C} \quad \hat{\mathcal{T}} z \hat{\mathcal{T}}^{-1} = z^*. \tag{4.5}$$

Here, $\hat{\mathcal{T}}$ is an antiunitary operator that acts on the many-body fermionic Fock space while $T = (T_{mn})_{m,n}$ is a unitary matrix in the single-particle Hilbert space. A system respects time-reversal invariance if the Hamiltonian $\hat{H}$ satisfies

$$\hat{\mathcal{T}}\hat{H}\hat{\mathcal{T}}^{-1} = \hat{H}. \tag{4.6}$$

In fact, if this relation is satisfied, we have $\hat{\mathcal{T}}\hat{O}(t)\,\hat{\mathcal{T}}^{-1} = \hat{O}(-t)$, where $\hat{O}(t) = e^{\mathrm{i}\hat{H}t}\hat{O}e^{-\mathrm{i}\hat{H}t}$ is the time-evolved operator of an arbitrary operator $\hat{O}$. In terms of the single-particle

Hamiltonian H, time-reversal invariance is equivalent to

$$T^{-1}H^{*}T = H. \tag{4.7}$$

Because of antiunitarity of time-reversal symmetry, the symmetry operators are required to satisfy

$$\hat{\mathcal{T}}^{2} = (\pm 1)^{\hat{N}}, \quad T^{*}T = \pm 1 \tag{4.8}$$

with the number operator $\hat{N} \coloneqq \sum_{n} \hat{c}_{n}^{\dagger}\hat{c}_{n}$. Then, the standard (Wigner-Dyson) classes—classes A, AI, and AII—are defined as follows:

- In the absence of time-reversal symmetry (and any other internal symmetry), Hamiltonians are defined to belong to the unitary class (class A).
- In the presence of time-reversal symmetry with the sign $T^{*}T = +1$, Hamiltonians are defined to belong to the orthogonal class (class AI).
- In the presence of time-reversal symmetry with the sign $T^{*}T = -1$, Hamiltonians are defined to belong to the symplectic class (class AII). An important feature of symplectic time-reversal symmetry is the Kramers degeneracy.

In the following, suppose the total system size is N, the subsystem size is N_A, and the particle number is M for classes A and AI. For class AII, on the other hand, the degree of freedom is double because of the Kramers degeneracy; the total system size is $2N$, the subsystem size is $2N_A$, and the particle number is $2M$. Importantly, depending on time-reversal symmetry, generic single-particle Hamiltonians H are diagonalized by the matrix U that belongs to the unitary group $\mathrm{U}(N)$, the orthogonal group $\mathrm{O}(N)$, and symplectic group

$\mathrm{Sp}\,(N)$:

$$U \in \begin{cases} \mathrm{U}\,(N) & (\text{class A})\,; \\ \mathrm{O}\,(N) & (\text{class AI})\,; \\ \mathrm{Sp}\,(N) & (\text{class AII})\,. \end{cases} \tag{4.9}$$

These groups are called classifying spaces and characterize each symmetry class.

Using the eigenstate matrix U introduced above, we calculate entanglement entropy [23, 25]. The truncated correlation matrix is given as

$$C_A = V^\dagger V, \tag{4.10}$$

where V is an $M \times N_A$ matrix satisfying

$$U = \begin{pmatrix} V & V' \\ W & W' \end{pmatrix}^T . \tag{4.11}$$

The entanglement entropy is obtained as

$$S = -\sum_i \left[\lambda_i \log \lambda_i + (1-\lambda_i) \log (1-\lambda_i)\right], \tag{4.12}$$

where λ_i's ($i = 1, 2, \cdots, N_A$) are the eigenvalues of C_A. In class AII, V is a $2M \times 2N_A$ matrix, and the number of eigenvalues of C_A is $2N_A$. The spectrum of the correlation matrix C_A is two-fold degenerate because of time-reversal symmetry with the sign -1, and we calculate the entanglement entropy only from half of the entanglement spectrum.

To obtain the typical entanglement entropy for the standard classes, we numerically calculate the entanglement entropy for U Haar-randomly distributed in the classifying spaces in Eq. (4.9). In Ref. [17], the average and variance of such typical entanglement entropy

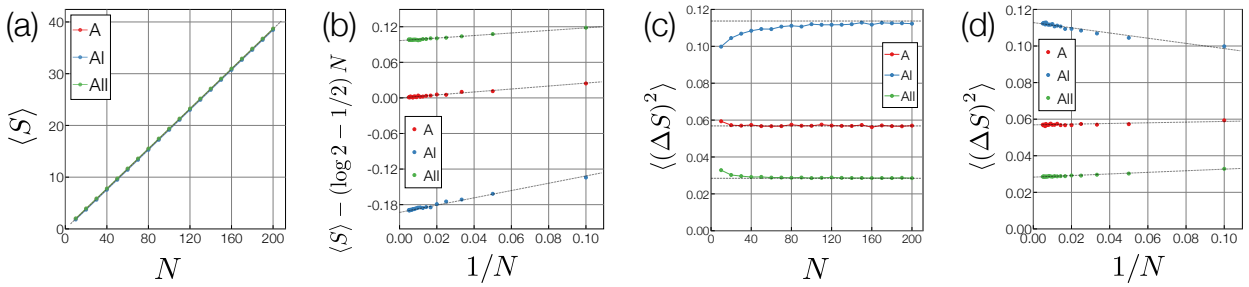

Figure 4.2: Typical quantum entanglement entropy in the standard (Wigner-Dyson) classes with the half bipartition and half filling for classes A (red dots), AI (blue dots), and AII (green dots). Each datum is averaged over 10^5 ensembles. (a) Average $\langle S \rangle$ of entanglement entropy as functions of the system size N. The black dashed line is the analytical result $\langle S \rangle \simeq (\log 2 - 1/2)\, N$. (b) Deviation of $\langle S \rangle$ from the volume-law term $(\log 2 - 1/2)\, N$ as functions of $1/N$. (c) Variance $\langle (\Delta S)^2 \rangle$ of entanglement entropy as functions of N. The black dashed lines are the analytical results $\langle (\Delta S)^2 \rangle = 2\,(3/4 - \log 2)\,/\beta$ with the Dyson index $\beta = 1$ (class AI), $\beta = 2$ (class A), and $\beta = 4$ (class AII). (d) Variance $\langle (\Delta S)^2 \rangle$ as functions of $1/N$.

without symmetry (i.e., class A) were analytically derived as

$$\langle S \rangle = \left(\log 2 - \frac{1}{2} \right) N + \frac{1}{4N} + O\left(1/N^3\right) = (0.193147 \cdots)\, N + \frac{1}{4N} + O\left(1/N^3\right), \tag{4.13}$$

$$\langle (\Delta S)^2 \rangle = \frac{3}{4} - \log 2 + o\,(1) = 0.0568528 \cdots + o\,(1) \tag{4.14}$$

for the half bipartition and the half filling. However, no analytical or numerical results have yet to be obtained in the presence of time-reversal symmetry (i.e., classes AI and AII). Below, we numerically calculate the average and variance of typical entanglement entropy and show that the $O\,(1)$ constant terms of the average and the variance crucially depend on time-reversal symmetry. In Sec. 4.3, we derive these results analytically.

As shown in Fig. 4.2 (a), the average $\langle S \rangle$ of entanglement entropy grows almost linearly with respect to the system size N for all the three symmetry classes. It is also consistent with the analytical result for class A in Eq. (4.13). Then, we fit the numerical results by

[Fig. 4.2 (b)]

$$\langle S \rangle = \left(\log 2 - \frac{1}{2} \right) N + S_0 + \frac{S_{-1}}{N} + o\left(1/N\right). \tag{4.15}$$

The fitting results for all the three symmetry classes are summarized in Table 4.2. The tiny $O\left(1\right)$ term $S_0 \simeq 2 \times 10^{-5}$ and $O\left(1/N\right)$ term $S_{-1} \simeq 0.245$ for class A are compatible with the analytical result in Eq. (4.13). In contrast to class A, the $O\left(1\right)$ constant terms are present in classes AI and AII. They are negative for class AI and positive for class AII. On the basis of $\log 2 - 1/2 = 0.193147\cdots$, the average entanglement is supposed to be

$$\langle S \rangle = \left(\log 2 - \frac{1}{2} \right) \left(N + 1 - \frac{2}{\beta} \right) + o\left(1\right) \tag{4.16}$$

with the Dyson index $\beta = 1$ (class AI), $\beta = 2$ (class A), and $\beta = 4$ (class AII). We analytically demonstrate this result in Sec. 4.3. Notably, this result implies that one particle is effectively removed in class AI and one half of particle is added in class AII in comparison with class A.

Figure 4.2 (c) shows the variance $\langle (\Delta S)^2 \rangle$ of entanglement entropy for the three symmetry classes. Clearly, each symmetry class is characterized by the different values of $\langle (\Delta S)^2 \rangle$; in comparison with class A, $\langle (\Delta S)^2 \rangle$ increases in class AI and decreases in class AII. In general, level repulsion of random matrices is suppressed (enhanced) in class AI (AII), which is also compatible with the larger (smaller) value of $\langle (\Delta S)^2 \rangle$ in class AI (AII) [147, 148, 116]. We fit the numerical results of $\langle (\Delta S)^2 \rangle$ by [Fig. 4.2 (d)]

$$\langle (\Delta S)^2 \rangle = \sigma_0^2 + \frac{\sigma_{-1}^2}{N} + o\left(1/N\right), \tag{4.17}$$

which are summarized in Table 4.2. Here, the numerically obtained variance $\sigma_0^2 \simeq 0.057$ in class A is compatible with the analytical result in Eq. (4.14). The variance σ_0^2 in class AI is

almost twice larger than that in class A while that in class AII is almost half of that in class A. These numerical results are

$$\langle (\Delta S)^2 \rangle = \frac{2}{\beta} \left(\frac{3}{4} - \log 2 \right) + o\left(1\right) \tag{4.18}$$

with the Dyson index $\beta = 1$ (class AI), $\beta = 2$ (class A), and $\beta = 4$ (class AII). This behavior of the variance of entanglement entropy reminds us of the universal conductance fluctuations, which are one of the important applications of random matrix theory in condensed matter physics [151, 133]. In fact, in the diffusive regime of mesoscopic wires, the variance of conductance universally behaves as $\propto 1/\beta$, similar to the variance of entanglement entropy in our work.

4.2.2 Chiral class (classes AIII, BDI, and CII)

In the chiral classes (classes AIII, BDI, and CII), Hamiltonians are concerned with chiral symmetry. In the many-body Fock space, chiral symmetry (or equivalently, sublattice symmetry) is defined by the antiunitary operation defined by

$$\hat{\mathcal{S}} \hat{c}_m \hat{\mathcal{S}}^{-1} = \sum_n S_{mn} \hat{c}_n^\dagger, \tag{4.19}$$

where $\hat{\mathcal{S}}$ is an antiunitary operator on the many-body fermionic Fock space, and $S = (S_{mn})_{m,n}$ is a unitary matrix on the single-particle Hilbert space. In contrast to time-reversal symmetry, this operation mixes fermion annihilation and creation operators. In the simultaneous presence of time-reversal symmetry and particle-hole symmetry, chiral symmetry appears as a combination of the two symmetries. Even in the absence of time-reversal symmetry and particle-hole symmetry, chiral symmetry can be respected, for example, in bipartite hopping models. The system respects chiral symmetry if the many-body Hamiltonian

satisfies

$$\hat{\mathcal{S}}\hat{H}\hat{\mathcal{S}}^{-1} = \hat{H}, \tag{4.20}$$

which leads to Tr $H = 0$ and

$$S^{-1}HS = -H. \tag{4.21}$$

The matrix S can be chosen to be Hermitian and satisfy $S^2 = 1$ without loss of generality. In the presence of chiral symmetry, single-particle eigenenergies appear in opposite-sign pairs $(E, -E)$, and zero-energy modes are subject to a special constraint. According to the combination of chiral symmetry and time-reversal symmetry, the chiral classes—classes AIII, BDI, and CII—are defined as follows:

- In the absence of time-reversal symmetry, chiral-symmetric Hamiltonians are defined to belong to the chiral unitary class (class AIII).
- In the presence of time-reversal symmetry with the sign $T^*T = +1$, chiral-symmetric Hamiltonians are defined to belong to the chiral orthogonal class (class BDI).
- In the presence of time-reversal symmetry with the sign $T^*T = -1$, chiral-symmetric Hamiltonians are defined to belong to the chiral symplectic class (class CII). Because of symplectic time-reversal symmetry, Hamiltonians in class CII generally exhibit the Kramers degeneracy.

In classes BDI and CII, time-reversal symmetry is imposed so that it will commute with chiral symmetry.

We obtain the typical quantum entanglement entropy in the chiral classes. Suppose the total system size is $2N$ $(4N)$, the subsystem size is N_A $(2N_A)$, and the particle number is

M ($2M$) in classes AIII and BDI (class CII). Here, N denotes the number of the unit cell. Because of chiral symmetry, the single-particle Hamiltonian can be expressed as

$$H = \begin{pmatrix} 0 & h \\ h^\dagger & 0 \end{pmatrix}, \tag{4.22}$$

where h is an $N \times N$ ($2N \times 2N$) matrix in classes AIII and BDI (class CII). In this representation, the chiral-symmetry operator is chosen as $S = \sigma_z \otimes I_{N(2N)}$, where $I_{N(2N)}$ is the $N \times N$ ($2N \times 2N$) identity matrix. In the following, we assume the absence of zero modes. The same assumption was imposed also in Refs. [105, 107, 17] for Bogoliubov-de Gennes (BdG) Hamiltonians in class D. We are interested only in the entanglement properties of eigenstates; we can flatten the spectrum of the Hamiltonian to ± 1 and deform the matrix h so that it will be unitary. Depending on additional time-reversal symmetry, the matrix h belongs to the unitary group $\mathrm{U}(N)$, orthogonal group $\mathrm{O}(N)$, and symplectic group $\mathrm{Sp}(N)$:

$$h \in \begin{cases} \mathrm{U}(N) & (\text{class AIII}); \\ \mathrm{O}(N) & (\text{class BDI}); \\ \mathrm{Sp}(N) & (\text{class CII}). \end{cases} \tag{4.23}$$

These groups give the classifying spaces in the chiral classes and characterize eigenstates and their entanglement (Table 4.2).

A generic normalized single-particle eigenstates of H in Eq. (4.22) is given as

$$|u_i\rangle = \frac{1}{\sqrt{2}} \begin{pmatrix} |n_i\rangle \\ \epsilon h^\dagger |n_i\rangle \end{pmatrix}, \tag{4.24}$$

where $\epsilon \in \{\pm 1\}$ is the flattened single-particle eigenenergy (i.e., $H|u_i\rangle = \epsilon |u_i\rangle$), and $|n_i\rangle$ is the N-dimensional ($2N$-dimensional) orthonormal basis in classes AIII and BDI (class CII)

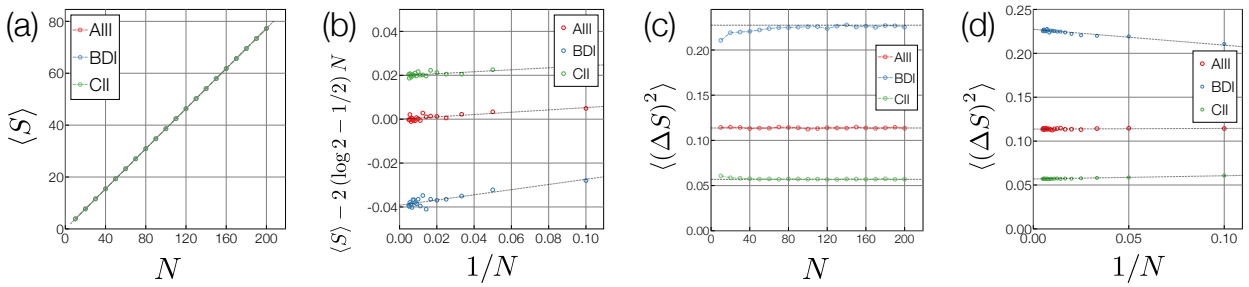

Figure 4.3: Typical quantum entanglement entropy in the chiral classes with the half bipartition and half filling for classes AIII (red dots), BDI (blue dots), and CII (green dots). Each datum is averaged over 10^5 ensembles. (a) Average $\langle S \rangle$ of entanglement entropy as functions of the system size N. The black dashed line is the analytical result $\langle S \rangle \simeq 2(\log 2 - 1/2) N$. (b) Deviation of $\langle S \rangle$ from the volume-law term $2(\log 2 - 1/2) N$ as functions of $1/N$. (c) Variance $\langle (\Delta S)^2 \rangle$ of entanglement entropy as functions of N. The black dashed lines are the analytical results $\langle (\Delta S)^2 \rangle = 4(3/4 - \log 2)/\beta$ with the Dyson index $\beta = 1$ (class BDI), $\beta = 2$ (class AIII), and $\beta = 4$ (class CII). (d) Variance $\langle (\Delta S)^2 \rangle$ as functions of $1/N$.

that satisfies $|n_i\rangle_j = \delta_{ij}$. Then, the $2N \times 2N$ ($4N \times 4N$) unitary matrix U collecting all the $2N$ ($4N$) eigenstates in classes AIII and BDI (class CII) is given as

$$U = \frac{1}{\sqrt{2}} \begin{pmatrix} I_{N(2N)} & I_{N(2N)} \\ h^\dagger & -h^\dagger \end{pmatrix}. \tag{4.25}$$

From this eigenstate matrix U, the truncated correlation matrix C_A is given as Eq. (4.10), and the entanglement entropy is obtained as Eq. (4.12). Because of chiral symmetry, the eigenvalues of C_A come in $(\lambda, 1-\lambda)$ pairs. We numerically calculate the average and variance of entanglement entropy in the chiral classes by Haar-randomly choosing h in each classifying space in Eq. (4.23). Here, we focus on the half-filled many-body eigenstates constructed from all the single-particle eigenstates with negative eigenenergies. Similarly to class AII, the spectrum of the correlation matrix C_A is two-fold degenerate in class CII, and we calculate the entanglement entropy only from half of the entanglement spectrum.

In a similar manner to the standard classes, the average $\langle S \rangle$ of entanglement entropy grows almost linearly with respect to the system size N for all the three symmetry classes

[Fig. 4.3 (a)]. Then, we fit the numerical results by [Fig. 4.3 (b)]

$$\langle S\rangle = 2\left(\log 2 - \frac{1}{2}\right) N + S_0 + \frac{S_{-1}}{N} + o\left(1/N\right). \tag{4.26}$$

We note that the total number of sites is chosen to be $2N$ in the chiral classes. The fitting results for all the three symmetry classes are summarized in Table 4.2. In class AIII, the $O\left(1\right)$ term $S_0 \simeq -1 \times 10^{-4}$ is tiny, similar to class A. On the other hand, the $O\left(1/N\right)$ term $S_1 \simeq 0.056$ in class AIII is much smaller than that in class A. Time-reversal symmetry with the sign $+1$ gives rise to the negative $O\left(1\right)$ term $S_0 \simeq -0.039$ in class BDI while time-reversal symmetry with the sign -1 gives rise to the positive $O\left(1\right)$ term $S_0 \simeq 0.020$ in class CII, both of which are much smaller than the $O\left(1\right)$ terms in classes AI and AII. In Sec. 4.3, we analytically show

$$\langle S\rangle = 2\left(\log 2 - \frac{1}{2}\right) N + \left(1 - \frac{2}{\beta}\right)\left(\frac{3}{2}\log 2 - 1\right) + o\left(1\right) \tag{4.27}$$

with the Dyson index $\beta = 1$ (class BDI), $\beta = 2$ (class AIII), and $\beta = 4$ (class CII), which are consistent with the numerical results.

Figure 4.3 (c) shows the variance $\langle(\Delta S)^2\rangle$ of entanglement entropy for the chiral classes. Each symmetry class is characterized by the different values of $\langle(\Delta S)^2\rangle$. In comparison with class AIII, $\langle(\Delta S)^2\rangle$ increases in class BDI and decreases in class CII, which is similar to the standard classes. We fit the numerical results of $\langle(\Delta S)^2\rangle$ by Eq. (4.17), as summarized in Fig. 4.3 (d) and Table 4.2. Notably, these numerical results are

$$\langle(\Delta S)^2\rangle = \frac{4}{\beta}\left(\frac{3}{4} - \log 2\right) + o\left(1\right) \tag{4.28}$$

with the Dyson index $\beta = 1$ (class BDI), $\beta = 2$ (class AIII), and $\beta = 4$ (class CII). This is twice larger than the variance in the standard classes [i.e., Eq. (4.18)].

4.2.3 Bogoliubov-de Gennes (BdG) class (classes D, DIII, C, and CI)

The BdG classes (classes, D, C, DIII, and CI) are concerned with particle-hole symmetry. Particle-hole symmetry (or equivalently, charge-conjugation symmetry) is described by the unitary operation defined by

$$\hat{\mathcal{C}}\hat{c}_m\hat{\mathcal{C}}^{-1} = \sum_n C^*_{mn}\hat{c}^\dagger_n, \tag{4.29}$$

where $\hat{\mathcal{C}}$ and $C = (C_{mn})_{m,n}$ are unitary many-body operators and single-particle matrices, respectively. It describes the transformation between particles and holes, and flips the sign of the electron charge with respect to the charge neutral point $\hat{\mathcal{C}}\hat{Q}\hat{\mathcal{C}}^{-1} = -\hat{Q}$ with $\hat{Q} \coloneqq \hat{N} - N/2$. The many-body Hamiltonian is particle-hole symmetric if it satisfies

$$\hat{\mathcal{C}}\hat{H}\hat{\mathcal{C}}^{-1} = \hat{H}, \tag{4.30}$$

which leads to Tr $H = 0$ and

$$C^{-1}H^TC = -H. \tag{4.31}$$

Thus, particle-hole symmetry acts as unitary symmetry on the many-body fermionic Fock space but acts as antiunitary symmetry on the single-particle Hilbert space. Similarly to time-reversal symmetry, the symmetry operator and matrix are required to satisfy

$$\hat{\mathcal{C}}^2 = (\pm 1)^{\hat{N}}, \quad C^*C = \pm 1. \tag{4.32}$$

In the presence of particle-hole symmetry, single-particle eigenenergies appear in opposite-sign pairs $(E, -E)$, and zero-energy modes are subject to a special constraint. According to the combination of particle-hole symmetry and time-reversal symmetry, the BdG classes—

classes D, C, DIII, and CI—are defined as follows:

- In the sole presence of particle-hole symmetry with the sign $C^*C = +1$, particle-hole-symmetric Hamiltonians are defined to belong to class D. In the additional presence of time-reversal symmetry with the sign $T^*T = -1$, Hamiltonians are defined to belong to class DIII.

- In the sole presence of particle-hole symmetry with the sign $C^*C = -1$, particle-hole-symmetric Hamiltonians are defined to belong to class C. In the additional presence of time-reversal symmetry with the sign $T^*T = +1$, Hamiltonians are defined to belong to class CI.

In classes DIII and CI, the combination of time-reversal symmetry and particle-hole symmetry gives rise to chiral symmetry, which anticommutes with time-reversal symmetry and particle-hole symmetry.

We obtain the typical quantum entanglement entropy in the BdG classes. Similarly to the chiral classes, we assume the absence of zero modes and flatten the spectrum to be $\{\pm 1\}$. First, $2N \times 2N$ single-particle Hamiltonians H in class D respect particle-hole symmetry

$$H^* = -H, \tag{4.33}$$

where the particle-hole-symmetry operator is chosen as $C = I_{2N}$. If we define A by $H =: \mathrm{i}A$, A is a real antisymmetric matrix. Then, we diagonalize A with a proper basis as

$$A = O \begin{pmatrix} 0 & I_N \\ -I_N & 0 \end{pmatrix} O^{-1}, \tag{4.34}$$

where O is a $2N \times 2N$ orthogonal matrix

$$O \in \mathrm{O}(2N). \tag{4.35}$$

This orthogonal matrix O contains all information about single-particle eigenstates, and the orthogonal group $O \in \mathrm{O}(2N)$ gives the classifying space in class D (Table 4.2). In fact, from this orthogonal matrix O, a generic normalized eigenstate of H is given as

$$|u_i\rangle = \frac{O}{\sqrt{2}} \begin{pmatrix} |n_i\rangle \\ -\mathrm{i}\epsilon\,|n_i\rangle \end{pmatrix}, \tag{4.36}$$

where $\epsilon \in \{\pm 1\}$ is the flattened eigenenergy (i.e., $H\,|u_i\rangle = \epsilon\,|u_i\rangle$), and $|n_i\rangle$ is the N-dimensional orthonormal basis that satisfies $|n_i\rangle_j = \delta_{ij}$. Then, the $2N \times 2N$ unitary matrix U collecting all the $2N$ eigenstates is given as

$$U = \frac{O}{\sqrt{2}} \begin{pmatrix} I_N & I_N \\ -\mathrm{i} \times I_N & \mathrm{i} \times I_N \end{pmatrix}, \tag{4.37}$$

where I_N is the $N \times N$ identify matrix. From this unitary matrix U, the truncated correlation matrix C_A is given as Eq. (4.10), and the entanglement entropy is obtained as Eq. (4.12). Because of particle-hole symmetry, the eigenvalues of C_A come in $(\lambda, 1-\lambda)$ pairs. We numerically calculate the average and variance of entanglement entropy in class D by Haar-randomly choosing O in the classifying space in Eq. (4.35). Similarly to the chiral classes, we focus on the half-filled many-body eigenstates constructed from all the single-particle eigenstates with negative eigenenergies.

Next, $2N \times 2N$ single-particle Hamiltonians H in class C respect particle-hole symmetry

$$\sigma_y H^* \sigma_y = -H, \tag{4.38}$$

where the particle-hole-symmetry operator is chosen as $C = \sigma_y \otimes I_N$. If we define A by $H =: \mathrm{i}A$, A satisfies $A^\dagger = -A$ and $\sigma_y A^* \sigma_y = A$. Then, we diagonalize A with a proper basis

as

$$A = U \begin{pmatrix} 0 & I_N \\ -I_N & 0 \end{pmatrix} U^{-1}, \tag{4.39}$$

where U is a $2N \times 2N$ symplectic matrix

$$U \in \mathrm{Sp}\,(N)\,. \tag{4.40}$$

Using this symplectic matrix U instead of the orthogonal matrix O in Eq. (4.35), we obtain entanglement entropy in a similar manner to class D.

In class DIII, chiral symmetry is present as a combination of time-reversal symmetry and particle-hole symmetry. Owing to chiral symmetry, $4N \times 4N$ single-particle Hamiltonians in class DIII are generally written as Eq. (4.22) with $h \in \mathrm{U}\,(2N)$, where the chiral-symmetry operator is chosen as $S \coloneqq \sigma_z \otimes I_{2N}$. In addition, we choose the time-reversal-symmetry operator as $T = \sigma_x \otimes \mathrm{i}\sigma_y \otimes I_N$. Then, time-reversal symmetry $T^{-1}H^*T = H$ imposes

$$\left(\sigma_y \otimes I_N\right) h^T \left(\sigma_y \otimes I_N\right) = h, \tag{4.41}$$

leading to the general representation

$$h = f^T \left(\sigma_y \otimes I_N\right) f \left(\sigma_y \otimes I_N\right), \quad f \in \mathrm{U}\,(2N)\,. \tag{4.42}$$

Thus, $f \in \mathrm{U}\,(2N)$ contains all information about the single-particle eigenstates, and the unitary group $\mathrm{U}\,(2N)$ gives the classifying space in class DIII (Table 4.2). In other words, h belongs to the circular symplectic ensemble. Similarly to classes AII and CII, the spectrum of the correlation matrix C_A is two-fold degenerate in class DIII, and we calculate the entanglement entropy only from half of the entanglement spectrum.

In class CI, $2N \times 2N$ single-particle Hamiltonians also respect chiral symmetry and are generally written as Eq. (4.22) with $h \in \mathrm{U}(N)$, where the chiral-symmetry operator is chosen as $S \coloneqq \sigma_z \otimes I_N$. Then, we choose the time-reversal-symmetry operator as $T = \sigma_x \otimes I_N$. Time-reversal symmetry imposes

$$h^T = h, \tag{4.43}$$

leading to the general representation

$$h = f^T f, \quad f \in \mathrm{U}(N). \tag{4.44}$$

Using this general representation of h, we calculate entanglement entropy in a similar manner to class DIII. Here, h belongs to the circular orthogonal ensemble.

In passing, we note that the random matrices in Eqs. (4.35), (4.40), (4.42), and (4.44) have gauge ambiguity. For example, in class D, the orthogonal matrix O in Eq. (4.35) obeys the gauge transformation

$$O \to O\tilde{O}, \quad \text{s.t.} \quad \tilde{O} \begin{pmatrix} 0 & I_N \\ -I_N & 0 \end{pmatrix} \tilde{O}^{-1} = \begin{pmatrix} 0 & I_N \\ -I_N & 0 \end{pmatrix}, \quad \tilde{O} \in \mathrm{O}(2N). \tag{4.45}$$

If we introduce a matrix G that rotates $\sigma_z \otimes I_N$ to $\sigma_y \otimes I_N$, i.e.,

$$\sigma_y \otimes I_N = G\left(\sigma_z \otimes I_N\right) G^{-1}, \quad G \coloneqq \frac{1}{\sqrt{2}} \begin{pmatrix} I_N & -\mathrm{i} \times I_N \\ \mathrm{i} \times I_N & I_N \end{pmatrix}, \tag{4.46}$$

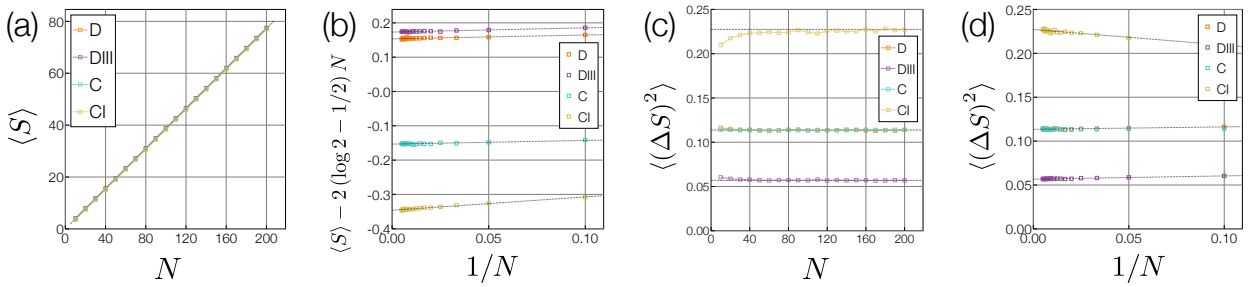

Figure 4.4: Typical quantum entanglement entropy in the Bogoliubov-de Gennes (BdG) classes with the half bipartition and half filling for classes D (orange dots), DIII (purple dots), C (light-blue dots), and CI (yellow dots). Each datum is averaged over 10^5 ensembles. (a) Average $\langle S \rangle$ of entanglement entropy as functions of the system size N. The black dashed line is the analytical result $\langle S \rangle \simeq 2(\log 2 - 1/2) N$. (b) Deviation of $\langle S \rangle$ from the volume-law term $2(\log 2 - 1/2) N$ as functions of $1/N$. (c) Variance $\langle (\Delta S)^2 \rangle$ of entanglement entropy as functions of N. The black dashed lines are the analytical results $\langle (\Delta S)^2 \rangle = 4(3/4 - \log 2)/\beta$ with the Dyson index $\beta = 1$ (class CI), $\beta = 2$ (classes D and C), and $\beta = 4$ (class DIII). (d) Variance $\langle (\Delta S)^2 \rangle$ as functions of $1/N$.

the above gauge transformation reduces to

$$(G^{-1}\tilde{O}G)\begin{pmatrix} I_N & 0 \\ 0 & -I_N \end{pmatrix}(G^{-1}\tilde{O}G)^{-1} = \begin{pmatrix} I_N & 0 \\ 0 & -I_N \end{pmatrix}, \quad \tilde{O} \in \mathrm{O}(2N). \tag{4.47}$$

Hence, the allowed gauge transformation is generally given by

$$\tilde{O} = G\begin{pmatrix} W_n & 0 \\ 0 & W_n^* \end{pmatrix} G^{-1}, \quad W_n \in \mathrm{U}(N). \tag{4.48}$$

Thus, O in Eq. (4.34) belongs to $\mathrm{O}(2N)/\mathrm{U}(N)$, which precisely gives the classifying space in class D. Such gauge ambiguity is also summarized in Table 4.2 for all the symmetry classes. In our calculations of typical quantum entanglement entropy, the gauge ambiguity of the classifying spaces is irrelevant, although it is relevant, for example, to Anderson localization [134] and topological insulators and superconductors [139].

From the above representations, we calculate the average and variance of entanglement entropy in the BdG classes (classes D, DIII, C, and CI), as summarized in Fig. 4.4. Similarly

to the other symmetry classes, the average $\langle S \rangle$ of entanglement entropy grows almost linearly with respect to the system size N for all the four symmetry classes [Fig. 4.4 (a)]. Then, we fit the numerical results by Eq. (4.26) [Fig. 4.4 (b)]. The fitting results for all the four symmetry classes are summarized in Table 4.2. The $O(1)$ term of $\langle S \rangle$ in class D is positive, and that in class C is negative, both of which have almost the same absolute value. In Sec. 4.3, we analytically show

$$\langle S \rangle = 2 \left(\log 2 - \frac{1}{2} \right) N + \frac{1}{2} (1 - \alpha) (1 - \log 2) + o(1) \tag{4.49}$$

with the index $\alpha = 0$ (class D) and $\alpha = 2$ (class C) [120, 116]. On the other hand, the $O(1)$ term of $\langle S \rangle$ in class CI is twice larger than that in class DIII, the signs of which are opposite to each other. This behavior is similar to the average entanglement in classes AI and AII, as well as that in classes BDI and CII. In Sec. 4.3, we analytically show

$$\langle S \rangle = 2 \left(\log 2 - \frac{1}{2} \right) N + \frac{1}{2} \left(1 - \frac{2}{\beta} \right) \log 2 + o(1) \tag{4.50}$$

with the Dyson index $\beta = 1$ (class CI) and $\beta = 4$ (class DIII), which are consistent with the numerical results.

Figure 4.4 (c) shows the variance $\langle (\Delta S)^2 \rangle$ of entanglement entropy for the BdG classes. The variance $\langle (\Delta S)^2 \rangle$ of entanglement entropy coincides with each other in classes D and C, and $\langle (\Delta S)^2 \rangle$ in classes DIII and CI is twice larger and smaller than that, respectively. We fit the numerical results of $\langle (\Delta S)^2 \rangle$ by Eq. (4.17), as summarized in Fig. 4.4 (d) and Table 4.2. Notably, these numerical results follow Eq. (4.28) with the Dyson index $\beta = 1$ (class CI), $\beta = 2$ (classes D and C), and $\beta = 4$ (class DIII). This is twice larger than the variances in the standard classes [i.e., Eq. (4.18)] and the same as those in the chiral classes.

4.3 Analytical derivation

Now, we analytically derive the typical entanglement entropy results in the last section. The derivation is performed by resolvent method and Weingarten calculas for symmetric groups. We review the resolvent method in Sec. 4.3.1 and give an example of class AI in Sec. 4.3.2. Due to the length limitation, we refer the interested readers to Ref. [152] for complete results of ten symmetry classes.

4.3.1 Resolvent method

Let us first review the basic ingredients of the resolvent method, which is a powerful method to compute the spectral density from the moments. As described in Sec. 2.1.4, in free fermions, entanglement entropy is computed by the truncated correlation matrix C_A supported on a subregion A. Let $D(\lambda) \coloneqq \sum_i \delta(\lambda - \lambda_i)$ be the spectral density of C_A and $\langle D(\lambda) \rangle$ be its ensemble average. The average entanglement entropy of the subregion A is

$$\langle S \rangle = \int_0^1 d\lambda \left[-\lambda \log \lambda - (1-\lambda) \log(1-\lambda) \right] \langle D(\lambda) \rangle. \tag{4.51}$$

To obtain the spectral density, we introduce the resolvent $R(z)$ of C_A by

$$R(z) \coloneqq \mathrm{Tr} \left(\frac{I}{zI - C_A} \right) \tag{4.52}$$

for $z \in \mathbb{C}$ and the identify matrix I. The spectral density $D(\lambda)$ is obtained from the resolvent $R(z)$ by

$$D(\lambda) \coloneqq \sum_i \delta(\lambda - \lambda_i) = -\frac{1}{\pi} \mathrm{Im} \lim_{\varepsilon \to 0^+} \mathrm{Tr} \left(\frac{I}{(\lambda + \mathrm{i}\varepsilon) I - C_A} \right) = -\frac{1}{\pi} \mathrm{Im} \lim_{\varepsilon \to 0^+} R(\lambda + \mathrm{i}\varepsilon), \tag{4.53}$$

where we use $\lim_{\varepsilon\to 0^+} 1/(x+\mathrm{i}\varepsilon) = \mathcal{P}(1/x) - \mathrm{i}\pi\delta(x)$ for $x \in \mathbb{R}$. To evaluate the resolvent, let us expand it at $z \to \infty$ by

$$R(z) = \mathrm{Tr}\left(\frac{I}{z}\right) + \sum_{n=1}^{\infty} \frac{\mathrm{Tr}\, C_A^n}{z^{n+1}}. \tag{4.54}$$

Thus, for random free fermions, the trace of moments of the truncated correlation matrix, $\mathrm{Tr}\, C_A^n$, allows us to obtain the spectral density of C_A and consequently the average entanglement entropy.

4.3.2 An example: class AI

In this section, we take the class AI as a nontrivial example to illustrate the techniques to compute the typical entanglement entropy. The evaluation is performed by resolvent method and Weingarten calculus for orthogonal group.

Recall that in class AI, Hamiltonians respect time-reversal symmetry with the sign $T^*T = +1$ and are diagonalized by matrices O that belong to the orthogonal group $\mathrm{O}(N)$. Therefore, the trace of moments is expressed by the submatrix V of the orthogonal matrix O:

$$\begin{aligned}
&\langle \mathrm{Tr}\, C_A^n \rangle = \langle \mathrm{Tr}\,(V^\dagger V)^n \rangle \\
&= \sum_{i_k=1}^{N/2} \int dO O_{i_2 i_1} O_{i_2 i_3} O_{i_4 i_3} O_{i_4 i_5} \cdots O_{i_{2n} i_{2n-1}} O_{i_{2n} i_1} \\
&= \sum_{\{i_k, i'_k, j_k, j'_k\}=1}^{N/2} \int dO O_{i_1 j_1} \cdots O_{i_n j_n} O_{i'_1 j'_1} \cdots O_{i'_n j'_n} \delta_{i'_1 i_1} \cdots \delta_{i'_n i_n} \delta_{j'_2 j_1} \cdots \delta_{j'_n j_{n-1}} \delta_{j'_1 j_n} \\
&= \sum_{\{i_k, j_k\}=1}^{N/2} \int dO O_{i_1 j_1} \cdots O_{i_n j_n} O_{i_{n+1} j_{n+1}} \cdots O_{i_{2n} j_{2n}} \\
&\qquad \cdot \delta_{i_{n+1} i_1} \cdots \delta_{i_{2n} i_n} \delta_{j_{n+2} j_1} \cdots \delta_{j_{2n} j_{n-1}} \delta_{j_{n+1} j_n}.
\end{aligned} \tag{4.55}$$

To perform the integral (average) over the $N \times N$ random orthogonal matrix O, the average is evaluated by the Weingarten formula for the orthogonal group [143]. Let M_{2n} be the set of all pair partitions on $\{1, 2, \cdots 2n\}$. Each pair partition $\sigma \in M_{2n}$ is uniquely expressed by

$$\{\{\sigma(1), \sigma(2)\}, \{\sigma(3), \sigma(4)\}, \cdots \{\sigma(2n-1), \sigma(2n)\}\}, \tag{4.56}$$

with $\sigma(2i-1) < \sigma(2i)$ for $1 \leq i \leq n$ and with $\sigma(1) < \sigma(3) < \cdots < \sigma(2n-1)$. As a simple example for $n = 2$, the set M_4 consists of three elements $\sigma_1 = \{\{1, 2\}, \{3, 4\}\}$, $\sigma_2 = \{\{1, 3\}, \{2, 4\}\}$, $\sigma_3 = \{\{1, 4\}, \{2, 3\}\}$. Now, the Weingarten formula for the orthogonal group is expressed by the summation over elements σ, τ in the set of pair partitions M_{2n}:

$$\int dO O_{i_1 j_1} \cdots O_{i_{2n} j_{2n}} = \sum_{\sigma, \tau \in M_{2n}} \mathrm{Wg}^{\mathrm{O}}(N; \sigma, \tau) \prod_{k=1}^{n} \delta_{i_{\sigma(2k-1)} i_{\sigma(2k)}} \delta_{j_{\tau(2k-1)} j_{\tau(2k)}}. \tag{4.57}$$

Here, $\mathrm{Wg}^{\mathrm{O}}(N; \sigma, \tau)$ is the Weingarten function for the orthogonal group, which is an element of the Weingarten matrix.

By definition, the Weingarten matrix is the pseudo-inverse matrix of the Gram matrix, which is determined by the graph constructed from σ and τ. For example, for $n = 2$, one can derive from the definition

$$\mathrm{Wg}^{\mathrm{O}}(N; \sigma_i, \sigma_j) = \begin{cases} \dfrac{N+1}{N(N+2)(N-1)} & (i = j)\,; \\ -\dfrac{1}{N(N+2)(N-1)} & (i \neq j)\,, \end{cases} \tag{4.58}$$

with $i, j = 1, 2, 3$. An immediate observation is that for the large-N expansion of the Weingarten function $\mathrm{Wg}^{\mathrm{O}}(N; \sigma_i, \sigma_j)$, the leading term and the subleading term differ by $1/N$, rather than $1/N^2$ in the large-N expansion of Wg^{U}. This suggests the appearance of $O(1)$ term in typical entanglement entropy for class AI, as shown below. In practice, the

Weingarten function for the orthogonal group is evaluated by the zonal spherical functions of the Gelfand pair; see, for example, Ref. [142] for the explicit expressions up to $n = 6$.

From the Weingarten formula and Eq. (4.55), the trace of moments of C_A reduces to

$$\langle \mathrm{Tr}\, C_A^n \rangle = \sum_{\sigma,\tau \in M_{2n}} \mathrm{Wg}^{\mathrm{O}}(N;\sigma,\tau) \left[\sum_{\{i_k\}=1}^{N/2} \prod_{k=1}^{n} \delta_{i_k i_{n+k}} \prod_{k=1}^{n} \delta_{i_{\sigma(2k-1)} i_{\sigma(2k)}} \right] \left[\sum_{\{j_k\}=1}^{N/2} \prod_{k=1}^{n} \delta_{j_k j_{n+1+(k \bmod n)}} \prod_{k=1}^{n} \delta_{j_{\tau(2k-1)} j_{\tau(2k)}} \right]. \tag{4.59}$$

The terms in the square brackets can be evaluated graphically. For the first square bracket, given $\sigma \in M_{2n}$, one can define a graph consisting of vertices $\{1, 2, \cdots 2n\}$ and the edge set consisting of $(k, n+k)$ and $(\sigma(2k-1), \sigma(2k))$. Namely, each delta function is regarded as an edge. Let us denote $L(\sigma, 0)$ as the number of loops in this graph, and the first square bracket takes the value $(N/2)^{L(\sigma,0)}$. Similar treatment can be applied to the second square bracket, where the edge set consists of $(k, n+1+(k \bmod n))$ and $(\tau(2k-1), \tau(2k))$, and we denote the number of loops as $L(\tau, 1)$. These graphical evaluations lead to

$$\langle \mathrm{Tr}\, C_A^n \rangle = \sum_{\sigma,\tau \in M_{2n}} \mathrm{Wg}^{\mathrm{O}}(N;\sigma,\tau) \left(\frac{N}{2}\right)^{L(\sigma,0)} \left(\frac{N}{2}\right)^{L(\tau,1)}. \tag{4.60}$$

From the explicit forms of Wg^{O}, we obtain $\langle \mathrm{Tr}\, C_A^n \rangle$; we list $\langle \mathrm{Tr}\, C_A^n \rangle$ below for $n = 1, 2, \cdots, 5$ up to $O(1)$:

n	1	2	3	4	5
$\langle \mathrm{Tr}\, C_A^n \rangle$	$\frac{1}{4}N$	$\frac{3}{16}N + \frac{1}{16}$	$\frac{5}{32}N + \frac{3}{32}$	$\frac{35}{256}N + \frac{29}{256}$	$\frac{63}{512}N + \frac{65}{512}$

(4.61)

Based on these values, we conjecture the closed-form formula:

$$\langle \mathrm{Tr}\, C_A^n \rangle = \frac{1}{2^{2n}} \binom{2n-1}{n} N + \frac{1}{4} - \frac{1}{2^{2n}} \binom{2n-1}{n} + O(N^{-1}) \qquad (n \geq 1). \tag{4.62}$$

Then, the average resolvent for C_A in class AI is

$$\langle R(z)\rangle = \frac{N}{2z} + \sum_{n=1}^{\infty} \frac{\langle \mathrm{Tr}\, C_A^n\rangle}{z^{n+1}} = \frac{N}{2\sqrt{z(z-1)}} + \frac{1}{4}\left(\frac{1}{z} + \frac{1}{z-1}\right) - \frac{1}{2\sqrt{z(z-1)}} + O(N^{-1}), \tag{4.63}$$

and the corresponding spectral density of C_A is

$$\langle D(\lambda)\rangle = \frac{N-1}{2\pi\sqrt{\lambda(1-\lambda)}} 1_{[0,1]} + \frac{1}{4}\delta(\lambda) + \frac{1}{4}\delta(\lambda-1) + O(N^{-1}). \tag{4.64}$$

As a consistency check, one can verify $\int_0^1 d\lambda \langle D(\lambda)\rangle = N/2$, which is the number of filled particles. The two delta functions $\delta(\lambda), \delta(\lambda-1)$ do not contribute to the entanglement entropy but are needed to ensure $\int_0^1 d\lambda \langle D(\lambda)\rangle = N/2$. Finally, the average entanglement entropy is

$$\langle S\rangle = \int_0^1 d\lambda \left[-\lambda\log\lambda - (1-\lambda)\log(1-\lambda)\right] \langle D(\lambda)\rangle = \left(\log 2 - \frac{1}{2}\right)(N-1) + O(N^{-1}). \tag{4.65}$$

Indeed, the Weingarten function for the orthogonal group leads to the $O(1)$ term in the average entanglement entropy

$$S_0 = -(\log 2 - \frac{1}{2}), \tag{4.66}$$

which effectively removes one fermion. For details on the evaluation to all ten symmetry classes, we refer the readers to [152].

4.3.3 Spectral density

We presented the result of spectral density of class AI in Eq. (4.64). More generally, from the aforementioned Weingarten calculus in the standard classes, we obtain

$$\langle D(\lambda)\rangle = \frac{N+1-2/\beta}{2\pi\sqrt{\lambda(1-\lambda)}} 1_{[0,1]} + O(1/N), \tag{4.67}$$

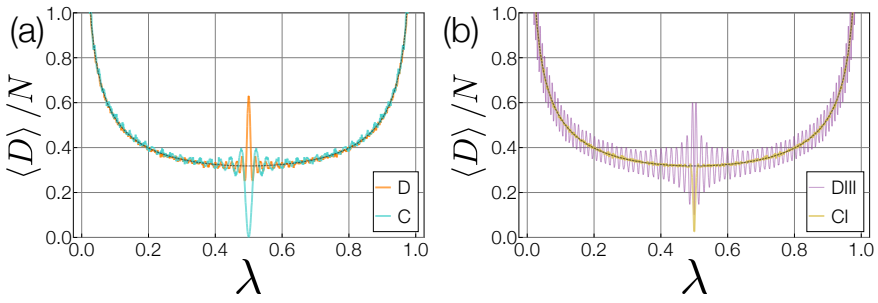

Figure 4.5: Average density of the single-particle entanglement spectrum for the quadratic Sachdev-Ye-Kitaev model enriched by symmetry, or equivalently, random Bogoliubov-de Gennes Hamiltonians in (a) classes D (orange curve), C (blue curve), (b) DIII (purple curve), and CI (yellow curve). Each datum is averaged over 10^5 disorder realizations for $N = 100$. The black dashed curves are the volume-law term $\langle D \rangle / N = 1/2\pi\sqrt{\lambda(1-\lambda)}$. The singular peaks or dips appear at $\lambda = 1/2$, consistent with the analytical results $(1 - \alpha/2 - 1/\beta)\,\delta(\lambda - 1/2)$.

which leads to Eq. (4.16). The overall difference in the entanglement spectrum, which originates from the different Weingarten functions for $\mathrm{U}(N)$, $\mathrm{O}(N)$, and $\mathrm{Sp}(N)$, results in the different constant terms of the typical entanglement entropy in Eq. (4.16).

In the chiral and BdG classes, by contrast, an additional delta function appears at the center $\lambda = 1/2$ of the entanglement spectrum. In the chiral classes, we have

$$\langle D(\lambda) \rangle = \frac{N + 1 - 2/\beta}{\pi\sqrt{\lambda(1-\lambda)}} 1_{[0,1]} - \frac{1}{2}\left(1 - \frac{2}{\beta}\right)\delta\left(\lambda - \frac{1}{2}\right) + O(1/N)\,. \tag{4.68}$$

Similarly, $\langle D(\lambda) \rangle$ includes $(1 - \alpha/2 - 1/\beta)\,\delta(\lambda - 1/2)$ in the BdG classes. These additional delta functions also contribute to the constant terms of the average entanglement entropy, leading to Eqs. (4.27), (4.49), and (4.50), similarly to the topological contribution [153, 154, 155, 156, 157, 158]. Notably, the two types of constant terms originate from different origins and behave in a different manner. In fact, while the density of states is generally less universal than the higher-order correlation functions (e.g., level-spacing statistics), that around the chiral-symmetric or particle-hole-symmetric point is known to be universal [120, 116]. Consequently, the delta functions at the center of the entanglement spectrum should be more universal than the other constant contributions.

We also numerically calculate the average density $\langle D(\lambda)\rangle$ of the single-particle entanglement spectrum for the quadratic SYK model with Majorana fermions (Fig. 4.5). The delta-function peaks or dips are resolved for finite N, their smooth signatures appearing at the center $\lambda = 1/2$ of the entanglement spectrum, consistent with the analytical results for infinite $N \to \infty$. Different symmetry leads to distinctive behavior at $\lambda = 1/2$, characterizing symmetry-enriched quantum chaos of the SYK model.

4.4 Summary

In this chapter, we developed the symmetry classification of typical quantum entanglement in free fermions. We demonstrated that while the volume-law term of average entanglement entropy is unaffected by symmetry, the constant terms of the average and variance of entanglement entropy yield the tenfold universal values unique to each symmetry class. Importantly, typical quantum entanglement underlies thermalization of isolated quantum systems and validates thermodynamics and statistical physics [93, 94, 95]. Our findings should be useful in understanding the role of symmetry in quantum chaos and thermalization. Furthermore, additional topology can make a constant contribution to entanglement entropy [153, 154, 155, 156, 157, 158]. It merits further study to investigate typical entanglement in topological insulators and superconductors in different AZ symmetry classes, as well as that subject to Anderson transitions [134].

CHAPTER 5

CRITICAL SPIN CHAIN

Universality is one of the most prominent features of phase transitions [159]. Near a continuous phase transition, physics at low energies is determined by the universal data. In 1+1 dimensions, a continuous phase transition is usually described by a conformal field theory (CFT) [160]. As reviewed in Sec. 2.2, A CFT is completely determined by the conformal data, which consists of a set of primary operators ϕ_α with scaling dimensions Δ_α and conformal spins s_α, the operator product expansion coefficients $C_{\alpha\beta\gamma}$ and the central charge c [161, 162].

Given a quantum critical spin chain, it is both important and challenging to compute the universal data. One approach, initiated by Cardy, Affleck and others in the 80's [163, 164, 165], is based on the operator-state correspondence. In this approach, one starts with the low-energy eigenstate $|\phi_\alpha\rangle$ of the critical quantum spin chain with periodic boundary conditions (PBC). Once the Hamiltonian is properly normalized, the scaling dimensions Δ_α and conformal spins s_α are given by the energies E_α and momenta p_α of the states. In order to compute the OPE coefficients, one has to first identify lattice operators that correspond to CFT primary operators [166, 167], which is in general hard to do without prior knowledge of the CFT.

To overcome this difficulty more recently, it has been proposed in Refs. [168, 169] that the OPE coefficients can be numerically extracted with the eigenstates alone. The key is to start with three normalized eigenstates $|\phi_\alpha\rangle$, $|\phi_\beta\rangle$, $|\phi_\gamma\rangle$ of the critical quantum spin chain with PBC and sizes N_1, N_2 and $N_3 = N_1 + N_2$, respectively. It is then shown that the wavefunction overlap

$$A_{\alpha\beta\gamma} = \langle\phi_\gamma|\phi_\alpha\phi_\beta\rangle \tag{5.1}$$

is related to the OPE coefficient $C_{\alpha\beta\gamma}$. This provides a numerically feasible way to extract the OPE coefficients by computing the wavefunction overlaps. In passing, we note that wavefunction overlaps of this type have also been investigated in integrable models [170, 171]. Our focus in this paper will be generic lattice quantum many-body systems at criticality without relying on integrability.

However, two important problems remain unsolved in Ref. [169]. Firstly, the paper only considered the case where $N_1 = N_2$. It remains a question if OPE coefficients can still be extracted when the sizes are not equal. Secondly and more importantly, the relation between wavefunction overlap $A_{\alpha\beta\gamma}$ and the OPE coefficient $C_{\alpha\beta\gamma}$ is only expected to hold in the thermodynamic limit. At finite sizes, the finite-size corrections to $A_{\alpha\beta\gamma}$ may be large. Unlike the finite-size corrections to the energies E_α, whose exponents are determined by the scaling dimensions of irrelevant operators of the CFT through standard conformal perturbation theory [172], an understanding of finite-size corrections to $A_{\alpha\beta\gamma}$ is still missing. This makes it hard to extrapolate the finite-size data to the thermodynamic limit.

In this chapter, we solve these two problems. First, using a generalized conformal map from three-sided cylinder to the complex plane which appeared in the string field theory literature [173, 174, 175], we establish a relation between wavefunction overlaps $A_{\alpha\beta\gamma}$ and OPE coefficients $C_{\alpha\beta\gamma}$ for general sizes. Second, we show that the exponents in the finite-size correction to $A_{\alpha\beta\gamma}$ are universal by mapping the wavefunction overlaps to three-point correlation functions of the cyclic orbifold of the original CFT. The exponents are determined by the operator content and fusion rules of the cyclic orbifold, which are in turn determined by the original CFT. The result also implies similar universal finite-size corrections in Renyi entropies of CFT, as observed in Ref. [176]. As a benchmark, we examine the finite-size corrections to $A_{\alpha\beta\gamma}$ for the Ising and XXZ spin chain. All numerical data agrees with the theoretical predictions in high precision.

Our result enables us to compute the conformal data from $A_{\alpha\beta\gamma}$ in a systematic way,

with a proper estimation of finite-size corrections. For example, when $N_1 = N_2 = N$, the overlap $\langle \phi_\gamma | \mathbb{1}\mathbb{1} \rangle$ scales as

$$A_{\mathbb{1}\mathbb{1}\gamma} = O(N^{-\frac{c}{8}-\frac{\Delta_\gamma}{2}}), \tag{5.2}$$

where $|\mathbb{1}\rangle$ is the ground state. The exponent gives the central charge and scaling dimensions without proper normalization of the lattice Hamiltonian. Another example is that if the CFT has a spin-1 conserved current J and its conjugate J^*, then

$$\frac{A_{JJ^*\mathbb{1}}}{A_{\mathbb{1}\mathbb{1}\mathbb{1}}} = \frac{1}{16} + O(N^{-2}). \tag{5.3}$$

As an application, we compute the overlaps in a recently proposed Haagerup model [177, 178], which is conjectured to have $c = 2$ and a spin-1 current J. Our numerical result, however, indicates that the CFT has $c \approx 2.1$ and that the proposed operator J cannot be a conserved current that saturates the unitarity bound $\Delta_J \geq 1$. Rather, our numerical result supports that the operator is a spin-1 primary operator close to the unitarity bound, with an upper bound of the scaling dimension $\Delta_J \leq 1.4$.

Our work is both of interest from numerical and theoretical perspectives. Numerically, we provide a simple method to compute the conformal data based solely on the low-energy wavefunctions. Compared with the prior work, our method does not rely on input such as identification of lattice operators with CFT operators, symmetry of the model or correct normalization of the Hamiltonian, which makes it practical to explore a less-known CFT. Theoretically, we show that the wavefunction overlaps encode the information of the corresponding cyclic orbifold CFT. It is therefore interesting to investigate how to relate other orbifold CFT data with measurable quantities in the original CFT model. Furthermore, as noted in Ref. [169], the overlaps considered here can be regarded as wavefunctions of a toy three-sided wormhole in holography [179]. Thus it may be desirable to find a holographic interpretation of our results.

The rest of the paper is structured as follows. In Sec. 5.1 we review the operator-state correspondence and derive the relation between wavefunction overlaps $A_{\alpha\beta\gamma}$ and the OPE coefficients $C_{\alpha\beta\gamma}$. In Sec. 5.2 we review the cyclic orbifold CFT and relate its operator content to the exponents in the universal finite-size corrections to $A_{\alpha\beta\gamma}$. As a corollary, we also derive finite-size corrections to the second Renyi entropy of CFT. In Sec. 5.3 we compute $A_{\alpha\beta\gamma}$ for the Ising and XXZ model and verify that the finite-size corrections all match the analytical predictions with good accuracy. In Sec. 5.4 we apply our method to the Haagerup model and extract part of the conformal data. Finally, we discuss possible applications and extensions of the present work.

5.1 Operator fusion from Wavefunction overlaps

In this section we derive the relation between wavefunction overlaps and OPE coefficients of the CFT. We first represent the wavefunction overlaps as path integral on a three-sided cylinder. Then we use a conformal transformation to map the path integral to a three-point correlation function on the complex plane. Our derivation generalizes that of Ref. [169] in that we do not restrict two sides of the cylinder to have the same size.

5.1.1 CFT on a cylinder

Consider a CFT on a Euclidean cylinder with circumference L. The compact dimension represents the space with coordinate $x \in [0, L)$, and the non-compact dimension represents the imaginary time with coordinate $\tau \in (-\infty, \infty)$. It is convenient to use the complex coordinates, denoted as $z = \tau + ix$ and $\bar{z} = \tau - ix$. The Hilbert space is supported on the equal-time slices. A CFT is composed of a set of local scaling operators that are covariant under global rescaling of the spacetime, where the eigenvalue is the scaling dimension. The scaling operators are organized into conformal towers. For each tower, there is a primary operator ϕ_α with the lowest scaling dimension Δ_α, and other descendant operators (later

abbreviated as des.) with scaling dimensions that differ Δ_α by integers.

A crucial property of the CFT is the operator-state correspondence, which states that each scaling operator corresponds to a state on the cylinder. The energies of the states are related to the scaling dimensions by

$$E_\alpha = \frac{2\pi}{L}\left(\Delta_\alpha - \frac{c}{12}\right), \tag{5.4}$$

where c is the central charge of the CFT. For a unitary CFT, the ground state $|\mathbb{1}\rangle$ corresponds to the identity operator $\mathbb{1}$ with scaling dimension $\Delta_{\mathbb{1}} = 0$. Other states can be created by acting with the scaling operator on the ground state at infinity,

$$|\phi_\alpha\rangle = \phi_\alpha(-\infty)|\mathbb{1}\rangle. \tag{5.5}$$

$$\langle\phi_\alpha| = \langle\mathbb{1}|\phi_\alpha^*(+\infty), \tag{5.6}$$

where

$$\phi_\alpha(\pm\infty) \equiv \left(\frac{2\pi}{L}\right)^{-\Delta_\alpha} \lim_{\tau\to\pm\infty} e^{\pm\frac{2\pi}{L}\Delta_\alpha\tau}\phi_\alpha(\tau, 0), \tag{5.7}$$

is a shorthand notation and ϕ_α^* is the conjugation of ϕ_α. In many cases the primary operator is self-conjugate and we will not distinguish the two. The states form an orthonormal basis,

$$\langle\phi_\alpha|\phi_\beta\rangle = \delta_{\alpha\beta}. \tag{5.8}$$

Given three primary operators $\phi_\alpha, \phi_\beta, \phi_\gamma$, the three-point correlation function is determined by the operator product expansion (OPE), where the only independent coefficient is given by

$$C_{\alpha\beta\gamma} = \left(\frac{2\pi}{L}\right)^{-\Delta_\alpha} \langle\phi_\gamma|\phi_\alpha(0)|\phi_\beta\rangle. \tag{5.9}$$

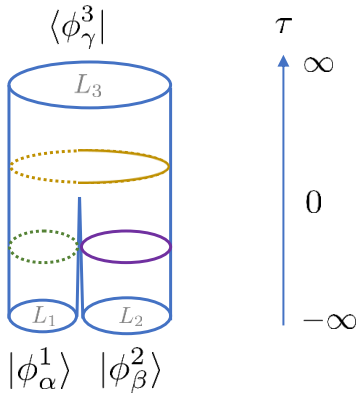

Figure 5.1: The path integral for the wavefunction overlap $A_{\alpha\beta\gamma} = \langle\phi^3_\gamma|\phi^1_\alpha\phi^2_\beta\rangle$. The geometry is a three-sided cylinder Σ with circumference $L_1 + L_2 = L_3$.

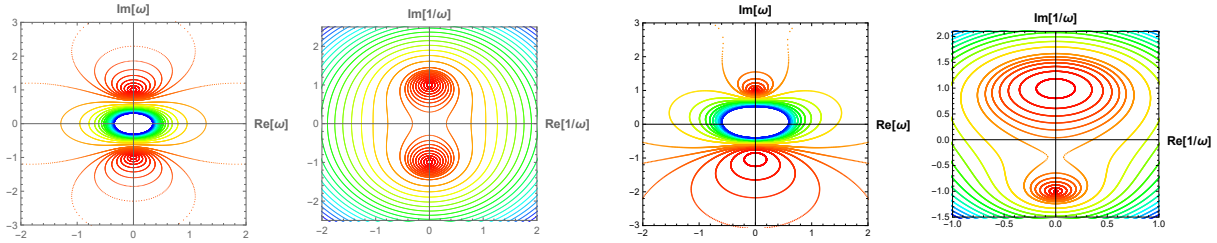

Figure 5.2: Illustration of the conformal transformations that map three-sided cylinder to the complex plane. (a) Left two figures: Eq. (5.15) for the case of $L_1 = L_2$ and (b) right two figures: Eq. (5.17), for the case of $L_2 = 2L_1$. Colored lines represent equal time slices with equal real part of z. Darker color corresponds to larger τ. Red lines correspond to equal time slices on cylinders 1 and 2, and the blue lines correspond to equal time slices on cylinder 3. For better illustration purposes we show both w and $1/w$ for the two conformal transformations.

Other correlation functions, including those of descendant operators, are completely determined by the OPE coefficients of primary operators. If $C_{\alpha\beta\gamma} \neq 0$, there is a fusion channel $\phi_\alpha \times \phi_\beta \to \phi_\gamma$, and we denote it by $\mathcal{N}_{\alpha,\beta,\gamma} \neq 0$. Otherwise, the fusion channel is said to be forbidden, and $\mathcal{N}_{\alpha,\beta,\gamma} = 0$. In all cases considered in this work, $\mathcal{N}_{\alpha,\beta,\gamma}$ is either 0 or 1, depending on whether the fusion channel is forbidden or allowed.

5.1.2 Path integral for wavefunction overlaps

Let us consider three cylinders with circumference L_1,L_2 and L_3 with $L_1+L_2=L_3$. On each cylinder a primary operator is inserted at infinity to create a state. Then the wavefunction overlaps can be represented by a path integral on the three-sided cylinder Σ with three insertions

$$\begin{aligned} A_{\alpha\beta\gamma} =& \langle \phi^3_\gamma | \phi^1_\alpha \phi^2_\beta \rangle \\ =& \int_\Sigma D\Phi\, \phi^1_\alpha(-\infty)\phi^2_\beta(-\infty)\phi^{3*}_\gamma(+\infty) e^{-S_{\mathrm{CFT}}[\Phi]}, \end{aligned} \tag{5.10}$$

where $D\Phi$ is the functional measure and S_{CFT} is the action of the CFT,

$$S_{\mathrm{CFT}}[\Phi] = \int_\Sigma d\tau dx\, \mathcal{L}_{\mathrm{CFT}}[\Phi], \tag{5.11}$$

where $\mathcal{L}_{\mathrm{CFT}}[\Phi]$ is the Lagrangian density. An illustration of the three-sided cylinder is shown in Fig. 5.1. The partition function is the path integral with no insertions, thus

$$\int_\Sigma D\Phi\, e^{-S_{\mathrm{CFT}}[\Phi]} = \langle \mathbb{1}^3 | \mathbb{1}^1 \mathbb{1}^2 \rangle. \tag{5.12}$$

Taking the ratio gives

$$\frac{\langle \phi^3_\gamma | \phi^1_\alpha \phi^2_\beta \rangle}{\langle \mathbb{1}^3 | \mathbb{1}^1 \mathbb{1}^2 \rangle} = \langle \phi^1_\alpha(-\infty)\phi^2_\beta(-\infty)\phi^{3*}_\gamma(+\infty) \rangle_\Sigma \tag{5.13}$$

Note that the three cylinders meet at $z_0 = iL_1$ on the $\tau = 0$ time slice.

Next, we use a conformal transformation $w(z)$ to map Σ to the complex plane $\mathbb{C}$. Inspired by the string field theory literature [173, 174], the conformal map is defined implicitly by

$$\begin{aligned} & z + \lambda = \\ & \frac{1}{2\pi}[L_1 \log(w - w_1) + L_2 \log(w - w_2) - L_3 \log(w - w_3)], \end{aligned} \tag{5.14}$$

where w_1, w_2 and w_3 are arbitrary complex numbers and λ depends on the w's. The role of λ will be evident shortly. It is clear that the conformal transformation maps the three infinity points to w_1, w_2 and w_3, respectively. One example considered in Ref. [169] is when $L_3 = 2L_1 = 2L_2 = L$, $w_1 = i, w_2 = -i, w_3 = 0$ and $\lambda = 0$, where the conformal transformation simplifies to an explicit form

$$w = \frac{1}{\sqrt{e^{4\pi z/L} - 1}}. \tag{5.15}$$

There is a second-order algebraic branch point at $z_0 = 0$ where the three cylinders meet. This is illustrated in Fig. 5.2 (a). For general choices of parameters, the conformal transformation $w(z)$ is hard to express explicitly. However, the conformal transformation still possesses a second-order algebraic branch point, which can be shifted to $z_0 = 0$ by tuning λ. Let $w(z_0) = w_0$, then the branch-point condition demands that

$$\frac{dz}{dw}(w_0) = 0. \tag{5.16}$$

Solving the equation gives w_0. Substituting w_0 back to $w(z_0) = w_0$ then fixes λ. For example, if we choose $L_2 = 2L_1 = 2L/3$ and $w_1 = i, w_2 = -i, w_3 = 0$, then $w_0 = 3i$ and $\lambda = (L \log(32/27))/(6\pi)$. The conformal transformation then becomes

$$\frac{32}{27} \cdot e^{\frac{6\pi z}{L}} = \frac{(w-i)(w+i)^2}{w^3}, \tag{5.17}$$

which is illustrated in Fig. 5.2 (b).

Using conformal transformation of primary operators, the correlation function on Σ trans-

forms into a three-point correlation function on the complex plane $\mathbb{C}$,

$$\begin{aligned} & \langle \phi_\alpha^1(-\infty)\phi_\beta^2(-\infty)\phi_\gamma^{3*}(+\infty)\rangle_\Sigma \\ = & \prod_i |J_i|^{-\Delta_i} \langle \phi_\alpha^1(w_1)\phi_\beta^2(w_2)\phi_\gamma^{3*}(w_3)\rangle_{\mathbb{C}}, \end{aligned} \tag{5.18}$$

where

$$J_i = e^{\pm\frac{2\pi}{L_i}\lambda} \frac{dz}{dw}(w_i) \tag{5.19}$$

is the conformal factor. The prefactor $e^{\pm\frac{2\pi}{L_i}\lambda}$ comes from the definition Eq. (5.7), where the plus sign is taken for ϕ_γ^3 and the minus sign is taken for ϕ_α^1 and ϕ_β^2. The three-point correlation function on the complex plane has the standard form

$$\langle \phi_\alpha^1(w_1)\phi_\beta^2(w_2)\phi_\gamma^{3*}(w_3)\rangle_{\mathbb{C}} = C_{\alpha\beta\gamma} \prod_{i<j} |w_i - w_j|^{-d_{ij}}, \tag{5.20}$$

where $d_{12} = \Delta_\alpha + \Delta_\beta - \Delta_\gamma$, and others follow from permutation symmetry.

Finally, combining Eqs. (5.18), (5.20) and the expression for λ, we obtain

$$\begin{aligned} & \frac{\langle \phi_\gamma^3 | \phi_\alpha^1 \phi_\beta^2 \rangle}{\langle \mathbb{1}^3 | \mathbb{1}^1 \mathbb{1}^2 \rangle} \\ = & \left[\left(\frac{L_3}{L_1}\right)^{\frac{L_1}{L_3}} \left(\frac{L_3}{L_2}\right)^{\frac{L_2}{L_3}} \right]^{-\frac{L_3}{L_1}\Delta_\alpha - \frac{L_3}{L_2}\Delta_\beta + \Delta_\gamma} C_{\alpha\beta\gamma}. \end{aligned} \tag{5.21}$$

The result is independent of the parameters w_1, w_2 and w_3, as expected. The special case in Ref. [169] corresponds to $L_3 = 2L_1 = 2L_2$, where the expression simplifies to

$$\frac{\langle \phi_\gamma^3 | \phi_\alpha^1 \phi_\beta^2 \rangle}{\langle \mathbb{1}^3 | \mathbb{1}^1 \mathbb{1}^2 \rangle} = 2^{-2\Delta_\alpha - 2\Delta_\beta + \Delta_\gamma} C_{\alpha\beta\gamma}. \tag{5.22}$$

On a finite lattice, Eqs. (5.21) and (5.22) are satisfied up to finite-size corrections. Physically, the finite-size corrections come from the singular point where the three cylinders meet.

In order to define the geometry, one has to put a UV cutoff ϵ around the singular point, analogous to the UV cutoff in the calculation of entanglement entropy in CFT [180, 181, 182, 183]. On the lattice, the UV cutoff ϵ is inversely proportional to the number of spins N. So far the conformal transformation works in the limit of $\epsilon \to 0$. Thus we expect that Eqs. (5.21) and (5.22) strictly hold in the thermodynamic limit $N \to \infty$. In what follows, we focus on the special case with $L_1 = L_2$ and study the finite-size corrections to Eq. (5.22). To this end, it is useful to switch from a path integral of a CFT on Σ to an equivalent viewpoint, the $\mathbb{Z}_2$ orbifold of the CFT defined on a cylinder.

5.2 Universal finite-size corrections

In this section we consider finite-size correction to Eq. (5.22). Specifically, we consider the normalized wavefunction overlap

$$\tilde{A}_{\alpha\beta\gamma} \equiv \frac{\langle \phi^3_\gamma | \phi^1_\alpha \phi^2_\beta \rangle}{\langle \mathbb{1}^3 | \mathbb{1}^1 \mathbb{1}^2 \rangle} \tag{5.23}$$

and its finite-size corrections

$$\tilde{A}_{\alpha\beta\gamma} = \tilde{A}^{(0)}_{\alpha\beta\gamma} + \sum_{p_{\alpha\beta\gamma}>0} \tilde{A}^{(p)}_{\alpha\beta\gamma} N^{-p_{\alpha\beta\gamma}}, \tag{5.24}$$

where

$$\tilde{A}^{(0)}_{\alpha\beta\gamma} = 2^{-2\Delta_\alpha - 2\Delta_\beta + \Delta_\gamma} C_{\alpha\beta\gamma}. \tag{5.25}$$

We show that $p_{\alpha\beta\gamma}$ only take on specific values determined by the scaling dimensions and fusion rules of the cyclic orbifold of the original CFT. They are given explicitly in Eq. (5.51).

When a CFT possesses a global symmetry, one can define an orbifold CFT by gauging the symmetry. The orbifold CFT has been extensively studied in string theory [184, 185, 186, 187, 188, 189, 190, 191], and in this work, we shall focus on the cyclic orbifold where

the cyclic permutation symmetry $\mathbb{Z}_{\mathsf{N}}$ is of interest [192, 193]. Cyclic orbifold has played an important role in the study of entanglement in quantum field theories. It is defined by gauging the cyclic permutation group $\mathbb{Z}_{\mathsf{N}}$ of N copies of the original CFT. In this work we focus on $\mathsf{N} = 2$, but generalizations to larger N is straightforward.

In the following, we first review the definition and the operator content of the cyclic orbifold. We then map the wavefunction overlaps to the OPEs of the cyclic orbifold and derive the universal finite-size corrections. Finally, we remark on the implication of our construction on the finite-size corrections to entanglement in CFT.

5.2.1 Cyclic orbifold on the cylinder

Given any CFT with Lagrangian density $\mathcal{L}_{\text{CFT}}[\Phi]$, the cyclic orbifold is defined as follows [192, 193]. We start with two copies of the original CFT known as the the mother CFT, whose Lagrangian density is given by

$$\mathcal{L}_{\text{mother}}[\Phi_1, \Phi_2] = \mathcal{L}_{\text{CFT}}[\Phi_1] + \mathcal{L}_{\text{CFT}}[\Phi_2]. \tag{5.26}$$

The mother CFT has a $\mathbb{Z}_2$ global symmetry that swaps the two copies. Denote the generator of the $\mathbb{Z}_2$ symmetry as σ, then

$$\sigma\Phi_i = \Phi_{i+1}, \tag{5.27}$$

where the subscript is understood to have periodicity 2. The cyclic orbifold theory is obtained by promoting the global symmetry to a gauge symmetry. The meaning of gauging a symmetry is twofold. Firstly, we enlarge the Hilbert space by allowing twisted boundary conditions,

$$\Phi_i(\tau, x + L) = \sigma\Phi_i(\tau, x). \tag{5.28}$$

This plays the role of gauge fields in usual gauge theory such as electrodynamics. Secondly, we project the Hilbert space onto subspace that is invariant under σ [1]. This amounts to enforcing gauge constraints in usual gauge theory.

To see the operator content of the cyclic orbifold, first note that there are two sectors of operators, the untwisted sector and the twisted sector. The untwisted sector contains eigenstates of the mother CFT with periodic boundary conditions. The twisted sector contains eigenstates of the mother CFT with twisted boundary conditions. Second, only the operators that are invariant under the σ swapping is kept. This is essential to obtain a consistent CFT because any operator that is not invariant under σ is non-local with respect to the twist sector. In the following subsection, we review the operator content of cyclic orbifold in more detail.

5.2.2 Operator content of cyclic orbifold

As has been well studied, the operator content of the cyclic orbifold is completely determined by the original CFT. The operator content is composed of the untwisted sector and the twisted sector. In the untwisted sector, the states are obtained from the tensor product theory. For $\alpha \neq \beta$, the symmetric states $|\phi_{\alpha,i}\rangle|\phi_{\beta,j}\rangle + |\phi_{\beta,j}\rangle|\phi_{\alpha,i}\rangle$ and anti-symmetric states $|\phi_{\alpha,i}\rangle|\phi_{\beta,j}\rangle - |\phi_{\beta,j}\rangle|\phi_{\alpha,i}\rangle$ in the Hilbert space are isomorphic. The labels i, j in the above expressions are the labels for descendants. Due to the isomorphism, we only keep one of the copies, say, the symmetric states. We denote the orbifold primary operator corresponds to this copy as:

$$\phi_{(\alpha,\beta)}, \tag{5.29}$$

1. More precisely, we need to keep every inequivalent irreducible representation once in order to have a modular invariant partition function. This subtlety arises in cyclic orbifold.

with scaling dimension:

$$\Delta_{(\alpha,\beta)} = \Delta_\alpha + \Delta_\beta. \tag{5.30}$$

For $\alpha = \beta$, the above isomorphism fails because when $\alpha = \beta, i = j$, the antisymmetric state does not exist. For this reason, both the copies should be kept, and we denote the two orbifold primary operators as:

$$\phi_{(\alpha,\alpha)_s}, \quad \phi_{(\alpha,\alpha)_a}, \tag{5.31}$$

where s stands for symmetric and a stands for anti-symmetric. Their scaling dimensions are:

$$\begin{aligned} \Delta_{(\alpha,\alpha)_s} &= 2\Delta_\alpha, \\ \Delta_{(\alpha,\alpha)_a} &= \begin{cases} 2\Delta_\alpha + 2, & \text{if } \phi_\alpha \text{ has level-1 des.} \\ 2\Delta_\alpha + 4, & \text{otherwise,} \end{cases} \end{aligned} \tag{5.32}$$

where 'des.' stands for descendant. Note that $\phi_{(\alpha,\alpha)_a}$ has larger scaling dimension than $\phi_{(\alpha,\alpha)_s}$, because antisymmetrization of the state with lowest L_0 eigenvalue $|\phi_\alpha\rangle|\phi_\alpha\rangle$ simply vanishes. Hence, a primary state $|\phi_\alpha\rangle$ must be combined with its descendant and then antisymmetrized. As far as the chiral algebra involves only conformal symmetry, only $\mathbb{1}$ operator does not have a level-1 descendant. (Namely, $|\mathbb{1}\rangle$ is the conformal vacuum.) This is no longer the case if the Kac-Moody algebra is taken into account, where the $\mathbb{1}$ operator does have level-1 descendants which are current operators. The identity operator in the orbifold theory is $\phi_{(\mathbb{1},\mathbb{1})_s}$, which has $\Delta = 0$.

Summarizing, if the original theory has n primary operators, then the untwisted sector of the orbifold theory has $n(n-1)/2 + 2n = n(n+3)/2$ primary operators. In Appendix B.1 we list the characters of each orbifold primary.

In the twisted sector, the operator with the lowest scaling dimension is denoted as $\tau_{(\mathbb{1},\hat{0})}$, whose scaling dimension is completely determined by the central charge,

$$\Delta_{(\mathbb{1},\hat{0})} = \frac{c}{8}. \tag{5.33}$$

This is known as the branch-point twist operator in the literature [182]. However, there are other primary operators in the twisted sector, which play an important role in this work. One may fuse $\tau_{(\mathbb{1},\hat{0})}$ with each primary operator $\phi_{(\alpha,\mathbb{1})}$ in the untwisted sector to generate other twist operators:

$$\tau_{(\mathbb{1},\hat{0})} \times \phi_{(\alpha,\mathbb{1})} \to \tau_{(\alpha,\hat{0})} + \tau_{(\alpha,\hat{1})}, \quad \alpha \neq \mathbb{1}. \tag{5.34}$$

For each α, there are two primary operators in the twisted sector[2]:

$$\tau_{(\alpha,\hat{0})}, \quad \tau_{(\alpha,\hat{1})}, \tag{5.35}$$

with scaling dimensions:

$$\begin{aligned} \Delta_{(\alpha,\hat{0})} &= \frac{c}{8} + \frac{\Delta_\alpha}{2} \\ \Delta_{(\alpha,\hat{1})} &= \begin{cases} \frac{c}{8} + \frac{\Delta_\alpha}{2} + 1, & \text{if } \phi_\alpha \text{ has level-1 des.} \\ \frac{c}{8} + \frac{\Delta_\alpha}{2} + 3, & \text{otherwise.} \end{cases} \end{aligned} \tag{5.36}$$

Summarizing, if the original theory has n primary operators, then the orbifold theory has $2n$ primary operators in the twisted sector. We would like to note that the fusion of twist operator and CFT operators has been useful for studying a wide range of properties of CFT, including entanglement in non-unitary CFTs [194, 195], symmetry-resolved entanglement

2. This is also true for $\alpha = \mathbb{1}$, and $\tau_{(\mathbb{1},\hat{1})}$ can be generated using channel $\tau_{(\beta,\hat{0})} \times \phi_{(\beta,\mathbb{1})}$, $\beta \neq \mathbb{1}$.

[196], and behavior resembling that of the c-theorem [197].

Finally, we need the fusion rules of the orbifold theory. It is intuitively clear that an operator in the untwisted sector fusing with an operator in the twisted sector only gives operators in the twisted sector. Furthermore, it has been shown [192] that the fusion rules are completely determined by the modular $\mathcal{S}$ and $\mathcal{T}$ matrices of the original CFT. For an introduction to modular matrices and details of the derivation, see Appendix B.1. We will need the following two fusion coefficients,

$$\mathcal{N}_{(\alpha,\beta),(\gamma,\hat{\psi}),(\delta,\hat{\chi})} = \sum_{\eta} \frac{\mathcal{S}_{\alpha\eta}\mathcal{S}_{\beta\eta}\mathcal{S}_{\gamma\eta}\mathcal{S}^*_{\eta\delta}}{\mathcal{S}^2_{\mathbb{1}\eta}}, \tag{5.37}$$

and

$$\begin{aligned}&\mathcal{N}_{(\alpha,\alpha)_s,(\gamma,\hat{\psi}),(\delta,\hat{\chi})} = \\ &\frac{1}{2}\sum_{\eta} \frac{\mathcal{S}^2_{\alpha\eta}\mathcal{S}_{\gamma\eta}\mathcal{S}^*_{\eta\delta}}{\mathcal{S}^2_{\mathbb{1}\eta}} + \frac{1}{2}e^{i\pi(\psi+\chi)}\sum_{\eta} \frac{\mathcal{S}_{\alpha\eta}\mathcal{P}_{\gamma\eta}\mathcal{P}^*_{\eta,\delta}}{\mathcal{S}_{\mathbb{1},\eta}},\end{aligned} \tag{5.38}$$

where $\mathcal{P} = \mathcal{T}^{1/2}\mathcal{S}\mathcal{T}^2\mathcal{S}\mathcal{T}^{1/2}$. In particular, Eq. (5.37) can be simplified to

$$\mathcal{N}_{(\alpha,\beta),(\gamma,\hat{\psi}),(\delta,\hat{\chi})} = \sum_{s} \mathcal{N}_{\alpha,\beta,s}\mathcal{N}_{\gamma,\delta,s^*} \tag{5.39}$$

if all primary fields are self-conjugate.

5.2.3 Universal finite-size corrections in wavefunction overlaps

Now we relate the wavefunction overlaps to path integral of the cyclic orbifold. Denote the field on Σ as

$$\Phi_1(\tau, x) = \Phi(\tau, x), \quad 0 \le x < L_1, \tag{5.40}$$

$$\Phi_2(\tau, x) = \Phi(\tau, x), \quad L_1 \le x < L_3. \tag{5.41}$$

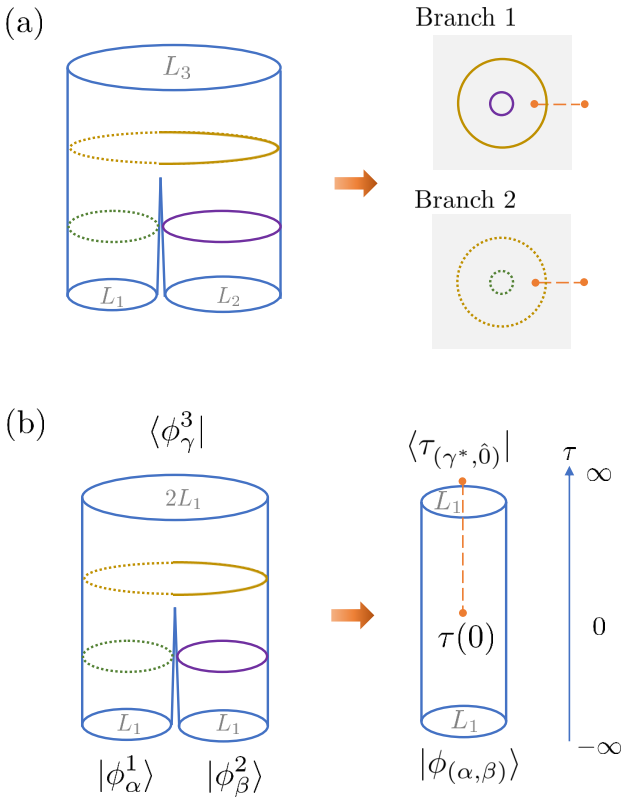

Figure 5.3: Mapping the path integral for the wavefunction overlap $A_{\alpha\beta\gamma}$ to the cyclic orbifold path integral. (a) The three-sided cylinder is conformally equivalent to the double-sheeted Riemann sphere with branch cut on $[1, \infty)$. The conformal transformation is achieved by $z' = e^{2\pi z/L_1}$. (b) The corresponding path integral of the cyclic orbifold for $A_{\alpha\beta\gamma}$. The insertions of branch-point twist operators at $\tau = 0$ and $\tau = +\infty$ correspond to the branch cut in (a).

It is then clear (as illustrated in Fig. 5.3(b)) that the fields are subject to the boundary conditions

$$\Phi_i(\tau, x + L_1) = \Phi_i(\tau, x), \quad \tau < 0, \tag{5.42}$$

$$\Phi_i(\tau, x + L_1) = \sigma\Phi_i(\tau, x), \quad \tau \geq 0, \tag{5.43}$$

where $\sigma\Phi_i \equiv \Phi_{i+1}$ and the subscript is understood to have periodicity 2. Now we see the path integral on Σ is exactly that of the cyclic orbifold on a cylinder with circumference L_1, with two twist operators τ inserting at $\tau = 0$ and $\tau = +\infty$,

$$\langle \mathbb{1}^3 | \mathbb{1}^1 \mathbb{1}^2 \rangle = \langle \mathbb{1} | \tau(+\infty)\tau(0) | \mathbb{1} \rangle_{\text{orb}}, \tag{5.44}$$

where the twist operator changes the boundary condition. The twist operator may contain all operators in the twisted sector, and it can be expanded as

$$\tau = \sum_{\alpha,\psi} a_{(\alpha,\hat{\psi})} \epsilon^{\Delta_{(\alpha,\hat{\psi})}} \tau_{(\alpha,\hat{\psi})} + \text{des.} \tag{5.45}$$

where we have introduced the UV cutoff ϵ, and $a_{(\alpha,\hat{\psi})}$ is presumably non-universal constant that depends on specific lattice realizations of the CFT. Some of the coefficients may also vanish due to symmetry of the lattice model, as we later examine specific models.

Using the operator-state correspondence, Eqs. (5.5) and (5.6), we obtain

$$\langle \mathbb{1}^3 | \mathbb{1}^1 \mathbb{1}^2 \rangle = \langle \tau_{(\mathbb{1},\hat{0})} | \tau(0) | \phi_{(\mathbb{1},\mathbb{1})_s} \rangle_{\text{orb}}, \tag{5.46}$$

where the bra is fixed to $\langle \tau_{(\mathbb{1},\hat{0})}|$ because other states in the twisted sector die off under the infinite imaginary time evolution. Using Eq. (5.9) and the fact that $C_{\mathbb{1}\phi\phi} = 1$ for any

primary operator ϕ (we are using $\phi = \tau_{(\mathbb{1},\hat{0})}$ here), we see

$$A_{\mathbb{1}\mathbb{1}\mathbb{1}} = \langle \mathbb{1}^3 | \mathbb{1}^1 \mathbb{1}^2 \rangle = a_{(\mathbb{1},\hat{0})} N^{-c/8}, \tag{5.47}$$

where $N = L_1/(2\pi\epsilon)$ is the system size of the lattice model, and $c/8$ is the scaling dimension of the leading twist operator $\tau_{(\mathbb{1},\hat{0})}$. This is remarkable, since it gives a way to compute the central charge of the CFT from wavefunction overlaps.

Now we consider the general wavefunction overlap $\langle \phi^3_\gamma | \phi^1_\alpha \phi^2_\beta \rangle$. The ket state can be created by inserting $\phi_{(\alpha,\beta)}$ at $\tau = -\infty$. Hereafter we take $\phi_{(\alpha,\alpha)}$ to mean $\phi_{(\alpha,\alpha)_s}$. The bra state can be created by inserting $\phi^*_{(\gamma,\mathbb{1})}$ at $\tau = +\infty$[3]. Recall that at $\tau = +\infty$ there is already a twist operator $\tau_{(\mathbb{1},\hat{0})}$ insertion, so the two operators fuse to give $\tau_{(\mathbb{1},\hat{0})} \times \phi^*_{(\gamma,\mathbb{1})} \to \tau_{(\gamma^*,\hat{0})} + \tau_{(\gamma^*,\hat{1})}$, and we only keep $\tau_{(\gamma^*,\hat{0})}$ at $\tau \to +\infty$. Therefore, we obtain

$$\langle \phi^3_\gamma | \phi^1_\alpha \phi^2_\beta \rangle = \langle \tau_{(\gamma,\hat{0})} | \tau(0) | \phi_{(\alpha,\beta)} \rangle_{\text{orb}}. \tag{5.48}$$

Using Eq. (5.45) and (5.9) we obtain the expansion

$$\langle \phi^3_\gamma | \phi^1_\alpha \phi^2_\beta \rangle = \sum_{\delta,\chi} a_{(\delta,\hat{\chi})} N^{-\Delta_{(\delta,\hat{\chi})}} C_{(\alpha,\beta),(\delta,\hat{\chi}),(\gamma,\hat{0})} + \cdots, \tag{5.49}$$

where $\cdots$ stands for contributions from descendant operators. The OPE coefficients can be computed from the OPEs in the original CFT following Ref. [194]. In particular,

$$C_{(\alpha,\beta),(\mathbb{1},\hat{0}),(\gamma,\hat{0})} = 2^{-2\Delta_\alpha - 2\Delta_\beta + \Delta_\gamma} C_{\alpha\beta\gamma}, \tag{5.50}$$

which recovers Eq. (5.22) in the thermodynamic limit. Furthermore, we obtain the finite-size

3. The reason that the second subindex is $\mathbb{1}$ can be understood in the following way. One considers a four-sided cylinder where the third side of the three-sided cylinder is further split into two cylinders. We insert primary operator ϕ_α and ϕ_β for the kets and ϕ^*_γ and $\mathbb{1}$ for the bras. On the bra side, the two insertions fuse into ϕ^*_γ which gives the desired overlap $\langle \phi_\gamma | \phi_\alpha \phi_\beta \rangle$.

corrections of the form Eq. (5.24), where the exponents are

$$p_{\alpha\beta\gamma} \in \{\Delta_{(\delta,\hat{\chi})} - \Delta_{(\mathbb{1},\hat{0})} | \mathcal{N}_{(\alpha,\beta),(\delta,\hat{\chi}),(\gamma,\hat{0})} \neq 0\}. \tag{5.51}$$

This is the central result of our work. We see that the exponents inside the finite-size corrections are universal, as claimed. Later we will consider various CFTs and their lattice realizations, where we numerically extract the leading exponent $p_{\alpha\beta\gamma}$ in the finite-size corrections. To compare it with Eq. (5.51), it is useful to use the crossing symmetry,

$$\mathcal{N}_{(\alpha,\beta),(\delta,\hat{\chi}),(\gamma,\hat{0})} = \mathcal{N}_{(\alpha,\beta),(\gamma^*,\hat{0}),(\delta^*,\hat{\chi})}. \tag{5.52}$$

The leading $\Delta_{(\delta,\hat{\chi})}$ in the set of Eq. (5.51) is the lowest scaling dimension of the twist operators (except $\tau_{(\mathbb{1},\hat{0})}$) in the OPE of $\phi_{(\alpha,\beta)}$ and $\tau_{(\gamma^*,\hat{0})}$.

One simple example is $\langle \phi_\gamma^3 | \mathbb{1}^1 \mathbb{1}^2 \rangle$ when $\phi_\gamma \neq \mathbb{1}$. The fusion channel is forbidden, meaning that $\tilde{A}^{(0)}_{\mathbb{1}\mathbb{1}\gamma} = 0$. Since the fusion of identity operator with $\tau_{(\gamma^*,\hat{0})}$ only gives $\tau_{(\gamma^*,\hat{0})}$, the leading exponent in finite-size correction is

$$p_{\mathbb{1}\mathbb{1}\gamma} = \Delta_{(\gamma^*,\hat{0})} - \Delta_{(\mathbb{1},\hat{0})} = \frac{\Delta_\gamma}{2}. \tag{5.53}$$

This provides another consistency check of scaling dimensions of primary operators.

We stress that the result Eq. (5.51) only applies to wavefunction overlaps with $N_1 = N_2$. For $N_1 \neq N_2$, the exponents $p_{\alpha\beta\gamma}$ in finite-size corrections may be different. Nevertheless, the exponents are still the difference between the scaling dimensions of an operator $\tau_{(\delta,\hat{\chi})}$ in the twisted sector and $\tau_{(\mathbb{1},0)}$, while the operator $\tau_{(\delta,\hat{\chi})}$ does not necessarily satisfy the fusion constraint in Eq. (5.51). This is examined and further explored in Appendix of [198].

5.2.4 *Finite-size corrections to Renyi entropy of CFT*

Cyclic orbifold has also played an important role in computing the entanglement of CFT. The twist operators as well as its fused version provide valuable tools for computing various entanglement measures [180, 181, 182, 183, 199, 200]. We expect that the second Renyi entropy of CFT has similar finite-size corrections as the wavefunction overlaps, since the twist operator insertion is essentially of the same nature as Eq. (5.45). Consider, for example, the ground state of a CFT on the complex plane and the reduced density matrix on $[0, l]$,

$$\rho = \mathrm{Tr}_{\mathbb{R}-[0,l]} \, |\mathbb{1}\rangle\langle\mathbb{1}|. \tag{5.54}$$

The Renyi entropies are defined by

$$S_{\mathsf{N}} = \frac{1}{1-\mathsf{N}} \log \frac{\mathrm{Tr}\ \rho^{\mathsf{N}}}{(\mathrm{Tr}\,\rho)^{\mathsf{N}}}. \tag{5.55}$$

Specializing to $\mathsf{N} = 2$, the purity can be computed as the path integral of the cyclic orbifold on the complex plane with two twist operators insertions,

$$\frac{\mathrm{Tr}\ \rho^2}{(\mathrm{Tr}\,\rho)^2} = \langle\mathbb{1}|\tau(0)\tau(l)|\mathbb{1}\rangle_{\mathrm{orb}}. \tag{5.56}$$

Using Eq. (5.45), the correlation function can be expanded as

$$\langle\mathbb{1}|\tau(0)\tau(l)|\mathbb{1}\rangle_{\mathrm{orb}} = \sum_{(\alpha,\hat{\chi})} a^2_{(\alpha,\hat{\chi})} l^{-2\Delta_{(\alpha,\hat{\chi})}} + \cdots, \tag{5.57}$$

where $\cdots$ contains contributions from descendant operators. In the limit where $l \gg \epsilon$, the second Renyi entropy also has universal finite-size corrections

$$S_2 = \frac{c}{4}\log\frac{l}{\epsilon} - 2\log a_{(\mathbb{1},\hat{0})} + \sum_{(\alpha,\hat{\chi})\neq(\mathbb{1},\hat{0})} \frac{a^2_{(\alpha,\hat{\chi})}}{a^2_{(\mathbb{1},\hat{0})}}\, l^{-2(\Delta_{(\alpha,\hat{\chi})}-\Delta_{(\mathbb{1},\hat{0})})}, \tag{5.58}$$

where the last term contains the universal finite-size corrections, which has been observed in Ref. [176]. As a side remark, one may consider similar finite-size corrections to other Renyi entropies on the same footing, and then analytically continue the result to the case of entanglement entropy ($\mathsf{N} = 1$). Finally, we note that only the twist operators $\tau_{(\alpha,\hat{0})}$ have been considered in previous work that discusses entanglement of CFT. As we will show numerically, in the context of wavefunction overlaps the other twist operator $\tau_{(\alpha,\hat{1})}$ also plays an important role. It remains to be explored whether operators such as $\tau_{(\alpha,\hat{1})}$ can be observed in the finite-size corrections to the entanglement entropy of CFT.

5.3 Applications to Ising and XXZ models

In this section, we apply the above general method to two specific lattice models: the Ising model and the XXZ model. The Ising model is the lattice realization of the $c = 1/2$ Ising CFT, which is a minimal model. The XXZ model is a lattice realization of the $c = 1$ compactified boson theory at radius R, which is a rational CFT at special radii. Both the Ising model and the XXZ model at $R = 2$ can be mapped to a free fermion problem. Thus we are able to obtain low-energy eigenstates for up to thousands of spins using the covariance matrix techniques [201].

We first review the operator content of each CFT and the $\mathsf{N} = 2$ cyclic orbifold, and then show how the orbifold fusion rule determines the universal finite-size corrections in wavefunction overlaps. We then verify the leading exponent in the finite-size corrections

Eq. (5.24) numerically. All the exponents agree with our analytical expression Eq. (5.51).

5.3.1 The Ising model

In this subsection we study the ferromagnetic Ising model. For later discussions, it will also be useful to study the antiferromagnetic Ising model which is described by the same CFT. Since the computations are largely identical, the result for the antiferromagnetic case is shown in Appendix B.2. The ferromagnetic Ising spin chain Hamiltonian at the critical point is:

$$H = -\sum_{i=1}^{N} X_i X_{i+1} - \sum_{i=1}^{N} Z_i, \tag{5.59}$$

where X, Z are Pauli matrices. There are three primary operators in the Ising CFT: $\mathbb{1}, \sigma, \epsilon$, with scaling dimension $\Delta = 0, \frac{1}{8}, 1$, respectively.

The non-trivial OPE coefficients in the Ising CFT are:

$$C_{\mathbb{1}\mathbb{1}\mathbb{1}} = 1, \quad C_{\epsilon\epsilon\mathbb{1}} = 1, \quad C_{\sigma\sigma\mathbb{1}} = 1, \quad C_{\sigma\sigma\epsilon} = \frac{1}{2}, \tag{5.60}$$

and the modular matrices are (in the basis $\mathbb{1}, \sigma, \epsilon$):

$$\mathcal{T} = \begin{pmatrix} e^{-\frac{i\pi}{24}} & 0 & 0 \\ 0 & e^{\frac{i\pi}{12}} & 0 \\ 0 & 0 & e^{i\pi\frac{23}{24}} \end{pmatrix}, \quad \mathcal{S} = \frac{1}{2}\begin{pmatrix} 1 & 1 & \sqrt{2} \\ 1 & 1 & -\sqrt{2} \\ \sqrt{2} & -\sqrt{2} & 0 \end{pmatrix}. \tag{5.61}$$

In the following, we consider the cyclic orbifold theory of the Ising CFT. It is straightforward to compute scaling dimensions of all primary operators and the fusion rules using general framework presented in Sec. 5.2.2. For the Ising CFT, however, it is possible to map the cyclic orbifold to a more familiar CFT, that is, a compactified boson $\mathbb{Z}_2$ orbifold at radius $R = 4$. The $U(1)$ charge conservation symmetry in the latter CFT makes it more intuitive to understand the fusion rules. We have checked that the fusion rules given by Eqs. (5.37)

and (5.38) coincide with the those of the free boson orbifold.

Orbifold operator content

Following the general discussion in Sec. 5.2.2, there exist 15 primary operators in the cyclic orbifold CFT, 9 in the untwisted sector and 6 in the twisted sector. The 15 primary operators are listed in the first column of Table. 5.1, along with their characters χ in the last column.

Untwisted sector The three primaries for $\alpha \neq \beta$ are

$$(\mathbb{1}, \sigma), \quad (\mathbb{1}, \epsilon), \quad (\sigma, \epsilon), \tag{5.62}$$

with scaling dimensions $\Delta = \frac{1}{8}, 1, \frac{9}{8}$. Additionally, there are 6 primary operators,

$$(\mathbb{1}, \mathbb{1})_s, \quad (\sigma, \sigma)_s, \quad (\epsilon, \epsilon)_s, \tag{5.63}$$

with $\Delta = 0, \frac{1}{4}, 2$ and

$$(\mathbb{1}, \mathbb{1})_a, \quad (\sigma, \sigma)_a, \quad (\epsilon, \epsilon)_a, \tag{5.64}$$

with $\Delta = 4, \frac{9}{4}, 4$.

Twisted sector In the twisted sector, twist operators $\tau_{(\alpha,\hat{0})}$ have scaling dimension $\Delta = \frac{c}{8} + \frac{\Delta_\alpha}{2}$, which gives $\Delta = \frac{1}{16}, \frac{1}{8}, \frac{9}{16}$. $\tau_{(\alpha,\hat{1})}$ have conformal dimension $\Delta = \frac{c}{8} + \frac{\Delta_\alpha}{2} + 1$, except for $\tau_{(\mathbb{1},\hat{1})}$, which has $\Delta = \frac{c}{8} + \frac{\Delta_i}{2} + 3$. This stems from the fact that $\mathbb{1}$ corresponds to conformal vacuum $|0\rangle$ and $L_{-1}|0\rangle = 0$. Thus, we have $\Delta = \frac{49}{16}, \frac{9}{8}, \frac{25}{16}$ for the primary operators $\tau_{(\alpha,\hat{1})}$.

Mapping to compactified boson orbifold

It has been noted in Ref. [193] that the scaling dimensions of the Ising orbifold listed above are identical to those of the compactified boson $\mathbb{Z}_2$ orbifold at radius $R = 4$. Indeed the two theories are dual to each other. The free boson action is:

$$S = \frac{1}{4\pi} \int d^2z \partial\varphi\bar{\partial}\varphi. \tag{5.65}$$

The compactified boson with radius R is obtained by identifying $\varphi \equiv \varphi + 2\pi nR, n \in \mathbb{Z}$. It has a $\mathbb{Z}_2$ reflection symmetry: $\varphi \to -\varphi$, and a $U(1)$ symmetry $\varphi \to \varphi + \alpha$. After gauging the $\mathbb{Z}_2$ reflection symmetry, we obtain the compactified boson orbifold theory.

The compactified boson orbifold at radius $R = \sqrt{2k}$ with $k \in \mathbb{Z}_+$ is a rational CFT with $k + 7$ extended primary fields, which consists of the following five families [27]:

1. $\phi_\lambda, \lambda = 1, 2, \cdots, k-1$ with dimension $\Delta_\lambda = \frac{\lambda^2}{2k}$.
2. $\Phi^{(1)}$ and $\Phi^{(2)}$, with dimension $\Delta = \frac{k^2}{2k} = \frac{k}{2}$.
3. $\sigma^{(1)}, \sigma^{(2)}$ with dimension $\Delta = \frac{1}{8}$, and $\tau^{(1)}, \tau^{(2)}$ with dimension $\Delta = \frac{9}{8}$.
4. Identity operator $\mathbb{1}$ with dimension 0.
5. Operator Θ with dimension $\Delta = 2$.

When taking $k = 8$, i.e., at radius $R = \sqrt{2k} = 4$, the conformal dimensions of these 15 extended primaries match those of the 15 primaries in the cyclic Ising orbifold, as shown in Table 5.1. This correspondence of conformal dimensions was first noticed in [193]. We took one step further and also verified numerically that this correspondence holds at the level of the characters χ and the modular matrices $\mathcal{T}, \mathcal{S}$.

Mapping to the compactified boson orbifold at radius $R = 4$ is useful in the problem concerned, because the fusion rule in the compactified boson orbifold is well understood,

which we will now exploit to derive the universal finite-size corrections. For example, the $U(1)$ charge conservation gives:

$$[\phi_\lambda] \times [\phi_\mu] = [\phi_{\lambda+\mu}] + [\phi_{\lambda-\mu}], \quad \mu \neq \lambda, 2k-\lambda, \tag{5.66}$$

and

$$[\Theta] \times [\phi_i] = [\phi_i]. \tag{5.67}$$

The latter corresponds to the fact that Θ is charge neutral.

Universal finite-size correction

Now we examine the universal finite-size corrections in Eq. (5.24). As the Ising model has a $\mathbb{Z}_2$ global symmetry, the expansion Eq. (5.45) does not contain $\tau_{(\sigma,\hat{\chi})}, \chi = 0, 1$. We further consider several examples.

As a first example, let us compute the universal finite-size correction to the wavefunction overlap $A_{\sigma\epsilon\sigma}$ for the following allowed OPE channel:

$$\sigma \times \epsilon \to \sigma. \tag{5.68}$$

To find all the scaling terms in the wavefunction overlap, we would need to find all operators $\tau_{(\alpha,\hat{\chi})}$ such that $C_{(\sigma,\epsilon),(\alpha,\hat{\chi}),(\sigma,\hat{0})}$ is non-zero. Using the crossing symmetry, we can compute $C_{(\sigma,\epsilon),(\sigma,\hat{0}),(\alpha,\hat{\chi})}$ equivalently. By mapping to compactified boson orbifold, (σ, ϵ) is mapped to $\tau^{(1)}$ and $\tau_{(\sigma,\hat{0})}$ is mapped to $\sigma^{(2)}$. The fusion rule reads:

$$[\tau^{(1)}] \times [\sigma^{(2)}] = [\phi_1] + [\phi_3] + [\phi_5] + [\phi_7], \tag{5.69}$$

Untwisted			
primary (Ising orb.)	Δ	primary (boson orb.)	χ
$(\mathbb{1},\sigma)$	$\frac{1}{8}$	$\sigma^{(1)}$	$\chi_{\mathbb{1}}(\tau)\chi_\sigma(\tau)$
$(\mathbb{1},\epsilon)$	1	ϕ_4	$\chi_{\mathbb{1}}(\tau)\chi_\epsilon(\tau)$
(σ,ϵ)	$\frac{9}{8}$	$\tau^{(1)}$	$\chi_\sigma(\tau)\chi_\epsilon(\tau)$
$(\mathbb{1},\mathbb{1})_s$	0	$\mathbb{1}$	$\frac{1}{2}\chi^2_{\mathbb{1}}(\tau)+\frac{1}{2}\chi_{\mathbb{1}}(2\tau)$
$(\mathbb{1},\mathbb{1})_a$	4	$\Phi^{(1)}$	$\frac{1}{2}\chi^2_{\mathbb{1}}(\tau)-\frac{1}{2}\chi_{\mathbb{1}}(2\tau)$
$(\sigma,\sigma)_s$	$\frac{1}{4}$	ϕ_2	$\frac{1}{2}\chi^2_{\sigma}(\tau)+\frac{1}{2}\chi_{\sigma}(2\tau)$
$(\sigma,\sigma)_a$	$\frac{9}{4}$	ϕ_6	$\frac{1}{2}\chi^2_{\sigma}(\tau)-\frac{1}{2}\chi_{\sigma}(2\tau)$
$(\epsilon,\epsilon)_s$	2	Θ	$\frac{1}{2}\chi^2_{\epsilon}(\tau)+\frac{1}{2}\chi_{\epsilon}(2\tau)$
$(\epsilon,\epsilon)_a$	4	$\Phi^{(2)}$	$\frac{1}{2}\chi^2_{\epsilon}(\tau)-\frac{1}{2}\chi_{\epsilon}(2\tau)$
Twisted			
primary (Ising orb.)	Δ	primary (boson orb.)	χ
$\tau_{(\mathbb{1},\hat{0})}$	$\frac{1}{16}$	ϕ_1	$\frac{1}{2}[\chi_{\mathbb{1}}(\frac{\tau}{2})+T_{\mathbb{1}}^{-\frac{1}{2}}\chi_{\mathbb{1}}(\frac{\tau}{2}+\frac{1}{2})]$
$\tau_{(\mathbb{1},\hat{1})}$	$\frac{49}{16}$	ϕ_7	$\frac{1}{2}[\chi_{\mathbb{1}}(\frac{\tau}{2})-T_{\mathbb{1}}^{-\frac{1}{2}}\chi_{\mathbb{1}}(\frac{\tau}{2}+\frac{1}{2})]$
$\tau_{(\sigma,\hat{0})}$	$\frac{1}{8}$	$\sigma^{(2)}$	$\frac{1}{2}[\chi_{\sigma}(\frac{\tau}{2})+T_{\sigma}^{-\frac{1}{2}}\chi_{\sigma}(\frac{\tau}{2}+\frac{1}{2})]$
$\tau_{(\sigma,\hat{1})}$	$\frac{9}{8}$	$\tau^{(2)}$	$\frac{1}{2}[\chi_{\sigma}(\frac{\tau}{2})-T_{\sigma}^{-\frac{1}{2}}\chi_{\sigma}(\frac{\tau}{2}+\frac{1}{2})]$
$\tau_{(\epsilon,\hat{0})}$	$\frac{9}{16}$	ϕ_3	$\frac{1}{2}[\chi_{\epsilon}(\frac{\tau}{2})+T_{\epsilon}^{-\frac{1}{2}}\chi_{\epsilon}(\frac{\tau}{2}+\frac{1}{2})]$
$\tau_{(\epsilon,\hat{1})}$	$\frac{25}{16}$	ϕ_5	$\frac{1}{2}[\chi_{\epsilon}(\frac{\tau}{2})-T_{\epsilon}^{-\frac{1}{2}}\chi_{\epsilon}(\frac{\tau}{2}+\frac{1}{2})]$

Table 5.1: Correspondence between the primary fields in the Ising cyclic $\mathbb{Z}_2$ orbifold (first column) and the free boson $\mathbb{Z}_2$ orbifold (third column) at $R=4$. $T_i = e^{2\pi i(h_i-\frac{c}{24})}$ is the i-th diagonal element of the modular $\mathcal{T}$ matrix.

which maps back to:

$$[(\sigma,\epsilon)]\times[\tau_{(\sigma,\hat{0})}]=[\tau_{(\mathbb{1},\hat{0})}]+[\tau_{(\epsilon,\hat{0})}]+[\tau_{(\epsilon,\hat{1})}]+[\tau_{(\mathbb{1},\hat{1})}]. \tag{5.70}$$

The four resulting primaries on the r.h.s. have scaling dimensions $\Delta=\frac{1}{16},\frac{9}{16},\frac{25}{16},\frac{49}{16}$, respectively, and the scaling of the wavefunction overlap is thus:

$$A_{\sigma\epsilon\sigma}\approx a_{(\mathbb{1},\hat{0})}C_{(\sigma,\epsilon),(\mathbb{1},\hat{0}),(\sigma,\hat{0})}N^{-\frac{1}{16}}+a_{(\epsilon,\hat{0})}C_{(\sigma,\epsilon),(\epsilon,\hat{0}),(\sigma,\hat{0})}N^{-\frac{9}{16}}, \tag{5.71}$$

where we only keep the leading and first subleading terms. The leading term scales as $N^{-\frac{1}{16}}$ with power agrees with $-\frac{c}{8}$. This aligns with the fact that the wavefunction overlap for an allowed fusion process has a leading term that scales as $N^{-\frac{c}{8}}$. After dividing by $A_{\mathbb{1}\mathbb{1}\mathbb{1}}$ and subtracting the leading term, the universal finite-size correction scales as $N^{-\frac{1}{2}}$, namely, $p_{\sigma\epsilon\sigma}=\frac{9}{16}-\frac{1}{16}=\frac{1}{2}$. This is exactly what we get from numerics in Fig. 5.4.

As a second example, let us study the channel:

$$\sigma\times\sigma\to\epsilon, \tag{5.72}$$

where we need to find non-zero $C_{(\sigma,\sigma)_s,\tau_p,\tau_{(\epsilon,\hat{0})}}$. The fusion rule $[\phi_2]\times[\phi_3]\to[\phi_1]+[\phi_5]$ is mapped to $[(\sigma,\sigma)_s]\times[\tau_{(\epsilon,\hat{0})}]\to[\tau_{(\mathbb{1},\hat{0})}]+[\tau_{(\epsilon,\hat{1})}]$. This shows τ_p can take $\tau_{(\mathbb{1},\hat{0})}$ or $\tau_{(\epsilon,\hat{1})}$, and the difference of their scaling dimension predicts $p_{\sigma\sigma\epsilon}=\frac{25}{16}-\frac{1}{16}=\frac{3}{2}$.

Following the same reasoning, for the OPE channel:

$$\epsilon\times\epsilon\to\mathbb{1}, \tag{5.73}$$

the corresponding orbifold fusion channel is $[\Theta]\times[\phi_1]\to[\phi_1]$, which translates into $[(\epsilon,\epsilon)_s]\times[\tau_{(\mathbb{1},\hat{0})}]\to[\tau_{(\mathbb{1},\hat{0})}]$. This indicates τ_p lies within the conformal tower of $[\tau_{(\mathbb{1},\hat{0})}]$. Indeed, the leading exponent is controlled by a level-two descendant, which gives $p_{\epsilon\epsilon\mathbb{1}}=2$.

Finally, we consider the following forbidden channel:

$$\mathbb{1} \times \epsilon \to \mathbb{1}. \tag{5.74}$$

The fusion rule $[\phi_4]\times[\phi_1] = [\phi_3]+[\phi_5]$ is translated to $[(\mathbb{1},\epsilon)]\times[\tau_{(\mathbb{1},\hat{0})}] = [\tau_{(\epsilon,\hat{0})}]+[\tau_{(\epsilon,\hat{1})}]$, which predicts the leading term in this forbidden channel scales as $N^{-\frac{9}{16}}$, i.e., $p_{\mathbb{1}\epsilon\mathbb{1}} = \frac{9}{16} - \frac{1}{16} = \frac{1}{2}$.

We show in Fig. 5.4 the numerically obtained finite-size scaling $F_{\alpha\beta\gamma}$ defined by:

$$\begin{aligned} F_{\alpha\beta\gamma} &\equiv \frac{\langle \phi_\gamma^3 | \phi_\alpha^1 \phi_\beta^2 \rangle}{\langle \mathbb{1}^3 | \mathbb{1}^1 \mathbb{1}^2 \rangle} - \tilde{A}^{(0)}_{\alpha\beta\gamma} \\ &= \frac{A_{\alpha\beta\gamma}}{A_{\mathbb{1}\mathbb{1}\mathbb{1}}} - 2^{-2\Delta_\alpha - 2\Delta_\beta + \Delta_\gamma} C_{\alpha\beta\gamma}, \end{aligned} \tag{5.75}$$

which agrees exactly with our prediction that for the leading order,

$$\log F_{\alpha\beta\gamma} = -p_{\alpha\beta\gamma} \log N + \text{const.} \tag{5.76}$$

For readers' reference, the finite-size corrections for all fusion channels are listed in Table 5.2.

5.3.2 The XXZ model

The XXZ model is a lattice realization of $c = 1$ compactified boson with radius R. The free boson has a $U(1)$ current $J = i\partial\varphi$. In the spin basis, the Hamiltonian is

$$H = -\sum_{i=1}^{N} (X_i X_{i+1} + Y_i Y_{i+1} + \Delta Z_i Z_{i+1}), \tag{5.77}$$

where the radius R is related to Δ via $\Delta = \cos(2\pi/R^2)$. At $\Delta = 0$ (namely, $k = 2, R = \sqrt{2k} = 2$), the spin Hamiltonian can be Jordan-Wigner transformed into the free fermion

overlap	Responsible operator τ_p	Responsible fusion channel	FS correction leading power p
$\mathbb{1}\times\mathbb{1}\to\epsilon$	$[\tau_{(\epsilon,\hat{0})}]$	$[(\mathbb{1},\mathbb{1})_s]\times[\tau_{(\epsilon,\hat{0})}]\to[\tau_{(\epsilon,\hat{0})}]$	$\frac{1}{2}$
$\mathbb{1}\times\epsilon\to\mathbb{1}$	$[\tau_{(\epsilon,\hat{0})}]$	$[(\mathbb{1},\epsilon)]\times[\tau_{(\epsilon,\hat{0})}]\to[\tau_{(\mathbb{1},\hat{0})}]$	$\frac{1}{2}$
$\epsilon\times\epsilon\to\mathbb{1}$	$[\tau_{(\mathbb{1},\hat{0})}]$ des.	$[(\epsilon,\epsilon)_s]\times[\tau_{(\mathbb{1},\hat{0})}]\to[\tau_{(\mathbb{1},\hat{0})}]$	2
$\epsilon\times\epsilon\to\epsilon$	$[\tau_{(\epsilon,\hat{0})}]$	$[(\epsilon,\epsilon)_s]\times[\tau_{(\epsilon,\hat{0})}]\to[\tau_{(\epsilon,\hat{0})}]$	$\frac{1}{2}$
$\mathbb{1}\times\epsilon\to\epsilon$	$[\tau_{(\mathbb{1},\hat{1})}]$	$[(\mathbb{1},\epsilon)]\times[\tau_{(\mathbb{1},\hat{1})}]\to[\tau_{(\epsilon,\hat{0})}]$	3
$\mathbb{1}\times\sigma\to\sigma$	$[\tau_{(\epsilon,\hat{0})}]$	$[(\mathbb{1},\sigma)]\times[\tau_{(\epsilon,\hat{0})}]\to[\tau_{(\sigma,\hat{0})}]$	$\frac{1}{2}$
$\sigma\times\epsilon\to\sigma$	$[\tau_{(\epsilon,\hat{0})}]$	$[(\sigma,\epsilon)]\times[\tau_{(\epsilon,\hat{0})}]\to[\tau_{(\sigma,\hat{0})}]$	$\frac{1}{2}$
$\sigma\times\sigma\to\mathbb{1}$	$[\tau_{(\epsilon,\hat{0})}]$	$[(\sigma,\sigma)_s]\times[\tau_{(\epsilon,\hat{0})}]\to[\tau_{(\mathbb{1},\hat{0})}]$	$\frac{1}{2}$
$\sigma\times\sigma\to\epsilon$	$[\tau_{(\epsilon,\hat{1})}]$	$[(\sigma,\sigma)_s]\times[\tau_{(\epsilon,\hat{1})}]\to[\tau_{(\epsilon,\hat{0})}]$	$\frac{3}{2}$

Table 5.2: Universal finite-size corrections to wavefunction overlaps of the ciritical Ising model for all fusion channels. The wavefunction overlaps for $\mathbb{1}\times\mathbb{1}\to\sigma$ and $\sigma\times\sigma\to\sigma$ are strictly zero due to the global $\mathbb{Z}_2$ symmetry in the Ising model.

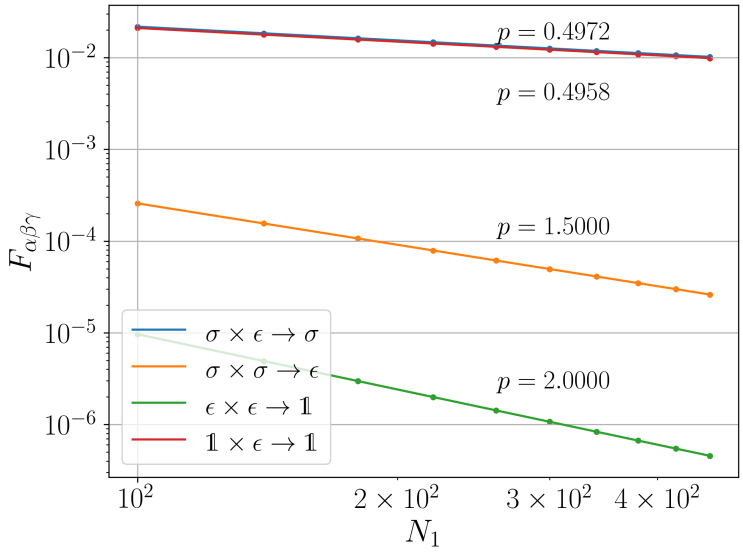

Figure 5.4: Finite-size corrections of wavefunction overlap in the critical Ising model, for the four channels: $\sigma\times\epsilon\to\sigma$, $\sigma\times\sigma\to\epsilon, \epsilon\times\epsilon\to\mathbb{1}, \mathbb{1}\times\epsilon\to\mathbb{1}$ under discussion. The powers of leading finite-size corrections are $p=\frac{1}{2},\frac{3}{2},2,\frac{1}{2}$, respectively, from the orbifold CFT. In the numerical computation we choose the system size $N_1\in[100,500)$, and we see the discrepancy between the theory and numerical value is less than 1%.

Hamiltonian

$$H = -2\sum_{i=1}^{N}(c_i^\dagger c_{i+1} + c_{i+1}^\dagger c_i). \tag{5.78}$$

In the following, we will focus on this free fermion point for its numerical efficiency.

Operator content

Original theory At radius $R = \sqrt{2k}$, the valid chiral and anti-chiral momentum modes in the compactified boson theory are

$$\begin{aligned} p &= \frac{m}{R} + \frac{nR}{2} = \frac{m}{2} + n, \\ \bar{p} &= \frac{m}{R} - \frac{nR}{2} = \frac{m}{2} - n, \quad m, n \in \mathbb{Z}, \end{aligned} \tag{5.79}$$

where m is the quantized momentum and n is the quantized winding. The operators can be labeled by $\mathcal{O}_{(m,n)}$. The partition function is obtained after summing over contribution from valid momentum modes:

$$Z = \frac{1}{|\eta|^2}\sum_{m,n} q^{\frac{1}{2}(\frac{m}{R}+\frac{nR}{2})^2}\bar{q}^{\frac{1}{2}(\frac{m}{R}-\frac{nR}{2})^2}, \tag{5.80}$$

where $\eta(\tau)$ is the Dedekind eta function. Equivalently, for integer k, this $U(1)$ chiral algebra can be viewed as being extended by two vertex operators $\{e^{i\sqrt{2k}\varphi}, e^{-i\sqrt{2k}\bar{\varphi}}\}$, which allows us to interpret it as $u(1)_k$ rational CFT and block diagonalize the partition function

$$Z = \frac{1}{|\eta|^2}\sum_{l=0}^{2k-1}|\Theta_{l,k}|^2, \quad \Theta_{l,k} = \sum_n q^{k(n+\frac{l}{2k})^2}. \tag{5.81}$$

From the block-diagonal partition function, we read off $2k$ extended primaries. For the $u(1)_2$ rational CFT at $k = 2$, there are $2k = 4$ extended primaries with scaling dimension

$\Delta_l = \frac{l^2}{2k} = \frac{l^2}{4}, l = 0, 1, 2, 3$. The first several modes in each extended primaries are

	(m, n)
$\mathbb{1}$	(0,0), (0,2), (2,1), (4,0)
$\mathcal{O}_1$	(1,0), $(-3, 0)$
$\mathcal{O}_2$	(2,0), $(-2, 0)$, (0,1)
$\mathcal{O}_3$	(3,0), $(-1, 0)$, (1,1)

(5.82)

Namely, $\mathcal{O}_{(1,0)}, \mathcal{O}_{(-3,0)}$ belong to the conformal family $\mathcal{O}_1$, etc.

The modular matrix $\mathcal{T}$ can be obtained directly from the scaling dimension: $\mathcal{T}_{ll} = \exp(2\pi i(\Delta_l/2 - c/24))$, and the modular matrix $\mathcal{S}$ is

$$\mathcal{S}_{l,l'} = \frac{1}{\sqrt{2k}} \exp(-i\pi \frac{ll'}{k}). \tag{5.83}$$

The original theory modular matrices allow us to compute the modular matrices in the orbifolded theory.

For later discussions, we focus on the wavefunction overlap associated with current operator $J = i\partial\varphi$. Specifically, we consider the process

$$J \times J \to \mathbb{1}. \tag{5.84}$$

In the $U(1)$ Kac-Moody algebra, J is the Kac-Moody descendant of $\mathcal{O}_{(0,0)} = \mathbb{1}$ (while not being the Virasoro descendant).

Orbifold theory Following the general procedure in Sec. 5.2.2, the untwisted sector has 14 primary operators, including operators like $(\mathbb{1}, \mathcal{O}_1), (\mathcal{O}_1, \mathcal{O}_2), (\mathcal{O}_1, \mathcal{O}_1)_{s/a}$, etc.; and there

are 8 primaries in the twisted sector:

	$\tau_{(\mathbb{1},\hat{0})}$	$\tau_{(\mathbb{1},\hat{1})}$	$\tau_{(\mathcal{O}_1,\hat{0})}$	$\tau_{(\mathcal{O}_1,\hat{1})}$
Δ	$\frac{1}{8}$	$\frac{9}{8}$	$\frac{1}{4}$	$\frac{5}{4}$
	$\tau_{(\mathcal{O}_2,\hat{0})}$	$\tau_{(\mathcal{O}_2,\hat{1})}$	$\tau_{(\mathcal{O}_3,\hat{0})}$	$\tau_{(\mathcal{O}_3,\hat{1})}$
Δ	$\frac{5}{8}$	$\frac{21}{8}$	$\frac{5}{4}$	$\frac{13}{4}$

(5.85)

Note that the difference between Δ for $\tau_{(\mathbb{1},\hat{0})}$ and $\tau_{(\mathbb{1},\hat{1})}$ is 1 rather than 3 as in the Ising orbifold. This is because we are considering the Kac-Moody algebra and J is a level-1 descendant of $\mathbb{1}$ with respected to the extended symmetry.

Universal finite-size correction

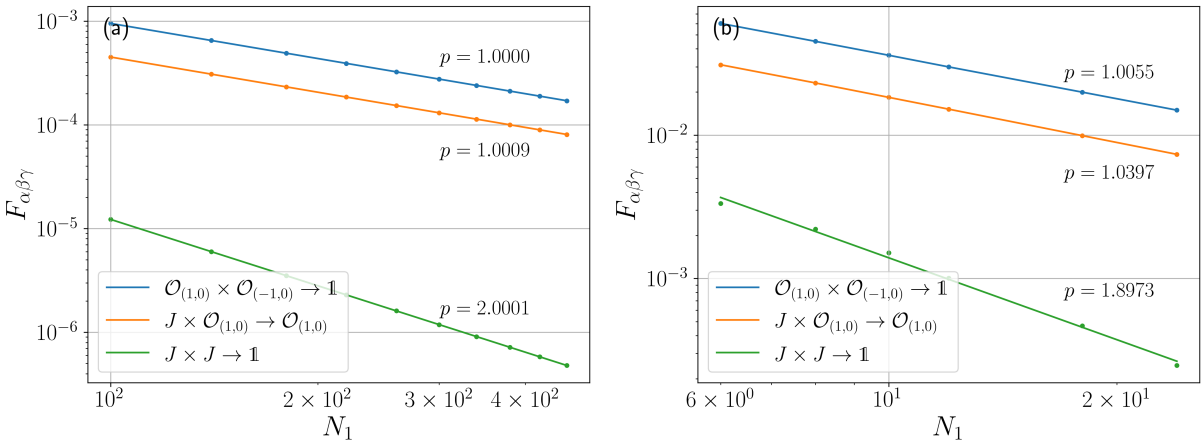

Figure 5.5: Finite-size correction of wavefunction overlap of the XXZ model at (a) $\Delta = 0$ and (b) $\Delta = 1/2$, for the three channels under discussion. At the free fermion point $\Delta = 0$, the system size is chosen in the range $N_1 \in [100, 500)$. The discrepancy between the theory and numerical value is less than 0.1%. At $\Delta = 1/2$, we resort to tensor network method and the system size is chosen in the range $N_1 \in [6, 24]$. Due to the relatively small system size, the largest discrepancy is 5.1%.

Since the XXZ model has a $U(1)$ global symmetry (which corresponds to m charge conservation in primary operators $\mathcal{O}_{(m,n)}$), the expansion Eq. (5.45) does not contain $\tau_{(\mathcal{O}_i,\hat{\chi})}, i =$

$1, 2, 3, \chi = 0, 1$. As a first example, consider the OPE channel

$$\mathcal{O}_{(1,0)} \times \mathcal{O}_{(-1,0)} \to \mathbb{1}. \tag{5.86}$$

From Eq. (5.82), $\mathcal{O}_{(1,0)}$ belongs to the conformal family $\mathcal{O}_1$ and $\mathcal{O}_{(-1,0)}$ belongs to the conformal family $\mathcal{O}_3$. We thus need to find τ_p such that $[(\mathcal{O}_1, \mathcal{O}_3)] \times [\tau_p] \to [\tau_{(\mathbb{1},\hat{0})}]$ is valid in the orbifold theory, namely, $C_{(\mathcal{O}_1,\mathcal{O}_3),\tau_p,(\mathbb{1},\hat{0})}$ is non-zero. Using the crossing symmetry $C_{(\mathcal{O}_1,\mathcal{O}_3),\tau_p,(\mathbb{1},\hat{0})} = C_{(\mathcal{O}_1,\mathcal{O}_3),(\mathbb{1},\hat{0}),\tau_{p^*}}$ and orbifold fusion rule

$$[(\mathcal{O}_1, \mathcal{O}_3)] \times [\tau_{(\mathbb{1},\hat{0})}] = [\tau_{(\mathbb{1},\hat{0})}] + [\tau_{(\mathbb{1},\hat{1})}], \tag{5.87}$$

we see τ_p can be either $\tau_{(\mathbb{1},\hat{0})}$ or $\tau_{(\mathbb{1},\hat{1})}$. The scaling dimension of the leading term $\tau_{(\mathbb{1},\hat{0})}$ gives the leading scaling $\Delta = \frac{1}{8}$, which agrees with $c/8$. The difference between the scaling dimensions of $\tau_{(\mathbb{1},\hat{0})}$ and $\tau_{(\mathbb{1},\hat{1})}$ gives the finite-size correction with power $p = \frac{9}{8} - \frac{1}{8} = 1$.

We may also consider the channel involving current operator J, which belongs to the conformal family $\mathbb{1}$. Consider the OPE channel

$$J \times \mathcal{O}_{(1,0)} \to \mathcal{O}_{(1,0)}, \tag{5.88}$$

we need to find non-zero $C_{(\mathbb{1},\mathcal{O}_1),\tau_p,(\mathcal{O}_1,\hat{0})}$, which is $C_{(\mathbb{1},\mathcal{O}_1),(\mathcal{O}_3,\hat{0}),\tau_{p^*}}$ by crossing symmetry. The relevant orbifold fusion rule is

$$[(\mathbb{1}, \mathcal{O}_1)] \times [\tau_{(\mathcal{O}_3,\hat{0})}] = [\tau_{(\mathbb{1},\hat{0})}] + [\tau_{(\mathbb{1},\hat{1})}]. \tag{5.89}$$

Again, this gives the finite-size correction with power $p = 1$ as the previous example.

In the third example, let us consider

$$J \times J \to \mathbb{1}, \tag{5.90}$$

where we need to find non-zero $C_{(\mathbb{1},\mathbb{1})_s,\tau_p,(\mathbb{1},\hat{0})}$. There is only one valid $\tau_p = [\tau_{(\mathbb{1},\hat{0})}]$ from

$$[(\mathbb{1},\mathbb{1})_s] \times [\tau_{(\mathbb{1},\hat{0})}] = [\tau_{(\mathbb{1},\hat{0})}]. \tag{5.91}$$

In this case, we observe $p = 2$, which means a level-2 descendant in the expansion Eq. (5.45) is responsible. Similarly, the process $J \times \mathcal{O}_{(2,1)} \to \mathcal{O}_{(2,1)}$ also has correction $p = 2$ using the same orbifold fusion rule. We summarize the numerical results for the above three channels in Fig. 5.5(a).

Moving away from the free fermion radius, we have to resort to exact diagonalization or tensor network methods. We have examined the case of $R = \sqrt{6}$ (namely, $\Delta = 1/2$) where the system size is chosen in the range $N_1 \in [6, 24]$. The results of finite-size correction exponents for the above three channels are shown in Fig. 5.5(b). We observe the fitting results agree with analytical predictions, with the largest discrepancy being 5.1%. The discrepancy is relatively larger for the channel involving higher energy states, as what usually happens for finite-size corrections in CFT; the state corresponding to J has higher energy than the states corresponding to $\mathcal{O}_{(1,0)},\ \mathcal{O}_{(-1,0)}$. The numerical results at $R = \sqrt{6}$ demonstrate the applicability of our method to interacting lattice models.

5.4 Applications to the Haagerup model

In the previous section, we have examined the universal finite-size corrections in the Ising model and XXZ model. We now move on to the Haagerup model, which is a recently proposed [177, 178] anyonic chain that is believed to be described by a CFT with $c \sim 2$. The input data for the lattice Hamiltonian is the $\mathcal{H}_3$ *fusion category*. The fusion rule in this category is non-commutative thus does not admit braiding. The operator content of the Haagerup CFT is still obscure due to strong finite-size corrections as only very small systems are numerically accessible. Due to its $\mathbb{Z}_3$ global symmetry, one of the candidate theory is the

$\mathbb{Z}_3$ orbifold of toroidal compactified sigma model, with central charge $c = 2$. The candidate has two current operators J and J^* with scaling dimension and conformal spin $\Delta = s = 1$. The holomorphic nature of the current operators strongly constrain possible fusion channels involving these operators, which enables us to check it numerically.

In what follows, we use the wavefunction overlaps to compute central charge, conformal dimensions of certain primary states. We present strong evidence that the lowest operator with $s = 1$ is not a holomorphic field, thus ruling out the possibility of this $\mathbb{Z}_3$ orbifold. Nevertheless, we will denote the operators as J and J^*. Our results give an upper bound of the scaling dimension $\Delta_J \leq 1.4$, and indicate that the central charge is roughly $c \approx 2.1$. Our code for numerical calculation is available in GitHub [4].

5.4.1 Haagerup anyon chain and spectrum

$\mathcal{H}_3$ fusion category

In the following we give a short review on $\mathcal{H}_3$ fusion category [202, 203]. There are six simple objects (anyons) in this category:

$$1, a, a^2, \rho, a\rho, a^2\rho. \tag{5.92}$$

We will use a^2 and a^* interchangeably. $1, a, a^*$ are invertible objects and $\rho, a\rho, a^*\rho$ are non-invertible simple objects. Their quantum dimensions are: $d_1 = d_a = d_{a^*} = 1$, $d_\rho = d_{a\rho} = d_{a^*\rho} = \frac{3+\sqrt{13}}{2}$. The non-trivial fusion rules read:

$$a^3 = 1, \quad a\rho = \rho a^* \quad \rho^2 = 1 + (1 + a + a^2)\rho. \tag{5.93}$$

4. `https://github.com/YuhanLiuSYSU/Haagerup_wave_function_overlap`

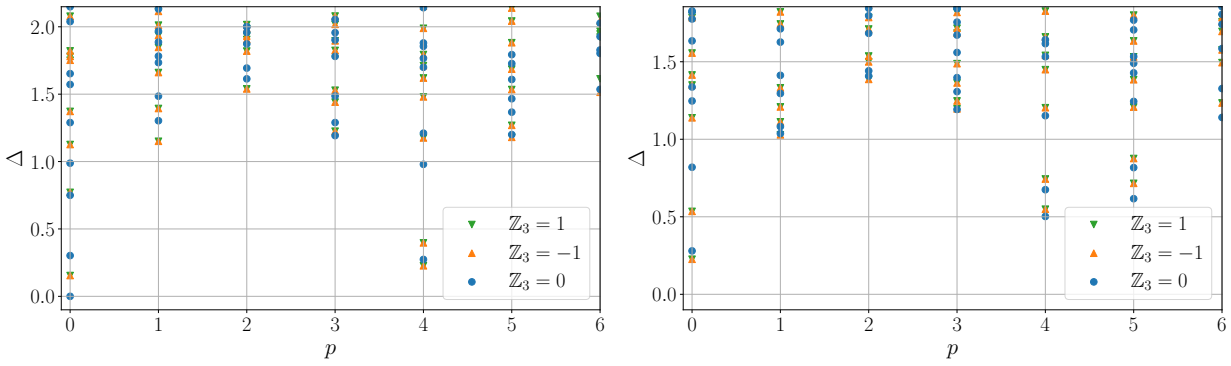

Figure 5.6: Energy-momentum spectrum of the Haagerup model at (a) $N = 12$, and (b) $N = 13$.

Note that for example, a and ρ does not commute, $a\rho \neq \rho a$. Given the fusion rule, the F-symbols can be determined by the pentagon equations (self-consistency requirement).

Anyon chain construction and spectrum

Given a fusion category as input data, the anyon chain Hamiltonian is constructed using the fusion rule and the F-symbol [204, 205, 177]. The Hilbert space consists of the anyon chains $|a_1, a_2, \cdots, a_N\rangle$ that satisfy the following fusion constraint:

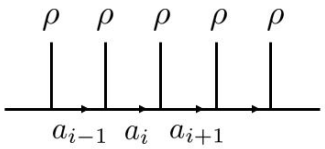

(5.94)

Namely, the fusion $a_i \times \rho$ needs to contain ρ. We assume periodic boundary condition for the anyon chain.

The Hamiltonian is then constructed as sum of projectors acting on three subsequent

anyon sites [177, 204]:

$$
\begin{aligned}
&H = -\sum_i P_\rho^{(i)}, \\
&P_c^{(i)} |a_{i-1} a_i a_{i+1}\rangle = \sum_{a_i'} [F_{a_{i+1}}^{a_{i-1}\rho\rho}]_{a_i c} [F_{a_{i+1}}^{a_{i-1}\rho\rho}]^*_{a_i' c} |a_{i-1} a_i' a_{i+1}\rangle.
\end{aligned}
\tag{5.95}
$$

The projector P_ρ projects the fusion $\rho \times \rho$ into channel ρ. The above anyonic chain construction is standard, and can be regarded as a generalization of the spin-1/2 Heisenberg chain [205].

It is nontrivial and has to be verified case-by-case whether an anyonic chain Hamiltonian corresponds to a lattice realization of a CFT. One should distinguish the input fusion category with the Moore-Seiberg tensor category of a rational CFT, where the object of the Moore-Seiberg tensor category are in one-to-one correspondence with primary operators which is not true for the input fusion category. For the Haagerup model, previous evidence of CFT comes from ground state energy and entanglement entropy [177]. We will see in the following that the ground state wavefunction overlap $A_{\mathbb{1}\mathbb{1}\mathbb{1}}$ provides another evidence for CFT with consistent central charge.

By the Haagerup fusion rules, the Hamiltonian has a global $\mathbb{Z}_3$ symmetry:

$$
\gamma : 1 \to a \to a^* \to 1, \quad \rho \to a\rho \to a^*\rho \to \rho. \tag{5.96}
$$

This can also be seen at the level of F-symbols. There is another intrinsic shift $\mathbb{Z}_3$ symmetry s, that is, translation by $3n, 3n+1$ and $3n+2$ sites. The shift symmetry is nontrivial because the energy spectrum depends on N mod 3. Similar phenomena occur in the antiferromagnetic Ising model, which we review in Appendix B.2. To gauge the shift $\mathbb{Z}_3$ symmetry s, we keep only the states near $P = 0$ at system size $N = 3n, 3n+1, 3n+2$, which correspond to the original Hilbert space $\mathcal{H}$, shift $\mathbb{Z}_3$ twisted Hilbert space $\mathcal{H}_s$ and $\mathcal{H}_{s^2}$. It is clear from the $\mathbb{Z}_3$

symmetry that $\mathcal{H}_s = \mathcal{H}_{s^2}$.

The energy-momentum spectrum of $N = 12$ ($\mathcal{H}$) and $N = 13$ ($\mathcal{H}_s$) anyon chain is shown in Fig. 5.6. To better understand the conformal towers, we also use the Koo-Saleur lattice Virasoro generators as in Refs. [206, 207, 167],

$$H_n = \frac{N}{2\pi} \sum_{j=1}^{N} h_j e^{ijn\frac{2\pi}{N}}, \tag{5.97}$$

where h_j is the Hamiltonian density operator at site j. These operators correspond to linear combinations of the Virasoro generators,

$$H_n = L_n + \bar{L}_{-n} - \frac{c}{12}\delta_{n,0}. \tag{5.98}$$

There are several numerical observations with the Koo-Saleur generators:

1. There is only one spin-2 low-energy state that has nonzero overlap with $H_{-2}|\mathbb{1}\rangle$, which we identify as the stress tensor state $|T\rangle$. This is used to normalize the energies in the plot by utilizing $|T\rangle$ has $\Delta = 2$. H_{-1} acting on $|\mathbb{1}\rangle$ gives zero overlap for every state in the spectrum, confirming this state is the conformal vacuum.

2. In the spectrum of $N = 13$ chain (shift $\mathbb{Z}_3$ twisted sector $\mathcal{H}_s$), there exists a state with $\mathbb{Z}_3 = 0$ being close to $P = 1, \Delta = 1$. This is proposed to be the chiral current operator J. There is a similar state in the $N = 14$ chain, which is proposed to be J^*.

3. In the $N = 13$ chain, H_{-1} acting on the lowest primary state in $\mathbb{Z}_3 = 0, P = 0$ gives the largest overlap with the second lowest state in $\mathbb{Z}_3 = 0, P = 1$. This overlap is significantly larger than that with the first excited state with $\mathbb{Z}_3 = 0, P = 1$. This indicates the lowest state in $\mathbb{Z}_3 = 0, P = 1$ is not a descendant of the primary state. Thus it is a primary state.

$\mathbb{Z}_3$ orbifold of sigma model

The $\mathbb{Z}_3$ orbifold theory referred in this paper is the nonlinear sigma model on torus target space modded out the $\mathbb{Z}_3$ rotational symmetry on the target space. We will briefly review the the relevant features of this CFT below.

Let us start with the toroidal compactified boson theory, namely, there are two bosonic fields and the target space is T^2 [208]. Recall that in the familiar example of compactified boson, the target space is S^1, which is equivalent to saying that the boson field Φ can only take value in $\Phi \in [0, 2\pi R)$, and $\Phi \sim \Phi + 2n\pi R, n \in \mathbb{Z}$ are identified. Analogously, the toroidal compactification free boson theory has two massless scalar fields $\Phi^\mu, \mu \in \{1, 2\}$. For the target space torus T^2 generated by $\boldsymbol{\lambda}_1, \boldsymbol{\lambda}_2$, we need to identify:

$$\begin{pmatrix} \Phi^1 \\ \Phi^2 \end{pmatrix} \sim \begin{pmatrix} \Phi^1 \\ \Phi^2 \end{pmatrix} + n_1\boldsymbol{\lambda}_1 + n_2\boldsymbol{\lambda}_2, \quad n_1 \in \mathbb{Z}, n_2 \in \mathbb{Z}. \tag{5.99}$$

This compactification gives constraint on the momentum modes $p, \bar{p}$, from which one can write down the partition function [208].

When the target space torus T^2 is generated by basis vectors proportional to $\boldsymbol{\lambda}_1 = (1, 0)^T$, $\boldsymbol{\lambda}_2 = (-\frac{1}{2}, \frac{\sqrt{3}}{2})^T$, the theory has an additional $\mathbb{Z}_3$ rotational symmetry. Gauging (modding out) this $\mathbb{Z}_3$ rotational symmetry gives the $\mathbb{Z}_3$ orbifold theory. The partition function of this rational CFT can be written out explicitly, from which we can read out the operator content. We list the several important features that are relevant to our problem, and refer the interested readers to Ref. [208] for more details. The features are:

1. The spectrum includes two chiral current operators: $J_1 = i\partial\Phi^1$ and $J_2 = i\partial\Phi^2$. This is true for all toroidal compactified theory, independent of the $\mathbb{Z}_3$ symmetry.

2. In the $\mathbb{Z}_3$ twisted sector, the lowest energy state is three-fold degenerate, with $(h, \bar{h}) = (\frac{1}{9}, \frac{1}{9})$. Similar feature appears in $\mathbb{Z}_3^2$ twisted sector. The degeneracy comes from the

three target space fixed points under rotation.

The exact degeneracy in the second feature is hard to confirm numerically, as the states suffer from strong finite-size corrections and the energies do not exactly coincide. However, the wavefunction overlap provides a way to check the first feature, with relatively small finite-size corrections. We will see below that the overlap indicates that the lowest spin-1 operator is not a current, which contradicts the proposal that Haagerup model is described by this $\mathbb{Z}_3$ orbifold.

5.4.2 Wavefunction overlaps

We now turn to the wavefunction overlaps, from which we can extract conformal data, such as central charge, scaling dimensions and OPE coefficients. We perform exact diagonalization for small system sizes $N \leq 15$ and the periodic uniform matrix product state (puMPS) techniques for up to $N = 27$.

Firstly, from the conformal vacuum state overlap, we can extract the central charge via:

$$A_{\mathbb{1}\mathbb{1}\mathbb{1}} \propto N^{-\frac{c}{8}}. \tag{5.100}$$

We obtain $c = 2.06$, in a reasonable agreement with previous results, which give $c = 2.03$ [178] and $c = 2.11$ [177]. If we discard the data from the smallest system size ($N = 3$), then we obtain $c = 2.12$ by fitting the remaining three points. Given that current numerical methods all give $c > 2$, it is possible that the true central charge is not exactly at $c = 2$, but $c \approx 2.1$.

Secondly, we compute the scaling dimension of the first spinless $\mathbb{Z}_3$ neutral excited state, which we denote as $|\varepsilon\rangle$. The relevant overlap is

$$\frac{A_{\mathbb{1}\mathbb{1}\varepsilon}}{A_{\mathbb{1}\mathbb{1}\mathbb{1}}} \propto N^{-\Delta_\varepsilon/2}. \tag{5.101}$$

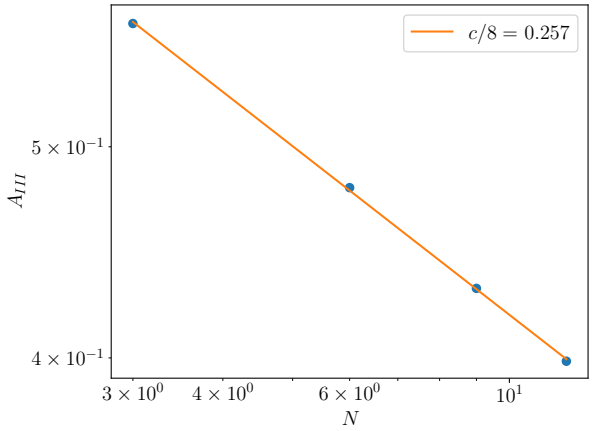

Figure 5.7: Ground state overlap $A_{\mathbb{1}\mathbb{1}\mathbb{1}}$ for the Haagerup model with N, N and $2N$ spins, where $N = 3, 6, 9, 12$. The first two points are obtained by exact diagonalization, and the last two points are obtained by puMPS with maximal bond dimension $D = 66$.

As shown in Fig. 5.8, we obtain $\Delta_\varepsilon \approx 0.26$. This agrees with the energy spectrum with reasonable accuracy.

Thirdly, we compute the $A_{JJ^*\mathbb{1}}$ where $|J\rangle$ is the lowest eigenstate with $s_J = 1$ at size $N = 3n+1$. Similarly, J^* is the lowest eigenstate with $s_{J^*} = 1$ at size $N = 3n+2$. Suppose the operator J and J^* are chiral currents with scaling dimension 1, then they would be Kac-Moody descendants of $\mathbb{1}$, and the wavefunction overlap $A_{JJ^*\mathbb{1}}$ would only involve one fusion channel in the cyclic orbifold,

$$[(\mathbb{1}, \mathbb{1})_s] \times [\tau_{(\mathbb{1},\hat{0})}] = [\tau_{(\mathbb{1},\hat{0})}]. \tag{5.102}$$

This implies that the finite-size corrections to $A_{JJ^*\mathbb{1}}$ would come from descendants of $\tau_{(\mathbb{1},\hat{0})}$, thus we would expect

$$\frac{A_{JJ^*\mathbb{1}}}{A_{\mathbb{1}\mathbb{1}\mathbb{1}}} = \frac{1}{16} + O(N^{-2}) \tag{5.103}$$

similar to the XXZ model considered in Sec. 5.3. However, our numerical result shown in Fig. 5.9 violates Eq. (5.103) as the extrapolation gives $A_{JJ^*\mathbb{1}}/A_{\mathbb{1}\mathbb{1}\mathbb{1}} \approx 0.02$. Therefore we

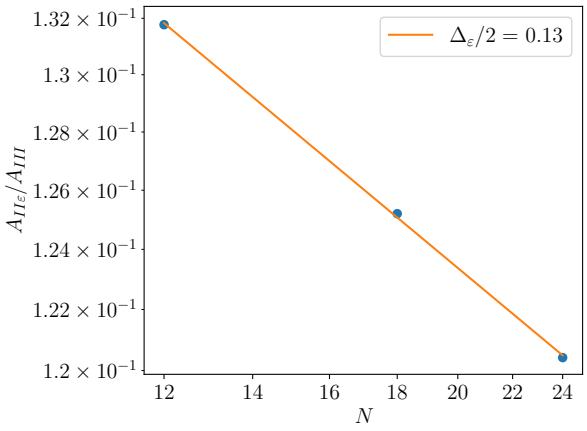

Figure 5.8: $A_{\mathbb{1}\mathbb{1}\varepsilon}/A_{\mathbb{1}\mathbb{1}\mathbb{1}}$ for the Haagerup model. The states are taken from the Haagerup model with sizes $3n, 3n$ and $N = 6n$, where $n = 2, 3, 4$.

can conclude that J is not a current. The scaling dimension can be estimated by

$$\Delta_J = -\frac{1}{4}\log_2 \frac{A_{JJ^*\mathbb{1}}}{A_{\mathbb{1}\mathbb{1}\mathbb{1}}}, \tag{5.104}$$

which gives $\Delta_J \approx 1.4$. Considering the error in finite size extrapolations, we conclude that $\Delta_J \leq 1.4$.

5.5 Summary

In this work we have studied wavefunction overlaps $A_{\alpha\beta\gamma} = \langle\phi_\gamma|\phi_\alpha\phi_\beta\rangle$ of a critical quantum spin chain, where the three states are primary states of the spin chain. Through a conformal mapping from the three-sided cylinder to the complex plane, we derive the relation between OPE coefficients $C_{\alpha\beta\gamma}$ and the ratio of wavefunction overlap $A_{\alpha\beta\gamma}/A_{\mathbb{1}\mathbb{1}\mathbb{1}}$. In order to study the finite-size corrections, we rewrite $A_{\alpha\beta\gamma}$ as a path integral of the cyclic orbifold on the cylinder, with twist operator insertion at the branch points. We then show that finite-size correction exponents $p_{\alpha\beta\gamma}$ are universal, and are completely determined by the orbifold operator content. As a benchmark, we extracted OPE coefficients $C_{\alpha\beta\gamma}$ and finite-size

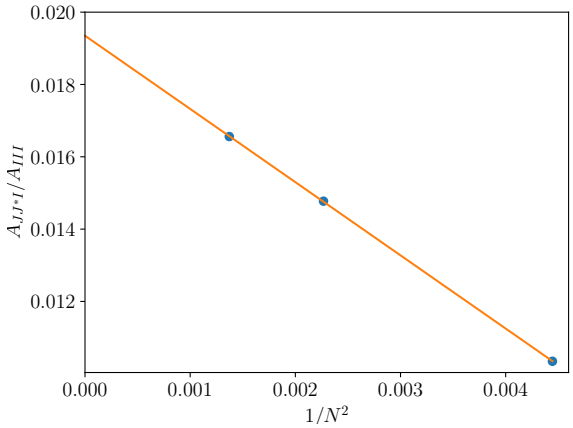

Figure 5.9: $A_{JJ^*\mathbb{1}}/A_{\mathbb{1}\mathbb{1}\mathbb{1}}$ for the Haagerup model. In $A_{JJ^*\mathbb{1}}$ the three states are taken from the Haagerup model with sizes $3n+1, 3n+2$ and $N = 6n+3$. In $A_{\mathbb{1}\mathbb{1}\mathbb{1}}$, the three states are taken from the Haagerup model with sizes $3n, 3n+3$ and $N = 6n+3$. The three points in the plot correspond to $n = 2, 3, 4$.

correction exponents $p_{\alpha\beta\gamma}$ for the Ising model and the XXZ model and found that they agree with the prediction using the cyclic orbifold.

We then illustrate an application of our method to a less-known CFT. We have computed the wavefunction overlaps for the Haagerup model, and found that it has central charge $c \approx 2.1$, lowest spinless primary operator with dimension $\Delta_\varepsilon \approx 0.3$ and lowest spin-1 primary operator with dimension $\Delta_J \leq 1.4$. The fact that $A_{JJ^*\mathbb{1}}/A_{\mathbb{1}\mathbb{1}\mathbb{1}}$ is not close to $1/16$ provides negative evidence against the conjecture that J is a current operator, so the Haagerup CFT is likely more complicated than the free boson $\mathbb{Z}_3$ orbifold.

As noted in Ref. [169], the overlap $A_{\alpha\beta\gamma}$ can be viewed as a wavefunction of a multiboundary wormhole state. In this work we interpret the same overlap as a three-point correlation function involving twist operators in the cyclic orbifold. It would be interesting for future work to explore the holographic interpretation of twist operators and cyclic orbifold.

Given three primary states, it is possible to construct other overlaps that are inequivalent to the three-sided cylinder, but nevertheless also contain similar universal information of the CFT. One useful example is given in Ref. [45], where the authors consider the vertex state

that describes a trisection of a two-dimensional chiral topological phase. It is shown in the appendix of [198] that conformal data, such as central charge and OPE coefficients, can be extracted from the wavefunction of the vertex state, with finite-size corrections that appear universal. It is an open question whether the finite-size corrections to these wavefunction overlaps are indeed universal, and if so, what operators are responsible. More generally, given a bunch of primary states, it is possible to construct many different overlaps, which may correspond to multi-point correlation functions of the CFT. The finite-size corrections remain elusive at this point.

In conclusion, we have developed a method based on wavefunction overlaps that compute conformal data solely from low-energy eigenstates of a critical quantum spin chain. We have shown that the finite-size corrections are universal, which provides consistency conditions on the wavefunction overlaps at finite sizes. It is interesting both practically and conceptually. Practically, the method is useful for identifying new CFTs realized in lattice models without too much prior knowledge. Conceptually, the method relates wavefunction overlaps to operator fusion in the cyclic orbifold, which may be easily generalized.

CHAPTER 6

SUMMARY AND OUTLOOK

In this thesis, we develop the quantum entanglement and conformal field theory toolkits and use them to study various systems, unveiling new universal fingerprints. Recently, more and more interest are drawn to the non-equilibrium phases of matter. Examples include the quench dynamics of unitary evolution, the dynamics of the system in the presence of a bath which can be described by the Lindbladian master equation, and the systems described by effective non-Hermitian Hamiltonian, to name but a few. Analogously to the spatial entanglement scaling, one can study the temporal entanglement scaling of such dynamical processes, which gives rise to new phases of matter.

The phase transition of dynamical systems is proposed to be described by more exotic conformal field theory. For example, the phase transition point of the non-Hermitian Hamiltonian is proposed to be captured by non-unitary conformal field theory, and the phase transition point of measurement-induced phase transition is proposed to be captured by logarithmic conformal field theory. However, little is understood about these exotic CFTs. In fact, many of the proposals are based on entanglement entropy scaling; the full CFT context is yet to be understood and remains a non-trivial task.

Finally, the experimental detection of bipartite and multipartite entanglement remains an important question. Up till today, experimentalists can measure entanglement witnesses and second Renyi entropy in solid state and cold atom systems; the measurement protocols are cleverly designed according to the experimental platforms. It is a crucial task to design protocols to measure the universal entanglement piece such as the topological entanglement entropy and the Markov gap in the experimental platforms.

APPENDIX A

DETAILS OF VERTEX STATE CALCULATION

A.1 Details of Neumann coefficient method

A.1.1 Different choice of the branch cuts in the R-R sector

For the vertex state for bipartition in the R-R sector, we can work alternatively with the following choice of the g^{IJ} function:

$$g^{IJ}_{\sigma-\sigma} = \frac{1}{2}\left[\sqrt{\frac{(\omega-\omega_{1,0})(\omega-\omega_{2,0})}{(\omega'-\omega_{1,0})(\omega'-\omega_{2,0})}} + (\omega \leftrightarrow \omega')\right]. \tag{A.1}$$

Both choices lead to the same vertex state as we demonstrate below. The choice we made in the main text is somewhat simpler, while this choice here is closer to the branch cuts we choose in our calculations in the R-R-R sectors for tripartition. Using $\omega_I = \omega_{I,0}(\frac{1+z}{1-z})$, and $\omega_{1,0} = i, \omega_{2,0} = -i$, the Neumann function is given by

$$\begin{aligned}
&R^{11} = R^{22} = \\
&\frac{\sqrt{zz'}}{z-z'}\frac{1}{2}\left[\sqrt{\frac{z}{z'}}\frac{1-z'}{1-z} + \sqrt{\frac{z'}{z}}\frac{1-z}{1-z'}\right] = \sum_{m\geq 1}\left(\frac{z'}{z}\right)^m + \frac{1}{2}\left[\sum_{n\geq 0} z^n - \sum_{n\geq 1}(z')^n\right], \\
&R^{12} = -R^{21} = \\
&\frac{i\sqrt{zz'}}{1-zz'}\frac{1}{2}\left[\sqrt{\frac{z}{z'}}\frac{1-z'}{1-z} + \sqrt{\frac{z'}{z}}\frac{1-z}{1-z'}\right] = (-i)\sum_{m>0}(zz')^m + \frac{i}{2}\left[\sum_{n>0} z^n + \sum_{n>0}(z')^n\right].
\end{aligned} \tag{A.2}$$

We note that we obtain the desired singular term $\sum_{m\geq 1}(z'/z)^m = \sum_{m\geq 1} e^{-im(\sigma-\sigma')}$ in R^{11} and R^{22}. From the expansion coefficients and use the same ansatz solution in Eq. (3.62), we

obtain the vertex state:

$$|V\rangle = \exp\left[-i\sum_{n\geq 1}\chi^1_{-n}\chi^2_{-n} + \sum_{n\geq 1}\left(\chi^1_{-n}\chi^1_0 + \chi^2_{-n}\chi^2_0 + i\chi^1_{-n}\chi^2_0 - i\chi^2_{-n}\chi^1_0\right)\right]|\Omega\rangle. \quad \text{(A.3)}$$

This is the same solution as Eq. (3.33) with the additional requirement $(\chi^1_0 + i\chi^2_0)|\Omega\rangle = 0$. Similarly, for the Dirac fermion field in the R-R sector, one can show the solutions from the two choices of the branch cuts also match.

A.1.2 Verification of the boundary condition in the R sector

In this subsection, we verify that the R-R-R sector vertex state ansatz satisfies the boundary condition for real and complex fermion. The verification for the NS-R two-string solution simply parallels the proof below[68], which we shall omit.

For the Majorana fermion case, the ansatz solution is:

$$|V\rangle = \exp\left[\frac{1}{2}\sum_{m,n\geq 1}\chi^I_{-m}R^{IJ}_{mn}\chi^J_{-n} + 2\sum_{m,n\geq 1}\chi^I_{-m}R^{IJ}_{m0}\chi^J_0\right]|\Omega\rangle. \quad \text{(A.4)}$$

Let us denote $A = \sum_{m,n\geq 1}\frac{1}{2}\chi^I_{-m}R^{IJ}_{mn}\chi^J_{-n} + \sum_{m\geq 1}2\chi^I_{-m}R^{IJ}_{m0}\chi^J_0$. To show explicitly that this state satisfies the boundary condition, we define

$$D^I = \sum_{m\geq 1}2\chi^J_{-m}R^{JI}_{m0}. \quad \text{(A.5)}$$

Using

$$\begin{aligned}
\chi^I_p|V\rangle &= \sum_{n\geq 1}R^{IJ}_{pn}\chi^J_{-n}|V\rangle + \exp(A)\left[2R^{IJ}_{p0}(\chi^J_0 - \sum_{m\geq 1}\chi^K_{-m}R^{KJ}_{m0})\right]|\Omega\rangle, \\
\chi^I_0|V\rangle &= \exp(A)\left[\chi^I_0 - \sum_{m\geq 1}2\chi^J_{-m}R^{JI}_{m0}\right]|\Omega\rangle,
\end{aligned} \quad \text{(A.6)}$$

one can check the following relation:

$$\begin{aligned}\chi^I(\sigma)|V\rangle &= \sum_{p\geq 1}\chi^I_p e^{-ip\sigma}|V\rangle + \chi^I_0|V\rangle + \sum_{p\geq 1}\chi^I_{-p}e^{ip\sigma}|V\rangle \\ &= \sum_{p,n\geq 1} e^{-ip\sigma}R^{IJ}_{pn}\chi^J_{-n}|V\rangle + \sum_{p\geq 1}e^{-ip\sigma}\exp(A)\left[2R^{IJ}_{p0}(\chi^J_0 - \sum_{m\geq 1}\chi^K_{-m}R^{KJ}_{m0})\right]|\Omega\rangle \\ &\quad + \chi^I_0|V\rangle + \sum_{p\geq 1}\chi^I_{-p}e^{ip\sigma}|V\rangle.\end{aligned} \tag{A.7}$$

On the other hand, defining

$$\tilde{\chi}^I_{cr.} = \sum_{n\geq 1}\chi^I_{-n}e^{in\sigma} + 2\chi^I_0 + D^I, \tag{A.8}$$

and using

$$(D^I + 2\chi^I_0)|V\rangle = \exp(A)\left[2\chi^I_0 - \sum_{m\geq 1}2\chi^J_{-m}R^{JI}_{m0}\right]|\Omega\rangle, \tag{A.9}$$

one can check,

$$\begin{aligned}&\int\frac{d\sigma'}{2\pi}R^{IJ}(\sigma,\sigma')\tilde{\chi}^J_{cr.}(\sigma')|V\rangle \\ &= \sum_{m,n\geq 1}e^{-im\sigma}R^{IJ}_{mn}\chi^J_{-n}|V\rangle + \sum_{m\geq 1}e^{-im\sigma}R^{IJ}_{m0}(D^J + 2\chi^J_0)|V\rangle \\ &\quad + \sum_{n\geq 1}R^{IJ}_{0n}\chi^J_{-n}|V\rangle + \delta_{IJ}\frac{1}{2}(D^J + 2\chi^J_0)|V\rangle + \sum_{m\geq 1}\chi^I_{-m}e^{im\sigma}|V\rangle \\ &= \chi^I(\sigma)|V\rangle,\end{aligned} \tag{A.10}$$

where we exploited the fact $R^{IJ}_{m0} = -R^{JI}_{0m}$ and $R^{IJ}_{00} = \delta_{IJ}\frac{1}{2}$. Finally, using the property $R^{I+1,J}(\sigma,\sigma') = iR^{I,J}(2\pi-\sigma,\sigma')$, it ensures that χ satisfies the desired boundary condition

$$\chi^{I+1}(\sigma)|V\rangle = i\chi^I(2\pi-\sigma)|V\rangle. \tag{A.11}$$

For the complex fermion, we start from the ansatz solution in Eq. (3.64):

$$|V\rangle = \exp\left(\sum_{m,n\geq 1} g^I_{-m} R^{IJ}_{mn} g^{\dagger,J}_n + \sum_{m\geq 1} 2R^{IJ}_{m0}(g^I_{-m} g^{\dagger,J}_0 + g^{\dagger,I}_m g^J_0)\right)|\Omega\rangle. \tag{A.12}$$

We can verify the following relations:

$$\begin{aligned} g^I(\sigma)|V\rangle &= \int \frac{d\sigma'}{2\pi} R^{IJ}(\sigma,\sigma')\tilde{g}^J_{cr.}(\sigma')|V\rangle, \\ g^{\dagger,I}(\sigma)|V\rangle &= \int \frac{d\sigma'}{2\pi} R^{IJ}(\sigma,\sigma')\tilde{g}^{\dagger,J}_{cr.}(\sigma')|V\rangle, \end{aligned} \tag{A.13}$$

where

$$\begin{aligned} \tilde{g}^I_{cr.}(\sigma) &= \sum_{n\geq 1} g^I_{-n} e^{in\sigma} + (2g^I_0 + D^I), \quad D^I = \sum_{m\geq 1} 2R^{JI}_{m0} g^J_{-m} \\ \tilde{g}^{\dagger,J}_{cr.}(\sigma') &= \sum_{n\geq 1} g^{\dagger,I}_n e^{in\sigma} + (2g^{\dagger,I}_0 + D^{\dagger,I}), \quad D^{\dagger,I} = \sum_{m\geq 1} 2R^{JI}_{m0} g^{\dagger,J}_m. \end{aligned} \tag{A.14}$$

These relations allow us to verify the boundary condition:

$$\begin{aligned} g^{I+1}(\sigma)|V\rangle &= \int \frac{d\sigma'}{2\pi} R^{I+1,J}(\sigma,\sigma')\tilde{g}^J_{cr.}(\sigma')|V\rangle \\ &= i\int \frac{d\sigma'}{2\pi} R^{IJ}(2\pi-\sigma,\sigma')\tilde{g}^J_{cr.}(\sigma')|V\rangle \\ &= ig^I(2\pi-\sigma)|V\rangle. \end{aligned} \tag{A.15}$$

Similarly, for $g^\dagger$, we can verify $g^{\dagger I+1}(\sigma)|V\rangle = ig^{\dagger I}(2\pi-\sigma)|V\rangle$.

A.1.3 Tripartition: Explicit form of the Neumann coefficients in the NS-NS-NS sector

The explicit form of the Neumann coefficient matrix K in the NS-NS-NS sector is derived following the methods of Ref. [65] and is summarized below:

$$
\begin{aligned}
&K = I_3 \otimes K^{aa} + J_+ \otimes K^{a,a+1} + J_- \otimes K^{a,a-1},\\
&I_{rs} = \begin{cases} \left(\frac{-m}{n+m+1} + \frac{-m}{n-m}\right) u_n u_m & n = \text{even}, m = \text{odd} \\ \left(\frac{n}{n+m+1} - \frac{n}{n-m}\right) u_n u_m & n = \text{odd}, m = \text{even} \end{cases},\\
&K^{aa}_{rs} = \frac{1}{3} I_{rs} + \left[\frac{M^+_{r-1/2,s-1/2}}{r+s} + \frac{M^-_{r-1/2,s-1/2}}{r-s}\right],\\
&M^+_{nm} = -\left[(n+1) g_{n+1} (m+1) g_{m+1} - n g_n m g_m\right] \cdot \left[(-1)^n - (-1)^m\right],\\
&M^-_{nm} = -\left[(n g_n (m+1) g_{m+1} - (n+1) g_{n+1} m g_m\right] \cdot \left[(-1)^n - (-1)^m\right],\\
&K^{a,a+1}_{rs} = \frac{1}{2} I_{rs} - \frac{1}{2} K^{aa}_{rs} - \frac{(-i)}{2}\sqrt{3}\left[\frac{\bar{M}^+_{r-1/2,s-1/2}}{r+s} + \frac{\bar{M}^-_{r-1/2,s-1/2}}{r-s}\right], \qquad \text{(A.16)}\\
&\bar{M}^+_{nm} = \left[(n+1) g_{n+1} (m+1) g_{m+1} - n g_n m g_m\right] \cdot \left[(-1)^n + (-1)^m\right],\\
&\bar{M}^-_{nm} = \left[(n g_n (m+1) g_{m+1} - (n+1) g_{n+1} m g_m\right] \cdot \left[(-1)^n + (-1)^m\right],\\
&K^{a,a-1}_{rs} = \frac{1}{2} I_{rs} - \frac{1}{2} K^{aa}_{rs} + \frac{(-i)}{2}\sqrt{3}\left[\frac{\bar{M}^+_{r-1/2,s-1/2}}{r+s} + \frac{\bar{M}^-_{r-1/2,s-1/2}}{r-s}\right],\\
&I_3 = \begin{pmatrix} 1 & 0 & 0 \\ 0 & 1 & 0 \\ 0 & 0 & 1 \end{pmatrix}, \quad J_+ = \begin{pmatrix} 0 & 1 & 0 \\ 0 & 0 & 1 \\ 1 & 0 & 0 \end{pmatrix}, \quad J_- = (J_+)^T,
\end{aligned}
$$

where $r = n + \frac{1}{2}, s = m + \frac{1}{2}$. u_n is the coefficient in the expansion of $(\frac{1+x}{1-x})^{1/2} = \sum_{n=0}^{\infty} u_n x^n$, which can be expressed compactly as $u_{2n} = u_{2n+1} = \binom{-\frac{1}{2}}{n}(-1)^n$. We note u_n satisfies the

recursion relation:

$$u_0 = u_1 = 1, \quad 2nu_{2n} = (2n-1)u_{2n-2}, \quad u_{2n} = u_{2n+1}. \tag{A.17}$$

g_n is the coefficient in $g(x) = (\frac{1+x}{1-x})^{1/6} = \sum_{n=0}^{\infty} g_n x^n$. Finally, $\Delta_n = \bar{M}^{-}_{nm}/(r-s)$ contained in the diagonal($r = s$) term should be evaluated using $\Delta_n = \frac{2}{3}\sum_{k=0}^{n}(-1)^{n-k}g_{n-k}^2$. We note, in addition, that the above coefficients differ from those appearing in Ref. [65] by factors of i. This is a consequence of the fact that we deal with free fermions with (anti-)periodic boundary conditions rather than open boundary conditions and hence different conformal maps ω_I [Eq. (3.16)] than those in Ref. [65]. One can also show explicitly that the singular terms are indeed $\delta_{IJ}\sum_{r\geq 1/2} e^{-ir(\sigma-\sigma')}$, as required.

A.1.4 Tetrapartition: Explicit form of solution with kink boundary condition

In this appendix, we write down the explicit form of vertex state solution $|V_k\rangle$ with kink boundary condition by finding the mode expansion of $K^{ij}(z, z')$ in Eq. (3.105):

$$K^{ij}(\sigma, \sigma') = \left(\frac{\partial w_i}{i\partial\sigma}\right)^{\frac{1}{2}} \frac{1}{w_i(\sigma) - w_j(\sigma')} \left(\frac{\partial w_j}{i\partial\sigma'}\right)^{\frac{1}{2}}. \tag{A.18}$$

Here w is the conformal transformation that brings p copies of half cylinders to a complex plane:

$$w_i(z) = w_{i,0}(\frac{1+z}{1-z})^{\frac{1}{2}}, \quad z = e^{i\sigma}, \tag{A.19}$$

with the constant terms satisfy $w_{i+1,0} = iw_{i,0}$. In the following we aim to write $K^{ij}(\sigma, \sigma')$ in terms of mode expansion $z^{n+\frac{1}{2}}, (z')^{m+\frac{1}{2}}$:

$$K^{ij}(\sigma, \sigma') = \sum_{n,m\geq 0} K^{ij}_{nm} z^{n+\frac{1}{2}}(z')^{m+\frac{1}{2}}. \tag{A.20}$$

To do so, we will write down the mode expansion of $(\frac{\partial w_i}{i\partial\sigma})^{1/2}$ and $\frac{1}{w_i(\sigma)-w_j(\sigma')}$.

Let us start from the mode expansion of $(\frac{\partial w_i}{i\partial\sigma})^{1/2}$. Using:

$$(\frac{\partial w_i}{i\partial\sigma}) = w_{i,0}\left(\frac{1-z}{1+z}\right)^{1/2}\frac{z}{(1-z)^2}, \tag{A.21}$$

and we denote

$$g(z) = (\frac{1+z}{1-z})^{\frac{1}{4}}, \tag{A.22}$$

the factor $(\frac{\partial w_i}{i\partial\sigma})^{1/2}$ can be rewritten as:

$$(\frac{\partial w_i}{i\partial\sigma})^{1/2} = (w_{i,0})^{1/2}\frac{z^{1/2}}{1-z}g(-z). \tag{A.23}$$

We thus need to obtain the mode expansion of $g(z)$.

For $g(z) = (\frac{1+z}{1-z})^{\frac{1}{4}} = \sum_{n\geq 0} g_n z^n$, the coefficients g_n satisfy the recursion relation:

$$\frac{1}{2}g_n = (n+1)g_{n+1} - (n-1)g_{n-1}, \tag{A.24}$$

and the first two coefficients are $g_0 = 1, g_1 = \frac{1}{2}$. This with the recursion relation allows us to obtain all the g_n.

Next, we would need to rewrite $\frac{1}{w_i(\sigma)-w_j(\sigma')}$. By using $\frac{1}{m-n} = \frac{m^3+m^2n+mn^2+n^3}{m^4-n^4}$ we can obtain:

$$\begin{aligned}
&\frac{1}{w_i(\sigma)-w_j(\sigma')} = \\
&\frac{(1-z)^{\frac{1}{2}}(1-z')^{\frac{1}{2}}}{4(z-z')(1-zz')}\Big\{w_{i,0}^3(1+z)^{\frac{3}{2}}(1-z')^{\frac{3}{2}} + w_{i,0}^2 w_{j,0}(1+z)(1-z')(1+z')^{\frac{1}{2}}(1-z)^{\frac{1}{2}} \\
&+w_{i,0}w_{j,0}^2(1+z)^{\frac{1}{2}}(1-z')^{\frac{1}{2}}(1+z')(1-z) + w_{j,0}^3(1+z')^{\frac{3}{2}}(1-z)^{\frac{3}{2}}\Big\}.
\end{aligned} \tag{A.25}$$

Combining (A.23) and (A.25), $K^{ij}(z,z')$ is rewritten as:

$$K^{ij}(z,z') = \left[(w_{i,0})^{\frac{1}{2}}(w_{j,0})^{\frac{1}{2}}\frac{z^{\frac{1}{2}}(z')^{\frac{1}{2}}}{4(z-z')(1-zz')}\right]\frac{g(-z)g(-z')}{(1-z)^{\frac{1}{2}}(1-z')^{\frac{1}{2}}}$$
$$\times\left\{w_{i,0}^3(1+z)^{\frac{3}{2}}(1-z')^{\frac{3}{2}} + w_{i,0}^2 w_{j,0}(1+z)(1-z')(1+z')^{\frac{1}{2}}(1-z)^{\frac{1}{2}}\right.$$
$$\left.+w_{i,0}w_{j,0}^2(1+z)^{\frac{1}{2}}(1-z')^{\frac{1}{2}}(1+z')(1-z) + w_{j,0}^3(1+z')^{\frac{3}{2}}(1-z)^{\frac{3}{2}}\right\}. \tag{A.26}$$

There are four terms in the curly bracket.

For the four-vertex state, i,j take values from $\{1,2,3,4\}$. Since K^{ij} only depends on the difference between i and j, there are four difference circumstances. For $i=j$:

$$K^{ii} = \frac{z^{\frac{1}{2}}(z')^{\frac{1}{2}}}{2(z-z')}[g(z)g(-z') + g(-z)g(z')]. \tag{A.27}$$

For $j=i+1$:

$$K^{i,i+1} = \frac{z^{1/2}(z')^{1/2}}{2(1-zz')}\left(\frac{w_{i,0}}{w_{j,0}}\right)^{-\frac{1}{2}}\left[g(z)g(-z') + ig(-z)g(z')\right]. \tag{A.28}$$

For $j=i+2$:

$$K^{i,i+2} = \frac{z^{\frac{1}{2}}(z')^{\frac{1}{2}}}{2(z-z')}\left(\frac{w_{i,0}}{w_{j,0}}\right)^{-\frac{1}{2}}[g(z)g(-z') - g(-z)g(z')]. \tag{A.29}$$

For $j=i+3$:

$$K^{i,i+3} = \frac{z^{1/2}(z')^{1/2}}{2(1-zz')}\left(\frac{w_{i,0}}{w_{j,0}}\right)^{-\frac{1}{2}}\left[g(z)g(-z') - ig(-z)g(z')\right]. \tag{A.30}$$

To evaluate the expansion coefficients of K^{ij}, we need to use the following two relations:

$$\begin{aligned}
&\frac{g(z)g(-z')}{2(z-z')} = \sum_{n,m\geq 0} P^{+}_{nm} z^n (z')^m + \text{sing.} \\
&\text{with} \quad P^{+}_{nm} = \frac{1}{n+m+1}[g_{n+1}g_{m+1}(n+1)(m+1) - g_n g_m nm](-1)^m,
\end{aligned} \tag{A.31}$$

where sing. denotes the singular term $\frac{1}{2(z-z')}$; and

$$\begin{aligned}
&\frac{g(z)g(-z')}{2(1-zz')} = \sum_{n,m\geq 0, n\neq m} P^{-}_{nm} z^n (z')^m + \sum_{m\geq 0} P_m z^m (z')^m \\
&\text{with} \quad P^{-}_{nm} = \begin{cases} \frac{1}{n-m}[n g_n (m+1) g_{m+1} - g_{n+1}(n+1) g_m m](-1)^m & n \neq m \\ \frac{1}{2}\sum_{0\leq n\leq m} g_n^2 (-1)^n & n = m \end{cases}.
\end{aligned} \tag{A.32}$$

The above two relations can be derived using:

$$(\partial_\rho + \partial_{\rho'} + 1)\frac{g(z)g(-z')}{z-z'} = -2(1+zz')\partial\partial'(g(z)g(-z'))$$

and

$$(\partial_\rho - \partial_{\rho'})\frac{g(z)g(-z')}{1-zz'} = -2(z+z')\partial\partial'(g(z)g(-z')).$$

By plugging (A.31) and (A.32) into (A.27) - (A.30), we obtain the mode expansion coefficients of $K^{ij}(z,z')$. We summarize the explicit expressions below.

Summary

To summarize, the mode expansions for K^{ij} are:

$$\begin{aligned}
K^{ii} &= \sum_{n\geq 0, m\geq 0} z^{n+\frac{1}{2}}(z')^{m+\frac{1}{2}}(P^+_{nm} - P^+_{mn}) + \sum_{n\geq 0}(\frac{z'}{z})^{n+\frac{1}{2}} \\
K^{i,i+1} &= \left(\frac{w_{i,0}}{w_{i+1,0}}\right)^{-\frac{1}{2}} \left[\sum_{n\geq 0, m\geq 0} z^{n+\frac{1}{2}}(z')^{m+\frac{1}{2}}(P^-_{nm} + iP^-_{mn})\right] \\
K^{i,i+2} &= \left(\frac{w_{i,0}}{w_{i+2,0}}\right)^{-\frac{1}{2}} \sum_{n\geq 0, m\geq 0} z^{n+\frac{1}{2}}(z')^{m+\frac{1}{2}}(P^+_{nm} + P^+_{mn}) \\
K^{i,i+3} &= \left(\frac{w_{i,0}}{w_{i+3,0}}\right)^{-\frac{1}{2}} \left[\sum_{n\geq 0, m\geq 0} z^{n+\frac{1}{2}}(z')^{m+\frac{1}{2}}(P^-_{nm} - iP^-_{mn})\right].
\end{aligned} \tag{A.33}$$

One nice feature is that the singular terms in K^{ii} take the form:

$$\frac{z^{\frac{1}{2}}(z')^{\frac{1}{2}}}{z - z'} = \sum_{n\geq 0}(\frac{z'}{z})^{n+\frac{1}{2}}, \tag{A.34}$$

which is what we desired in order to satisfy the boundary condition (as discussed near Eq. (3.107)).

Let's denote $K_0 = P^+ - (P^+)^T$, $K_1 = P^- + i(P^-)^T$, $K_2 = P^+ + (P^+)^T$ and $K_3 = P^- - i(P^-)^T$. The whole K matrix is:

$$K = \begin{pmatrix}
K_0 & \left(\frac{w_{1,0}}{w_{2,0}}\right)^{-\frac{1}{2}} K_1 & \left(\frac{w_{1,0}}{w_{3,0}}\right)^{-\frac{1}{2}} K_2 & \left(\frac{w_{1,0}}{w_{4,0}}\right)^{-\frac{1}{2}} K_3 \\
\left(\frac{w_{2,0}}{w_{1,0}}\right)^{-\frac{1}{2}} K_3 & K_0 & \left(\frac{w_{2,0}}{w_{3,0}}\right)^{-\frac{1}{2}} K_1 & \left(\frac{w_{2,0}}{w_{4,0}}\right)^{-\frac{1}{2}} K_2 \\
\left(\frac{w_{3,0}}{w_{1,0}}\right)^{-\frac{1}{2}} K_2 & \left(\frac{w_{3,0}}{w_{2,0}}\right)^{-\frac{1}{2}} K_3 & K_0 & \left(\frac{w_{3,0}}{w_{4,0}}\right)^{-\frac{1}{2}} K_1 \\
\left(\frac{w_{4,0}}{w_{1,0}}\right)^{-\frac{1}{2}} K_1 & \left(\frac{w_{4,0}}{w_{2,0}}\right)^{-\frac{1}{2}} K_2 & \left(\frac{w_{4,0}}{w_{3,0}}\right)^{-\frac{1}{2}} K_3 & K_0
\end{pmatrix}. \tag{A.35}$$

As a consistency check, let us verify K is antisymmetric. Note that by definition K_0 is antisymmetric and K_2 is symmetric. Using our previous choice of branch cut ($w_{1,0} =$

$i, w_{2,0} = -1, w_{3,0} = -i, w_{4,0} = 1$ and $w_{1,0}^{1/2} = e^{i\pi/4}, w_{2,0}^{1/2} = e^{i3\pi/2}, w_{3,0}^{1/2} = e^{i3\pi/4}, w_{4,0}^{1/2} = 1$), the factors are $(\frac{w_{1,0}}{w_{3,0}})^{-1/2} = i$, $(\frac{w_{2,0}}{w_{4,0}})^{-1/2} = i$, so the blocks associated with K_2 has the desired property under tranposition. For the blocks associated with K_1 and K_3, for example:

$$\begin{aligned}
&\begin{pmatrix} 0 & \left(\frac{w_{1,0}}{w_{2,0}}\right)^{-\frac{1}{2}} K_1 \\ \left(\frac{w_{2,0}}{w_{1,0}}\right)^{-\frac{1}{2}} K_3 & 0 \end{pmatrix} \\
&= \begin{pmatrix} 0 & \left(\frac{w_{1,0}}{w_{2,0}}\right)^{-\frac{1}{2}} (P^- + i(P^-)^T) \\ \left(\frac{w_{2,0}}{w_{1,0}}\right)^{-\frac{1}{2}} (P^- - i(P^-)^T) & 0 \end{pmatrix}.
\end{aligned} \tag{A.36}$$

Using our previous choice, $(\frac{w_{1,0}}{w_{2,0}})^{-1/2} = e^{i5\pi/4} \sim -1 - i$. One can check:

$$\begin{aligned}
(-1-i)(P^- + i(P^-)^T)^T &= (-1-i)((P^-)^T + iP^-), \\
(-1+i)(P^- - i(P^-)^T) &= (1+i)(P^-)^T + (-1+i)P^-,
\end{aligned}$$

which shows this block is indeed antisymmetric. Note that the antisymmetric property is dependent on the choice of w_0. If we make another choice of branch cut $(\frac{w_{1,0}}{w_{2,0}})^{-1/2} = e^{i3\pi/4}$, this block would not be antisymmetric.

A.2 Details of direct method

A.2.1 Solution to single fermion boundary condition

In this section, we give the solution of a single fermion boundary condition, which is useful in the direct method for obtaining the vertex state. Here, the solution is stated without proof and we refer to [45] for the detailed derivation.

The single fermion boundary condition is formulated as:

$$[\eta(\sigma) + g(\sigma)\eta(2\pi - \sigma)] \, |B\rangle = 0, \quad 0 \le \sigma \le 2\pi, \tag{A.37}$$

with the consistency relation $g(\sigma)g(-\sigma) = 1$. To write down the solution, let's first expand $g(\sigma)$ in terms of the Fourier modes: $g(\sigma) = \sum_{n\in\mathbb{Z}} e^{in\sigma} g_n$. If we define matrix N with components $N_{n,m} = g_{-n-m}$, the boundary condition in terms of the Fourier mode is $[\eta_r + \sum_s N_{rs}\eta_s]|B\rangle = 0$, where r, s runs through both positive and negative half integers. To separate the creation operators (η_r with negative r) and annihilation operators (η_r with positive r), we then introduce a block structure:

$$\begin{aligned} N &= \begin{pmatrix} N^{++} & N^{+-} \\ N^{-+} & N^{--} \end{pmatrix}, \\ N^{++}_{r,s} &= N_{r,s} = g_{-r-s}, \quad N^{+-}_{r,s} = N_{r,-s} = g_{-r+s} \\ N^{-+}_{r,s} &= N_{-r,s} = g_{r-s}, \quad N^{--}_{r,s} = N_{-r-s} = g_{r+s}. \end{aligned} \tag{A.38}$$

In the above blocks r, s only take positive values, namely, $r, s \geq 1/2$. We state without proof that the solution of boundary condition (A.37) is:

$$|B\rangle \propto \exp\left(\frac{1}{2}\sum_{r,s\geq 1/2} K_{rs}\eta_{-r}\eta_{-s}\right)|0\rangle, \tag{A.39}$$

where K matrix is given in terms of the four blocks of N matrix:

$$K := (\mathbb{1} + N^{++})^{-1}(N^{+-}) = (N^{-+})^{-1}(\mathbb{1} + N^{--}). \tag{A.40}$$

In the discussion of the vertex state, the function $g(\sigma)$ takes the form of

$$g(\sigma) = -i\mathrm{sgn}\,(\sigma)e^{i\mathrm{sgn}\,(\sigma)\theta}$$

which carries a parameter θ. The corresponding matrices N and K are denoted as $N(\theta)$ and $K(\theta)$.

A.2.2 Direct method: kink boundary condition

In this appendix, we solve the vertex state with kink boundary condition $|V_k\rangle$ by the direct method. As a consistency check, we have numerically verified that this solution is the same as $|V_k\rangle$ obtained from the Neumann coefficient method.

Consider the kink boundary condition on $0 < \sigma < \pi$,

$$\begin{aligned} [\psi^i(\sigma) + i\psi^{i+1}(2\pi - \sigma)]|V_k\rangle = 0, \quad i = 1, 2, 3 \\ [\psi^i(\sigma) - i\psi^{i+1}(2\pi - \sigma)]|V_k\rangle = 0, \quad i = 4, \end{aligned} \tag{A.41}$$

We would like to find a matrix U that diagonalizes the "shift" matrix and use it to rotate the basis. The boundary condition thus decouples in the rotated basis. To start, we notice the "shift" matrix can be diagonalized by:

$$\begin{pmatrix} 0 & 1 & 0 & 0 \\ 0 & 0 & 1 & 0 \\ 0 & 0 & 0 & 1 \\ -1 & 0 & 0 & 0 \end{pmatrix} = U^\dagger \begin{pmatrix} \frac{\sqrt{2}}{2}(1+i) & 0 & 0 & 0 \\ 0 & \frac{\sqrt{2}}{2}(1-i) & 0 & 0 \\ 0 & 0 & \frac{\sqrt{2}}{2}(-1-i) & 0 \\ 0 & 0 & 0 & \frac{\sqrt{2}}{2}(-1+i) \end{pmatrix} U, \tag{A.42}$$

with unitary matrix U:

$$U = \frac{1}{2} \begin{pmatrix} \frac{\sqrt{2}}{2}(-1+i) & i & \frac{\sqrt{2}}{2}(1+i) & 1 \\ \frac{\sqrt{2}}{2}(-1-i) & -i & \frac{\sqrt{2}}{2}(1-i) & 1 \\ \frac{\sqrt{2}}{2}(1-i) & i & \frac{\sqrt{2}}{2}(-1-i) & 1 \\ \frac{\sqrt{2}}{2}(1+i) & -i & \frac{\sqrt{2}}{2}(-1+i) & 1 \end{pmatrix}. \tag{A.43}$$

The rotated real fermions are thus $\boldsymbol{\eta} = U\boldsymbol{\psi}$. By

$$UU^T = \begin{pmatrix} 0 & 1 & 0 & 0 \\ 1 & 0 & 0 & 0 \\ 0 & 0 & 0 & 1 \\ 0 & 0 & 1 & 0 \end{pmatrix}, \tag{A.44}$$

the anticommutation relation of the rotated basis $\boldsymbol{\eta}$ is $\{\eta^1_r, \eta^2_s\} = \delta_{r+s,0}, \{\eta^3_r, \eta^4_s\} = \delta_{r+s,0}$.

Let's first consider the η^1, η^2 pair. For η^1, the boundary condition is:

$$\begin{aligned} &[\eta^1(\sigma) + ie^{i\frac{\pi}{4}}\eta^1(2\pi - \sigma)]|V_{(12)}\rangle = 0, \quad 0 < \sigma < \pi \\ &[\eta^1(\sigma) - ie^{-i\frac{\pi}{4}}\eta^1(2\pi - \sigma)]|V_{(12)}\rangle = 0, \quad \pi < \sigma < 2\pi \end{aligned} \tag{A.45}$$

This amounts to choosing $\theta_1 = \frac{5}{4}\pi$ in the boundary condition $[\eta(\sigma) - i\mathrm{sgn}\,(\sigma)e^{i\mathrm{sgn}\,(\sigma)\theta}\eta(2\pi - \sigma)]|V\rangle = 0$ $(0 \leq \sigma \leq 2\pi)$. Similarly, for η^2, the corresponding angle is $\theta_2 = \frac{3}{4}\pi$. Now in terms of the Fourier modes, the boundary condition can be rewritten as:

$$\left[\begin{pmatrix} \eta^2_r \\ \eta^1_r \end{pmatrix} + \sum_s \begin{pmatrix} 0 & N_{rs}(\theta_2 = \frac{3\pi}{4}) \\ N_{rs}(\theta_1 = \frac{5\pi}{4}) & 0 \end{pmatrix} \begin{pmatrix} \eta^1_s \\ \eta^2_s \end{pmatrix}\right] |V_{(12)}\rangle = 0. \tag{A.46}$$

We can separate the creation and annihilation parts explicitly, where $r, s > 0$:

$$\left[\begin{pmatrix} \eta^2_r \\ \eta^1_r \\ \eta^1_{-r} \\ \eta^2_{-r} \end{pmatrix} + \sum_{s \geq 1/2} \begin{pmatrix} N^{++}_{rs}(\theta_2) & 0 & 0 & N^{+-}_{rs}(\theta_2) \\ 0 & N^{++}_{rs}(\theta_1) & N^{+-}_{rs}(\theta_1) & 0 \\ 0 & N^{-+}_{rs}(\theta_1) & N^{--}_{rs}(\theta_1) & 0 \\ N^{-+}_{rs}(\theta_2) & 0 & 0 & N^{--}_{rs}(\theta_2) \end{pmatrix} \begin{pmatrix} \eta^2_s \\ \eta^1_s \\ \eta^1_{-s} \\ \eta^2_{-s} \end{pmatrix}\right] |V\rangle = 0, \tag{A.47}$$

from which we read out:

$$
\begin{aligned}
N^{++}_{(12)} &= \begin{pmatrix} N^{++}(\theta_2) & 0 \\ 0 & N^{++}(\theta_1) \end{pmatrix}, \quad N^{+-}_{(12)} = \begin{pmatrix} 0 & N^{+-}(\theta_2) \\ N^{+-}(\theta_1) & 0 \end{pmatrix}, \\
N^{-+}_{(12)} &= \begin{pmatrix} 0 & N^{-+}(\theta_1) \\ N^{-+}(\theta_2) & 0 \end{pmatrix}, \quad N^{--}_{(12)} = \begin{pmatrix} N^{--}(\theta_1) & 0 \\ 0 & N^{--}(\theta_2) \end{pmatrix}.
\end{aligned}
\tag{A.48}
$$

Using the four block matrices, the vertex state solution for η^1, η^2 pair is:

$$
\begin{aligned}
&|V_{(12)}\rangle \propto \exp\left(\frac{1}{2} \sum_{r,s\geq\frac{1}{2}} \sum_{i,j=1,2} \eta^i_{-r} K^{ij}_{(12),rs} \eta^j_{-r} \right) |0\rangle, \\
&\text{with} \quad K_{(12)} = (\mathbb{1} + N^{++}_{(12)})^{-1} (N^{-+}_{(12)}).
\end{aligned}
\tag{A.49}
$$

Similarly, for the η^3, η^4 pair, the corresponding angles are $\theta_3 = \frac{\pi}{4}$ and $\theta_4 = -\frac{\pi}{4}$, and $K_{(34)}$ can be obtained in a similar way. Finally, we need to rotate back to the original ψ basis. The vertex state solution in the basis ψ is thus:

$$
\begin{aligned}
&|V_k\rangle \propto \exp\left(\frac{1}{2} \sum_{r,s\geq\frac{1}{2}} \sum_{i,j=1,2,3,4} \boldsymbol{\psi}^i_{-r} K^{ij}_{rs} \psi^j_{-s} \right) |0\rangle, \\
&\text{with} \quad K = U^T \begin{pmatrix} K_{(12)} & 0 \\ 0 & K_{(34)} \end{pmatrix} U.
\end{aligned}
\tag{A.50}
$$

Although the vertex state solution for kink boundary condition $|V_k\rangle$ can be obtained from either the direct method or the Neumann coefficient method, the Neumann coefficient method is more desirable for numerical calculation, because it does not involve the matrix inverse which would lead to numerical inaccuracy.

A.3 Correlation matrix for the vertex state

Once the vertex states are obtained, we can compute various entanglement measures by the correlator method. Here, we collect some details for the numerical calculations of the correlation matrices. For numerical purposes, we need to truncate the matrix at size N_c. Then, $\boldsymbol{K}$ is a $6N_c \times 6N_c$ real anti-symmetric matrix, so we can use an orthogonal matrix Q to bring it to standard block diagonal form

$$\boldsymbol{K} = Q^T \Sigma Q, \quad \Sigma = \oplus_{k=1}^{3N_c} \Sigma_k, \quad \Sigma_k = \begin{pmatrix} 0 & \sigma_k \\ -\sigma_k & 0 \end{pmatrix}. \tag{A.51}$$

In the block diagonal basis $\boldsymbol{b}^\dagger = Q\boldsymbol{V}^\dagger$, the state $|G\rangle$ is

$$\begin{aligned} |G\rangle &= \mathcal{N} \exp\left[\frac{1}{2}(\boldsymbol{b}^\dagger)^T \Sigma \boldsymbol{b}^\dagger\right]|0\rangle \\ &= \mathcal{N} \exp\left[\sum_{k=1}^{3N_c} \sigma_k b_{2k-1}^\dagger b_{2k}^\dagger\right]|0\rangle. \end{aligned} \tag{A.52}$$

In order to calculate the entanglement entropy and negativity, we need to compute the correlation matrices C and F. The non-zero elements are

$$\begin{aligned} &\langle G|b_{2k-1}^\dagger b_{2k}^\dagger|G\rangle = -\langle G|b_{2k}^\dagger b_{2k-1}^\dagger|G\rangle \\ &\quad = -\langle G|b_{2k-1}b_{2k}|G\rangle = \langle G|b_{2k}b_{2k-1}|G\rangle = \frac{\sigma_k}{1+\sigma_k^2}, \\ &\langle G|b_{2k-1}^\dagger b_{2k-1}|G\rangle = \langle G|b_{2k}^\dagger b_{2k}|G\rangle = \frac{\sigma_k^2}{1+\sigma_k^2}, \\ &\langle G|b_{2k-1}b_{2k-1}^\dagger|G\rangle = \langle G|b_{2k}b_{2k}^\dagger|G\rangle = \frac{1}{1+\sigma_k^2}, \end{aligned} \tag{A.53}$$

and the correlation matrices C, F are expressed as

$$\begin{aligned} C_{rs} &= \langle G|V_r^\dagger V_s|G\rangle = \langle G|b_p^\dagger b_q|G\rangle Q_{pr}Q_{qs} \\ &= \sum_{k=1}^{3N_c} \frac{\sigma_k^2}{1+\sigma_k^2}(Q_{2k-1,r}Q_{2k-1,s} + Q_{2k,r}Q_{2k,s}), \\ F_{rs} &= \langle G|V_r^\dagger V_s^\dagger|G\rangle = \langle G|b_p^\dagger b_q^\dagger|G\rangle Q_{pr}Q_{qs} \\ &= \sum_{k=1}^{3N_c} \frac{\sigma_k}{1+\sigma_k^2}(Q_{2k-1,r}Q_{2k,s} - Q_{2k,r}Q_{2k-1,s}). \end{aligned} \tag{A.54}$$

These correlators need to be rotated back to the original basis f_A, f_B, f_C by unitary transformation U. Noting that $f^\dagger$ transforms with U^* rather than U, the full transformation matrix U' is

$$U' = U^* \otimes \begin{pmatrix} \mathbb{1} & 0 \\ 0 & 0 \end{pmatrix} + U \otimes \begin{pmatrix} 0 & 0 \\ 0 & \mathbb{1} \end{pmatrix} \tag{A.55}$$

where $\mathbb{1}$ is the $N_c \times N_c$ identity matrix. The correlation matrices transform via

$$C \to (U')^\dagger C U', \quad F \to (U')^\dagger F (U')^*. \tag{A.56}$$

With C, F, we can obtain the correlation matrix Γ using Eq. (2.19) and compute various entanglement measures.

APPENDIX B

DETAILS OF WAVEFUNCTION OVERLAP METHOD

B.1 Fusion rules of cyclic orbifold from modular transformations

We first recall basic aspects of modular invariance which are crucial to the consistency of a CFT defined on a torus. A torus is characterized by two period vectors w_1 and w_2, which can be represented as complex numbers. Scale invariance of CFT implies that the partition function only depend on the modular parameter $\tau = w_2/w_1$. There are two basic operations $\mathcal{S} : \tau \to -1/\tau$ and $\mathcal{T} : \tau \to \tau + 1$ that generate equivalent descriptions of the same torus. Therefore, the two operations generate the modular group under which the CFT partition function is invariant.

Modular invariance puts strong constraints on the operator content of the CFT. To see this, we first recall that the partition function is bilinear in the character of conformal towers,

$$\chi_a(\tau) = \mathrm{Tr}_a\, q^{L_0 - c/24}, \tag{B.1}$$

where $q = \exp(2\pi i \tau)$, and a is the label of primary operator. Expanding the character in the power of q gives degeneracy of the conformal tower at each level of descendants. In a diagonal theory, the partition function is simply

$$Z(\tau) = \sum_a |\chi_a(\tau)|^2, \tag{B.2}$$

where the summation is finite for minimal model [1], for example, the Ising CFT. Modular

1. For rational CFT, the partition function can be organized into finite summation of extended characters. See the example of compactified boson (the XXZ model in the main text).

invariance then demands that

$$\chi_a(-1/\tau) = \sum_b \mathcal{S}_{ab}\chi_b(\tau), \tag{B.3}$$

$$\chi_b(\tau+1) = \sum_b \mathcal{T}_{ab}\chi_b(\tau), \tag{B.4}$$

where $\mathcal{S}$ and $\mathcal{T}$ are unitary matrices that form a representation of the modular group. One can further show that

$$\mathcal{T}_{ab} = e^{2\pi i(h_a - c/24)}\delta_{ab} \tag{B.5}$$

is diagonal with $h_a = \Delta_a/2$ and

$$\mathcal{S}_{ab} = \mathcal{S}_{ba} \tag{B.6}$$

is symmetric. The celebrated Verlinde formula relates the fusion rule to the modular matrices,

$$\mathcal{N}_{i,j,k} = \sum_m \frac{\mathcal{S}_{im}\mathcal{S}_{jm}\mathcal{S}^*_{mk}}{S_{\mathbb{1}m}}. \tag{B.7}$$

Next, we review how characters of the orbifold theory can be constructed from the original theory and use the Verlinde formula to derive the fusion rules.

The characters in the orbifold theory are related to the characters in the original theory via:

$$\begin{aligned}
&\chi_{(\alpha,\beta)}(\tau) = \chi_\alpha(\tau)\chi_\beta(\tau) \\
&\chi_{(\alpha,\alpha)_\phi}(\tau) = \frac{1}{2}\left[\chi^2_\alpha(\tau) + e^{i\pi\phi}\chi_\alpha(2\tau)\right] \\
&\chi_{(\alpha,\hat{\psi})}(\tau) = \frac{1}{2}\left[\chi_\alpha(\frac{\tau}{2}) + e^{i\pi\psi}T_\alpha^{-1/2}\chi_\alpha(\frac{\tau}{2}+\frac{1}{2})\right].
\end{aligned} \tag{B.8}$$

Here $T_\alpha = \exp\left(2\pi i(h_\alpha - c/24)\right)$ is the diagonal matrix element in $\mathcal{T}$ matrix, ϕ can take 0 (symmetric sector, denoted as s in the main text) or 1 (antisymmetric sector, denoted as a

in the main text), and ψ can take 0 or 1. The partition function of the orbifold theory is:

$$\begin{aligned} Z &= Z_{un} + Z_{tw}, \\ Z_{un} &= \sum_{\alpha<\beta} |\chi_{(\alpha,\beta)}(\tau)|^2 + \sum_{\alpha,\phi} |\chi_{(\alpha,\alpha)_\phi}(\tau)|^2 \\ &= \frac{1}{2}\sum_{\alpha\beta} |\chi_\alpha(\tau)|^2 |\chi_\beta(\tau)|^2 + \frac{1}{2}\sum_\alpha |\chi_\alpha(2\tau)|^2, \\ Z_{tw} &= \sum_{\alpha,\psi} |\chi_{(\alpha,\hat{\psi})}(\tau)|^2 \\ &= \frac{1}{2}\sum_\alpha (|\chi_\alpha(\frac{\tau}{2})|^2 + |\chi_\alpha(\frac{\tau}{2}+\frac{1}{2})|^2). \end{aligned} \tag{B.9}$$

We see that since the characters of $\phi_{(\alpha,\alpha)_{s/a}}$ include $\chi_\alpha(2\tau)$, it is necessary to include the twisted sector with characters $\chi_\alpha(\tau/2)$ and $\chi_\alpha(\tau/2+1/2)$ such that the partition function is modular invariant.

For the purpose of computing wavefunction overlap, we need to use the following two orbifold fusion coefficients: $\mathcal{N}_{(\alpha,\beta),(\gamma,\hat{\psi}),(\delta,\hat{\chi})}$, $\alpha \neq \beta$ and $\mathcal{N}_{(\alpha,\alpha)_s,(\gamma,\hat{\psi}),(\delta,\hat{\chi})}$, where ψ, χ take value in $\{0,1\}$.

We now derive the Eq. (5.37), (5.38) in the main text. Using the Verlinde formula, the first fusion coefficient can be expressed as:

$$\begin{aligned} &\mathcal{N}_{(\alpha,\beta),(\gamma,\hat{\psi}),(\delta,\hat{\chi})} \\ &= \sum_m \frac{\mathcal{S}_{(\alpha,\beta),m}\mathcal{S}_{(\gamma,\hat{\psi}),m}\mathcal{S}^*_{m,(\delta,\hat{\chi})}}{\mathcal{S}_{(\mathbb{1},\mathbb{1})_s,m}} \\ &= \sum_{\eta,\phi} \frac{\mathcal{S}_{(\alpha,\beta),(\eta,\eta)_\phi}\mathcal{S}_{(\gamma,\hat{\psi}),(\eta,\eta)_\phi}\mathcal{S}^*_{(\eta,\eta)_\phi,(\delta,\hat{\chi})}}{\mathcal{S}_{(\mathbb{1},\mathbb{1})_s,(\eta,\eta)_\phi}} \\ &= \sum_{\eta,\phi} \frac{\left(\mathcal{S}_{\alpha\eta}\mathcal{S}_{\beta\eta}\right)\left(\frac{1}{2}e^{i\pi\phi}\mathcal{S}_{\gamma\eta}\right)\left(\frac{1}{2}e^{-i\pi\phi}\mathcal{S}^*_{\eta\delta}\right)}{\frac{1}{2}\mathcal{S}^2_{\mathbb{1}\eta}} \\ &= \sum_\eta \frac{\mathcal{S}_{\alpha\eta}\mathcal{S}_{\beta\eta}\mathcal{S}_{\gamma\eta}\mathcal{S}^*_{\eta\delta}}{\mathcal{S}^2_{\mathbb{1}\eta}}. \end{aligned} \tag{B.10}$$

From the second to the third line, we use the relation between the orbifold modular $\mathcal{S}$ matrix and the original $\mathcal{S}$ matrix, which can be derived using the orbifold character Eq. (B.8) as in [192][2]. For the case where $\mathcal{S}$ is real (e.g., the Ising CFT), this still gives the correct result; while for the general case where $\mathcal{S}$ is complex (e.g., the compactified boson rational CFT), this would change the final expression. Only when $\mathcal{S}$ is real can we decompose $\mathcal{N}_{(\alpha,\beta),(\gamma,\hat{\psi}),(\delta,\hat{\chi})}$ into the product of $\mathcal{N}$ in the original CFT. In short, the fusion rule of the orbifold CFT is fully determined by the modular matrices of the original theory.

Similarly, the second fusion coefficient can be written as:

$$
\begin{aligned}
&\mathcal{N}_{(\alpha,\alpha)_s,(\gamma,\hat{\psi}),(\delta,\hat{\chi})} \\
&= \sum_{m} \frac{\mathcal{S}_{(\alpha,\alpha)_s,m}\mathcal{S}_{(\gamma,\hat{\psi}),m}\mathcal{S}^*_{m,(\delta,\hat{\chi})}}{\mathcal{S}_{(\mathbb{1},\mathbb{1})_s,m}} \\
&= \sum_{\eta,\phi} \frac{\mathcal{S}_{(\alpha,\alpha)_s,(\eta,\eta)_\phi}\mathcal{S}_{(\gamma,\hat{\psi}),(\eta,\eta)_\phi}\mathcal{S}^*_{(\eta,\eta)_\phi,(\delta,\hat{\chi})}}{\mathcal{S}_{(\mathbb{1},\mathbb{1})_s,(\eta,\eta)_\phi}} + \sum_{\eta,\xi} \frac{\mathcal{S}_{(\alpha,\alpha)_s,(\eta,\hat{\xi})}\mathcal{S}_{(\gamma,\hat{\psi}),(\eta,\hat{\xi})}\mathcal{S}^*_{(\eta,\hat{\xi}),(\delta,\hat{\chi})}}{\mathcal{S}_{(\mathbb{1},\mathbb{1})_s,(\eta,\hat{\xi})}} \\
&= \sum_{\eta,\phi} \frac{\left(\frac{1}{2}\mathcal{S}^2_{\alpha\eta}\right)\left(\frac{1}{2}e^{i\pi\phi}\mathcal{S}_{\gamma\eta}\right)\left(\frac{1}{2}e^{-i\pi\phi}\mathcal{S}^*_{\eta\delta}\right)}{\frac{1}{2}\mathcal{S}^2_{\mathbb{1}\eta}} \\
&\quad + \sum_{\beta,\xi} \frac{\left(\frac{1}{2}\mathcal{S}_{\alpha\eta}\right)\left(\frac{1}{2}e^{i\pi(\psi+\xi)}\mathcal{P}_{\gamma\eta}\right)\left(\frac{1}{2}e^{-i\pi(\xi+\chi)}\mathcal{P}^*_{\eta,\delta}\right)}{\frac{1}{2}\mathcal{S}_{\mathbb{1}\eta}} \\
&= \frac{1}{2}\sum_{\eta} \frac{\mathcal{S}^2_{\alpha\eta}\mathcal{S}_{\gamma\eta}\mathcal{S}^*_{\eta\delta}}{\mathcal{S}^2_{\mathbb{1}\eta}} + \frac{1}{2}e^{i\pi(\psi+\chi)}\sum_{\eta} \frac{\mathcal{S}_{\alpha\eta}\mathcal{P}_{\gamma\eta}\mathcal{P}^*_{\eta,\delta}}{\mathcal{S}_{\mathbb{1},\eta}},
\end{aligned}
\tag{B.11}
$$

where $\mathcal{P} = \mathcal{T}^{1/2}\mathcal{S}\mathcal{T}^2\mathcal{S}\mathcal{T}^{1/2}$.

2. Note that there is a typo in the fusion coefficient $\mathcal{N}$ derived in [192], where the conjugate sign is missing.

B.2 Wavefunction overlaps for antiferromagnetic Ising model

In the main text, we consider the ferromagnet Ising model, where $\mathbb{1}, \sigma, \epsilon$ are the primary operators when taking periodic boundary condition (PBC), and $\mu, \psi, \bar{\psi}$ appears in anti-periodic boundary condition (APBC). There is no distinction of low-energy spectrum for even and odd number of sites, and all the primary operators are inside the light cone at $P = 0$.

On the other hand, the low-energy spectrum of the antiferromagnetic Ising model depends on even or odd number of sites. Furthermore, there exists lightcones centered at $P = 0$ as well as $P = \pi$. The Haagerup model is more similar to the antiferromagnetic Ising model, in the sense that (1) the operator content changes with different system sizes $N = 3n, 3n+1, 3n+2$; and (2) there appear three light cones which are located at $P = 0, P = \pi/3, P = -\pi/3$ if $N = 3n$. For this reason, we study the wavefunction overlap for the antiferromagnetic Ising model in this appendix, with an emphasis on the case where low-energy eigenstates with odd number of sites fuse into low-energy eigenstates with even number of sites. This provides an analogy to what we did for the Haagerup CFT.

The operator content of the antiferromagnetic Ising model is summarized below, for both boundary conditions (PBC/APBC) and for both types of lattice site (even/odd):

	spin PBC	spin APBC	fermion
even	$\mathbb{1}, \epsilon : P = 0$	$\psi, \bar{\psi} : P = 0$	NS
	$\sigma : P = \pi$	$\mu : P = \pi$	R
odd	$\psi, \bar{\psi} : P = \pi$	$\mathbb{1}, \epsilon : P = \pi$	NS
	$\mu : P = 0$	$\sigma : P = 0$	R

(B.12)

A possible fusion may be, for example, obtaining $A_{\sigma\sigma\mathbb{1}}$ by fusing σ at size $N_1 = 2N + 1$ and σ at size $N_2 = 2N - 1$ into $\mathbb{1}$ at size $N_3 = 4N$. This is analog to what we did for the current operator in the Haagerup model. We then take the ratio $A_{\sigma\sigma\mathbb{1}}/A_{\mathbb{1}\mathbb{1}\mathbb{1}}$ where the $\mathbb{1}$ in

the denominator is taken from $N_1 = N_2 = 2N$ and $N_3 = 4N$. For a better comparison with Haagerup model, we use the small systems, where N takes value from 5 to 12, and show the results in Fig. B.1.

In Fig. B.1(a), we show the scaling of $A_{\mathbb{1}\mathbb{1}\mathbb{1}}$ computed using $N_1 = 2N, N_2 = 2N, N_3 = 4N$, where the theoretical derivation gives $A_{\mathbb{1}\mathbb{1}\mathbb{1}} = a_{(\mathbb{1},\hat{0})} N^{-1/16}$. The fit gives the power -0.0623, which is within 1% error even for such a small system. In Fig. B.1(b-f), we show the finite-size correction $F_{\alpha\beta\gamma}$ for the five different channels $\sigma\sigma\epsilon, \mu\mu\epsilon, \sigma\sigma\mathbb{1}, \mu\mu\mathbb{1}, \epsilon\epsilon\mathbb{1}$, where $A_{\alpha\beta\gamma}$ is computed using $N_1 = 2N-1, N_2 = 2N+1, N_3 = 4N$, and $A^{(0)}_{\alpha\beta\gamma}$ is computed using Eq. (5.21) with different system size. From the value of $\log F$, we see in (f) the numerical value approaches the theoretical value much quicker that (b,c); and (b,c) are quicker than (d,e). This is expected because $p = 2$ for $\epsilon\epsilon\mathbb{1}$, $p = \frac{3}{2}$ for $\sigma\sigma\mathbb{1}$ and $\mu\mu\mathbb{1}$; and $p = \frac{1}{2}$ for $\sigma\sigma\epsilon, \mu\mu\epsilon$. At this system size, the largest error for p is 8%, and the error for p gets smaller with increasing N.

The above observation shows that the overlap result $A_{\alpha\beta\gamma}/A_{\mathbb{1}\mathbb{1}\mathbb{1}}$ is indeed more accurate for larger $p_{\alpha\beta\gamma}$.

The extraction for p matches with the value in Table 5.2 as we further increase the system size N.

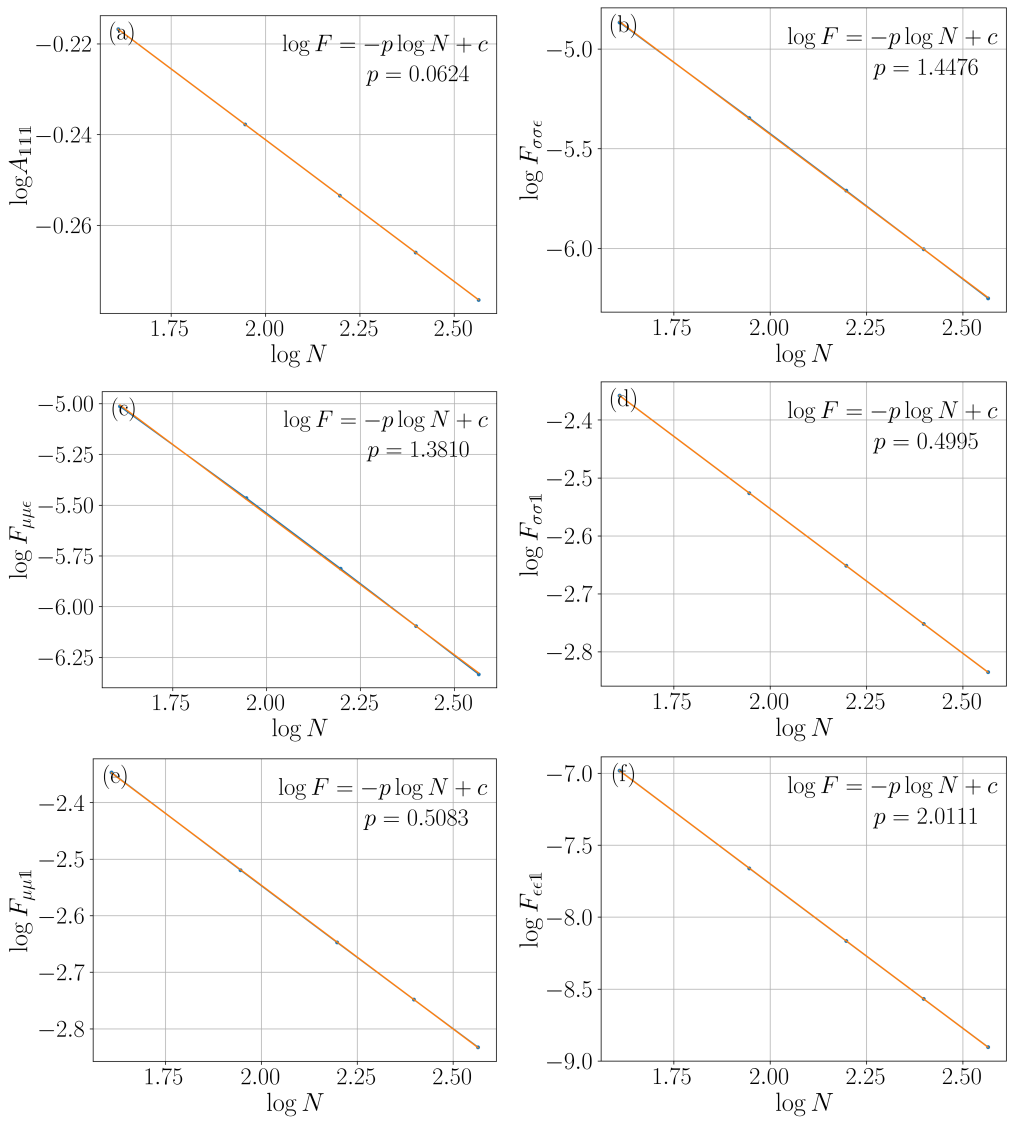

Figure B.1: (a) Scaling of $A_{\mathbb{1}\mathbb{1}\mathbb{1}}$, computed for $N_1 = 2N$, $N_2 = 2N$, and $N_3 = 4N$. (b-f) Scaling of $F_{\alpha\beta\gamma}$, where $A_{\alpha\beta\gamma}$ is computed for $N_1 = 2N + 1$,$N_2 = 2N - 1$, and $N_3 = 4N$. To simulate small system, N takes value from 5 to 12.

APPENDIX C

NUMERICAL METHOD

Back in the Southern Song Dynasty (around the twelfth century), Lu You wrote, "The knowledge from reading the papers is sometimes shallow; deep understanding is gained from putting the ideas into practice." In my exploration of physics, much understanding is gained from or solidified by numerical simulation. In this appendix, I will introduce two numerical methods, the exact diagonalization (ED) method and the tensor network method[1]. The exact diagonalization method is ansatz-free and applies to any system; however, the system size it can reach is relatively small due to the "exponential wall". In contrast, the tensor network method is designed to handle the many-body ground state with a large system size. However, its power is limited to the low-entanglement states, including the ground states. In the following introduction, I will also summarize the numerical techniques and practice that I found useful.

C.1 Exact diagonalization

Unsurprisingly, exact diagonalization is the first resort when one wants to understand the eigenspectrum and eigenstates of a Hamiltonian. One obstacle for simulating many-body Hamiltonian using ED is the exponential wall: the time complexity and the memory grows exponentially when increasing the system size. For example, to simulate a 1d chain made from qubits, the local Hilbert space dimension is $d = 2$; therefore, the complete basis for a chain of length N consists of 2^N states. Nevertheless, being an ansatz-free numerical method, ED is still a valuable tool for studying small systems, and serve as a benchmark for other numerical methods such as tensor network where various ansatz are used. In fact, our simulation for the Haagerup model is performed using ED up to $N = 13$ (where the local

1. I thank Yijian Zou for a lot of discussions on tensor network methods.

Hilbert space dimension is $d = 6$). Below, we introduce several techniques that allow us to reduce the computational cost, so as to push the boundary of ED and reach a larger system size N before hitting the exponential wall.

Sparse matrix and iterative solver In condensed matter systems, we typically focus on the ground state; the Hamiltonian typically only involves local interactions (nearest or next-to-nearest-neighbor couplings). These two observations are crucial for the first reduction of computational cost: the Hamiltonian can be implemented by sparse matrix, and one can use iterative methods such as the Lanzcos algorithm and Arnoldi algorithm to find the lowest several eigenstates. To see the computational cost reduction, let's consider the simple example of the spin-1/2 XXZ chain with length N,

$$H = \sum_{i=1}^{N} \left[\frac{J_{xy}}{2}(S_i^+ S_{i+1}^- + S_i^- S_{i+1}^+) + J_z S_i^z S_{i+1}^z \right]. \tag{C.1}$$

The Hamiltonian is a $2^N \times 2^N$ matrix, consisting of 4^N elements. However, by a quick estimation, one can show the number of nonzero elements is $N \cdot 2^N$ approximately. The Hamiltonian is indeed sparse, and sparse matrix implementation can greatly reduce the memory cost. Furthermore, the average number of nonzero elements in each row is of order N; therefore, the time complexity of the Lanczos algorithm for computing m lowest eigenvalues is $O(N \cdot 2^N \cdot m)$. This is greatly reduced from $O(2^{3N})$, which is the complexity of solving the full eigenspectrum of a $2^N \times 2^N$ matrix.

For an elegant implementation of the sparse matrix for Hamiltonian, we refer the readers to Ref. [209].

Symmetry Many of the physical systems have conserved charges. For example, the quantum XXZ chain under the periodic boundary condition commutes with the summation of S^z, $Q = \sum_i S_i^z$ (which is the $U(1)$ charge after Jordan-Wigner transformation). There-

fore, the Hamiltonian is block-diagonal under a proper choice of basis. The eigenstates are simultaneous eigenstates of H and Q.

When trying to simultaneously diagonalize the Hamiltonian H and the conserved charge operator Q, one can construct

$$H' = H + \epsilon Q, \tag{C.2}$$

where ϵ is a small quantity (smaller than the energy gap), and diagonalizes H'. This construction creates a tiny splitting for the degenerate eigenstates with different symmetry charges [2], and the resulting eigenstates are also eigenstates of Q.

In fact, symmetry can lead to a second reduction of computational cost by restricting the basis states in the symmetric sector [210]. For example, if we want to study the ground state in the half-filled sector of the spin-1/2 XXZ model on a 1d chain of length N, we only need to generate the Hamiltonian elements on the basis $|s_1, s_2, \cdots, s_N\rangle$ where $\sum_{i=1}^{N} s_i = 0$ (each s_i takes value in $s_i = \pm\frac{1}{2}$). This reduces the number of required basis states from 2^N to $\binom{N}{N/2}$, allowing us to reach a larger N. The coupling terms in the Hamiltonian are located using the hashing key of the basis states (each state is assigned to a unique hashing key).

Genrate the basis and Hamiltonian iteratively Depending on the nature of the Hamiltonian and symmetry, more efficient ways can be used to implement the symmetric constraint. For example, in the Haagerup model, the valid basis state is constrained by the fusion rule, which makes it natural to generate the basis in an iterative manner. Namely, we first generate the valid basis for the length N chain, then use them to generate the valid basis for the length $N+1$ chain. Similarly, the matrix elements of the Hamiltonian are generated iteratively, where the Hamiltonian of the length $N+1$ chain is generated by that of the length N chain. To identify the matrix components of Hamiltonian, a user-defined data class (modified from the linked list data type) was used to keep track of the relationship

2. This technique reminds me of the Zeeman effect (and the good old days of modern physics experiments back in undergraduate).

of basis states. The implementation details can be found in our GitHub repository. Depending on the specific problem, this may lead to further reduction of computational cost. In the Haagerup model, the time complexity of our implementation is $O(3.4^N)$, outperforming $O(6^N)$ for a 1d chain with local Hilbert space dimension being $d = 6$.

In summary, exact diagonalization remains a useful method and serves as a starting point before turning to advanced algorithms. As discussed in this subsection, various techniques can be applied to maximize the value of the exact diagonalization method before hitting the exponential wall.

C.2 Tensor network

Tensor network method is perhaps one of the most important numerical methods [11, 211, 212, 213]. It empowers us to find the quasi-exact solution of the eigenstates that satisfy the area-law entanglement scaling and study the time evolution dynamics from a given quantum state. Here we briefly summarize the matrix product state (MPS) representation with a focus on the canonical forms, and the various existing tensor network algorithms. As an example, we will introduce the time-evolving block decimation (TEBD) algorithm on a finite chain in detail and point out the important ingredients of tensor network algorithms.

C.2.1 MPS representation

Any quantum state can be represented using the matrix product state (MPS) representation by a series of singular value decomposition (SVD). The MPS representation takes the following form,

$$|\psi\rangle = \sum_{\boldsymbol{\sigma}} M^{\sigma_1} M^{\sigma_2} \cdots M^{\sigma_N} |\boldsymbol{\sigma}\rangle. \tag{C.3}$$

Here, σ_i is the degree of freedom on the local Hilbert space of site i; for the qubit degree of freedom, $\sigma_i = \pm\frac{1}{2}$. Each M^{σ_i} is a matrix with dimension $\chi_i \times \chi_{i+1}$. Schematically, the

above MPS representation can be diagrammatically represented as

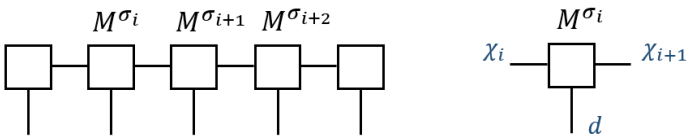

(C.4)

Here, the vertical legs are the physical bonds (connected with $|\sigma_i\rangle$) and the horizontal legs are the virtual bonds. The dimension for the physical bond d is equal to the dimension of the local Hilbert space d ($d = 2$ for qubit). For the area-law state, due to its non-growing entanglement, we can set a constant upper bound χ for the dimension of the virtual bond, independent of the length of the 1d chain N. In comparison, for the volume-law scaling state, the virtual bond dimension χ grows exponentially with the system size. The complexity of a valid tensor network algorithm scales as $O(\chi^3)$. Therefore, the MPS representation and the related tensor network algorithm are useful for the area-law state and can get over the exponential wall; while for the volume-law state, the exponential wall persists for the tensor network algorithm.

The state represented by the MPS representation is unchanged under the "gauge transformation",

$$M^{\sigma_i} \to G_i M^{\sigma_i} G_{i+1}^{-1}. \tag{C.5}$$

By using the gauge degree of freedom, one can bring the MPS into canonical form. There are two commonly used canonical forms, one in the "AB notation"; and the other in the "$\Gamma\Lambda$ notation" [214, 211]. One can show the canonical forms in these two notations can be easily transformed into each other.

The canonical form in the "AB notation" is defined as follows. Any quantum state can be brought into left-canonical form by performing SVD from the left to the right,

$$|\psi\rangle = \sum_{\boldsymbol{\sigma}} A^{\sigma_1} A^{\sigma_2} \cdots A^{\sigma_N} |\boldsymbol{\sigma}\rangle, \tag{C.6}$$

where

$$\sum_{\sigma_i}(A^{\sigma_i})^\dagger A^{\sigma_i} = \mathbb{1}. \tag{C.7}$$

Similarly, we can define the right-canonical form,

$$|\psi\rangle = \sum_{\boldsymbol{\sigma}} B^{\sigma_1} B^{\sigma_2} \cdots B^{\sigma_N} |\boldsymbol{\sigma}\rangle, \tag{C.8}$$

where

$$\sum_{\sigma_i} B^{\sigma_i}(B^{\sigma_i})^\dagger = \mathbb{1}. \tag{C.9}$$

The canonical form will be useful when we introduce the tensor network algorithm.

C.2.2 Tensor network algorithm

In this section, we focus on solving the ground state in one-dimensional systems. Various algorithms exist for ground state searching, and part of them are listed in Table. C.1. Among various algorithms, the most basic ones are density matrix renormalization group (DMRG) and time-evolving block decimation (TEBD) [214]. The more advanced algorithms such as the time-dependent variational principle (TDVP) and variational uniform matrix product state (VUMPS) are implemented in practice, for a higher efficiency and explicit preservation of symmetries.

When learning or developing a new algorithm, we need to bear in mind several questions: (1) Which canonical form is used? (2) How to perform the truncation? (3) How to normalize the tensor in each step? (4) Is the runtime at the same scale or below $O(\chi^3)$, where χ is the bond dimension? In the following, we take the TEBD algorithm on a finite chain as a pedagogical example to illustrate the above questions.

In the TEBD algorithm, we consider the local Hamiltonian with the nearest neighbor

Algorithm	Idea	Suitability	Benefit/Drawback
TEBD	Imaginary time evolution	Infinite chain finite chain	Saturation time is long when near the critical point
DMRG	Optimize the local Hamiltonian	finite chain	More accurate than TEBD for finite chain
TDVP	Gradient descent in the variational manifold of the uniform MPS.	Infinite chain	Symmetries are preserved.
VUMPS	Combine the tangent space idea with DMRG	Infinite chain	Most efficient

Table C.1: List of tensor network algorithms for solving the ground state. Here, TDVP stands for the time-dependent variational principle [2], and VUMPS stands for the variational uniform matrix product state [3].

interactions,

$$H = \sum_{r=1}^{N-1} h_{r,r+1}. \tag{C.10}$$

Now, given an initial state $|\psi_0\rangle$, the ground state of H can be simulated using an imaginary time evolution,

$$|\psi\rangle = \frac{\exp(-H\tau)|\psi_0\rangle}{||\exp(-H\tau)|\psi_0\rangle||}. \tag{C.11}$$

To numerically simulate the evolution, we break the total time τ into N_τ number of steps, so that $\delta\tau = \tau/N_\tau$, and use the Suzuki-Trotter decomposition

$$e^{-\sum_r h_{r,r+1}\tau} = \left(\prod_{r=1}^{N-1} e^{-h_{r,r+1}\delta_\tau}\right)^{N_\tau} + O(N^2\tau^2/N_\tau). \tag{C.12}$$

In other words, the whole evolution is broken into N_τ steps and each step consists of $N-1$ two-qubit gates $U_{r,r+1} = e^{-h_{r,r+1}\delta_\tau}$. If N_τ scales as $N^2\tau^2/\epsilon$, the error is at most ϵ.

For convenience, in each step, the two-qubit gates can be arranged into two layers. The first layer consists of $U_{12}, U_{34}, \cdots$ and the second layer consists of $U_{23}, U_{45}, \cdots$. During each step, we sweep from the left to the right of the MPS chain to implement the evolution operators $U_{r,r+1}$ in the first layer; then sweep from the right to the left to implement the

second layer. During the evolution, the left sites of the site r are kept in the left-canonical form, and the right sites of the site $r+1$ are kept in the right-canonical form. The canonical form is guaranteed by SVD. Moreover, the singular spectrum of the SVD is truncated to size χ (only the largest χ singular values are kept and others are abandoned). Finally, since the imaginary time evolution is not unitary, the singular values λ_k after truncation should be normalized at each two-qubit gate evolution to guarantee the norm of the MPS is one, $\lambda_k \to \lambda_k / \sqrt{\sum_{p=1}^{\chi} \lambda_p^2}$.

The details of the algorithm are as follows. In the pictorial illustration, the sites in the left canonical form are in red, and the sites in the right canonical form are in green.

1. Initialize state $|\psi_0\rangle$ as a direct product of N random qubit state. At this step, the virtual bond dimension is $\chi = 1$ and the physical bond dimension is 2.

2. Sweep from left to right by acting $U_{12}, U_{34}, U_{56}, \cdots$ and bring the MPS to the left-canonical form. The details of implementing each $U_{i,i+1}$ are as follows. (1) After acting $U_{i,i+1}$ on site $i, i+1$, we first perform an SVD $\Theta = X\Lambda Y$ to update $A_i = X$. As discussed, Λ shall be truncated to size χ and then normalized. (2) We next perform another SVD to bring ΛY into the left canonical form. This is done using $\Lambda Y = X'\Lambda' Y'$ and update $A_{i+1} = X'$, $A_{i+2} = \Lambda' Y' A_{i+2}$. Now, A_i, A_{i+1} are in the left-canonical form. A_{i+2} is not in the canonical form; but this is fine because we will perform $U_{i+2,i+3}$ at the next step, which does not require the canonical form for site $i+2$ and

$i+3$.

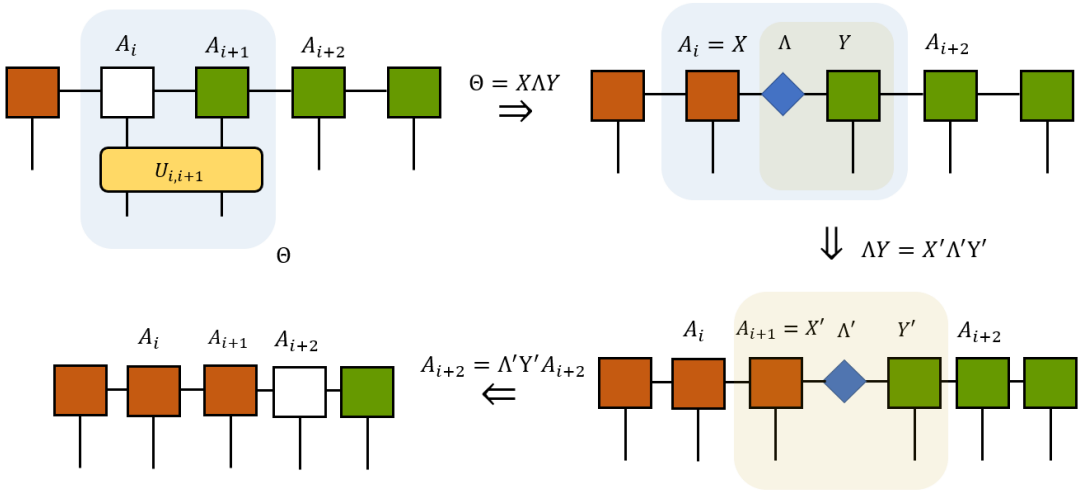

(C.13)

3. Sweep from the right to the left by acting $U_{N-2,N-1}, U_{N-4,N-3}, \cdots, U_{2,3}$ and bring the MPS to the right-canonical form in a similar way.

4. Repeat step 2 and step 3 until convergence. The final MPS is in the right-canonical form and can be used to compute the expectation of ground-state energy. To utilize the right canonical form, we compute $\langle H_{i,i+1} \rangle$ from the left to right, and after each step, we bring A_i to the left-canonical form by SVD: $A_i = X, A_{i+1} = \Lambda Y A_{i+1}$. We then compute $\langle H_{i+1,i+2} \rangle$. This is illustrated below with emphasis on the order of

contraction,

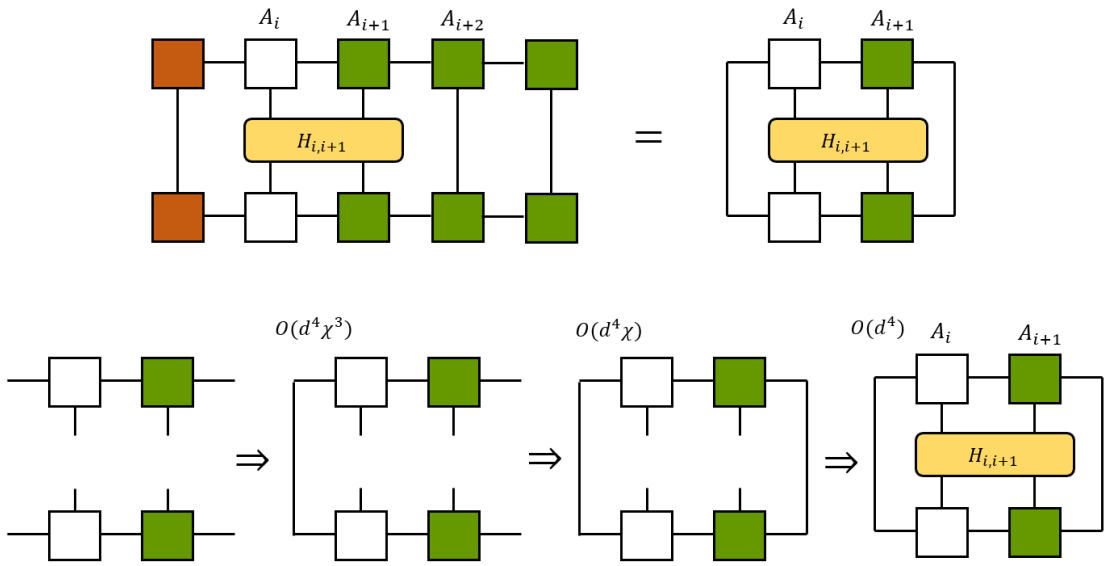

(C.14)

The order of contraction is important so that the time complexity is no more than $O(\chi^3)$.

Let's stress again that in the above description, the canonical form, truncation, normalization, and complexity are taken care of. These details are important for numerical implementation, albeit frequently omitted in publications.

Although TEBD is not the most efficient ground-state searching tensor network algorithm, it is easy to implement and always serves as a benchmark. Furthermore, TEBD is useful for another task, time evolution, which plays an important role in the simulation of time-dependent dynamics. For example, TEBD-like algorithms are widely used in simulating the Lindbladian dynamics [215, 216]. It is worthy to carefully examine the canonical form, truncation, normalization, and complexity of the tensor network algorithm for the mixed state dynamics, so as to understand the applicability of such algorithms. We leave this to our future work.

REFERENCES

[1] J. L. Cardy, O. A. Castro-Alvaredo, and B. Doyon, "Form factors of branch-point twist fields in quantum integrable models and entanglement entropy," *Journal of Statistical Physics*, vol. 130, pp. 129–168, 2008.

[2] J. Haegeman, J. I. Cirac, T. J. Osborne, I. Pižorn, H. Verschelde, and F. Verstraete, "Time-dependent variational principle for quantum lattices," *Physical review letters*, vol. 107, no. 7, p. 070601, 2011.

[3] V. Zauner-Stauber, L. Vanderstraeten, M. T. Fishman, F. Verstraete, and J. Haegeman, "Variational optimization algorithms for uniform matrix product states," *Physical Review B*, vol. 97, no. 4, p. 045145, 2018.

[4] M. J. Donald, M. Horodecki, and O. Rudolph, "The uniqueness theorem for entanglement measures," *Journal of Mathematical Physics*, vol. 43, no. 9, pp. 4252–4272, 2002.

[5] R. Horodecki *et al.*, "Information-theoretic aspects of inseparability of mixed states," *Physical Review A*, vol. 54, no. 3, p. 1838, 1996.

[6] K. G. H. Vollbrecht and M. M. Wolf, "Conditional entropies and their relation to entanglement criteria," *Journal of Mathematical Physics*, vol. 43, no. 9, pp. 4299–4306, 2002.

[7] R. Horodecki, P. Horodecki, M. Horodecki, and K. Horodecki, "Quantum entanglement," *Reviews of modern physics*, vol. 81, no. 2, p. 865, 2009.

[8] H. Li and F. D. M. Haldane, "Entanglement spectrum as a generalization of entanglement entropy: Identification of topological order in non-abelian fractional quantum hall effect states," *Physical review letters*, vol. 101, no. 1, p. 010504, 2008.

[9] J. Eisert, M. Cramer, and M. B. Plenio, "Colloquium: Area laws for the entanglement entropy," *Reviews of modern physics*, vol. 82, no. 1, p. 277, 2010.

[10] M. B. Hastings, "An area law for one-dimensional quantum systems," *Journal of statistical mechanics: theory and experiment*, vol. 2007, no. 08, p. P08024, 2007.

[11] D. Perez-Garcia, F. Verstraete, M. M. Wolf, and J. I. Cirac, "Matrix product state representations," *arXiv preprint quant-ph/0608197*, 2006.

[12] A. Kitaev and J. Preskill, "Topological entanglement entropy," *Physical review letters*, vol. 96, no. 11, p. 110404, 2006.

[13] M. Levin and X.-G. Wen, "Detecting topological order in a ground state wave function," *Physical review letters*, vol. 96, no. 11, p. 110405, 2006.

[14] D. N. Page, "Average entropy of a subsystem," *Physical review letters*, vol. 71, no. 9, p. 1291, 1993.

[15] S. Sen, "Average entropy of a quantum subsystem," *Physical review letters*, vol. 77, no. 1, p. 1, 1996.

[16] S. Foong and S. Kanno, "Proof of page's conjecture on the average entropy of a subsystem," *Physical review letters*, vol. 72, no. 8, p. 1148, 1994.

[17] E. Bianchi, L. Hackl, M. Kieburg, M. Rigol, and L. Vidmar, "Volume-Law Entanglement Entropy of Typical Pure Quantum States," *PRX Quantum*, vol. 3, p. 030201, Jul 2022.

[18] W. Fu and S. Sachdev, "Numerical study of fermion and boson models with infinite-range random interactions," *Physical Review B*, vol. 94, no. 3, p. 035135, 2016.

[19] C. Liu, X. Chen, and L. Balents, "Quantum entanglement of the sachdev-ye-kitaev models," *Physical Review B*, vol. 97, no. 24, p. 245126, 2018.

[20] D. Gioev and I. Klich, "Entanglement entropy of fermions in any dimension and the widom conjecture," *Physical review letters*, vol. 96, no. 10, p. 100503, 2006.

[21] T. Nishioka, "Entanglement entropy: holography and renormalization group," *Reviews of Modern Physics*, vol. 90, no. 3, p. 035007, 2018.

[22] S. Bravyi, "Lagrangian representation for fermionic linear optics," *arXiv preprint quant-ph/0404180*, 2004.

[23] I. Peschel, "Calculation of reduced density matrices from correlation functions," *Journal of Physics A: Mathematical and General*, vol. 36, no. 14, p. L205, 2003.

[24] M.-C. Chung and I. Peschel, "Density-matrix spectra of solvable fermionic systems," *Physical Review B*, vol. 64, no. 6, p. 064412, 2001.

[25] I. Peschel and V. Eisler, "Reduced density matrices and entanglement entropy in free lattice models," *Journal of physics a: mathematical and theoretical*, vol. 42, no. 50, p. 504003, 2009.

[26] P. M. Tam, M. Claassen, and C. L. Kane, "Topological multipartite entanglement in a fermi liquid," *Physical Review X*, vol. 12, no. 3, p. 031022, 2022.

[27] P. Francesco, P. Mathieu, and D. Sénéchal, *Conformal field theory*. Springer Science & Business Media, 2012.

[28] R. Blumenhagen and E. Plauschinn, *Introduction to conformal field theory: with applications to string theory*, vol. 779. Springer Science & Business Media, 2009.

[29] P. Ginsparg, "Applied conformal field theory," *arXiv preprint hep-th/9108028*, 1988.

[30] A. Milsted and G. Vidal, "Extraction of conformal data in critical quantum spin chains using the koo-saleur formula," *Physical Review B*, vol. 96, no. 24, p. 245105, 2017.

[31] Y. Zou, A. Milsted, and G. Vidal, "Conformal fields and operator product expansion in critical quantum spin chains," *Physical Review Letters*, vol. 124, no. 4, p. 040604, 2020.

[32] Y. Zou and G. Vidal, "Emergence of conformal symmetry in quantum spin chains: Antiperiodic boundary conditions and supersymmetry," *Physical Review B*, vol. 101, no. 4, p. 045132, 2020.

[33] Y. Zou, "Universal information of critical quantum spin chains from wavefunction overlap," *Physical Review B*, vol. 105, no. 16, p. 165420, 2022.

[34] W. Koo and H. Saleur, "Representations of the virasoro algebra from lattice models," *Nuclear Physics B*, vol. 426, no. 3, pp. 459–504, 1994.

[35] J. L. Cardy, "Boundary conditions, fusion rules and the verlinde formula," *Nuclear Physics B*, vol. 324, no. 3, pp. 581–596, 1989.

[36] M. Miyaji, S. Ryu, T. Takayanagi, and X. Wen, "Boundary states as holographic duals of trivial spacetimes," *Journal of High Energy Physics*, vol. 2015, no. 5, pp. 1–31, 2015.

[37] P. Calabrese and J. Cardy, "Entanglement entropy and quantum field theory," *Journal of statistical mechanics: theory and experiment*, vol. 2004, no. 06, p. P06002, 2004.

[38] P. Calabrese and J. Cardy, "Entanglement entropy and conformal field theory," *Journal of physics a: mathematical and theoretical*, vol. 42, no. 50, p. 504005, 2009.

[39] X.-L. Qi, H. Katsura, and A. W. Ludwig, "General relationship between the entanglement spectrum and the edge state spectrum of topological quantum states," *Physical review letters*, vol. 108, no. 19, p. 196402, 2012.

[40] R. Lundgren, Y. Fuji, S. Furukawa, and M. Oshikawa, "Entanglement spectra between coupled tomonaga-luttinger liquids: Applications to ladder systems and topological phases," *Phys. Rev. B*, vol. 88, p. 245137, Dec 2013.

[41] J. Cano, T. L. Hughes, and M. Mulligan, "Interactions along an entanglement cut in $2+1$D abelian topological phases," *Phys. Rev. B*, vol. 92, p. 075104, Aug 2015.

[42] X. Wen, S. Matsuura, and S. Ryu, "Edge theory approach to topological entanglement entropy, mutual information, and entanglement negativity in chern-simons theories," *Physical Review B*, vol. 93, no. 24, p. 245140, 2016.

[43] R. Sohal, B. Han, L. H. Santos, and J. C. Y. Teo, "Entanglement entropy of generalized moore-read fractional quantum hall state interfaces," *Phys. Rev. B*, vol. 102, p. 045102, Jul 2020.

[44] P. K. Lim, H. Asasi, J. C. Y. Teo, and M. Mulligan, "Disentangling (2+1)d topological states of matter with the entanglement negativity," 2021.

[45] Y. Liu, R. Sohal, J. Kudler-Flam, and S. Ryu, "Multipartitioning topological phases by vertex states and quantum entanglement," *Physical Review B*, vol. 105, no. 11, p. 115107, 2022.

[46] D. Das and S. Datta, "Universal features of left-right entanglement entropy," *Phys. Rev. Lett.*, vol. 115, p. 131602, Sep 2015.

[47] S. Dong, E. Fradkin, R. G. Leigh, and S. Nowling, "Topological entanglement entropy in chern-simons theories and quantum hall fluids," *Journal of High Energy Physics*, vol. 2008, no. 05, p. 016, 2008.

[48] Y. Zhang, T. Grover, A. Turner, M. Oshikawa, and A. Vishwanath, "Quasiparticle statistics and braiding from ground-state entanglement," *Physical Review B*, vol. 85, no. 23, p. 235151, 2012.

[49] K. Siva, Y. Zou, T. Soejima, R. S. K. Mong, and M. P. Zaletel, "Universal tripartite entanglement signature of ungappable edge states," *Phys. Rev. B*, vol. 106, p. L041107, Jul 2022.

[50] I. H. Kim, B. Shi, K. Kato, and V. V. Albert, "Chiral central charge from a single bulk wave function," *Physical Review Letters*, vol. 128, no. 17, p. 176402, 2022.

[51] I. H. Kim, B. Shi, K. Kato, and V. V. Albert, "Modular commutator in gapped quantum many-body systems," *Phys. Rev. B*, vol. 106, p. 075147, Aug. 2022.

[52] Y. Liu, Y. Kusuki, J. Kudler-Flam, R. Sohal, and S. Ryu, "Multipartite entanglement in two-dimensional chiral topological liquids," *arXiv preprint arXiv:2301.07130*, 2023.

[53] S. Dutta and T. Faulkner, "A canonical purification for the entanglement wedge cross-section," *Journal of High Energy Physics*, vol. 2021, p. 178, Mar. 2021.

[54] C. Akers and P. Rath, "Entanglement wedge cross sections require tripartite entanglement," *Journal of High Energy Physics*, vol. 2020, no. 4, pp. 1–21, 2020.

[55] Y. Zou, K. Siva, T. Soejima, R. S. K. Mong, and M. P. Zaletel, "Universal Tripartite Entanglement in One-Dimensional Many-Body Systems," *Physical Review Letter*, vol. 126, p. 120501, Mar. 2021.

[56] P. Hayden, O. Parrikar, and J. Sorce, "The Markov gap for geometric reflected entropy," *Journal of High Energy Physics*, vol. 2021, p. 47, Oct. 2021.

[57] R. Sohal and S. Ryu, "Entanglement in tripartitions of topological orders: a diagrammatic approach," *arXiv preprint arXiv:2301.07763*, 2023.

[58] Y. Kusuki and K. Tamaoka, "Entanglement wedge cross section from CFT: dynamics of local operator quench," *Journal of High Energy Physics*, vol. 2020, p. 17, Feb. 2020.

[59] Y. Kusuki and K. Tamaoka, "Dynamics of entanglement wedge cross section from conformal field theories," *Physics Letters B*, vol. 814, p. 136105, Mar. 2021.

[60] J. Kudler-Flam, Y. Kusuki, and S. Ryu, "Correlation measures and the entanglement wedge cross-section after quantum quenches in two-dimensional conformal field theories," *Journal of High Energy Physics*, vol. 2020, p. 74, Apr. 2020.

[61] Y. Zou and G. Vidal, "Multiboundary generalization of thermofield double states and their realization in critical quantum spin chains," *Physical Review B*, vol. 105, no. 12, p. 125125, 2022.

[62] P. Hayden, O. Parrikar, and J. Sorce, "The markov gap for geometric reflected entropy," *Journal of High Energy Physics*, vol. 2021, no. 10, pp. 1–58, 2021.

[63] P. Bueno and H. Casini, "Reflected entropy, symmetries and free fermions," *Journal of High Energy Physics*, vol. 2020, no. 2003.09546, pp. 1–29, 2020.

[64] D. J. Gross and A. Jevicki, "Operator formulation of interacting string field theory (i)," *Nuclear Physics*, vol. 283, pp. 1–49, 1987.

[65] D. J. Gross and A. Jevicki, "Operator formulation of interacting string field theory (iii). nsr superstring," *Nuclear Physics B*, vol. 293, pp. 29–82, 1987.

[66] D. J. Gross and A. Jevicki, "Operator formulation of interacting string field theory (ii)," *Nuclear Physics B*, vol. 287, pp. 225–250, 1987.

[67] A. LeClair, M. E. Peskin, and C. R. Preitschopf, "String field theory on the conformal plane (i).: Kinematical principles," *Nuclear Physics B*, vol. 317, no. 2, pp. 411–463, 1989.

[68] A. Jevicki and B. Sazdović, "Supersymmetry transformations in the operator formulation of string field theory," *Annals of Physics*, vol. 188, no. 2, pp. 347–385, 1988.

[69] E. Witten, "Non-commutative geometry and string field theory," *Nuclear Physics B*, vol. 268, no. 2, pp. 253–294, 1986.

[70] Y. Imamura, H. Isono, and Y. Matsuo, "Boundary states in the open string channel and cft near a corner," *Progress of theoretical physics*, vol. 115, no. 5, pp. 979–1002, 2006.

[71] Y. Imamura, H. Isono, and Y. Matsuo, "Boundary state of superstring in open string channel," *Progress of Theoretical Physics*, vol. 119, no. 4, pp. 643–662, 2008.

[72] H. Yao and X.-L. Qi, "Entanglement entropy and entanglement spectrum of the kitaev model," *Physical review letters*, vol. 105, no. 8, p. 080501, 2010.

[73] H. Shapourian, P. Ruggiero, S. Ryu, and P. Calabrese, "Twisted and untwisted negativity spectrum of free fermions," *SciPost Phys.*, vol. 7, p. 37, 2019.

[74] K. Inamura, R. Kobayashi, and S. Ryu, "Non-local order parameters and quantum entanglement for fermionic topological field theories," *Journal of High Energy Physics*, vol. 2020, no. 1, p. 121, 2020.

[75] I. D. Rodríguez and G. Sierra, "Entanglement entropy of integer quantum hall states in polygonal domains," *Journal of Statistical Mechanics: Theory and Experiment*, vol. 2010, p. P12033, dec 2010.

[76] B. Sirois, L. M. Fournier, J. Leduc, and W. Witczak-Krempa, "Geometric entanglement in integer quantum Hall states," *Physical Review B*, vol. 103, p. 115115, Mar. 2021.

[77] D. Ye, Y. Yang, Q. Li, and Z.-X. Hu, "Entanglement entropy of the quantum hall edge and its geometric contribution," *Frontiers in Physics*, vol. 10, nov 2022.

[78] B. Estienne, J.-M. Stéphan, and W. Witczak-Krempa, "Cornering the universal shape of fluctuations," *Nature Communications*, vol. 13, jan 2022.

[79] C. Berthiere, B. Estienne, J.-M. Stéphan, and W. Witczak-Krempa, "Full-counting statistics of charge fluctuations in quantum hall states," 2022.

[80] B. Estienne and J.-M. Stéphan, "Entanglement spectroscopy of chiral edge modes in the quantum hall effect," *Physical Review B*, vol. 101, mar 2020.

[81] C.-C. Liu, J. Geoffrion, and W. Witczak-Krempa, "Entanglement negativity versus mutual information in the quantum hall effect and beyond," 2022.

[82] J. E. Avron, M. Klein, A. Pnueli, and L. Sadun, "Hall conductance and adiabatic charge transport of leaky tori," *Physical Review Letter*, vol. 69, pp. 128–131, July 1992.

[83] T. Can, "Central charge from adiabatic transport of cusp singularities in the quantum hall effect," *Journal of Physics A: Mathematical and Theoretical*, vol. 50, p. 174004, mar 2017.

[84] T. Can and P. Wiegmann, "Quantum Hall states and conformal field theory on a singular surface," *Journal of Physics A Mathematical General*, vol. 50, p. 494003, Dec. 2017.

[85] K. Sakai and Y. Satoh, "Entanglement through conformal interfaces," *Journal of High Energy Physics*, vol. 2008, p. 001, Dec. 2008.

[86] E. Brehm, I. Brunner, D. Jaud, and C. Schmidt-Colinet, "Entanglement and topological interfaces," *Fortschritte der Physik*, vol. 64, pp. 516–535, June 2016.

[87] Y. Kusuki, "Reflected Entropy in Boundary/Interface Conformal Field Theory," *arXiv e-prints*, p. arXiv:2206.04630, June 2022.

[88] I. D. Rodríguez and G. Sierra, "Entanglement entropy of integer quantum hall states," *Physical Review B*, vol. 80, oct 2009.

[89] A. Gromov, K. Jensen, and A. G. Abanov, "Boundary effective action for quantum hall states," *Physical Review Letters*, vol. 116, mar 2016.

[90] H. Shapourian, K. Shiozaki, and S. Ryu, "Partial time-reversal transformation and entanglement negativity in fermionic systems," *Physical Review B*, vol. 95, apr 2017.

[91] H. Shapourian and S. Ryu, "Entanglement negativity of fermions: Monotonicity, separability criterion, and classification of few-mode states," *Physical Review A*, vol. 99, feb 2019.

[92] P. Calabrese, J. Cardy, and E. Tonni, "Entanglement negativity in quantum field theory," *Physical Review Letters*, vol. 109, sep 2012.

[93] R. Nandkishore and D. A. Huse, "Many-Body Localization and Thermalization in Quantum Statistical Mechanics," *Annu. Rev. Condens. Matter Phys.*, vol. 6, p. 15, 2015.

[94] L. D'Alessio, Y. Kafri, A. Polkovnikov, and M. Rigol, "From quantum chaos and eigenstate thermalization to statistical mechanics and thermodynamics," *Adv. Phys.*, vol. 65, p. 239, 2016.

[95] D. A. Abanin, E. Altman, I. Bloch, and M. Serbyn, "Colloquium: Many-body localization, thermalization, and entanglement," *Rev. Mod. Phys.*, vol. 91, p. 021001, May 2019.

[96] S. Goldstein, J. L. Lebowitz, R. Tumulka, and N. Zanghì, "Canonical Typicality," *Phys. Rev. Lett.*, vol. 96, p. 050403, Feb 2006.

[97] S. Popescu, A. J. Short, and A. Winter, "Entanglement and the foundations of statistical mechanics," *Nat. Phys.*, vol. 2, p. 754, 2006.

[98] P. Reimann, "Foundation of Statistical Mechanics under Experimentally Realistic Conditions," *Phys. Rev. Lett.*, vol. 101, p. 190403, Nov 2008.

[99] J. R. Garrison and T. Grover, "Does a Single Eigenstate Encode the Full Hamiltonian?," *Phys. Rev. X*, vol. 8, p. 021026, Apr 2018.

[100] Y. O. Nakagawa, M. Watanabe, H. Fujita, and S. Sugiura, "Universality in volume-law entanglement of scrambled pure quantum states," *Nat. Commun.*, vol. 9, p. 1635, 2018.

[101] L. Vidmar and M. Rigol, "Entanglement Entropy of Eigenstates of Quantum Chaotic Hamiltonians," *Phys. Rev. Lett.*, vol. 119, p. 220603, Nov 2017.

[102] T.-C. Lu and T. Grover, "Renyi entropy of chaotic eigenstates," *Phys. Rev. E*, vol. 99, p. 032111, Mar 2019.

[103] P. Hayden and J. Preskill, "Black holes as mirrors: quantum information in random subsystems," *J. High Energ. Phys.*, vol. 2007, no. 120, 2007.

[104] H.-H. Lai and K. Yang, "Entanglement entropy scaling laws and eigenstate typicality in free fermion systems," *Phys. Rev. B*, vol. 91, p. 081110, Feb 2015.

[105] C. Liu, X. Chen, and L. Balents, "Quantum entanglement of the Sachdev-Ye-Kitaev models," *Phys. Rev. B*, vol. 97, p. 245126, Jun 2018.

[106] P. Łydżba, M. Rigol, and L. Vidmar, "Eigenstate Entanglement Entropy in Random Quadratic Hamiltonians," *Phys. Rev. Lett.*, vol. 125, p. 180604, Oct 2020.

[107] E. Bianchi, L. Hackl, and M. Kieburg, "Page curve for fermionic Gaussian states," *Phys. Rev. B*, vol. 103, p. L241118, Jun 2021.

[108] B. Bhattacharjee, P. Nandy, and T. Pathak, "Eigenstate capacity and Page curve in fermionic Gaussian states," *Phys. Rev. B*, vol. 104, p. 214306, Dec 2021.

[109] S. Murciano, P. Calabrese, and L. Piroli, "Symmetry-resolved Page curves," *Phys. Rev. D*, vol. 106, p. 046015, Aug 2022.

[110] X.-H. Yu, Z. Gong, and J. I. Cirac, "Free-fermion page curve: Canonical typicality and dynamical emergence," *Physical Review Research*, vol. 5, no. 1, p. 013044, 2023.

[111] J. M. Magán, "Random Free Fermions: An Analytical Example of Eigenstate Thermalization," *Physical Review Letter*, vol. 116, p. 030401, Jan. 2016.

[112] P. Łydżba, Y. Zhang, M. Rigol, and L. Vidmar, "Single-particle eigenstate thermalization in quantum-chaotic quadratic Hamiltonians," *Physical Review B*, vol. 104, p. 214203, Dec. 2021.

[113] I. Ulčakar and L. Vidmar, "Tight-binding billiards," *Physical Review E*, vol. 106, p. 034118, Sept. 2022.

[114] M. Lucas, L. Piroli, J. De Nardis, and A. De Luca, "Generalized deep thermalization for free fermions," *Physical Review A*, vol. 107, no. 3, p. 032215, 2023.

[115] P. Łydżba, M. Mierzejewski, M. Rigol, and L. Vidmar, "Generalized thermalization in quantum-chaotic quadratic hamiltonians," *arXiv preprint arXiv:2210.00016*, 2022.

[116] F. Haake, S. Gnutzmann, and M. Kuś, *Quantum Signatures of Chaos*. Cham, Switzerland: Springer, 2018.

[117] K. Efetov, *Supersymmetry in Disorder and Chaos*. Cambridge, England: Cambridge University Press, 1996.

[118] O. Bohigas, M. J. Giannoni, and C. Schmit, "Characterization of Chaotic Quantum Spectra and Universality of Level Fluctuation Laws," *Phys. Rev. Lett.*, vol. 52, pp. 1–4, Jan 1984.

[119] M. V. Berry and M. Tabor, "Level clustering in the regular spectrum," *Proc. R. Soc. A*, vol. 356, p. 375, 1977.

[120] A. Altland and M. R. Zirnbauer, "Nonstandard symmetry classes in mesoscopic normal-superconducting hybrid structures," *Phys. Rev. B*, vol. 55, p. 1142, Jan 1997.

[121] S. Sachdev and J. Ye, "Gapless spin-fluid ground state in a random quantum Heisenberg magnet," *Phys. Rev. Lett.*, vol. 70, pp. 3339–3342, May 1993.

[122] A. Kitaev, "A simple model of quantum holography." KITP Program: Entanglement in Strongly-Correlated Quantum Matter, 2015.

[123] V. Rosenhaus, "An introduction to the SYK model," *J. Phys. A*, vol. 52, p. 323001, 2019.

[124] D. Chowdhury, A. Georges, O. Parcollet, and S. Sachdev, "Sachdev-Ye-Kitaev models and beyond: Window into non-Fermi liquids," *Rev. Mod. Phys.*, vol. 94, p. 035004, Sep 2022.

[125] Y.-Z. You, A. W. W. Ludwig, and C. Xu, "Sachdev-Ye-Kitaev model and thermalization on the boundary of many-body localized fermionic symmetry-protected topological states," *Phys. Rev. B*, vol. 95, p. 115150, Mar 2017.

[126] W. Fu and S. Sachdev, "Numerical study of fermion and boson models with infinite-range random interactions," *Phys. Rev. B*, vol. 94, p. 035135, Jul 2016.

[127] A. M. García-García and J. J. M. Verbaarschot, "Spectral and thermodynamic properties of the Sachdev-Ye-Kitaev model," *Phys. Rev. D*, vol. 94, p. 126010, Dec 2016.

[128] J. S. Cotler, G. Gur-Ari, M. Hanada, J. Polchinski, P. Saad, S. H. Shenker, D. Stanford, A. Streicher, and M. Tezuka, "Black holes and random matrices," *J. High Energ. Phys.*, vol. 2017, no. 118, 2017.

[129] T. Li, J. Liu, Y. Xin, and Y. Zhou, "Supersymmetric SYK model and random matrix theory," *J. High Energ. Phys.*, vol. 2017, no. 111, 2017.

[130] T. Kanazawa and T. Wettig, "Complete random matrix classification of SYK models with $\mathcal{N} = 0, 1$ and 2 supersymmetry," *J. High Energ. Phys.*, vol. 2017, no. 50, 2017.

[131] J. Behrends, J. H. Bardarson, and B. Béri, "Tenfold way and many-body zero modes in the Sachdev-Ye-Kitaev model," *Phys. Rev. B*, vol. 99, p. 195123, May 2019.

[132] F. Sun and J. Ye, "Periodic Table of the Ordinary and Supersymmetric Sachdev-Ye-Kitaev Models," *Phys. Rev. Lett.*, vol. 124, p. 244101, Jun 2020.

[133] C. W. J. Beenakker, "Random-matrix theory of quantum transport," *Rev. Mod. Phys.*, vol. 69, p. 731, 1997.

[134] F. Evers and A. D. Mirlin, "Anderson transitions," *Rev. Mod. Phys.*, vol. 80, p. 1355, 2008.

[135] A. P. Schnyder, S. Ryu, A. Furusaki, and A. W. W. Ludwig, "Classification of topological insulators and superconductors in three spatial dimensions," *Phys. Rev. B*, vol. 78, p. 195125, Nov 2008.

[136] A. Kitaev, "Periodic table for topological insulators and superconductors," *AIP Conf. Proc.*, vol. 1134, p. 22, 2009.

[137] M. Z. Hasan and C. L. Kane, "Colloquium: Topological insulators," *Rev. Mod. Phys.*, vol. 82, pp. 3045–3067, Nov 2010.

[138] X.-L. Qi and S.-C. Zhang, "Topological insulators and superconductors," *Rev. Mod. Phys.*, vol. 83, pp. 1057–1110, Oct 2011.

[139] C.-K. Chiu, J. C. Y. Teo, A. P. Schnyder, and S. Ryu, "Classification of topological quantum matter with symmetries," *Rev. Mod. Phys.*, vol. 88, p. 035005, 2016.

[140] B. Collins, "Moments and cumulants of polynomial random variables on unitary groups, the Itzykson-Zuber integral, and free probability," *Int. Math. Res. Not.*, vol. 2003, p. 953, 2003.

[141] B. Collins and P. Śniady, "Integration with Respect to the Haar Measure on Unitary, Orthogonal and Symplectic Group," *Commun. Math. Phys.*, vol. 264, p. 773, 2006.

[142] B. Collins and S. Matsumoto, "On some properties of orthogonal Weingarten functions," *J. Math. Phys.*, vol. 50, pp. 113516–113516, Nov. 2009.

[143] S. Matsumoto, "Weingarten calculus for matrix ensembles associated with compact symmetric spaces," *Random Matrices: Theory Appl.*, vol. 2, p. 1350001, 2013.

[144] B. Collins, S. Matsumoto, and J. Novak, "The Weingarten Calculus," *Not. Am. Math. Soc.*, vol. 69, p. 734, 2022.

[145] E. P. Wigner, "On the statistical distribution of the widths and spacings of nuclear resonance levels," *Math. Proc. Cambridge Philos. Soc.*, vol. 47, p. 790, 1951.

[146] F. J. Dyson, "The Threefold Way. Algebraic Structure of Symmetry Groups and Ensembles in Quantum Mechanics," *J. Math. Phys.*, vol. 3, p. 1199, 1962.

[147] M. L. Mehta, *Random Matrices*. Amsterdam: Elsevier, 2004.

[148] P. J. Forrester, *Log-Gases and Random Matrices*. Princeton: Princeton University Press, 2010.

[149] See the Supplemental Material for details about the Altland-Zirnbauer (AZ) symmetry classification, the Wigner surmise, and the Weingarten calculus.

[150] P. H. C. Lau, T. Noumi, Y. Takii, and K. Tamaoka, "Page curve and symmetries," *J. High Energ. Phys.*, vol. 2022, no. 15, 2022.

[151] S. Washburn and R. A. Webb, "Aharonov-Bohm effect in normal metal quantum coherence and transport," *Adv. Phys.*, vol. 35, p. 375, 1986.

[152] Y. Liu, J. Kudler-Flam, and K. Kawabata, "Symmetry classification of typical quantum entanglement," *arXiv preprint arXiv:2301.07778*, 2023.

[153] A. Kitaev and J. Preskill, "Topological Entanglement Entropy," *Phys. Rev. Lett.*, vol. 96, p. 110404, Mar 2006.

[154] M. Levin and X.-G. Wen, "Detecting Topological Order in a Ground State Wave Function," *Phys. Rev. Lett.*, vol. 96, p. 110405, Mar 2006.

[155] S. Ryu and Y. Hatsugai, "Entanglement entropy and the Berry phase in the solid state," *Phys. Rev. B*, vol. 73, p. 245115, Jun 2006.

[156] H. Li and F. D. M. Haldane, "Entanglement Spectrum as a Generalization of Entanglement Entropy: Identification of Topological Order in Non-Abelian Fractional Quantum Hall Effect States," *Phys. Rev. Lett.*, vol. 101, p. 010504, Jul 2008.

[157] L. Fidkowski, "Entanglement Spectrum of Topological Insulators and Superconductors," *Phys. Rev. Lett.*, vol. 104, p. 130502, Apr 2010.

[158] F. Pollmann, A. M. Turner, E. Berg, and M. Oshikawa, "Entanglement spectrum of a topological phase in one dimension," *Phys. Rev. B*, vol. 81, p. 064439, Feb 2010.

[159] K. G. Wilson and J. Kogut, "The renormalization group and the ϵ expansion," *Phys. Rep.*, vol. 12, pp. 75–199, Aug. 1974.

[160] P. Di Francesco, P. Mathieu, and D. Senechal, *Conformal Field Theory*. New York: Springer, 2012.

[161] A. A. Belavin, A. M. Polyakov, and A. B. Zamolodchikov, "Infinite conformal symmetry in two-dimensional quantum field theory," *Nucl. Phys. B*, vol. 241, pp. 333–380, July 1984.

[162] D. Friedan, Z. Qiu, and S. Shenker, "Conformal Invariance, Unitarity, and Critical Exponents in Two Dimensions," *Phys. Rev. Lett.*, vol. 52, pp. 1575–1578, Apr. 1984.

[163] J. L. Cardy, "Conformal invariance and universality in finite-size scaling," *Journal of Physics A: Mathematical and General*, vol. 17, pp. L385–L387, may 1984.

[164] H. W. J. Blöte, J. L. Cardy, and M. P. Nightingale, "Conformal invariance, the central charge, and universal finite-size amplitudes at criticality," *Phys. Rev. Lett.*, vol. 56, p. 742, Feb. 1986.

[165] I. Affleck, "Universal term in the free energy at a critical point and the conformal anomaly," *Phys. Rev. Lett.*, vol. 56, pp. 746–748, Feb. 1986.

[166] J. L. Cardy, "Operator content of two-dimensional conformally invariant theories," *Nucl. Phys. B*, vol. 270, pp. 186–204, 1986.

[167] Y. Zou, A. Milsted, and G. Vidal, "Conformal fields and operator product expansion in critical quantum spin chains," *Phys. Rev. Lett.*, vol. 124, no. 4, p. 040604, 2020.

[168] Y. Zou, "Universal information of critical quantum spin chains from wavefunction overlaps," 2021.

[169] Y. Zou and G. Vidal, "Multi-boundary generalization of thermofield double states and their realization in critical quantum spin chains," *Physical Review B*, vol. 105, no. 12, p. 125125, 2022.

[170] J. Escobedo, N. Gromov, A. Sever, and P. Vieira, "Tailoring three-point functions and integrability," *Journal of High Energy Physics*, vol. 2011, p. 28, Sept. 2011.

[171] Y. Jiang, I. Kostov, A. Petrovskii, and D. Serban, "String bits and the spin vertex," *Nuclear Physics B*, vol. 897, pp. 374–404, 2015.

[172] M. Henkel, *Conformal Perturbation Theory*, pp. 261–278. Berlin, Heidelberg: Springer Berlin Heidelberg, 1999.

[173] S. Mandelstam, "Interacting-string picture of dual-resonance models," *Nuclear Physics B*, vol. 64, pp. 205–235, Nov. 1973.

[174] Y. Baba, N. Ishibashi, and K. Murakami, "Light-cone gauge string field theory in noncritical dimensions," *Journal of High Energy Physics*, vol. 2009, p. 010, Dec. 2009.

[175] N. Ishibashi and K. Murakami, *Sting field theory.* Toko: Saiensu-Sha, 2012.

[176] K. Ohmori and Y. Tachikawa, "Physics at the entangling surface," *Journal of Statistical Mechanics: Theory and Experiment*, vol. 2015, p. P04010, apr 2015.

[177] T.-C. Huang, Y.-H. Lin, K. Ohmori, Y. Tachikawa, and M. Tezuka, "Numerical evidence for a Haagerup conformal field theory," *arXiv e-prints*, p. arXiv:2110.03008, Oct. 2021.

[178] R. Vanhove, L. Lootens, M. V. Damme, R. Wolf, T. Osborne, J. Haegeman, and F. Verstraete, "A critical lattice model for a haagerup conformal field theory," 2021.

[179] V. Balasubramanian, P. Hayden, A. Maloney, D. Marolf, and S. F. Ross, "Multiboundary wormholes and holographic entanglement," *Classical and Quantum Gravity*, vol. 31, p. 185015, sep 2014.

[180] C. Holzhey, F. Larsen, and F. Wilczek, "Geometric and renormalized entropy in conformal field theory," *Nuclear Physics B*, vol. 424, p. 443–467, Aug 1994.

[181] P. Calabrese and J. L. Cardy, "Entanglement entropy and quantum field theory," *J. Stat. Mech.*, vol. 0406, p. P06002, 2004.

[182] J. L. Cardy, O. A. Castro-Alvaredo, and B. Doyon, "Form Factors of Branch-Point Twist Fields in Quantum Integrable Models and Entanglement Entropy," *Journal of Statistical Physics*, vol. 130, pp. 129–168, Jan. 2008.

[183] P. Calabrese and J. Cardy, "Entanglement entropy and conformal field theory," *J. Phys. A*, vol. 42, p. 504005, 2009.

[184] V. G. Knizhnik, "Analytic fields on Riemann surfaces. II," *Communications in Mathematical Physics*, vol. 112, pp. 567–590, Dec. 1987.

[185] L. Dixon, D. Friedan, E. Martinec, and S. Shenker, "The conformal field theory of orbifolds," *Nuclear Physics B*, vol. 282, pp. 13–73, Jan. 1987.

[186] R. Dijkgraaf, E. Verlinde, and H. Verlinde, "C=1 conformal field theories on Riemann surfaces," *Communications in Mathematical Physics*, vol. 115, pp. 649–690, Dec. 1988.

[187] R. Dijkgraaf, C. Vafa, E. Verlinde, and H. Verlinde, "The operator algebra of orbifold models," *Communications in Mathematical Physics*, vol. 123, pp. 485–526, Sept. 1989.

[188] V. G. Kac and M. Wakimoto, "Branching functions for winding subalgebras and tensor products," *Topics in Computational Algebra*, pp. 3–39, 1990.

[189] L. Dolan, P. Goddard, and P. Montague, "Conformal field theory of twisted vertex operators," *Nuclear Physics B*, vol. 338, pp. 529–601, July 1990.

[190] P. Bouwknegt, "Coset construction for winding subalgebras and applications," *eprint arXiv:q-alg/9610013*, pp. q–alg/9610013, Oct. 1996.

[191] C. Dong, H. Li, and G. Mason, "Twisted representations of vertex operator algebras and associative algebras," *eprint arXiv:q-alg/9702027*, pp. q–alg/9702027, Feb. 1997.

[192] L. Borisov, M. B. Halpern, and C. Schweigert, "Systematic Approach to Cyclic Orbifolds," *International Journal of Modern Physics A*, vol. 13, pp. 125–168, Jan. 1998.

[193] A. Klemm and M. G. Schmidt, "Orbifolds by cyclic permutations of tensor product conformal field theories," *Physics Letters B*, vol. 245, pp. 53–58, Aug. 1990.

[194] T. Dupic, B. Estienne, and Y. Ikhlef, "Entanglement entropies of minimal models from null-vectors," *SciPost Physics*, vol. 4, p. 031, June 2018.

[195] D. Bianchini, O. A. Castro-Alvaredo, and B. Doyon, "Entanglement entropy of non-unitary integrable quantum field theory," *Nuclear Physics B*, vol. 896, pp. 835–880, July 2015.

[196] M. Goldstein and E. Sela, "Symmetry-Resolved Entanglement in Many-Body Systems," *Physical Review Letter*, vol. 120, p. 200602, May 2018.

[197] O. A. Castro-Alvaredo, B. Doyon, and E. Levi, "Arguments towards a c-theorem from branch-point twist fields," *arXiv e-prints*, p. arXiv:1107.4280, July 2011.

[198] Y. Liu, Y. Zou, and S. Ryu, "Operator fusion from wavefunction overlaps: Universal finite-size corrections and application to haagerup model," *arXiv preprint arXiv:2203.14992*, 2022.

[199] P. Calabrese, J. Cardy, and E. Tonni, "Entanglement negativity in extended systems: a field theoretical approach," *Journal of Statistical Mechanics: Theory and Experiment*, vol. 2013, p. 02008, Feb. 2013.

[200] P. Calabrese, J. Cardy, and E. Tonni, "Entanglement Negativity in Quantum Field Theory," *Physical Review Letter*, vol. 109, p. 130502, Sept. 2012.

[201] I. Peschel and V. Eisler, "Reduced density matrices and entanglement entropy in free lattice models," *Journal of Physics A: Mathematical and Theoretical*, vol. 42, p. 504003, dec 2009.

[202] T.-C. Huang and Y.-H. Lin, "The F-Symbols for Transparent Haagerup-Izumi Categories with $G = \mathbb{Z}_{2n+1}$," *arXiv e-prints*, p. arXiv:2007.00670, July 2020.

[203] T. J. Osborne, D. E. Stiegemann, and R. Wolf, "The F-Symbols for the H3 Fusion Category," *arXiv e-prints*, p. arXiv:1906.01322, June 2019.

[204] A. Feiguin, S. Trebst, A. W. W. Ludwig, M. Troyer, A. Kitaev, Z. Wang, and M. H. Freedman, "Interacting Anyons in Topological Quantum Liquids: The Golden Chain," *Physical Review Letter*, vol. 98, p. 160409, Apr. 2007.

[205] M. Buican and A. Gromov, "Anyonic Chains, Topological Defects, and Conformal Field Theory," *Communications in Mathematical Physics*, vol. 356, pp. 1017–1056, Dec. 2017.

[206] W. Koo and H. Saleur, "Representations of the virasoro algebra from lattice models," *Nuclear Physics B*, vol. 426, no. 3, pp. 459–504, 1994.

[207] A. Milsted and G. Vidal, "Extraction of conformal data in critical quantum spin chains using the koo-saleur formula," *Phys. Rev. B*, vol. 96, p. 245105, Dec 2017.

[208] S. Dulat and K. Wendland, "Crystallographic orbifolds: towards a classification of unitary conformal field theories with central charge c = 2," *Journal of High Energy Physics*, vol. 2000, p. 012, June 2000.

[209] "Numerical diagonalization of the hamiltonian of the quantum spin model." `https://qiita.com/fockl/items/52593901b9a5f78cda92`. Accessed: 2021-02-21.

[210] J. Zhang and R. Dong, "Exact diagonalization: the bose–hubbard model as an example," *European Journal of Physics*, vol. 31, no. 3, p. 591, 2010.

[211] U. Schollwöck, "The density-matrix renormalization group in the age of matrix product states," *Annals of physics*, vol. 326, no. 1, pp. 96–192, 2011.

[212] U. Schollwöck, "The density-matrix renormalization group," *Reviews of modern physics*, vol. 77, no. 1, p. 259, 2005.

[213] S. R. White and A. E. Feiguin, "Real-time evolution using the density matrix renormalization group," *Physical review letters*, vol. 93, no. 7, p. 076401, 2004.

[214] G. Vidal, "Classical simulation of infinite-size quantum lattice systems in one spatial dimension," *Physical review letters*, vol. 98, no. 7, p. 070201, 2007.

[215] Z. Cai and T. Barthel, "Algebraic versus exponential decoherence in dissipative many-particle systems," *Physical review letters*, vol. 111, no. 15, p. 150403, 2013.

[216] M. Žnidarič, "Relaxation times of dissipative many-body quantum systems," *Physical Review E*, vol. 92, no. 4, p. 042143, 2015.